

A NUMERICAL APPROACH FOR THE SOLUTIONS OF FLUID DYNAMICS
PROBLEMS IN THE PRESENCE OF MAGNETIC FIELD

A THESIS SUBMITTED TO
THE GRADUATE SCHOOL OF NATURAL AND APPLIED SCIENCES
OF
MIDDLE EAST TECHNICAL UNIVERSITY

BY

FATMA SİDRE OĞLAKKAYA

IN PARTIAL FULFILLMENT OF THE REQUIREMENTS
FOR
THE DEGREE OF DOCTOR OF PHILOSOPHY
IN
MATHEMATICS

MAY 2018

Approval of the thesis:

**A NUMERICAL APPROACH FOR THE SOLUTIONS OF FLUID
DYNAMICS PROBLEMS IN THE PRESENCE OF MAGNETIC FIELD**

submitted by **FATMA SİDRE OĞLAKKAYA** in partial fulfillment of the requirements for the degree of **Doctor of Philosophy in Mathematics Department, Middle East Technical University** by,

Prof. Dr. Halil Kalıpçılar
Dean, Graduate School of **Natural and Applied Sciences**

Prof. Dr. Yıldırım Ozan
Head of Department, **Mathematics**

Assoc. Prof. Dr. Canan Bozkaya
Supervisor, **Department of Mathematics , METU**

Examining Committee Members:

Prof. Dr. Münevver Tezer
Mathematics Dept., METU

Assoc. Prof. Dr. Canan Bozkaya
Mathematics Dept., METU

Prof. Dr. Hakan Işık Tarman
Mechanical Engineering Dept., METU

Prof. Dr. Mustafa Türkyılmazoğlu
Mathematics Dept., Hacettepe University

Assoc. Prof. Dr. Niyazi Şahin
Mathematics-Computer Dept., Yıldırım Beyazıt University

Date:

I hereby declare that all information in this document has been obtained and presented in accordance with academic rules and ethical conduct. I also declare that, as required by these rules and conduct, I have fully cited and referenced all material and results that are not original to this work.

Name, Last Name: FATMA SİDRE OĞLAKKAYA

Signature :

ABSTRACT

A NUMERICAL APPROACH FOR THE SOLUTIONS OF FLUID DYNAMICS PROBLEMS IN THE PRESENCE OF MAGNETIC FIELD

OĞLAKKAYA, FATMA SİDRE

Ph.D., Department of Mathematics

Supervisor : Assoc. Prof. Dr. Canan Bozkaya

May 2018, 178 pages

This thesis is conducted to investigate numerically the two-dimensional steady or unsteady, laminar flow of viscous, incompressible and electrically conducting fluids in complex geometries subject to either uniform inclined magnetic field or nodal magnetic sources. Specifically, the hydromagnetic natural/mixed convection of either conventional fluid or water-based nanofluid flow and the heat transfer are considered in irregular enclosures with wavy walls. The equations governing the steady magnetohydrodynamic (MHD) convection flow, which are obtained from the Navier-Stokes, the energy equations of fluid dynamics and the electromagnetic equations of the magnetohydrodynamics discretized by using the dual reciprocity boundary element method (DRBEM). The DRBEM uses the fundamental solution of the Laplace equation and treats all the other terms in the equations as non-homogeneity which is approximated by radial basis functions. On the other hand, for the unsteady MHD convection flow and heat transfer problems the DRBEM in space is combined with a two-level integration scheme in time; and the numerical stability analysis is further performed in terms of time increment, time relaxation parameters and the several

physical controlling parameters. The proposed numerical technique is first applied for the steady/unsteady mixed convection flow in a lid-driven cavity with a wall involving flat, semi-rectangular, semi-circular or sinusoidal heaters with Joule heating effect in the presence of inclined magnetic field. Later, the numerical simulation of the MHD natural convection flow not only in an inclined semi-circular annulus enclosure but also in a semi-annulus enclosure with a sinusoidal wavy inner wall filled with a water-based nanofluid is studied under the influence of a uniform inclined magnetic field. Finally, the effects of the nodal magnetic sources and the complex geometry of the computational domain on the ferrofluid flow and the heat transfer are investigated in annulus enclosures with different types of sinusoidal inner walls determined by using different number of undulation. The results obtained for all problems under consideration are visualized in terms of streamlines, isotherms and average Nusselt number for various combinations of physical controlling parameters, namely Hartmann number, Rayleigh number, Joule heating parameter, inclination angle of the externally applied magnetic field, number of undulation determining the shape of the wavy wall and the solid volume fraction. It is well-observed that the strength of the magnetic field and incorporating nanoparticles to conventional fluids can be used to control the fluid flow and the heat transfer enhancement in irregular enclosures with wavy walls.

Keywords: DRBEM, MHD, FHD, irregular enclosure, nodal magnetic source, numerical stability

ÖZ

MANYETİK ALAN ETKİSİNDEKİ AKIŞKANLAR MEKANİĞİ PROBLEMLERİ İÇİN SAYISAL ÇÖZÜM YAKLAŞIMLARI

OĞLAKKAYA, FATMA SİDRE

Doktora, Matematik Bölümü

Tez Yöneticisi : Doç. Dr. Canan Bozkaya

Mayıs 2018 , 178 sayfa

Bu tez, düzgün eğimli manyetik alana veya noktasal manyetik kaynaklara tabi olan kompleks geometrilerdeki viskoz, sıkıştırılamayan ve elektriksel olarak iletken akışkanların iki boyutlu zamana bağlı ya da zamana bağlı olmayan laminar akışını sayısal olarak araştırmak için yürütülmüştür. Özellikle, düz ya da dalgalı duvarları olan düzensiz ve karmaşık bir yapıya sahip olan kanal kesitlerinde klasik sıvı ya da su bazlı nano-sıvı akışının ve ısı transferinin hidromanyetik doğal / karışık konveksiyonu düşünülmektedir. Akışkanlar mekaniğinin Navier-Stokes ve enerji denklemleri ile manyetohidrodinamiğin elektromanyetik denklemlerinden elde edilen zaman bağımsız magnetohidrodinamik (MHD) konveksiyon akışını niteleyen denklemler, karşılıklı sınır elemanları yöntemi (DRBEM) kullanılarak ayrıştırılır. Karşılıklı sınır elemanları yöntemi Laplace denkleminin temel çözümünü kullanır ve denklemlerdeki homojen olmayan diğer tüm terimleri radyal bazlı fonksiyonları kullanarak yaklaşık olarak hesaplar. Öte yandan, zamana bağlı MHD konveksiyon akış ve ısı transferi problemlerinin ayrıklaştırılmasında uzay koordinatları için DRBEM, zaman yönünde ise iki seviyeli bir zaman entegrasyon yöntemi kullanılır. Ayrıca, kullanılan yöntem

min sayısal kararlılık analizi, zaman artışı, zaman yumuşatma parametreleri ve bazı fiziksel kontrol parametrelerine bağlı olarak gerçekleştirilir. Önerilen sayısal teknik, ilk önce eğimli manyetik alan varlığında Joule ısıtma parametresinin dikkate alındığı düz, yarı-dikdörtgen, yarı-dairesel veya sinüzoidal dalgalı ısıtıcılar içeren duvar ve kapakla yönlendirilen bir oyuktaki zaman bağımsız/zaman bağımlı karışık konveksiyon akışının çözümünde kullanılır. Daha sonra MHD doğal konveksiyon akışının sayısal simülasyonu, içerisi su-bazlı nanosıvı ile doldurulmuş eğimli bir yarı dairesel halka şeklindeki oyukun yanı sıra sinüzoidal dalgalı bir iç duvara sahip yarı-halka şeklindeki bir oyukta düzgün eğimli manyetik alan etkisi altında incelenmiştir. Son olarak, noktasal manyetik kaynakların ferro-akışkan akış ve ısı transferi üzerindeki etkileri, farklı sayıda dalgalanma kullanılarak belirlenen sinüzoidal iç duvarlara sahip karmaşık yapıdaki halka oyuklar içerisinde incelenmiştir. Ele alınan tüm problemler için elde edilen sonuçlar, Hartmann sayısı, Rayleigh sayısı, Joule ısıtma parametresi, manyetik alanın eğim açısı, dalgalı duvarın şeklini belirleyen dalgalanma ve katı hacim fraksiyonu gibi sayısal kontrol parametrelerinin çeşitli kombinasyonları için akış çizgileri, eş sıcaklık eğrileri ve ortalama Nusselt sayısı açısından görselleştirilmiştir. Bu çalışma ile dalgalı duvarlar ile oluşturulan düzensiz yapıya sahip oyuklardaki magnetohidrodinamik akış problemlerinde sisteme uygulanan manyetik alan kuvvetinin arttırılmasının ve klasik akışlara nanopartiküllerin eklenmesinin, akışkan akışını ve ısı transferi arttırımını kontrol etmek için kullanılabileceği gözlemlenmiştir.

Anahtar Kelimeler: Karşılıklı sınır elemanları yöntemi, Magnetohidrodinamik, Ferrohidrodinamik, düzensiz oyuklar, sayısal kararlılık

*To my parents; İsmet & Güner,
and my sister, Ayşe Nur*

ACKNOWLEDGMENTS

Foremost, I would like to express my sincere gratitude to my advisor Assoc. Prof. Dr. Canan Bozkaya for the continuous support of my Ph.D study and research, for her patience, motivation, enthusiasm, and immense knowledge. Her guidance helped me in all the time of research and writing of this thesis.

Besides my advisor, I am also grateful to the members of my defense committee, Prof. Dr. Münevver Tezer, Prof. Dr. Hakan Tarman, Prof. Dr. Mustafa Türkyılmazoğlu, Assoc. Prof. Dr. Niyazi Şahin for their insightful comments, encouragement and reviewing my work.

I would like to thank my friends and my colleagues from the Department of Mathematics who have contributed immensely to my personal and professional time at Middle East Technical University. They have been a source of friendships as well as good academicians and collaborations.

Last, but not the least, I would like to express my gratitude to my family, İsmet, Güner and Ayşe Nur for all their love and encouragement and also their supports during this long period of writing my Ph.D thesis.

TABLE OF CONTENTS

ABSTRACT	v
ÖZ	vii
ACKNOWLEDGMENTS	x
TABLE OF CONTENTS	xi
LIST OF TABLES	xv
LIST OF FIGURES	xvii
LIST OF ABBREVIATIONS	xxiii
CHAPTERS	
1 INTRODUCTION	1
1.1 Literature Review	6
1.2 Contribution of the Thesis	12
1.3 Basic Fluid Dynamics Equations	13
1.3.1 Continuity equation	13
1.3.2 Momentum equation	14
1.3.3 Navier-Stokes equations	16
1.3.4 Energy equation	18
1.4 The MHD Flow Equations	20

1.4.1	The unsteady MHD mixed convection of conventional purefluid flow equations	21
1.4.2	The unsteady MHD convection of nanofluid flow equations	23
1.4.3	The steady MHD convection of ferrofluid flow equations	25
1.5	Nusselt Number	30
1.6	Plan of the Thesis	31
2	THE BOUNDARY AND THE DUAL RECIPROCITY BOUNDARY ELEMENT METHODS	33
2.1	Boundary Element Method	35
2.1.1	Application of BEM to the Laplace equation	35
2.1.2	Discretization of the boundary	37
2.1.2.1	Discretization with constant elements	38
2.1.2.2	Discretization with linear elements	40
2.2	Integral Formulation of The Poisson's Equation	41
2.3	Dual Reciprocity Boundary Element Method	42
2.3.1	DRBEM for Poisson's equation	43
2.3.2	Approximating functions f_j	47
2.3.3	DRBEM for the time-dependent Poisson's type equations	47
2.3.3.1	Time integration scheme	49
2.4	Numerical Stability Analysis	50
2.4.1	Stability Analysis of single step method	50
2.4.2	Stability analysis of DRBEM	53

3	MIXED CONVECTION FLOW IN LID-DRIVEN CAVITIES IN THE PRESENCE OF UNIFORM MAGNETIC FIELD	55
3.1	Governing Equations for the Unsteady MHD Mixed Convection Flow	55
3.2	Numerical Method and Stability Analysis	57
3.2.1	Application of dual reciprocity boundary element method	58
3.2.2	Stability analysis of the numerical method	62
3.3	Steady MHD Mixed Convection Flow in Lid-Driven Cavities with Different Types of Heaters	62
3.3.1	Semi-rectangular and semi-circular heaters	64
3.3.2	Two semi-rectangular and two semi-circular heaters	73
3.3.3	Sinusoidal heater	77
3.4	Unsteady MHD Mixed Convection Flow in a Lid-Driven Cavity with Sinusoidal Heater	82
3.5	Summary of the Results Obtained in Chapter 3	97
4	NATURAL CONVECTION FLOW IN SEMI-ANNULUS ENCLOSURES FILLED WITH WATER-BASED NANOFLUIDS UNDER THE EFFECT OF UNIFORM MAGNETIC FIELD	101
4.1	Governing Equations for the Unsteady MHD Natural Convection Nanofluid Flow	102
4.2	Numerical Method and Stability Analysis	104
4.2.1	Application of DRBEM	104
4.2.2	Stability analysis of the numerical method	106
4.3	Steady MHD Convective Nanofluid Flow in an Inclined Semi-Annulus with Circular Inner Wall	107
4.4	Unsteady MHD Natural Convection Nanofluid Flow in a Semi-Annulus with a Sinusoidal Inner Wall	118

4.5	Summary of the Results Obtained in Chapter 4	126
5	NATURAL CONVECTION FLOW IN SEMI-ANNULUS ENCLOSURES FILLED WITH WATER-BASED FERROFLUID IN THE PRESENCE OF SPATIALLY VARIABLE MAGNETIC SOURCES .	129
5.1	Governing Equations for the Steady MHD Convection Ferrofluid Flow	130
5.2	Application of Dual Reciprocity Boundary Element Method .	132
5.3	Steady MHD Convection Ferrofluid Flow in a Semi-Annulus with Sinusoidal Inner Wall under the Effect of a Nodal Magnetic Source	135
5.4	Steady MHD Convection Ferrofluid Flow in a Semi-Annulus with Sinusoidal Inner Wall under the Effect of Multiple Nodal Magnetic Sources	144
5.5	Summary of the Results Obtained in Chapter 5	153
6	CONCLUSION	157
	REFERENCES	163
	CURRICULUM VITAE	175

LIST OF TABLES

TABLES

Table 3.1	Average Nusselt number along the semi-circular heater: $Ra = 10^5$, $J = 1$	67
Table 3.2	Spectral radius of vorticity and temperature equations: $Ra = 10^4$, $Ha = 25$, $\Delta t = 0.8$, $J = 1$, $\lambda = 0$, $\epsilon = 10^{-4}$	84
Table 3.3	Spectral radius of vorticity and temperature equations: $Ra = 10^4$, $Ha = 25$, $J = 1$, $\lambda = 0$, $\beta = \beta_q = 0.7$, $\epsilon = 10^{-4}$	84
Table 3.4	Spectral radius of vorticity and temperature equations: $Ra = 10^4$, $Ha = 25$, $\Delta t = 0.8$, $J = 1$, $\lambda = 0$, $\epsilon = 10^{-4}$	85
Table 3.5	Spectral radius of vorticity and temperature equations for several Ra : $Ha = 25$, $J = 1$, $\lambda = 0$, $\beta = \beta_q = 0.7$, $\Delta t = 0.8$, $\epsilon = 10^{-4}$	85
Table 3.6	Spectral radius of vorticity and temperature equations for several Ha : $Ra = 10^4$, $J = 1$, $\lambda = 0$, $\beta = \beta_q = 0.7$, $\Delta t = 0.8$, $\epsilon = 10^{-4}$	86
Table 4.1	Thermo-physical properties of water and nanoparticle [86]	103
Table 4.2	Spectral radius of vorticity and temperature equations when $Ra =$ 10^4 , $Ha = 20$, $\lambda = 0$, $\phi = 0.06$, $n = 4$, $\epsilon = 10^{-4}$	120
Table 4.3	Spectral radius of vorticity and temperature equations when $Ra =$ 10^4 , $Ha = 20$, $\lambda = 0$, $\phi = 0.06$, $\Delta t = 0.9$, $n = 4$, $\epsilon = 10^{-4}$	120
Table 4.4	Spectral radius of vorticity and temperature equations: $\phi = 0.06$, $\lambda = 0$, $\beta = \beta_q = 0.9$, $\Delta t = 0.9$, $\epsilon = 10^{-4}$	121

Table 5.1	Thermo-physical properties of water and nanoparticle [81] 132
Table 5.2	Code validation in terms of $ \psi _{max}$, $ \theta _{max}$ and \overline{Nu} 139
Table 5.3	Comparison of the effect of magnetic field produced by either one magnet or two magnets in terms of $ \psi _{max}$, $ \theta _{max}$ and \overline{Nu} 153

LIST OF FIGURES

FIGURES

Figure 2.1	Geometry of the problem	35
Figure 2.2	Meshing with constant and linear elements	38
Figure 3.1	Geometry of the problem: (a) semi-rectangular, (b) semi-circular heaters	64
Figure 3.2	Grid dependency: $Ha = 10$, $Ra = 10^5$, $J = 1$	65
Figure 3.3	The streamlines and isotherms drawn by using (a) equally-spaced, (b) GCL grids: $Ha = 50$, $Ra = 10^5$, $J = 1$	66
Figure 3.4	Streamlines and isotherms for (a) $Ha = 10$, (b) $Ha = 50$: $Ra =$ 10^5 , $J = 1$	67
Figure 3.5	Effect of Ha on streamlines and isotherms at $Ra = 10^5$, $J = 1$: (a) semi-rectangular heater, (b) semi-circular heater.	68
Figure 3.6	Effect of Ra on streamlines and isotherms at $Ha = 10$, $J = 1$: (a) semi-rectangular heater, (b) semi-circular heater.	69
Figure 3.7	Effect of J on streamlines and isotherms at $Ra = 10^5$, $Ha = 10$: (a) semi-rectangular heater, (b) semi-circular heater.	70
Figure 3.8	Effects of (a) Ra and (b) Ha on \overline{Nu} at $J = 0$	71
Figure 3.9	Effects of (a) Ra and (b) Ha on \overline{Nu} at $J = 1$	72
Figure 3.10	Effect of the shape of the heater on \overline{Nu} at (a) $Ra = 10^4$, (b) $Ha =$ 10 , (c) $Ra = 10^5$, (d) $Ha = 50$	73

Figure 3.11 Geometry of the problem: (a) semi-rectangular, (b) semi-circular heaters	74
Figure 3.12 Effect of Ha on streamlines and isotherms at $Ra = 10^5$, $J = 1$: (a) semi-rectangular heaters, (b) semi-circular heaters.	74
Figure 3.13 Effect of Ra on streamlines and isotherms at $Ha = 10$, $J = 1$: (a) semi-rectangular heaters, (b) semi-circular heaters.	75
Figure 3.14 Effect of J on streamlines and isotherms at $Ra = 10^5$, $Ha = 10$: (a) semi-rectangular heaters, (b) semi-circular heaters.	76
Figure 3.15 Effects of (a) Ra and (b) Ha on \overline{Nu} at $J = 1$	77
Figure 3.16 Geometry of the problem for sinusoidal heater	78
Figure 3.17 Grid dependency: $Ra = 10^5$, $Ha = 50$, $n = 3$	78
Figure 3.18 Effects of Ha and Ra on streamlines at $n = 3$	79
Figure 3.19 Effects of Ha and Ra on isotherms at $n = 3$	80
Figure 3.20 Variation of \overline{Nu} with Ra at different numbers of undulation n when $J = 0$: (a) $Ha = 0$, (b) $Ha = 10$, (c) $Ha = 25$, (d) $Ha = 50$	81
Figure 3.21 Effects of (a) Ha and (b) Ra on \overline{Nu} at $n = 3$	82
Figure 3.22 Geometry of the unsteady problem for sinusoidal hot wall	82
Figure 3.23 Grid dependency: $Ra = 10^5$, $Ha = 50$, $J = 1$, $n = 3$ and $\lambda = 0$	83
Figure 3.24 Time evolution of ψ , ω , θ along (a) vertical centerline $x = 0.5$, and (b) horizontal centerline $y = 0.5$: $Ra = 10^4$, $Ha = 25$, $\Delta t = 0.8$, $J = 1$ and $\lambda = 0$	86
Figure 3.25 Effects of Ha and Ra on streamlines: $n = 3$, $\lambda = 0$, $J = 1$	87
Figure 3.26 Effects of Ha and Ra on isotherms: $n = 3$, $\lambda = 0$, $J = 1$	88
Figure 3.27 Effects of J and Ra on streamlines: $n = 3$, $\lambda = 0$, $Ha = 10$	89

Figure 3.28 Effects of J and Ra on isotherms: $n = 3, \lambda = 0, Ha = 10$	90
Figure 3.29 Effects of λ and Ra on streamlines: $n = 3, Ha = 10, J = 1$	91
Figure 3.30 Effects of λ and Ra on isotherms: $n = 3, Ha = 10, J = 1$	92
Figure 3.31 Effects of n and Ra on streamlines: $Ha = 10, \lambda = 0, J = 1$	93
Figure 3.32 Effects of n and Ra on isotherms: $Ha = 10, \lambda = 0, J = 1$	94
Figure 3.33 Effects of (a) Ha and (b) Ra on \overline{Nu} : $n = 3, J = 0, \lambda = 0$	94
Figure 3.34 Effects of (a) Ha and (b) Ra on \overline{Nu} : $n = 3, J = 1, \lambda = 0$	95
Figure 3.35 Effect of J on \overline{Nu} at $n = 3, \lambda = 0$ by fixing (a) $Ra = 10^5$, (b) $Ha = 10$	95
Figure 3.36 Variation of \overline{Nu} with n at $Ra = 10^3, 10^4, 10^5$ when $J = 0, \lambda = 0$: (a) $Ha = 0$, (b) $Ha = 10$, (c) $Ha = 25$, (d) $Ha = 50$	96
Figure 3.37 Variation of \overline{Nu} with n at $J = 0, 1, 3$ when $Ra = 10^3, \lambda = 0$: (a) $Ha = 0$, (b) $Ha = 10$, (c) $Ha = 25$, (d) $Ha = 50$	97
Figure 3.38 Variation of \overline{Nu} with Ra at different inclination angles of magnetic field λ when $J = 0, n = 3$: (a) $Ha = 10$, (b) $Ha = 100$	97
Figure 4.1 Geometry of the problem.	108
Figure 4.2 Grid dependency: $Ra = 10^5, Ha = 50, \phi = 0.06, \lambda = \beta = 0$	109
Figure 4.3 Effect of λ on streamlines and isotherms: $\beta = 0, \phi = 0.06, Ra = 10^4, Ha = 20$	110
Figure 4.4 Effects of Ha and Ra on streamlines and isotherms: $\lambda = \beta = 0, \phi = 0.06$	111
Figure 4.5 Effects of Ha and Ra on streamlines and isotherms: $\lambda = \beta = \pi/4, \phi = 0.06$	112

Figure 4.6 Effects of Ha and Ra on streamlines and isotherms: $\lambda = \beta = \pi/2$, $\phi = 0.06$	113
Figure 4.7 Streamlines and isotherms: $Ra = 10^4$, $\phi = 0.06$, $Ha = 100, 300$, 500 $\lambda = \beta = 0, \pi/4, \pi/2$	114
Figure 4.8 Effect of β on streamlines and isotherms: $\lambda = \pi/4$, $\phi = 0.06$, $Ra = 10^4$, $Ha = 20$	116
Figure 4.9 Variation of ψ , ω and θ along (a) vertical centerline $x = 0$, $1 \leq$ $y \leq 2$, (b) horizontal line $y = 1.25$, $-2 \leq x \leq 2$ at different ϕ : $Ra = 10^3$, $Ha = 20$, $\lambda = \beta = 0$	117
Figure 4.10 Effects of (a) Ra and (b) Ha on \overline{Nu} : $\lambda = \beta = 0, \pi/4, \pi/2$	117
Figure 4.11 Horizontal velocity u and vertical velocity v along the vertical cen- terline $x = 0$, $1 \leq y \leq 2$: $Ra = 10^3, 10^4$ for $Ha = 0, 20, 50$	118
Figure 4.12 Geometry of the problem with boundary conditions.	119
Figure 4.13 Grid dependency: $Ra = 10^5$, $Ha = 50$, $\phi = 0.06$, $A = 0.2$, $n = 4$, $\lambda = 0$	119
Figure 4.14 Effect of λ on the steady-state streamlines and isotherms: $n = 4$, $\phi = 0.06$, $Ra = 10^4$, $Ha = 20$	122
Figure 4.15 Time evolution of ψ , ω , θ along (a) vertical centerline $x = 0$, $1.2 \leq y \leq 2$, (b) horizontal line $y = 1.6$, $-2 \leq x \leq 2$: $Ra = 10^4$, $Ha = 20$, $\Delta t = 0.9$, $\phi = 0.06$, $n = 4$, $\lambda = 0$	122
Figure 4.16 Effects of Ha and Ra on streamlines and isotherms: $\lambda = 0$, $\phi =$ 0.06 , $n = 4$	123
Figure 4.17 Effects of (a) Ha and (b) Ra on \overline{Nu} : $n = 4$, $\phi = 0.06$, $\lambda = 0$	124
Figure 4.18 Variation of \overline{Nu} with (a) Ha and (b) Ra at different ϕ : $n = 4$, $\lambda = 0$	124
Figure 4.19 Variation of \overline{Nu} with Ra at different numbers of undulation n when $\phi = 0.06$, $\lambda = 0$: (a) $Ha = 0$, (b) $Ha = 10$, (c) $Ha = 50$, (d) $Ha = 100$	125

Figure 4.20 Variation of \overline{Nu} with Ra at different amplitudes A when $n = 4$, $\phi = 0.06$, $\lambda = 0$: (a) $Ha = 0$, (b) $Ha = 10$, (c) $Ha = 50$, (d) $Ha = 100$.	126
Figure 5.1 Geometry of the problem with boundary conditions	136
Figure 5.2 Comparison of streamlines and isotherm between nanofluid ($\phi =$ 0.04) (---) and pure fluid ($\phi = 0$) () when $Ra = 10^4$, $Ha = 5$ and $Mn_f = 500$	137
Figure 5.3 Grid dependency: $Ra = 10^4$, $Ha = 5$, $Mn_f = 500$, $\phi = 0.04$, $A = 0.2$, $n = 4$	138
Figure 5.4 Effects of Ha and Mn_f on streamlines and isotherms: $Ra = 10^3$, $\phi = 0.04$, (a) $n = 0$, (b) $n = 4$	139
Figure 5.5 Effects of Ha and Mn_f on streamlines and isotherms: $Ra = 10^4$, $\phi = 0.04$, (a) $n = 0$, (b) $n = 4$	140
Figure 5.6 Effects of Ha and Mn_f on streamlines and isotherms: $Ra = 10^5$, $\phi = 0.04$, (a) $n = 0$, (b) $n = 4$	141
Figure 5.7 Effects of (a) Ha and (b) Ra on \overline{Nu} : $n = 4$, $\phi = 0.04$	142
Figure 5.8 Variation of \overline{Nu} with Ra at different numbers of undulation n and amplitude A when $\phi = 0.04$, $Ha = 0$, $Mn_f = 0$	143
Figure 5.9 Variation of \overline{Nu} with (a) Ha and (b) Ra at different ϕ : $n = 4$	143
Figure 5.10 Geometry of the problem with boundary conditions	144
Figure 5.11 Grid dependency: $Ra = 10^4$, $Ha = 10$, $Mn_f = 100$, $\phi = 0.04$, $A = 0.2$, $n = 4$	145
Figure 5.12 Effects of Ha and Mn_f on streamlines and isotherms: $Ra = 10^3$, $\phi = 0.04$	146
Figure 5.13 Effects of Ha and Mn_f on streamlines and isotherms: $Ra = 10^4$, $\phi = 0.04$	147

Figure 5.14 Effects of Ha and Mn_f on streamlines and isotherms: $Ra = 10^5$, $\phi = 0.04$	148
Figure 5.15 Effects of (a) Ha and (b) Ra on \overline{Nu} : $n = 4$, $\phi = 0.04$	149
Figure 5.16 Variation of \overline{Nu} with Ra at different numbers of undulation n and amplitude A when $\phi = 0.04$, $Ha = 0$, $Mn_f = 0$	150
Figure 5.17 Variation of \overline{Nu} with (a) Ha and (b) Ra at different ϕ : $n = 4$	150
Figure 5.18 The effects of the number of undulation n and the amplitude A of sinusoidal wall on streamlines and isotherms at $Ha = 0$, $Mn_f = 0$, $Ra = 10^4$	151
Figure 5.19 Effects of Ha and Mn_f on streamlines and isotherms: $Ra = 10^4$, $\phi = 0.04$, (a) one nodal source, (b) multiple nodal sources.	152

LIST OF ABBREVIATIONS

A	amplitude of wavy wall
B_0	magnetic induction
C_p	specific heat at constant pressure
\mathbf{E}	electric field
Ec	Eckert number
g	gravitational acceleration
H	the strength of magnetic field
Ha	Hartmann number
J	Joule heating parameter
k	fluid conductivity
ℓ	length of cavity
L	number of interior nodes
M	magnetization
Mn	magnetic number
\mathbf{n}	unit outward normal
N	number of boundary elements
Nu	local Nusselt number
\overline{Nu}	average Nusselt number
\bar{p}	dimensional pressure
p	dimensionless pressure
Pr	Prandtl number
Re	Reynolds number
Ra	Rayleigh number
S	arc length of wavy wall

\bar{t}	dimensional time
t	dimensionless time
T	dimensional temperature
Δt	time step size
\bar{u}, \bar{v}	dimensional velocity components
u, v	dimensionless velocity components
U_0	lid velocity
\bar{x}, \bar{y}	dimensional coordinates
x, y	dimensionless coordinates
α	thermal diffusivity
β	thermal expansion coefficient
θ	dimensionless temperature
λ	inclination angle of magnetic field
μ	dynamic viscosity
ν	kinematic viscosity
ρ	density
σ	electrical conductivity
Φ	viscous dissipation
ψ	stream function
ω	vorticity

Subscripts

c	cold
h	hot
f	fluid
s	solid

CHAPTER 1

INTRODUCTION

Fluid dynamics is the investigation of the interactive motion of liquids, gases and plasmas. It provides methods for studying the evolution of stars, meteorology, oceanography, astrophysics, biology, oil recovery and even blood circulation. Some important technological applications of fluid dynamics include rocket engines, wind turbines, aircraft, turbo-machinery, car and ship design and etc.

A fluid is composed of a large number of individual particles, namely molecules and atoms, which are in constant motion and collision. However, in most engineering problems, the principle interest is not the motion of the individual molecules but the overall behavior of the fluid as a continuous material. Thus, a fluid can be regarded as continuum. That is, the smallest element of a fluid in continuum contains sufficient number of molecules to make statistical averages.

The most important properties of simple fluids are the density and viscosity. The density of a fluid is a function of temperature and pressure. When the density of the fluid is slightly affected from these properties and is almost constant, the fluid is often referred to as incompressible, otherwise it is compressible. On the other hand, viscosity describes the internal friction of a moving fluid. The fluids with no viscosity are referred to as inviscid (ideal) fluids. On the other hand, the speed of flow also affects its properties in a number of ways. That is, when the speed increases inertia becomes important and each fluid particle follows a smooth trajectory, and the flow is called laminar. An additional increase in speed may lead to instability that produces a more random type of flow which is called turbulent. Finally, the flow is called steady when the change of various parameters of the flow at any point does not depend on time. Otherwise, it is called unsteady. In this thesis, both the steady

and unsteady flow problems are considered and the numerical solutions are obtained involving the stability analysis of the numerical scheme for the unsteady flow.

On the other hand, the study of heat transfer analysis has been a major topic in fluid dynamics due to its fundamental nature and wide spectrum of engineering applications such as solar collector, heat exchanger, cooling of electrical equipment, nuclear reactors, etc. Heat transfer deals with the rate of energy transfer by time and the temperature distribution through a thermal system. The basic principles of heat transfer are the temperature and the flow of the heat. On a microscopic scale, there is direct relation between the kinetic energy of molecules and the thermal energy. Regions including higher kinetic energy, transfer the energy to the regions with lower kinetic energy, and hence heat may take place in three modes which is conduction, convection and radiation. The physical mechanism of conduction is explained by the energy which is transferred via direct molecule collisions. Higher temperatures are associated with higher molecular energies. When molecules collide, energy is transferred from the molecules with more energy to the ones with less energy. On the other hand, convection is known as the heat transfer between a surface and a moving fluid at different temperatures. Thus, the convective heat transfer occurs when the heat is transferred from one place to another by the movement of fluid; which is the dominant form of heat transfer in liquids and gases. In physics, convective heat transfer contains the combination of the random molecular motion (diffusion) and the bulk motion of fluid (advection). Convective heat transfer can be classified due to the nature of the flow. When the flow is affected from external source like a fan, a pump or atmospheric winds, it is called *forced convection*. On the contrary, for *natural (free) convection* the flow is induced by buoyancy forces depending on the density differences which are caused by temperature variations in the fluid. Further, the combination of these two (forced and natural) convections is referred to as *mixed (combined) convection*. Thus, mixed convection occurs if either the effect of buoyancy dominates on a forced flow or visa versa. Finally, radiation is the energy emitted by matter in the form of rays or high-speed particles. All matters are composed of atoms. The emission occurs when there is a change in the electron configuration of these atoms. The energy of the radiation field is transported by electromagnetic waves. While the transfer of energy by conduction or convection need the presence of a material medium, radiation does

not.

Magnetohydrodynamics (MHD) is the science which studies the interaction between the flow of electrically-conducting fluids and the applied magnetic fields. This phenomenon brings together the concepts of fluid dynamics and electromagnetism. In magnetohydrodynamics, the flow of an electrically conducting fluid under a magnetic field causes induced electric currents, which produce a resistive force known as Lorentz force. The generated electric current flows both perpendicular to the magnetic field and in the direction of motion of the fluid. However, the induced currents form their own magnetic field, which affects the original magnetic field. MHD has received great interest due to its importance in a vast field of applied and fundamental research in engineering and physical sciences. For example, it is useful in astrophysical problems (sun-spot theory, motion of inter-stellar gas, re-entry problem of inter-continental ballistic missiles) since a large part of the universe is filled with widely spaced, charged particles permeated by magnetic fields. In addition, geophysics meets with MHD while dealing with the presence of conducting fluids and magnetic fields in and around the earth. On the other hand, MHD has a great significance in the design of many industrial applications such as MHD generators, pumps, flow meters, cooling of nuclear reactors, geothermal energy extractors, nuclear waste disposal, heat exchangers and space vehicle propulsion. A more recent innovation is the application of MHD in drug targeting for the treatment of cancer. In the first part of the present thesis (Chapter 3), we focus on the numerical solution of the convective flow of a conventional fluid (purefluid) and the heat transfer in enclosures under the influence of externally applied magnetic field.

On the other hand, in many engineering applications the primary requirement is the transfer of heat from one point to another. Different types of base fluids, such as water, engine oil, kerosene, ethanol, methanol, ethylene glycol, are usually used for the heat transfer. However, these conventional heat transfer fluids generally have various limitations, one of which is their low thermal conductivity that causes a low heat transfer rate in thermal engineering systems. This also affects the performance of different equipments used in the heat transfer process. For this reason, improving the heat transfer efficiency is significant in any industrial facilities; and hence researchers have considered a new class of heat transfer fluids, simply known as

nanofluids. Nanofluids are the fluids which contain nanometer-sized particles (i.e. nanoparticles). Nanofluids have better thermo-physical properties and might achieve a better heat transfer performance compared to the conventional fluids. Combinations of nanoparticles and the base fluids can be used for the preparation of many heterogeneous nanofluids. The commonly used materials for the nanoparticles are made of metals (e.g. Al, Cu), nonmetals (e.g. graphite, carbon nanotubes), oxide ceramic (e.g. Al_2O_3 , CuO), metal carbides (e.g. SiC), layered (e.g. Al + Al_2O_3 , Cu + C) and functionalized nanoparticles, whereas base fluids may include water, ethylene- or triethylene-glycols and other coolants, oil and other lubricants, and polymer solutions.

Ferrohydrodynamics (FHD) is the field of study concerning the interactions between the magnetic fields and the magnetically polarizable fluids. FHD appeared in the mid-1960s, and actuated by the objective of converting heat to work with no mechanical parts. FHD is similar to MHD, but the difference between FHD and MHD is the body force acting on the fluid. That is, in magnetohydrodynamics Lorentz force is generated by the electric current whereas in FHD there is no electric current in the fluid and the body force is due to the polarization force required for the magnetization of the material. In FHD there are various magnetic nanofluids; the principal type of magnetic nanofluid is the ferrofluid which is a synthesized colloidal mixture of nanomagnetic carrier liquid, (i.e. water, oil) including permanently magnetized nanoparticles such as; magnetite (Fe_3O_4) and hematite (Fe_2O_3). A major benefit of ferrofluid is that the liquid can be forced to flow via the positioning and strength of the magnetic field. Ferrofluids have the capability of reducing friction, which makes them useful in a variety of electronic and transportation applications such as; hydraulic suspension pistons, pressure seals for compressors, vacuum feedthroughs for semiconductor manufacturing and computer hard-drives. Ferrofluids have also plenty of medical applications such as; carrying medications to exact locations within the body and being used as a contrasting agent for MRI scans. Further, disparate fields in which the ferrofluids can be used, are the heat transfer, analytic instrumentation, art and aerospace. The second part of the present thesis (Chapter 4 and Chapter 5) is devoted for the numerical solutions and the analysis of the obtained results for the convective heat transfer flow of nanofluids and ferrofluids in irregular enclosures either subject to uniform magnetic field or nodal magnetic sources.

The motion of the fluid flow and its thermal behavior in the presence of a magnetic field can be modelled by the Navier-Stokes equations of hydrodynamics, Maxwell's equation of electromagnetism and energy equation. These equations are so complex that very few problems involving the full set of these equations can be solved exactly. Therefore, numerical simulations play a crucial role in obtaining approximate solutions for these equations. Thus, various numerical methods have been developed and employed for the solution of these equations. The most notable ones are the finite difference method (FDM), the finite element method (FEM), the finite volume method (FVM) and the boundary element method (BEM). All these techniques except BEM are based on the domain discretization process. BEM is the boundary-only nature technique which reduces the boundary value problems into equivalent integral equations on the boundary of the physical computational domain. This boundary reduction has the advantage of diminishing the number of space dimension by one, and hence BEM provides saving in computational time and data preparation effort. Thus, in this sense BEM is more efficient than the domain discretization methods. On the other hand, BEM owes its computational accuracy and efficiency to the existence of the fundamental solution for the governing equations. However, difficulties arise while finding a corresponding fundamental solution for the fluid flow problems with non-homogeneous and non-linear terms. Consequently, the BEM can not be applied directly to such problems. In order to overcome this shortcoming the dual reciprocity boundary element method (DRBEM) is developed. The basic idea behind the DRBEM is to treat all the terms except the ones, for which the fundamental solution is known, as the non-homogeneity; and these non-homogeneous terms are approximated by radial basis functions in order to transform the domain integrals into integrals only on the boundary. Therefore, this thesis uses the DRBEM for the discretization of the non-linear coupled differential equations governing the MHD convective heat transfer fluid flow problems under consideration.

This chapter is devoted to introductory concepts of the basic equations governing the fluid flow and the associated phenomena. The discussion starts with the literature review in Section 1.1 and continues with the contribution of the thesis to the research field in Section 1.2. The principal equations of fluid dynamics involving the continuity, momentum and energy equations derived from the conservation of mass,

conservation of momentum and the conservation of energy respectively, are given in Section 1.3. In Section 1.4, the MHD flow equations are considered, where the fluid is assumed to be electrically conducting, and governing equations are equations of motion from fluid dynamics coupled with Maxwell's equations from electromagnetism. Then, the equations of the unsteady MHD convection of a classical fluid flow and a nanofluid flow are presented, respectively, in Section 1.4.1 and Section 1.4.2. Further, the governing equations for the convective ferrofluid flow in the presence of an externally applied nodal magnetic source are presented in Section 1.4.3. Finally, the heat transfer rate in terms of Nusselt number is given in Section 1.5, which continues with the plan of the thesis in Section 1.6.

1.1 Literature Review

Convective heat transfer, which is mentioned before, is the transfer of heat from one place to another by the motion of fluid, and can be classified due to the nature of the flow. In the natural convection, the buoyancy forces appear due to density variation and affects the mechanism significantly. Natural convection occurs in many technological and industrial applications such as solar collectors, heat exchanger, building heating and cooling etc. Hence, it is important to understand the heat transfer characteristics of natural convection in an enclosure or cavity. On the other hand, mixed convection appears as a result of two competing mechanism. The first one is the shear force due to motion of the wall in the enclosure whereas the second one is the buoyancy force produced by thermal non-homogeneity along the walls of enclosure. Mixed convection in fluid-filled cavities or enclosures plays an important role in the area of heat transfer and has been given an considerable attention due to the wide variety of applications in science and engineering such as in material processing [37], flow and heat transfer in solar ponds [15], dynamics of lakes, reservoirs and cooling ponds [35], crystal growing [72], float glass production [65], etc. Many studies have been produced for the solution of the convective flow in regular enclosures with flat walls such as rectangular, circular or annular cavities by using several numerical methods such as FVM in the works (e.g. [20, 30, 50]), FEM in the works (e.g. [47, 59, 68]) and FDM in the works (e.g. [2, 14, 80]). Öztop and Dağtekin [60] used

a finite control volume using the non-staggered grid arrangement with the SIMPLEM algorithm to examine the effect of Richardson number on mixed convection problem in a vertical two-sided lid-driven cavity. Khanafer et al. [45] extended the investigation of the mixed convection flows in a lid-driven cavity to the unsteady case by using a finite element scheme based on the Galerkin method of weighted residuals and they studied the effects of Reynolds and Grashof numbers, and the lid oscillation frequency on the flow. Further, Waheed [99] studied on the effects of the Richardson and Prandtl numbers, and the length-to-height aspect ratio on the flow and thermal fields using the finite difference method. Their results indicated that an increase in the Prandtl number results in an increase in the heat flux on the heated wall, while an increase in aspect ratio suppresses it. Moreover, there have also been a quite number of studies on the convective flow in complex geometries, (e.g. cavities with wavy and/or irregular walls) solved by mainly domain discretization methods (e.g. [34, 38, 48, 53, 73]). Yao [100] has studied on the natural convection flow along a vertical wavy surface using FDM. Their results showed that the local Nusselt number is smaller than that of the flat plate case and decreases with increase of wave amplitude. Das and Mahmud [19] solved natural convection problem in an enclosure which consists of two wavy and two straight walls using FVM. They found that amplitude-wavelength ratio affects both local heat transfer rate and the flow fields as well as thermal field. In [54], FVM is also employed to solve the mixed convection flow in an inclined lid-driven cavity with wavy wall. Further, Al-Amiri [1] conducted to analyze mixed convection heat transfer in a lid-driven cavity with sinusoidal wavy bottom surface using FEM. The results showed that the average Nusselt number increases with an increase in both the amplitude of the wavy surface and Reynolds number.

On the other hand, magnetic field is also an important control parameter for convective heat transfer in enclosures. When the fluid is electrically conducting and the flow is subject to an external magnetic field, fluid experiences a Lorentz force which reduces the velocity of the fluid as mentioned previously. This is the well-known retarding effect of the magnetic field on the fluid flow and a main point of MHD theory. In recent years, many numerical studies have been produced for the solution of the MHD convective flows in regular enclosures by using mainly domain discretization methods such as FVM in the works (e.g. [3, 16, 21, 74, 91, 101]) and FEM in the

works (e.g. [32, 33, 66, 69, 77, 79]), whereas there have been only a few studies (e.g. [11, 63, 94, 97]) on the solution of MHD convection flow obtained by using dual reciprocity BEM. On the other hand, there is a limited amount of literature on the MHD convection in enclosures of complex geometries with wavy walls, due to the difficulty of obtaining enclosure boundaries and the complexity of the flow inside the enclosure. However, the hydromagnetic mixed convective heat transfer in wavy enclosures has received more attention recently since enclosures with irregular surfaces are often encountered in many engineering applications such as solar collectors, underground cable systems, nuclear reactors, wall bricks and cooling system of micro-electronic devices. Moreover, the irregular enclosures with a form of wavy surfaces has an important role in the enhancement of the heat transfer since the variations in surface fluctuation have a great impact on the surface temperature. The effect of wavy surfaces depends on some controlling parameters such as amplitude, number of undulation and phase angle which determine the shape of the irregular surface and hence the computational domain of the problem under consideration. Although there are a quite number of studies given in the literature of MHD natural convection flow in enclosures with wavy surfaces (e.g. [39, 40, 62, 84, 90]), there have been only a few studies when an external magnetic field is applied on the mixed convection in wavy enclosures. Rahman et.al. [67] investigated the combined influence of the uniform magnetic field and Joule heating in a lid-driven cavity with a wall of semi-circular heater. They observed that the flow strength and temperature distribution are affected by the magnetic field and Joule heating parameter. Gajbhiye and Eswaran [24] solved the MHD flow in a rectangular enclosure of which middle section is smoothly constricted by using a finite volume solver. Their results revealed that with an increase in Hartmann number or in constriction ratio, the motion of the fluid is suppressed and hence the Nusselt number decreases. Moreover, the number of eddies in flow increases with increase in the constriction ratio. Nasrin and Parvin [56] conducted a study to analyze the mixed convection flow in a lid-driven cavity with a sinusoidal wavy bottom surface in the presence of a transverse magnetic field by using the finite element method based on the Galerkin method of weighted residuals. They observed that the average Nusselt number at the heated surface increases with an increase in the number of waves and Reynolds number, while decreases with increasing Hartmann number.

The studies given above are on the convection flow of a conventional fluid (e.g. water, ethylene glycol and oil) which has low thermal conductivity that limits the heat transfer capacitance considerably. In view of this, in order to enhance the heat transfer performance, the use of nanofluids are preferred instead of traditional energy transmission fluids as previously mentioned. Thus, using nanofluids to improve the heat transfer capacitance in enclosures has attracted the great attention of many researchers, which results in yielding many studies both in the absence and the presence of magnetic field. In this manner, the nanofluids introduced by Choi [18], which is a mixture of nanoparticles suspended in a base fluid, can be utilized as a solution due to their high thermal conductivity. The numerical simulations have been carried out using several numerical techniques in different shaped enclosures in the absence of magnetic field. Khanafer et al. [44] investigated the heat transfer enhancement in a rectangular enclosure for a range of Grashof numbers and volume fractions by using a finite volume approach. They found that the heat transfer rate increases at any Grashof numbers with an increase in the nanoparticle volume fraction. Sourtiji et al. [92] have also applied FVM using Patankar's SIMPLE algorithm for the solution of the unsteady natural convection flow through an alumina-water nanofluid in a square enclosure. Their results showed that the heat transfer is enhanced in the presence of the nanoparticles for all values of the oscillation period and the Rayleigh number. Natural convection in a nanofluid filled annulus between outer square and inner elliptic cylinders was solved by the lattice Boltzmann method (LBM) in [85].

There have also been many studies which analyze further the effect of the magnetic field on the nanofluid natural convection flow. One of the commonly used technique is the control volume (CV) technique. Ghasemi et al. [27] and Bahiraei et al. [8] solved the magnetohydrodynamic natural convection of nanofluid in a square enclosure by using CV formulation with SIMPLE algorithm. The same technique was employed to solve the natural convection flow in a triangular enclosure filled with magnetic nanofluid in the work of Aminossadati [6] while a finite volume method was applied by Mahmoudi et al. [51]. The CV formulation with SIMPLE algorithm was also performed by Ghasemi [26] for the natural convection nanofluid in an U -shaped enclosure. The results of above studies revealed that the thermal performance of the cavity is enhanced with an increase in the Rayleigh

number and solid volume fraction, and with a decrease in the Hartmann number. On the other hand, the fully implicit finite difference method was employed to discretize the governing equations of the natural convection problem in an inclined L -shaped enclosure with differentially heated wall by Elshehabey [22]. Another commonly used numerical method for the solution of natural convection subjected to a magnetic field in a nanofluid filled enclosure is the control volume finite element method (CVFEM), which uses the advantages of both finite element and finite volume methods in complex-geometries. The magnetohydrodynamic free convection of water-based nanofluid in an annulus-type enclosure (namely, circular, half-annulus, cylindrical-triangular, circular-sinusoidal cylinder, circular-elliptic cylinder annulus enclosures) was studied in the works [83, 86, 87, 88, 93]. On the other hand, Nematı et al. [57] applied the lattice Boltzman method to investigate the effect of CuO nanoparticles on the natural convection with MHD flow in a square cavity. LBM was also used by Ashorynejad et. al. [7] to analyze the natural convection under the effect of radial-applied magnetic field in a horizontal cylindrical annulus enclosure filled with a Ag-water nanofluid. The results of both studies showed that the average Nusselt number increases for nanofluids when increasing the solid volume fraction, and it decreases in the presence of a high magnetic field. Finally, the finite element method application for the nanofluid filled enclosure under a magnetic field was analyzed in terms of the effects of physical parameters such as Rayleigh and Hartmann numbers and the solid volume fraction on the flow field and heat transfer rate in the works [31, 46, 75]. On the other hand, in literature, there have been a few studies on the convection flow in an enclosure filled with nanofluids solved by DRBEM. Ravnı et al. [71] studied on the flow and heat transfer characteristics of the natural convection nanofluid flows in closed cavities. The simulations performed for Rayleigh number and three types of water-based nanofluids by using a three dimensional boundary element method based on flow solver. Results showed that using water-based nanofluids instead of pure water enhances heat transfer. Gümğüm et al. [29] employed DRBEM for the solution of the unsteady natural convective flow of nanofluids in a square enclosure with heated source. Later, this problem in a square enclosure under a uniform magnetic field was investigated by using both FEM and DRBEM techniques in the work of Tezer-Sezgin et.al. [95]. Plenty of studies are employed in the regular enclosures as mentioned above, however, there have been

only a few studies in the literature of convective nanofluids flow in a cavity with complex geometries. A finite volume approach was conducted for the mixed convection heat transfer of water-based nanofluids (Cu-water, Al_2O_3 -water, TiO_2 -water) in a lid-driven cavity with wavy surface in the work of Cho et.al. [17]. The numerical results were obtained for nanoparticle volume fraction, the type of nanofluid, the Richardson number, the Grashof number and the wavy surface geometry parameters. The results showed that Cu-water nanofluid gives the best heat transfer performance among the three nanofluids. Sheremet et.al.[89] solved numerically the MHD natural convection of Cu-water nanofluid within an inclined wavy cavity with a corner heater on the basis of FDM. The obtained results showed that a variation in the inclination angle of the cavity leads to essential changes in the fluid flow and heat transfer due to different positions of the heater and cooler; and insertion of nanoparticles leads to an increase on the average Nusselt number. Further, an increase in undulation number of cooled wavy wall results in a weak attenuation of the convective flow and more intensive cooling of the cavity. Sheikholeslami et. al. [84] investigated the numerical solution of MHD natural convection flow in a cavity with sinusoidal wall filled with Cu-water nanofluid using control volume finite element method (CVFEM). It can be found that increasing the volume fraction, dimensionless amplitude of the sinusoidal wall and Rayleigh number leads to an increase in average Nusselt number whereas the average Nusselt number decreases with an increase in Hartmann number.

Another type of nanofluids used to enhance the heat transfer is the so-called ferrofluids. Many investigations are carried out numerically in the study of convective ferrofluid flow in smooth geometries under the effect of spatially variable magnetic field by using FEM in the works (e.g [41, 76, 78, 96]), FDM in the works (e.g. [25, 49]), and CVFEM in the works (e.g. [4, 28, 42]). However, it is also important to study the ferrofluid flow driven in more complex geometries since ferrofluid flows in cavities/channels with irregular surfaces are widely encountered in many engineering applications. Sheikholeslami and Ganji [81] investigated the effect of a nodal magnetic source on ferrofluid flow and heat transfer in a semi-annulus enclosure with a sinusoidal wall using CVFEM. Their results showed that for low Rayleigh number, the heat transfer enhancement is an increasing function of Hartmann number and decreasing function of magnetic number while opposite situation can be observed for

high Rayleigh number. Sheikholeslami et.al. [82] also applied CVFEM method to solve the problem of hydro-thermal characteristics of a ferrofluid in a semi-annulus enclosure in the presence of magnetic source. In this problem they considered thermal radiation. Their results revealed that average Nusselt number increases with an increase in magnetic and Rayleigh numbers but it decreases with increase of Hartmann number and radiation parameter. In [98], the fundamental problem of the biomagnetic fluid flow in a channel with stenosis in the presence of magnetic field is investigated by using FDM, and it has been observed that the presence of the magnetic field affects the flow field considerably.

1.2 Contribution of the Thesis

The literature survey given in Section 1.1 indicates that there have been only a few studies which investigate the influence of irregular surfaces on the steady/unsteady convective MHD flows and heat transfer in enclosures filled with either convectational fluids and/or nano/ferrofluids. Moreover, in many of the related works basically a domain discretization method (i.e. FEM, FVM, FDM, CVFEM, etc.) has been employed for the numerical simulation, while the governing equations have been discretized by a boundary element approach in a very limited number of works in which only regular cavities in the absence of magnetic field have been considered. Thus, the objective of the thesis is to incorporate the use of dual reciprocity BEM for spatial discretization with the effects of the irregular cavities for the MHD convective flow and heat transfer problems.

In the first part of the thesis, we focus on the numerical solution of both steady and unsteady mixed convection flow of a conventional fluid in lid-driven cavities with wavy walls subject to a uniform inclined magnetic field. The equations are discretized by using DRBEM for the spatial domain and a two-level integration scheme is employed in time direction, which can be counted one of the contribution of the thesis. Moreover, the stability analysis of the numerical algorithm is also performed in terms of several problem parameters to determine the optimal value of the time increment and relaxation parameters for the numerical stability. Further, the influence of the externally applied inclined magnetic field and Joule heating parameter on the mixed

convection are investigated.

On the other hand, in the second part of the thesis we extend the application of the present proposed numerical technique, DRBEM in space-two level integration in time, to the solution of convective heat transfer and flow of nanofluids and ferrofluids in enclosures with complex geometries under the influence of both uniform and non-uniform (i.e. nodal magnetic sources) magnetic fields which is another main contribution of the thesis to the related research area. In addition, the effects of the shape of the computational domain, the inclination angle of the uniform magnetic field, and the position and the number of nodal magnetic sources are investigated through the streamlines, isotherms and average Nusselt number displayed for a wide range of physical parameters. The stability analysis of the present technique for the solution of the unsteady MHD convective flow of nanofluid problems is also performed through the eigenvalue decomposition of the matrix system which can be also counted as a contribution for the MHD convective flow in complex geometries.

1.3 Basic Fluid Dynamics Equations

The derivation of the principal equations of fluid dynamics, namely continuity, momentum and energy equations, is based on the dynamical behavior of a fluid which is determined by the conservation of mass, conservation of momentum and the conservation of energy. In the following sections, the derivation of these basic equations will be given over a control volume.

1.3.1 Continuity equation

The application of conservation of mass to the fluid flow gives the continuity equation. The law of mass conservation comes from the fact that mass neither created nor destroyed in a fluid system, hence the system has the same quantity of matter at all times. This means that the mass of a system is constant, thus the rate of change of the mass of the system is zero, that is,

$$\frac{\partial m}{\partial t} = 0 \quad (1.1)$$

where m is the mass, and \bar{t} is the time. The mass per unit volume is $dm_\Omega = \rho d\Omega$ where ρ is the density of the fluid and Ω is the finite control volume, so that the total mass is obtained by

$$m = \int_{\Omega} \rho d\Omega. \quad (1.2)$$

Then, the time rate of change of the total mass inside Ω can be written as

$$\frac{\partial m}{\partial \bar{t}} = \frac{\partial}{\partial \bar{t}} \int_{\Omega} \rho d\Omega = 0. \quad (1.3)$$

The mass flow of a fluid through a surface fixed in space equals to $\rho(\bar{\mathbf{u}} \cdot \mathbf{n})dS$ in which $\bar{\mathbf{u}}$, \mathbf{n} , dS represent the flow velocity, the unit normal vector and surface area element, respectively. If the term $\bar{\mathbf{u}} \cdot \mathbf{n}$ is negative it is called inflow, otherwise, it is called outflow, hence the mass leaves the control volume. Thus, the net mass flow rate over the surface of volume is given in terms of a surface integral

$$\int_S \rho(\bar{\mathbf{u}} \cdot \mathbf{n})dS \quad (1.4)$$

where S is the control surface. Then, Equations 1.3 and 1.4 yield

$$\int_S \rho(\bar{\mathbf{u}} \cdot \mathbf{n})dS = \int_{\Omega} \frac{\partial \rho}{\partial \bar{t}} d\Omega. \quad (1.5)$$

The surface integral on the left can be transform into a volume integral by applying the Divergence theorem. Thus, Equation (1.5) becomes

$$\int_{\Omega} \nabla(\rho \bar{\mathbf{u}})d\Omega = - \int_{\Omega} \frac{\partial \rho}{\partial \bar{t}} d\Omega \quad (1.6)$$

or more explicitly it can be written as [10, 23]

$$\nabla(\rho \bar{\mathbf{u}}) = - \frac{\partial \rho}{\partial \bar{t}}. \quad (1.7)$$

In the thesis, we focus only on the incompressible fluid, that is the density ρ of the fluid is constant, and hence the continuity equation reduces to

$$\nabla \cdot \bar{\mathbf{u}} = 0. \quad (1.8)$$

1.3.2 Momentum equation

The derivation of the momentum equation is performed by using a particular form of the Newton's second law of motion which states that the rate of change of linear

momentum for a system is equal to the sum of the external forces acting on the system. That is, the change in momentum depends on the action of the forces which can be written as

$$d\mathbf{F} = \frac{d(m_\Omega \bar{\mathbf{u}})}{d\bar{t}} \quad (1.9)$$

where \mathbf{F} represents the net force acting on the control mass and $m_\Omega = \rho d\Omega$ is the mass per unit volume as given in Section 1.3.1. Thus, the Newton's second law can be formulated as:

$$\mathbf{F} = \frac{d}{dt} \int_\Omega \rho \bar{\mathbf{u}} d\Omega. \quad (1.10)$$

Hence, for a fixed control volume Reynolds transport theorem results in

$$\frac{d}{dt} \int_\Omega \rho \bar{\mathbf{u}} d\Omega = \frac{\partial}{\partial \bar{t}} \int_\Omega \rho \bar{\mathbf{u}} d\Omega + \int_S \rho \bar{\mathbf{u}} (\bar{\mathbf{u}} \cdot \mathbf{n}) dS \quad (1.11)$$

where the first integral of right hand side denotes the rate of change of momentum in the control volume, and the second integral represents the rate of change of outflow of momentum across the control surface. The net force \mathbf{F} on the finite control volume can be expressed as

$$\mathbf{F} = \mathbf{F}_S + \mathbf{F}_B \quad (1.12)$$

where $\mathbf{F}_S = \mathbf{F}_P + \mathbf{F}_V$ is the surface force (\mathbf{F}_P : pressure force and \mathbf{F}_V : viscous force), and \mathbf{F}_B is the body force (i.e. gravity, electric forces, magnetic forces, centrifugal force etc.). Then, the pressure force \mathbf{F}_P , the viscous force \mathbf{F}_V and the body force \mathbf{F}_B can be expressed as

$$\mathbf{F}_P = - \int_S (\bar{\mathbf{p}} \cdot \mathbf{n}) dS, \quad \mathbf{F}_V = \int_S (\boldsymbol{\tau} \cdot \mathbf{n}) dS, \quad \mathbf{F}_B = \int_\Omega \rho \mathbf{b} d\Omega \quad (1.13)$$

where $\bar{\mathbf{p}}$ is the pressure, $\boldsymbol{\tau}$ is the stress tensor and \mathbf{b} is the body force per unit mass. Combining Equations (1.10) and (1.13), the integral form of momentum equation can be written as

$$\frac{\partial}{\partial \bar{t}} \int_\Omega \rho \bar{\mathbf{u}} d\Omega + \int_S \rho \bar{\mathbf{u}} (\bar{\mathbf{u}} \cdot \mathbf{n}) dS = - \int_S (\bar{\mathbf{p}} \cdot \mathbf{n}) dS + \int_S (\boldsymbol{\tau} \cdot \mathbf{n}) dS + \int_\Omega \rho \mathbf{b} d\Omega. \quad (1.14)$$

The second term on the left and right hand sides represent the convective flux and the diffusive flux, respectively. After the application of Divergence theorem, we have

$$\frac{\partial}{\partial \bar{t}} \int_\Omega \rho \bar{\mathbf{u}} d\Omega + \int_\Omega \rho \bar{\mathbf{u}} \cdot (\nabla \bar{\mathbf{u}}) d\Omega = - \int_\Omega (\nabla \bar{\mathbf{p}}) d\Omega + \int_\Omega (\nabla \cdot \boldsymbol{\tau}) d\Omega + \int_\Omega \rho \mathbf{b} d\Omega. \quad (1.15)$$

Since, Equation (1.15) is valid for any control volume, the integral vanishes and one can obtain

$$\bar{\mathbf{u}} \frac{\partial \rho}{\partial t} + \rho \frac{\partial \bar{\mathbf{u}}}{\partial t} + \rho \bar{\mathbf{u}} \cdot (\nabla \bar{\mathbf{u}}) = -\nabla \bar{p} + \nabla \boldsymbol{\tau} + \rho \mathbf{b}. \quad (1.16)$$

When the fluid is assumed to be incompressible (i.e. density is constant) and viscous, by using the relationship between $\bar{\mathbf{u}}$ and $\boldsymbol{\tau}$, the momentum equation can be written as [10]

$$\rho \frac{\partial \bar{\mathbf{u}}}{\partial t} + \rho \bar{\mathbf{u}} \cdot (\nabla \bar{\mathbf{u}}) = -\nabla \bar{p} + \mu \nabla^2 \bar{\mathbf{u}} + \rho \mathbf{b} \quad (1.17)$$

where μ is the viscosity parameter of the fluid.

1.3.3 Navier-Stokes equations

The Navier-Stokes equations play an important role in computational fluid dynamics (CFD) since they describe the physics of many scientific and engineering phenomena, namely ocean current, weather, water flow in a pipe, the design of power stations, the motion of stars inside a galaxy and blood flow analysis. The Navier-Stokes equations consist of the continuity equation for conservation of mass (Equation (1.8)) and momentum equations obtained from Newton's second law of motion for fluids (Equation (1.17)).

Thus, the two-dimensional, laminar flow of unsteady incompressible Navier-Stokes equations in terms of primitive variables are formulated by the continuity equation

$$\nabla \cdot \bar{\mathbf{u}} = 0 \quad (1.18)$$

and the momentum equation, which is written by neglecting the body forces,

$$\rho \left(\frac{\partial \bar{\mathbf{u}}}{\partial t} + \bar{\mathbf{u}} \cdot \nabla \bar{\mathbf{u}} \right) = -\nabla \bar{p} + \mu \nabla^2 \bar{\mathbf{u}}. \quad (1.19)$$

Here the vector $\bar{\mathbf{u}} = (\bar{u}, \bar{v})$ is the velocity field for a two-dimensional flow and \bar{p} is the pressure, ρ and μ are the density and the dynamic viscosity of the fluid, respectively.

The non-dimensional form of Equations (1.18) and (1.19) are obtained by introducing a characteristic length ℓ and a characteristic velocity U_0 and defining the dimensionless quantities as follows

$$x = \frac{\bar{x}}{\ell}, \quad y = \frac{\bar{y}}{\ell}, \quad u = \frac{\bar{u}}{U_0}, \quad v = \frac{\bar{v}}{U_0}, \quad t = \frac{\bar{t}}{(\ell/U_0)}, \quad p = \frac{\bar{p}}{U_0^2 \rho}. \quad (1.20)$$

Thus, the non-dimensional form of Navier-Stokes equations in component-wise can be written as

$$\frac{\partial u}{\partial x} + \frac{\partial v}{\partial y} = 0 \quad (1.21)$$

$$\nabla^2 u = Re \left(\frac{\partial p}{\partial x} + \frac{\partial u}{\partial t} + u \frac{\partial u}{\partial x} + v \frac{\partial u}{\partial y} \right) \quad (1.22)$$

$$\nabla^2 v = Re \left(\frac{\partial p}{\partial y} + \frac{\partial v}{\partial t} + u \frac{\partial v}{\partial x} + v \frac{\partial v}{\partial y} \right) \quad (1.23)$$

where dimensionless *Reynolds number* is defined as

$$Re = \frac{\rho U_0 \ell}{\mu}. \quad (1.24)$$

The Reynolds number states the ratio of inertia forces to the viscous forces, that is, Re classifies the relativity of the two types of the forces and determines the regime of the flow. Thus, if the viscous forces are more influential (i.e. $Re < 2100$) the flow regime is laminar, otherwise, the flow is said to be turbulent. The time dependent Navier-Stokes equations are usually supplied with the essential boundary conditions for velocity as

$$u(x_b, y_b, t) = f_{u_b}, \quad v(x_b, y_b, t) = f_{v_b}, \quad t > 0, \quad (1.25)$$

where the subscript b represents the restriction of (x, y) to the boundary of the region. The case when $f_{u_b} = f_{v_b} = 0$ implies the no-slip condition on the velocity field. The initial condition on velocity field is

$$u(x, y, 0) = u_0, \quad v(x, y, 0) = v_0 \quad (1.26)$$

where u_0 and v_0 are given. In conclusion, the two-dimensional incompressible Navier-Stokes equations in the traditional velocity-pressure formulation are given in Equations (1.21)-(1.23). Although this formulation describes the fluid flow phenomena precisely, it is difficult to obtain the direct solution to the system of differential equations due to the lack of the physical boundary conditions for pressure. In order to avoid the pressure term, stream function-vorticity formulation is used as an alternative formulation to the primitive variable formulation. When the stream function ψ and vorticity ω are introduced, respectively, as

$$u = \frac{\partial \psi}{\partial y}, \quad v = -\frac{\partial \psi}{\partial x} \quad (1.27)$$

$$\omega = \frac{\partial v}{\partial x} - \frac{\partial u}{\partial y} \quad (1.28)$$

Equation (1.27) satisfies the continuity equation automatically, and invoking Equation (1.27) into Equation (1.28) yields the stream function equation

$$\nabla^2\psi = -\omega. \quad (1.29)$$

Differentiating Equation (1.22) and (1.23) with respect to y and x , respectively, and subtracting differentiated Equation (1.23) from differentiated Equation (1.22) one can obtain the vorticity transport equation

$$\nabla^2\omega = Re\left(\frac{\partial\omega}{\partial t} + u\frac{\partial\omega}{\partial x} + v\frac{\partial\omega}{\partial y}\right). \quad (1.30)$$

Hence, the unsteady Navier-Stokes equations in the form of stream function and vorticity become

$$\nabla^2\psi = -\omega \quad (1.31)$$

$$\nabla^2\omega = Re\left(\frac{\partial\omega}{\partial t} + u\frac{\partial\omega}{\partial x} + v\frac{\partial\omega}{\partial y}\right). \quad (1.32)$$

1.3.4 Energy equation

The energy equation is obtained under the light of the first law of thermodynamics, which dictates the fact that the change in the internal energy of a system equals to the heat added to the system minus the work done by the system. The conserved quantity is the total energy stored per unit volume i.e. $\rho C_p \bar{T}$ where C_p is the specific heat capacitance at constant pressure and \bar{T} is the temperature. Then, the rate of change of the total thermal energy stored inside the control volume Ω with respect to time can be expressed as

$$\frac{\partial}{\partial t} \int_{\Omega} \rho C_p \bar{T} d\Omega.$$

The contribution of the convective flux is defined as

$$- \int_S (\mathbf{q}'' \cdot \mathbf{n}) dS$$

where \mathbf{q}'' represents the heat flux. Then, by the conservation of mass one can obtain the integral equation over the control volume:

$$\frac{\partial}{\partial t} \int_{\Omega} \rho C_p \bar{T} d\Omega = - \int_S (\mathbf{q}'' \cdot \mathbf{n}) dS. \quad (1.33)$$

When we apply the Divergence theorem and the Fourier law ($q'' = -k\nabla\bar{T}$) to Equation (1.33), the energy equation for an incompressible fluid over any control volume can be written as:

$$\rho C_p \frac{\partial \bar{T}}{\partial t} = k \nabla^2 \bar{T} \quad (1.34)$$

where k is the thermal conductivity and $\nabla\bar{T}$ is temperature gradient. The energy equation contains additional terms when the temperature of the fluid is under the influence of external forces as [9]

$$\rho C_p \frac{\partial \bar{T}}{\partial t} = k \nabla^2 \bar{T} + \mathbf{J}_B + \mu \Phi + Q_V \quad (1.35)$$

where μ is the dynamic viscosity of the fluid. Here the terms $\mathbf{J}_B = \frac{1}{\sigma} \mathbf{J}^2$, Φ , and Q_V represent the Joule dissipation, viscous dissipation (internal friction) and volumetric heat sources, respectively. The electric current density \mathbf{J} is induced and is given through the Ohm's law as

$$\mathbf{J} = \sigma(\mathbf{E} + \bar{\mathbf{u}} \times \bar{\mathbf{B}}) \quad (1.36)$$

where σ is the electrical conductivity of the fluid. In addition, the electric field is defined as $\mathbf{E} = -\nabla\phi$ where ϕ is the electric potential. Since the insulated boundaries makes ϕ uniform in the cavity, the electrical field becomes zero ($\mathbf{E} = 0$). Then, the term $\mathbf{J}_B = \frac{\mathbf{J}^2}{\sigma}$ representing the Joule dissipation can be converted to the term $\sigma B_0^2 (\bar{u} \sin \lambda - \bar{v} \cos \lambda)^2$ in which B_0 is the intensity of the applied magnetic field $\bar{\mathbf{B}}$ making an angle λ with the positive x -axis, and the velocity field $\bar{\mathbf{u}} = (\bar{u}, \bar{v}, 0)$. On the other hand, the viscosity of the fluid in the viscous fluid flow takes energy from the motion of the fluid (kinetic energy) and converts it into the internal energy of the fluid. The viscous dissipation is expressed as

$$\Phi = 2\left(\frac{\partial \bar{u}}{\partial \bar{x}}\right)^2 + 2\left(\frac{\partial \bar{v}}{\partial \bar{y}}\right)^2 + \left(\frac{\partial \bar{u}}{\partial \bar{y}} + \frac{\partial \bar{v}}{\partial \bar{x}}\right)^2.$$

Hence, the energy equation with viscous and Joule heating dissipations can be written as

$$\rho C_p \frac{\partial \bar{T}}{\partial t} = k \nabla^2 \bar{T} + \sigma B_0^2 (\bar{u} \sin \lambda - \bar{v} \cos \lambda)^2 + \mu \left[2\left(\frac{\partial \bar{u}}{\partial \bar{x}}\right)^2 + 2\left(\frac{\partial \bar{v}}{\partial \bar{y}}\right)^2 + \left(\frac{\partial \bar{u}}{\partial \bar{y}} + \frac{\partial \bar{v}}{\partial \bar{x}}\right)^2 \right]. \quad (1.37)$$

1.4 The MHD Flow Equations

Magnetohydrodynamics is the mathematical and physical framework which studies on the macroscopic interaction of the electrically-conducting liquids and gases with a magnetic field as mentioned previously. This interaction gives rise to a complex system called a magneto-fluid whose dynamics is quite different from that of either a non-conducting fluid or that of a magnetic field in a vacuum. The fundamental idea behind the MHD is that conductive fluids can spontaneously generate magnetic fields which is called induced magnetic field. The influence of magnetic fields create a force on the fluid thence potentially changing the magnetic field itself. The partial differential equations of MHD can be derived from Boltzmann's equation. In the standard non-relativistic form, the MHD equations consist of the basic conservation laws of mass, momentum and energy (if the heat change is considered) together with the induction equation for the magnetic field. The set of equations that describe MHD flow are a combination of the Navier-Stokes equations of fluid dynamics and Maxwell's equations of electromagnetism through the Ohm's law. The motion of a two-dimensional electrically conducting magneto-fluid satisfies the continuity equation

$$\nabla \cdot \bar{\mathbf{u}} = 0 \quad (1.38)$$

and the momentum equations [55]

$$\rho \left(\frac{\partial \bar{\mathbf{u}}}{\partial t} + \bar{\mathbf{u}} \cdot \nabla \bar{\mathbf{u}} \right) = -\nabla \bar{p} + \mu \nabla^2 \bar{\mathbf{u}} + (\mathbf{J} \times \bar{\mathbf{B}}) \quad (1.39)$$

where $\bar{\mathbf{u}} = (\bar{u}, \bar{v}, 0)$, \bar{p} , ρ are the velocity field, pressure and density of the fluid, respectively. Here, the term $\mathbf{J} \times \bar{\mathbf{B}}$ is the Lorentz force due to the magnetic field applied on the electrically conducting fluid. The electric current density \mathbf{J} is induced and is given through the Ohm's law in Equation (1.36), i.e. $\mathbf{J} = \sigma(\mathbf{E} + \bar{\mathbf{u}} \times \bar{\mathbf{B}})$. Thus

$$\mathbf{J} \times \bar{\mathbf{B}} = \sigma(\mathbf{E} + \bar{\mathbf{u}} \times \bar{\mathbf{B}}) \times \bar{\mathbf{B}} = \sigma[-\bar{B}_y(\bar{u}\bar{B}_y - \bar{v}\bar{B}_x)i + \bar{B}_x(\bar{u}\bar{B}_y - \bar{v}\bar{B}_x)j]$$

where the applied magnetic field $\bar{\mathbf{B}} = (\bar{B}_x, \bar{B}_y, 0)$ of intensity B_0 with $\bar{B}_x = B_0 \cos \lambda$, $\bar{B}_y = B_0 \sin \lambda$ and λ is the angle between $\bar{\mathbf{B}}$ and x -axis, in the case when $\mathbf{E} = 0$. Hence, the governing equations of the two-dimensional, unsteady, MHD flow can be written in component-wise as

$$\frac{\partial \bar{u}}{\partial x} + \frac{\partial \bar{u}}{\partial y} = 0 \quad (1.40)$$

$$\frac{\partial \bar{u}}{\partial t} + \bar{u} \frac{\partial \bar{u}}{\partial \bar{x}} + \bar{v} \frac{\partial \bar{u}}{\partial \bar{y}} = -\frac{1}{\rho} \frac{\partial \bar{p}}{\partial \bar{x}} + \nu \left(\frac{\partial^2 \bar{u}}{\partial \bar{x}^2} + \frac{\partial^2 \bar{u}}{\partial \bar{y}^2} \right) + \frac{\sigma B_0^2}{\rho} (\bar{v} \cos \lambda \sin \lambda - \bar{u} \sin^2 \lambda) \quad (1.41)$$

$$\frac{\partial \bar{v}}{\partial t} + \bar{u} \frac{\partial \bar{v}}{\partial \bar{x}} + \bar{v} \frac{\partial \bar{v}}{\partial \bar{y}} = -\frac{1}{\rho} \frac{\partial \bar{p}}{\partial \bar{y}} + \nu \left(\frac{\partial^2 \bar{v}}{\partial \bar{x}^2} + \frac{\partial^2 \bar{v}}{\partial \bar{y}^2} \right) + \frac{\sigma B_0^2}{\rho} (\bar{u} \cos \lambda \sin \lambda - \bar{v} \cos^2 \lambda) \quad (1.42)$$

where $\nu = \frac{\mu}{\rho}$ is the kinematic viscosity of the fluid.

When the MHD flow equations (1.40)-(1.42) is combined with the temperature equation (1.34) through the Boussinesq approximation, we end up with the MHD convection flow equations. The equations governing the unsteady MHD convection flow of a conventional pure fluid will be given in Section 1.4.1. Later, the equations of MHD nanofluid and ferrofluid flows will be expressed in Section 1.4.2 and Section 1.4.3, respectively.

1.4.1 The unsteady MHD mixed convection of conventional purefluid flow equations

As mentioned above, the equations governing the MHD convection flow are the combination of the Navier-Stokes equations with the equations of electrodynamics through the Ohm's law, and inclusion of the energy equation obeying the Boussinesq approximation. In this thesis, the equations governing the MHD mixed convection flow and heat transfer which are obtained under the following assumptions are considered. The flow is considered to be unsteady and laminar in which the Joule heating effect is taken into account while the radiation and viscous dissipation are neglected. The magnetic Reynolds number is assumed to be small so that the induced magnetic field is neglected. Moreover, an oblique magnetic field of strength B_0 forming an angle λ with the x -axis is applied and the gravity acts in the negative y -direction. Thus, under the light of these assumptions the governing equations of the unsteady MHD convection flow of a conventional fluid can be written as [55]

$$\frac{\partial \bar{u}}{\partial \bar{x}} + \frac{\partial \bar{v}}{\partial \bar{y}} = 0 \quad (1.43)$$

$$\frac{\partial \bar{u}}{\partial t} + \bar{u} \frac{\partial \bar{u}}{\partial \bar{x}} + \bar{v} \frac{\partial \bar{u}}{\partial \bar{y}} = -\frac{1}{\rho} \frac{\partial \bar{p}}{\partial \bar{x}} + \nu \left(\frac{\partial^2 \bar{u}}{\partial \bar{x}^2} + \frac{\partial^2 \bar{u}}{\partial \bar{y}^2} \right) + \frac{\sigma B_0^2}{\rho} (\bar{v} \sin \lambda \cos \lambda - \bar{u} \sin^2 \lambda), \quad (1.44)$$

$$\begin{aligned} \frac{\partial \bar{v}}{\partial \bar{t}} + \bar{u} \frac{\partial \bar{v}}{\partial \bar{x}} + \bar{v} \frac{\partial \bar{v}}{\partial \bar{y}} = & -\frac{1}{\rho} \frac{\partial \bar{p}}{\partial \bar{y}} + \nu \left(\frac{\partial^2 \bar{v}}{\partial \bar{x}^2} + \frac{\partial^2 \bar{v}}{\partial \bar{y}^2} \right) + \frac{\sigma B_0^2}{\rho} (\bar{u} \sin \lambda \cos \lambda - \bar{v} \cos^2 \lambda) \\ & + g\beta(T_h - T_c), \end{aligned} \quad (1.45)$$

$$\rho C_p \left(\frac{\partial \bar{T}}{\partial \bar{t}} + \bar{u} \frac{\partial \bar{T}}{\partial \bar{x}} + \bar{v} \frac{\partial \bar{T}}{\partial \bar{y}} \right) = k \left(\frac{\partial^2 \bar{T}}{\partial \bar{x}^2} + \frac{\partial^2 \bar{T}}{\partial \bar{y}^2} \right) + \sigma B_0^2 (\bar{u} \sin \lambda - \bar{v} \cos \lambda)^2 \quad (1.46)$$

which are the MHD equations given in Equations (1.40)-(1.42) in which the Buoyancy force $g\beta(T_h - T_c)$ is involved through the Boussinesq approximation; and the energy equation (1.37) in which the Joule heating effect is considered. Here, g is the gravitational acceleration, β is the thermal expansion coefficient.

By introducing the dimensionless variables

$$\begin{aligned} x = \frac{\bar{x}}{\ell}, \quad y = \frac{\bar{y}}{\ell}, \quad u = \frac{\bar{u}}{U_0}, \quad v = \frac{\bar{v}}{U_0}, \quad t = \frac{\bar{t}}{(\ell/U_0)}, \quad p = \frac{\bar{p}}{U_0^2 \rho} \\ \psi = \frac{\bar{\psi}}{U_0 \ell}, \quad \omega = \frac{\bar{\omega} \ell}{U_0}, \quad \alpha = \frac{k}{\rho C_p}, \quad \theta = \frac{\bar{T} - T_c}{T_h - T_c} \end{aligned} \quad (1.47)$$

we obtain the following equations for the stream function ψ , vorticity ω and temperature θ as:

$$\nabla^2 \psi = -\omega \quad (1.48)$$

$$\begin{aligned} \frac{1}{Re} \nabla^2 \omega = & \frac{\partial \omega}{\partial t} + u \frac{\partial \omega}{\partial x} + v \frac{\partial \omega}{\partial y} - \frac{Ha^2}{Re} \left(\frac{\partial u}{\partial x} \sin \lambda \cos \lambda - \frac{\partial v}{\partial y} \sin \lambda \cos \lambda \right. \\ & \left. - \frac{\partial v}{\partial x} \cos^2 \lambda + \frac{\partial u}{\partial y} \sin^2 \lambda \right) - \frac{Ra}{Re^2 Pr} \frac{\partial \theta}{\partial x} \end{aligned} \quad (1.49)$$

$$\frac{1}{Re Pr} \nabla^2 \theta = \frac{\partial \theta}{\partial t} + u \frac{\partial \theta}{\partial x} + v \frac{\partial \theta}{\partial y} - J (u \sin \lambda - v \cos \lambda)^2. \quad (1.50)$$

The dimensionless parameters are defined as the Reynolds number ($Re = \frac{U_0 \ell}{\nu}$), the Hartmann number ($Ha = B_0 \ell \sqrt{\frac{\sigma}{\mu}}$), the Prandtl number ($Pr = \frac{\nu}{\alpha}$), the Rayleigh number ($Ra = \frac{g\beta(T_h - T_c)\ell^3}{\nu\alpha}$) and the Joule heating parameter ($J = \frac{\sigma B_0^2 \ell U_0}{\rho C_p (T_h - T_c)}$).

Reynolds number is defined as the ratio of the inertia forces to friction forces in the fluid which determines the flow regime. Hartmann number is the ratio of electromagnetic force to the viscous force which characterizes the flow of conducting fluid in a transverse magnetic field. The measure of relative effectiveness of the momentum

and the energy diffusion in the velocity and thermal boundary layer is defined by the Prandtl number. The Rayleigh number is associated with the heat transfer within the fluid. That is, when the Rayleigh number is less than the critical value for a fluid, the heat transfer is in the form of conduction, while it is in the form of convection when Rayleigh number is greater than that critical value. Joule heating parameter is the quantity of Joule heating or ohmic heating which is the process by the passage of an electric current through a conductor which releases heat.

1.4.2 The unsteady MHD convection of nanofluid flow equations

A wide range of industrial processes contain the heat transfer. During any industrial facility, heat must be added, removed or moved from one process to another. The enhancement of heating or cooling in an industrial process may create a saving in energy, reduce process time, raise thermal rating and lengthen the working life of equipment. For this reason, various techniques are applied to improve the heat transfer efficiency. One of these techniques is increasing the thermal conductivity by using nanofluids as the working fluid in the convection flow as previously mentioned. Thus, this section is devoted to the equations of MHD convection flow of a nanofluid. The same assumptions for the flow given in Section 1.4.1 are considered, and the Joule heating is also neglected here. Moreover, the thermo-physical properties of the nanofluid are assumed to be constant except the density variations due to the Boussinesq approximation. Further, the nanoparticles and the base fluid are supposed to be in thermal equilibrium.

Hence, the dimensional governing equations can be written as [86]:

$$\frac{\partial \bar{u}}{\partial \bar{x}} + \frac{\partial \bar{v}}{\partial \bar{y}} = 0 \quad (1.51)$$

$$\begin{aligned} \frac{\partial \bar{u}}{\partial \bar{t}} + \bar{u} \frac{\partial \bar{u}}{\partial \bar{x}} + \bar{v} \frac{\partial \bar{u}}{\partial \bar{y}} = & -\frac{1}{\rho_{nf}} \frac{\partial \bar{p}}{\partial \bar{x}} + \nu_{nf} \left(\frac{\partial^2 \bar{u}}{\partial \bar{x}^2} + \frac{\partial^2 \bar{u}}{\partial \bar{y}^2} \right) \\ & + \frac{\sigma_{nf} B_0^2}{\rho_{nf}} (\bar{v} \sin \lambda \cos \lambda - \bar{u} \sin^2 \lambda) \end{aligned} \quad (1.52)$$

$$\begin{aligned} \frac{\partial \bar{v}}{\partial \bar{t}} + \bar{u} \frac{\partial \bar{v}}{\partial \bar{x}} + \bar{v} \frac{\partial \bar{v}}{\partial \bar{y}} = & -\frac{1}{\rho_{nf}} \frac{\partial \bar{p}}{\partial \bar{y}} + \nu_{nf} \left(\frac{\partial^2 \bar{v}}{\partial \bar{x}^2} + \frac{\partial^2 \bar{v}}{\partial \bar{y}^2} \right) + g\beta_{nf}(T - T_c) \\ & + \frac{\sigma_{nf} B_0^2}{\rho_{nf}} (\bar{u} \sin \lambda \cos \lambda - \bar{v} \cos^2 \lambda) \end{aligned} \quad (1.53)$$

$$\frac{\partial \bar{T}}{\partial \bar{t}} + \bar{u} \frac{\partial \bar{T}}{\partial \bar{x}} + \bar{v} \frac{\partial \bar{T}}{\partial \bar{y}} = \alpha_{nf} \left(\frac{\partial^2 \bar{T}}{\partial \bar{x}^2} + \frac{\partial^2 \bar{T}}{\partial \bar{y}^2} \right). \quad (1.54)$$

The effective density (ρ_{nf}), the heat capacitance $(\rho C_p)_{nf}$, the thermal expansion coefficient (β_{nf}), the thermal diffusivity (α_{nf}) and the dynamic viscosity (μ_{nf}) of the nanofluid are given respectively as [86]:

$$\begin{aligned} \rho_{nf} &= \rho_f(1 - \phi) + \rho_s\phi, \quad (\rho C_p)_{nf} = (\rho C_p)_f(1 - \phi) + (\rho C_p)_s\phi \\ \beta_{nf} &= \beta_f(1 - \phi) + \beta_s\phi, \quad \alpha_{nf} = \frac{k_{nf}}{(\rho C_p)_{nf}}, \quad \mu_{nf} = \frac{\mu_f}{(1 - \phi)^{2.5}} \end{aligned} \quad (1.55)$$

where ϕ is the solid volume fraction of nanoparticles, the subscripts nf and f denote the nanofluid and fluid, respectively. On the other hand, the effective thermal conductivity (k_{nf}) and the effective electrical conductivity (σ_{nf}) of the nanofluid are presented by the Maxwell-Garnetts model as [52]:

$$\frac{k_{nf}}{k_f} = \frac{k_s + 2k_f - 2\phi(k_f - k_s)}{k_s + 2k_f + \phi(k_f - k_s)}, \quad \frac{\sigma_{nf}}{\sigma_f} = 1 + \frac{3(\frac{\sigma_s}{\sigma_f} - 1)\phi}{(\frac{\sigma_s}{\sigma_f} + 2) - (\frac{\sigma_s}{\sigma_f} - 1)\phi}. \quad (1.56)$$

Equations (1.51)-(1.54) can be written in the stream function-vorticity-temperature form by defining $\bar{u} = \frac{\partial \bar{\psi}}{\partial \bar{y}}$, $\bar{v} = -\frac{\partial \bar{\psi}}{\partial \bar{x}}$, $\bar{\omega} = \frac{\partial \bar{v}}{\partial \bar{x}} - \frac{\partial \bar{u}}{\partial \bar{y}}$ as follows:

$$\nabla^2 \bar{\psi} = -\bar{\omega} \quad (1.57)$$

$$\begin{aligned} \nabla^2 \bar{\omega} = & \frac{1}{\nu_{nf}} \left[\left(\frac{\partial \bar{\omega}}{\partial \bar{t}} + \bar{u} \frac{\partial \bar{\omega}}{\partial \bar{x}} + \bar{v} \frac{\partial \bar{\omega}}{\partial \bar{y}} \right) - \beta_{nf} g \frac{\partial \bar{T}}{\partial \bar{y}} \right. \\ & \left. - \frac{\sigma_{nf} B_0^2}{\rho_{nf}} \left(\left(\frac{\partial \bar{u}}{\partial \bar{x}} - \frac{\partial \bar{v}}{\partial \bar{y}} \right) \sin \lambda \cos \lambda - \frac{\partial \bar{v}}{\partial \bar{x}} \cos^2 \lambda + \frac{\partial \bar{u}}{\partial \bar{y}} \sin^2 \lambda \right) \right] \end{aligned} \quad (1.58)$$

$$\nabla^2 \bar{T} = \frac{1}{\alpha_{nf}} \left(\bar{u} \frac{\partial \bar{T}}{\partial \bar{x}} + \bar{v} \frac{\partial \bar{T}}{\partial \bar{y}} \right). \quad (1.59)$$

Then, the non-dimensional form of Equations (1.57)-(1.59) becomes:

$$\nabla^2 \psi = -\omega \quad (1.60)$$

$$\begin{aligned}\nabla^2\omega &= \frac{\mu_f\rho_{nf}}{\mu_{nf}\rho_fPr_f}\left[\left(\frac{\partial\omega}{\partial t}+u\frac{\partial\omega}{\partial x}+v\frac{\partial\omega}{\partial y}\right)-Ra_fPr_f\frac{\beta_{nf}}{\beta_f}\frac{\partial\theta}{\partial x}-Ha^2Pr_f\frac{\sigma_{nf}\rho_f}{\sigma_f\rho_{nf}}\right. \\ &\quad \left.\times\left(\left(\frac{\partial u}{\partial x}-\frac{\partial v}{\partial y}\right)\sin\lambda\cos\lambda-\frac{\partial v}{\partial x}\cos^2\lambda+\frac{\partial u}{\partial y}\sin^2\lambda\right)\right]\end{aligned}\quad (1.61)$$

$$\nabla^2\theta = \frac{(\rho Cp)_{nf}k_f}{(\rho Cp)_fk_{nf}}\left(\frac{\partial\theta}{\partial t}+u\frac{\partial\theta}{\partial x}+v\frac{\partial\theta}{\partial y}\right) \quad (1.62)$$

by introducing the following non-dimensional variables [86]

$$x = \frac{\bar{x}}{\ell}, \quad y = \frac{\bar{y}}{\ell}, \quad \omega = \frac{\bar{\omega}\ell^2}{\alpha_f}, \quad \psi = \frac{\bar{\psi}}{\alpha_f}, \quad \theta = \frac{\bar{T}-\bar{T}_c}{(q''\ell/k_f)}, \quad u = \frac{\bar{u}\ell}{\alpha_f}, \quad v = \frac{\bar{v}\ell}{\alpha_f}, \quad t = \frac{\bar{t}\alpha_f}{\ell^2}.$$

The dimensionless physical parameters for the base fluid are the Rayleigh number $Ra_f = (\beta_f g \ell^4 q'')/(k_f \alpha_f \nu_f)$, Prandtl number $Pr_f = \nu_f/\alpha_f$ and the Hartmann number $Ha = \ell B_0 \sqrt{\sigma_f/\mu_f}$. Moreover, the coefficients are

$$\begin{aligned}\frac{\mu_f\rho_{nf}}{\mu_{nf}\rho_f} &= (1-\phi)^{2.5}\left[(1-\phi)+\frac{\rho_s}{\rho_f}\phi\right], \quad \frac{\beta_{nf}}{\beta_f} = (1-\phi)+\frac{\beta_s}{\beta_f}\phi, \\ \frac{\sigma_{nf}\rho_f}{\sigma_f\rho_{nf}} &= \left[1+\frac{3(\frac{\sigma_s}{\sigma_f}-1)\phi}{(\frac{\sigma_s}{\sigma_f}+2)}-(\frac{\sigma_s}{\sigma_f}-1)\phi\right]\frac{1}{(1-\phi)+\frac{\rho_s}{\rho_f}\phi}, \\ \frac{(\rho Cp)_{nf}k_f}{(\rho Cp)_fk_{nf}} &= \left[(1-\phi)+\frac{(\rho Cp)_s}{(\rho Cp)_f}\phi\right]\frac{k_s+2k_f-2\phi(k_f-k_s)}{k_s+2k_f+\phi(k_f-k_s)}.\end{aligned}\quad (1.63)$$

1.4.3 The steady MHD convection of ferrofluid flow equations

In the present section, we consider the convective ferrofluid flow equations under the effect of spatially variable magnetic sources (i.e. one nodal or multiple nodal magnetic sources, i.e. magnets). The combination of magnetohydrodynamic and ferrohydrodynamic effects will be taken into account. The governing equations are obtained by using the same assumptions given in Section 1.4.2. Moreover, the flow is assumed to be steady here. For the expression of the magnetic field strength, it can be considered that the magnetic sources represent the magnetic wires placed vertically to the xy -plane. The components of magnetic field intensity (\bar{H}_x, \bar{H}_y) and the strength of magnetic field (\bar{H}) for a single or multiple magnetic nodal sources can be written

as, respectively, for a single nodal magnetic source:

$$\begin{aligned}\bar{H}_x &= \frac{\gamma}{2\pi} \frac{1}{(\bar{x} - \bar{a})^2 + (\bar{x} - \bar{b})^2} (\bar{y} - \bar{b}), \quad \bar{H}_y = -\frac{\gamma}{2\pi} \frac{1}{(\bar{x} - \bar{a})^2 + (\bar{x} - \bar{b})^2} (\bar{x} - \bar{a}) \\ \bar{H} &= \sqrt{\bar{H}_x^2 + \bar{H}_y^2} = \frac{\gamma}{2\pi} \frac{1}{\sqrt{(\bar{x} - \bar{a})^2 + (\bar{x} - \bar{b})^2}}\end{aligned}\tag{1.64}$$

and for two nodal magnetic sources:

$$\bar{H}_x = \frac{\gamma}{2\pi} \frac{1}{(\bar{x} - \bar{a}_1)^2 + (\bar{y} - \bar{b}_1)^2} (\bar{y} - \bar{b}_1) + \frac{\gamma}{2\pi} \frac{1}{(\bar{x} - \bar{a}_2)^2 + (\bar{y} - \bar{b}_2)^2} (\bar{y} - \bar{b}_2), \tag{1.65}$$

$$\bar{H}_y = -\frac{\gamma}{2\pi} \frac{1}{(\bar{x} - \bar{a}_1)^2 + (\bar{y} - \bar{b}_1)^2} (\bar{x} - \bar{a}_1) - \frac{\gamma}{2\pi} \frac{1}{(\bar{x} - \bar{a}_2)^2 + (\bar{y} - \bar{b}_2)^2} (\bar{x} - \bar{a}_2), \tag{1.66}$$

$$\bar{H} = \sqrt{\bar{H}_x^2 + \bar{H}_y^2}. \tag{1.67}$$

Here, γ is the magnetic field strength at the source of the wire and (\bar{a}, \bar{b}) , (\bar{a}_1, \bar{b}_1) and (\bar{a}_2, \bar{b}_2) are the positions where the sources (magnetic wires) are located vertically on the xy -plane for a single and two nodal magnetic sources, respectively.

Thus, the dimensional governing equations of the steady, two-dimensional and laminar ferrofluid flow under the effect of a nodal or multiple magnetic sources can be written as follows:

$$\frac{\partial \bar{u}}{\partial \bar{x}} + \frac{\partial \bar{v}}{\partial \bar{y}} = 0 \tag{1.68}$$

$$\begin{aligned}\rho_{nf}(\bar{u} \frac{\partial \bar{u}}{\partial \bar{x}} + \bar{v} \frac{\partial \bar{u}}{\partial \bar{y}}) &= -\frac{\partial \bar{p}}{\partial \bar{x}} + \mu_{nf}(\frac{\partial^2 \bar{u}}{\partial \bar{x}^2} + \frac{\partial^2 \bar{u}}{\partial \bar{y}^2}) + \mu_0 M \frac{\partial \bar{H}}{\partial \bar{x}} \\ &\quad - \sigma_{nf} \bar{B}_y^2 \bar{u} + \sigma_{nf} \bar{B}_x \bar{B}_y \bar{v}\end{aligned}\tag{1.69}$$

$$\begin{aligned}\rho_{nf}(\bar{u} \frac{\partial \bar{v}}{\partial \bar{x}} + \bar{v} \frac{\partial \bar{v}}{\partial \bar{y}}) &= -\frac{\partial \bar{p}}{\partial \bar{y}} + \mu_{nf}(\frac{\partial^2 \bar{v}}{\partial \bar{x}^2} + \frac{\partial^2 \bar{v}}{\partial \bar{y}^2}) + \mu_0 M \frac{\partial \bar{H}}{\partial \bar{y}} \\ &\quad - \sigma_{nf} \bar{B}_x^2 \bar{v} + \sigma_{nf} \bar{B}_x \bar{B}_y \bar{u} + \rho_{nf} \beta_{nf} g(\bar{T} - \bar{T}_c)\end{aligned}\tag{1.70}$$

$$\begin{aligned}(\rho C_p)_{nf}(\bar{u} \frac{\partial \bar{T}}{\partial \bar{x}} + \bar{v} \frac{\partial \bar{T}}{\partial \bar{y}}) &= k_{nf}(\frac{\partial^2 \bar{T}}{\partial \bar{x}^2} + \frac{\partial^2 \bar{T}}{\partial \bar{y}^2}) + \sigma_{nf} (\bar{u} \bar{B}_y - \bar{v} \bar{B}_x)^2 \\ &\quad - \mu_0 \bar{T} \frac{\partial M}{\partial \bar{T}} (\bar{u} \frac{\partial \bar{H}}{\partial \bar{x}} + \bar{v} \frac{\partial \bar{H}}{\partial \bar{y}}) \\ &\quad + \mu_{nf} \left\{ 2(\frac{\partial \bar{u}}{\partial \bar{x}})^2 + 2(\frac{\partial \bar{v}}{\partial \bar{y}})^2 + (\frac{\partial \bar{u}}{\partial \bar{y}} + \frac{\partial \bar{v}}{\partial \bar{x}})^2 \right\}\end{aligned}\tag{1.71}$$

where μ_0 is the magnetic permeability of the vacuum ($4\pi \times 10^{-7} Tm/A$), \bar{B} is the magnetic induction ($\bar{B} = \mu_0 \bar{H}$). The effective density (ρ_{nf}), the heat capacitance (ρC_p)_{nf}, the thermal expansion coefficient (β_{nf}), the thermal diffusivity (α_{nf}) and the dynamic viscosity (μ_{nf}) of the nanofluid are given Section 1.4.2.

The terms $\mu_0 M \frac{\partial \bar{H}}{\partial \bar{x}}$ and $\mu_0 M \frac{\partial \bar{H}}{\partial \bar{y}}$ in Equations (1.69)- (1.70), represent the components of magnetic force per unit volume in x and y -directions, respectively. These two terms are called Kelvin force and they come from FHD. The terms $-\sigma_{nf} \bar{B}_y^2 \bar{u} + \sigma_{nf} \bar{B}_x \bar{B}_y \bar{v}$ and $-\sigma_{nf} \bar{B}_x^2 \bar{v} + \sigma_{nf} \bar{B}_x \bar{B}_y \bar{u}$ which appear in Equations (1.69)-(1.70) represent the Lorentz force per unit volume in the x and y -directions respectively, and they arise due to the electrical conductivity of the fluid. These two terms are known in MHD. The term $-\mu_0 \bar{T} \frac{\partial M}{\partial \bar{T}} (\bar{u} \frac{\partial \bar{H}}{\partial \bar{x}} + \bar{v} \frac{\partial \bar{H}}{\partial \bar{y}})$ in Equation (1.71) represents the thermal power per unit volume due to the magneto-caloric effect. Also the term $\sigma_{nf} (\bar{u} \bar{B}_y - \bar{v} \bar{B}_x)^2$ in Equation (1.71) represents the Joule heating. The magnetization M is given by $M = K' \bar{H} (T'_c - \bar{T})$, where \bar{H} and T'_c are the magnetic field intensity and the Curie temperature, respectively, and K' is a constant.

By introducing the non-dimensional variables:

$$\begin{aligned} a &= \frac{\bar{a}}{\ell}, \quad b = \frac{\bar{b}}{\ell}, \quad a_1 = \frac{\bar{a}_1}{\ell}, \quad b_1 = \frac{\bar{b}_1}{\ell}, \quad a_2 = \frac{\bar{a}_2}{\ell}, \quad b_2 = \frac{\bar{b}_2}{\ell} \\ x &= \frac{\bar{x}}{\ell}, \quad y = \frac{\bar{y}}{\ell}, \quad \theta = \frac{\bar{T} - T_c}{T_h - T_c}, \quad u = \frac{\bar{u} \ell}{\alpha_f}, \quad v = \frac{\bar{v} \ell}{\alpha_f}, \quad H = \frac{\bar{H}}{\bar{H}_0} \\ H_x &= \frac{\bar{H}_x}{\bar{H}_0}, \quad H_y = \frac{\bar{H}_y}{\bar{H}_0}, \quad p = \frac{\bar{p}}{\rho_f (\alpha_f / \ell)^2} \end{aligned}$$

where $\bar{H}_0 = \bar{H}(\bar{a}, 0) = \frac{\gamma}{2\pi |\bar{b}|}$ for a nodal magnetic source while $\bar{H}_0 = \bar{H}(\bar{a}, 0) = \frac{\gamma}{2\pi} \left| \frac{\bar{b}_1 + \bar{b}_2}{\bar{b}_1 \bar{b}_2} \right|$ where $\bar{a}_1 = \bar{a}_2 = \bar{a}$ for multiple nodal magnetic sources. One can obtain the dimensionless form of Equations (1.68)-(1.71) as:

$$\frac{\partial u}{\partial x} + \frac{\partial v}{\partial y} = 0 \tag{1.72}$$

$$\begin{aligned}
u \frac{\partial u}{\partial x} + v \frac{\partial u}{\partial y} = & -\frac{\rho_f}{\rho_{nf}} \frac{\partial p}{\partial x} + Pr_f \frac{\mu_{nf}/\mu_f}{\rho_{nf}/\rho_f} \left(\frac{\partial^2 u}{\partial x^2} + \frac{\partial^2 u}{\partial y^2} \right) \\
& + Mn_f Pr_f \left(\frac{\rho_f}{\rho_{nf}} \right) (\epsilon_2 - \epsilon_1 - \theta) H \frac{\partial H}{\partial x} \\
& - Ha^2 Pr_f \frac{\sigma_{nf}/\sigma_f}{\rho_{nf}/\rho_f} (H_y^2 u - H_x H_y v)
\end{aligned} \tag{1.73}$$

$$\begin{aligned}
u \frac{\partial v}{\partial x} + v \frac{\partial v}{\partial y} = & -\frac{\rho_f}{\rho_{nf}} \frac{\partial p}{\partial y} + Pr_f \frac{\mu_{nf}/\mu_f}{\rho_{nf}/\rho_f} \left(\frac{\partial^2 v}{\partial x^2} + \frac{\partial^2 v}{\partial y^2} \right) \\
& + Mn_f Pr_f \left(\frac{\rho_f}{\rho_{nf}} \right) (\epsilon_2 - \epsilon_1 - \theta) H \frac{\partial H}{\partial y} \\
& - Ha^2 Pr_f \frac{\sigma_{nf}/\sigma_f}{\rho_{nf}/\rho_f} (H_x^2 v - H_x H_y u) + Ra Pr_f \frac{\beta_{nf}}{\beta_f} \theta
\end{aligned} \tag{1.74}$$

$$\begin{aligned}
u \frac{\partial \theta}{\partial x} + v \frac{\partial \theta}{\partial y} = & \frac{\frac{k_{nf}}{k_f}}{(\rho C p)_{nf}} \left(\frac{\partial^2 \theta}{\partial x^2} + \frac{\partial^2 \theta}{\partial y^2} \right) + Ha^2 Ec \frac{\frac{\sigma_{nf}}{\sigma_f}}{(\rho C p)_{nf}} (u H_y - v H_x)^2 \\
& + Mn_f Ec \frac{(\rho C p)_f}{(\rho C p)_{nf}} \left(u \frac{\partial H}{\partial x} + v \frac{\partial H}{\partial y} \right) H (\epsilon_1 + \theta) \\
& + Ec \frac{\frac{\mu_{nf}}{\mu_f}}{(\rho C p)_{nf}} \left(2 \left(\frac{\partial u}{\partial x} \right)^2 + 2 \left(\frac{\partial v}{\partial y} \right)^2 + \left(\frac{\partial u}{\partial y} + \frac{\partial v}{\partial x} \right)^2 \right)
\end{aligned} \tag{1.75}$$

where $Ra_f = g \beta_f \ell^3 (T - T_c) / (\alpha_f \nu_f)$, $Pr_f = \nu_f / \alpha_f$, $Ha = \ell \mu_0 H_0 \sqrt{\sigma_f / \mu_f}$, $\epsilon_1 = T_1 / \Delta T$, $\epsilon_2 = T'_c / \Delta T$, $Ec = (\mu_f \nu_f) / [(\rho C p)_f \Delta T \ell^2]$ and $Mn_f = \mu_0 H_0^2 K' (T_h - T_c) \ell^2 / (\mu_f \alpha_f)$ are the Rayleigh number, Prandtl number, Hartmann number arising from MHD, temperature number, Curie temperature number, Eckert number and magnetic number arising from FHD for the base fluid, respectively. Equations (1.72)-(1.75) can be written in the stream function-vorticity-temperature form as:

$$\nabla^2 \psi = -\omega \tag{1.76}$$

$$\begin{aligned}
\nabla^2 \omega = & \frac{\rho_{nf}/\rho_f}{Pr_f (\mu_{nf}/\mu_f)} \left(\frac{\partial \psi}{\partial y} \frac{\partial \omega}{\partial x} - \frac{\partial \psi}{\partial x} \frac{\partial \omega}{\partial y} \right) \\
& - Mn_f \frac{\rho_{nf}/\rho_f}{\mu_{nf}/\mu_f} \left(\frac{\rho_f}{\rho_{nf}} \right) \left[-\frac{\partial \theta}{\partial x} H \frac{\partial H}{\partial y} + \frac{\partial \theta}{\partial y} H \frac{\partial H}{\partial x} \right] \\
& + Ha^2 \frac{\rho_{nf}/\rho_f}{\mu_{nf}/\mu_f} \frac{\sigma_{nf}/\sigma_f}{\rho_{nf}/\rho_f} \left[2H_x \frac{\partial H_x}{\partial x} v + H_x^2 \left(\frac{\partial v}{\partial x} \right) \right. \\
& - \frac{\partial H_x}{\partial x} H_y u - H_x \frac{\partial H_y}{\partial x} u - H_x H_y \left(\frac{\partial u}{\partial x} \right) - 2H_y \frac{\partial H_y}{\partial y} u \\
& \left. - H_y^2 \left(\frac{\partial u}{\partial y} \right) + \frac{\partial H_x}{\partial y} H_y v + H_x \frac{\partial H_y}{\partial y} v + H_x H_y \left(\frac{\partial v}{\partial y} \right) \right] \\
& - Ra \frac{\rho_{nf}/\rho_f}{\mu_{nf}/\mu_f} \frac{\beta_{nf}}{\beta_f} \frac{\partial \theta}{\partial x}
\end{aligned} \tag{1.77}$$

$$\begin{aligned}
\nabla^2 \theta = & \frac{\frac{(\rho Cp)_{nf}}{(\rho Cp)_f}}{\frac{k_{nf}}{k_f}} \left(\frac{\partial \psi}{\partial y} \frac{\partial \theta}{\partial x} - \frac{\partial \psi}{\partial x} \frac{\partial \theta}{\partial y} \right) \\
& - Ha^2 Ec \frac{\frac{(\rho Cp)_{nf}}{(\rho Cp)_f}}{\frac{k_{nf}}{k_f}} \frac{\frac{\sigma_{nf}}{\sigma_f}}{\frac{(\rho Cp)_{nf}}{(\rho Cp)_f}} (uH_y - vH_x)^2 \\
& - Mn_f Ec \frac{\frac{(\rho Cp)_{nf}}{(\rho Cp)_f}}{\frac{k_{nf}}{k_f}} \frac{(\rho Cp)_f}{(\rho Cp)_{nf}} \left[u \frac{\partial H}{\partial x} + v \frac{\partial H}{\partial y} \right] H (\epsilon_1 + \theta) \\
& - Ec \frac{\frac{(\rho Cp)_{nf}}{(\rho Cp)_f}}{\frac{k_{nf}}{k_f}} \frac{\frac{\mu_{nf}}{\mu_f}}{\frac{(\rho Cp)_{nf}}{(\rho Cp)_f}} \left[2 \left(\frac{\partial u}{\partial x} \right)^2 + 2 \left(\frac{\partial v}{\partial y} \right)^2 + \left(\frac{\partial u}{\partial y} + \frac{\partial v}{\partial x} \right)^2 \right].
\end{aligned} \tag{1.78}$$

The intensity (H_x, H_y) and the strength of the magnetic field (H) for a single mag-

netic source are given in non-dimensional form as follows:

$$\begin{aligned} H_x &= \frac{|b|(y-b)}{(x-a)^2 + (x-b)^2}, \quad H_y = -\frac{|b|(x-a)}{(x-a)^2 + (x-b)^2}, \\ H &= \frac{|b|}{\sqrt{(x-a)^2 + (x-b)^2}}. \end{aligned} \quad (1.79)$$

While for two nodal magnetic sources we have:

$$\begin{aligned} H_x &= \left| \frac{b_1 b_2}{b_1 + b_2} \right| \left(\frac{y-b_1}{(x-a_1)^2 + (y-b_1)^2} + \frac{y-b_2}{(x-a_2)^2 + (y-b_2)^2} \right), \\ H_y &= -\left| \frac{b_1 b_2}{b_1 + b_2} \right| \left(\frac{x-a_1}{(x-a_1)^2 + (y-b_1)^2} + \frac{x-a_2}{(x-a_2)^2 + (y-b_2)^2} \right), \\ H &= \left| \frac{b_1 b_2}{b_1 + b_2} \right| \sqrt{\frac{(2x-a_1-a_2)^2 + (2y-b_1-b_2)^2}{[(x-a_1)^2 + (y-b_1)^2][(x-a_2)^2 + (y-b_2)^2]}}. \end{aligned} \quad (1.80)$$

1.5 Nusselt Number

In order to examine the heat transfer between heated and cooled surfaces, the Nusselt number is used, which is the ratio of convection heat transfer to conduction heat transfer.

The derivation of the Nusselt number is obtained by the following process. Suppose that a cold fluid stream cools a hot surface. The heat, which has a constant temperature, is diffused through a boundary layer from hot surface to cold surface. This idea is defined by Newton's law of cooling per unit surface area as follows [9]

$$h(T_h - T_c) = -k \frac{\partial \bar{T}}{\partial n} \quad (1.81)$$

where h is the heat transfer coefficient, k is the thermal conductivity of fluid, T_c free stream temperature of the fluid and n is the normal direction to the heat transfer surface. Equation (1.81) can be written as

$$\frac{h\ell}{k} = -\frac{1}{T_h - T_c} \frac{\partial \bar{T}}{\partial n} \ell \quad (1.82)$$

where ℓ is the characteristic length. Applying non-dimensional scales which are discussed in Equation (1.47), Equation (1.82) can be written as

$$Nu = -\frac{\partial \theta}{\partial n} \quad (1.83)$$

where Nu is the local Nusselt number, which is equal to the local, dimensionless, normal temperature gradient. This definition is valid whether the surface temperature is constant or a temperature of reference wall is known. All the above discussions are about the local part of the surface but, it is necessary to have the *average* heat transfer coefficient to get off the dependence on the spatial variables x and y . The average heat transfer coefficient, referred as the average Nusselt number, can be obtained by integrating local results over an appropriate length (in two dimensions) or surface (in three dimensions). For example, the average Nusselt number along the heated wall is

$$\overline{Nu} = \frac{1}{S} \int_0^s Nu \, ds \quad (1.84)$$

where s is the coordinate along the heated surface, S is the arc length of the boundary of the surface and ds is the arc length element.

1.6 Plan of the Thesis

In Chapter 2, the basic formulations of the BEM and DRBEM for solving the Laplace and Poisson type equations, respectively, are presented. The applications of the BEM to the Laplace equation and of the DRBEM to the unsteady Poisson's type equations are explained in details. Converting the unsteady problems into a system of first order time-dependent ordinary differential equations via DRBEM is explained and a two-level time integration scheme is introduced for the solution of the time-dependent system. Finally, the stability of the DRBEM for the unsteady problems is explained.

In Chapter 3, the steady/unsteady two-dimensional, laminar flow of an incompressible, viscous and electrically conducting fluid subject to an externally applied uniform magnetic field is solved numerically by DRBEM in space-two level time integration scheme in time. First, the steady, mixed convection flow in a channel of square cross-section with a moving left wall and a right wall involving heaters of different shapes (semi-circular, semi-rectangular or sinusoidal wavy heaters) subject to an externally applied uniform magnetic field is considered. Later, the problem in a lid-driven cavity with sinusoidal wavy hot right wall is solved for the unsteady case to analyze the numerical stability of dual reciprocity BEM with a two-level time integration scheme.

In Chapter 4 and Chapter 5, the dual reciprocity BEM solution of steady/unsteady

two-dimensional, laminar flow of an incompressible, viscous and electrically conducting nanofluid and ferrofluid, respectively, in semi-annulus with either circular or sinusoidal wavy inner walls is considered. In the nanofluid flow, the effect of uniform inclined magnetic field is investigated while in the ferrofluid flow the effect of magnetic field produced by a single or multiple nodal magnetic sources is studied. The physical problems and their mathematical models are introduced, and then the application of the numerical method which is the combination of DRBEM in space and the two-level scheme in time to the problems under consideration is explained briefly. The numerical simulations are carried out in semi-annulus with different shape of inner walls determined by the number of undulation. For the unsteady problems, the stability analysis of the numerical method is also performed.

CHAPTER 2

THE BOUNDARY AND THE DUAL RECIPROCITY BOUNDARY ELEMENT METHODS

The numerical solution of partial differential equations (PDEs) encountered in mathematical physics and engineering can be obtained with one of the known methods such as finite difference method (FDM), finite element method (FEM), finite volume method (FVM) and boundary element method (BEM). In finite difference, finite element and finite volume methods the domain of the problem is discretized into a number of cells and the governing equations of the problem are approximated over the whole domain by functions which fully or partially satisfy the boundary conditions. On the other hand, the boundary element method is a boundary-only nature technique which discretize only the boundary of the computational domain to obtain the solution of the problem under consideration. In this sense, BEM offers an elegant and economic alternative to the domain discretization methods. The advantage of using BEM lies in the fact that the dependence of complete problem is reduced to only on the boundary, which provides simplicity in computer code and reduces the time for data preparation in the solution process of partial differential equations. However, the main drawback of BEM occurs in partial differential equations with non-homogeneous and non-linear terms that do not have an explicit fundamental solution since BEM requires an inherent use of the fundamental solution to the whole governing equations of the problem under consideration. In this case, the domain integrals appearing in the integral equation prevent the dimensional reduction of the problem due to the internal discretization. This causes the BEM lose its main usefulness, which is the boundary-only formulation of the problem.

In order to deal with this problem, some alternative methodologies have been re-

vealed. The most accomplished one is the dual reciprocity BEM (DRBEM). The basic idea of the DRBEM is to treat all the terms except the ones for which the fundamental solution is known as the non-homogeneity and these non-homogeneous terms are approximated by some well-known interpolation functions called radial basis (co-ordinate) functions (RBFs). Basically, the differential equation is transformed into an equivalent integral equation which contains both domain and boundary integrals by weighting the differential equation with the appropriate fundamental solution and integrating over the computational domain through the Divergence theorem. The resulting domain integrals are treated by means of so called RBFs which are linked to the particular solution of the governing terms for which the fundamental solution is employed.

In this chapter, the basic formulations of the BEM and DRBEM for solving the Laplace and Poisson type equations, respectively, are presented. In Section 2.1.1, the application of the BEM to the Laplace equation is explained in details including the discretization of the boundary (see Section 2.1.2) with both constant and linear elements. Then, the BEM idea in obtaining the integral formulation is extended for the Poisson's equation in Section 2.2. Section 2.3 deals with the DRBEM solution of Poisson's type equations. The application of DRBEM to Poisson's equation by taking all the terms except the Laplacian operator to the right hand side and treating them as non-homogeneity is given in Section 2.3.1. The approximation of the non-homogeneous terms by several kinds of radial basis functions, such as linear polynomials, multi-quadratics, inverse multi-quadratics and thin-plate splines is explained in Section 2.3.2. The idea of DRBEM is extended further for the Poisson's type equation in which the right hand side involves the unknown and its derivatives with respect to both time and space variables (see Section 2.3.3). The application of DRBEM to the unsteady problems converts the system into an initial value problem represented by a system of first order time-dependent ordinary differential equations. For the solution of the time-dependent system, a time integration scheme introduced in Section 2.3.3.1 is employed. Finally, the stability of the DRBEM for the time dependent problems is explained in Section 2.4.

2.1 Boundary Element Method

The boundary element formulation for the solution of boundary value problems can be presumed as a weighted residual technique. That is, the general integral formulation for the governing partial differential equations is obtained by multiplying them with a weight function and integrating them over the problem domain. Then, the resulting integral equation is transformed into an equivalent boundary integral by the use of the fundamental solution of the governing equations and the application of Divergence Theorem as explained in [12]. This procedure is going to be illustrated in details for the solution of Laplace equation in Section 2.1.1 and 2.1.2, and given in general for the Poisson's equation in Section 2.2.

2.1.1 Application of BEM to the Laplace equation

The two dimensional Laplace equation

$$\nabla^2 u = 0 \quad \text{in } \Omega \quad (2.1)$$

with the boundary conditions:

$$u = \bar{u} \quad \text{on } \Gamma_1 \quad (\text{Dirichlet Type}), \quad (2.2)$$

$$q = \frac{\partial u}{\partial n} = \bar{q} \quad \text{on } \Gamma_2 \quad (\text{Neumann Type}) \quad (2.3)$$

is considered. Here, ∇^2 is the Laplace operator, \bar{u} , \bar{q} are given functions, q is the normal derivative of unknown u and \mathbf{n} denotes the outward unit normal to the boundary $\Gamma = \Gamma_1 + \Gamma_2$ (see Figure 2.1).

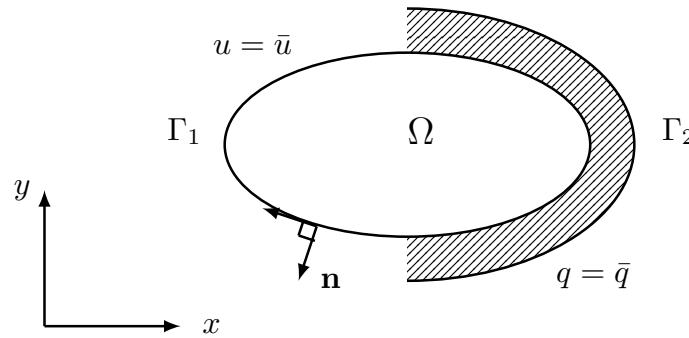


Figure 2.1: Geometry of the problem

The replacement of the exact values u and q with the approximate values \hat{u} and \hat{q} in Equations (2.1)-(2.3) results in the following errors (so-called residuals):

$$\begin{aligned}\varepsilon &= \nabla^2 \hat{u} \neq 0 \quad \text{in } \Omega \\ \varepsilon_1 &= \hat{u} - \bar{u} \neq 0 \quad \text{on } \Gamma_1 \\ \varepsilon_2 &= \frac{\partial \hat{u}}{\partial n} - \bar{q} \neq 0 \quad \text{on } \Gamma_2\end{aligned}\tag{2.4}$$

which are minimized by orthogonalizing them with respect to the weight functions u^* , \bar{u}^* , $\bar{\bar{u}}^*$ as:

$$\int_{\Omega} \varepsilon u^* d\Omega + \int_{\Gamma_1} \varepsilon_1 \bar{u}^* d\Gamma + \int_{\Gamma_2} \varepsilon_2 \bar{\bar{u}}^* d\Gamma = 0.\tag{2.5}$$

Once the residuals are inserted in Equation (2.5), we have

$$\int_{\Omega} (\nabla^2 \hat{u}) u^* d\Omega + \int_{\Gamma_1} (\hat{u} - \bar{u}) \bar{u}^* d\Gamma + \int_{\Gamma_2} \left(\frac{\partial \hat{u}}{\partial n} - \bar{q} \right) \bar{\bar{u}}^* d\Gamma = 0.\tag{2.6}$$

The application of Divergent theorem results in

$$- \int_{\Omega} \frac{\partial \hat{u}}{\partial n} \frac{\partial u^*}{\partial n} d\Omega + \int_{\Gamma_1 + \Gamma_2} \frac{\partial \hat{u}}{\partial n} u^* d\Gamma + \int_{\Gamma_1} (\hat{u} - \bar{u}) \bar{u}^* d\Gamma + \int_{\Gamma_2} \left(\frac{\partial \hat{u}}{\partial n} - \bar{q} \right) \bar{\bar{u}}^* d\Gamma = 0\tag{2.7}$$

and when u^* is taken as $-\bar{\bar{u}}^*$ one gets

$$- \int_{\Omega} \frac{\partial \hat{u}}{\partial n} \frac{\partial u^*}{\partial n} d\Omega + \int_{\Gamma_1} \frac{\partial \hat{u}}{\partial n} u^* d\Gamma + \int_{\Gamma_1} (\hat{u} - \bar{u}) \bar{u}^* d\Gamma + \int_{\Gamma_2} \bar{q} u^* d\Gamma = 0.\tag{2.8}$$

When the the Divergence theorem is employed for the second time with the choice of $\bar{u}^* = \partial u^* / \partial n$, Equation (2.8) becomes

$$\int_{\Omega} \hat{u} \nabla^2 u^* d\Omega - \int_{\Gamma_2} \hat{u} q^* d\Gamma + \int_{\Gamma_1} \hat{q} u^* d\Gamma - \int_{\Gamma_1} \bar{u} q^* d\Gamma + \int_{\Gamma_2} \bar{q} u^* d\Gamma = 0\tag{2.9}$$

where $q^* = \frac{\partial u^*}{\partial n}$ and $\hat{q} = \frac{\partial \hat{u}}{\partial n}$. The domain integral is eliminated by the use of a special type of weight function u^* called the fundamental solution. Thus, the weighting function u^* is taken as the fundamental solution of Laplace equation, that is, u^* satisfies the following Poisson's equation

$$\nabla^2 u^* = -\delta_i\tag{2.10}$$

where δ_i represents the Dirac delta function [12]. Thus, the domain integral in Equation (2.5) can be written as

$$\int_{\Omega} \hat{u} \nabla^2 u^* d\Omega = \int_{\Omega} \hat{u} (-\delta_i) d\Omega = -c_i \hat{u}_i\tag{2.11}$$

since the integral of Dirac delta function multiplied by any function is equal to the value of the latter at $i = (x_i, y_i)$, and here the subscript i represents the source point. The constant c_i is equal to

$$c_i = \begin{cases} \frac{\theta_i}{2\pi}, & \text{if } i \in \Gamma, \\ 1, & \text{if } i \in \Omega \setminus \Gamma, \end{cases}$$

with the internal angle θ_i at the point i in radians. Thus, Equation (2.9) becomes

$$-c_i \hat{u}_i + \int_{\Gamma_1} \hat{q} u^* d\Gamma + \int_{\Gamma_2} \bar{q} u^* d\Gamma - \int_{\Gamma_1} \bar{u} q^* d\Gamma - \int_{\Gamma_2} \hat{u} q^* d\Gamma = 0. \quad (2.12)$$

For a two-dimensional medium the fundamental solution u^* of the Laplace equation and its normal derivative q^* are

$$u^* = \frac{1}{2\pi} \ln\left(\frac{1}{r}\right) = -\frac{1}{2\pi} \ln r, \quad q^* = \frac{\partial u^*}{\partial n} = \frac{1}{2\pi} \frac{(\mathbf{r} - \mathbf{r}_i) \cdot \vec{n}}{|\mathbf{r} - \mathbf{r}_i|^2} \quad (2.13)$$

where $r = |\mathbf{r} - \mathbf{r}_i| = \sqrt{(x - x_i)^2 + (y - y_i)^2}$ is the distance between the field point $\mathbf{r} = (x, y)$ and the source point $\mathbf{r}_i = (x_i, y_i)$. Equation (2.12) is rewritten in the following compact form

$$c_i \tilde{u}_i + \int_{\Gamma} \tilde{u} q^* d\Gamma = \int_{\Gamma} \tilde{q} u^* d\Gamma \quad (2.14)$$

where \tilde{u} and \tilde{q} are defined as

$$\tilde{u} = \begin{cases} \bar{u}, & \text{if } i \in \Gamma_1 \\ \hat{u}, & \text{if } i \in \Gamma_2 \end{cases}, \quad \tilde{q} = \begin{cases} \bar{q}, & \text{if } i \in \Gamma_1 \\ \hat{q}, & \text{if } i \in \Gamma_2 \end{cases}. \quad (2.15)$$

In order to simplify the notation, the symbol \sim will be dropped in the remaining formulations. Thus, Equation (2.14) can be written as

$$c_i u_i + \int_{\Gamma} u q^* d\Gamma = \int_{\Gamma} q u^* d\Gamma \quad (2.16)$$

which is the integral equation only on the boundary and is generally used as the starting point for the boundary element formulation.

2.1.2 Discretization of the boundary

We consider now how the boundary integral Equation (2.16) can be discretized to construct the system of equations from which the boundary values are obtained. The

discretization can be made by partitioning the boundary into small line segments or elements which are called *boundary elements*, and the points where the unknown values are considered, are called *nodes* [61]. The elements of which the nodes are taken to be in the middle of each elements are called *constant elements* (see Figure 2.2(a)) and the elements for which the nodes are at the ends of each elements are called *linear elements* (see Figure 2.2). The discretization of the boundary with the constant and linear elements for Equation (2.16) will be performed here in details.

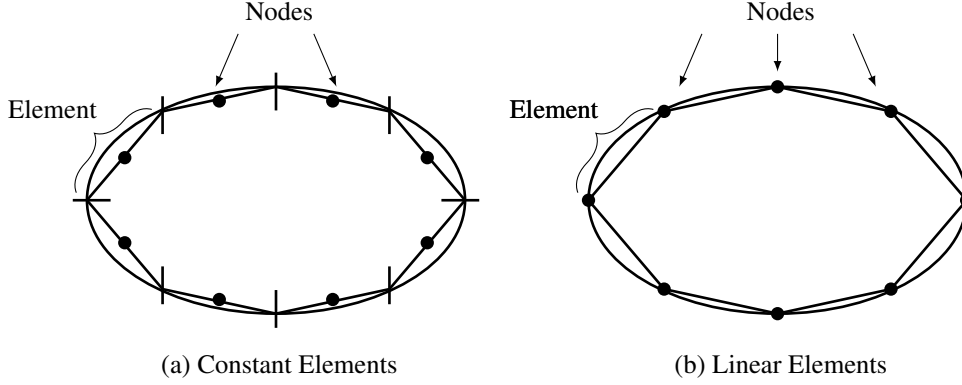


Figure 2.2: Meshing with constant and linear elements

2.1.2.1 Discretization with constant elements

We first consider the discretization of the boundary with constant elements. Equation (2.16) can be discretized for a given point (x_i, y_i) before applying any boundary conditions as

$$c_i u_i + \sum_{j=1}^N \int_{\Gamma_j} u q^* d\Gamma = \sum_{j=1}^N \int_{\Gamma_j} q u^* d\Gamma \quad (2.17)$$

where N is the number of boundary elements. In constant element case, the values of u and q are assumed to be constant over each element and equal to the value at the middle-node of the elements. The end points of the elements are used only to define the geometry of the problem. Moreover, for the constant elements the boundary is always smooth at the nodes since these are located at the center of elements. Since u and q are constants on each elements, they can be taken out of the integrals. Thus, Equation (2.17) becomes

$$\frac{1}{2} u_i + \sum_{j=1}^N u_j \int_{\Gamma_j} q^* d\Gamma = \sum_{j=1}^N q_j \int_{\Gamma_j} u^* d\Gamma \quad (2.18)$$

in which u and q are denoted by u_j and q_j for each element j . The integrals $\bar{H}_{ij} = \int_{\Gamma_j} q^* d\Gamma$ and $G_{ij} = \int_{\Gamma_j} u^* d\Gamma$ relate the node i where the fundamental solution is applied to any other node j . Hence for a particular point i , Equation (2.18) can be written as

$$\sum_{j=1}^N H_{ij} u_j = \sum_{j=1}^N G_{ij} q_j \quad (2.19)$$

where $H_{ij} = \bar{H}_{ij} + \frac{1}{2}\delta_{ij}$ for $i = 1, \dots, N$. Thus, a system of equations is obtained which can be expressed in matrix form as

$$\mathbf{H}\mathbf{u} = \mathbf{G}\mathbf{q} \quad (2.20)$$

where \mathbf{H} and \mathbf{G} are the BEM matrices of size $N \times N$, and \mathbf{u} and \mathbf{q} are vectors of length N .

The elements of \mathbf{H} and \mathbf{G} for the two-dimensional Laplace equation are

$$H_{ij} = \frac{1}{2}\delta_{ij} + \frac{1}{2\pi} \int_{\Gamma_j} \frac{(\mathbf{r} - \mathbf{r}_i) \cdot \mathbf{n}}{|\mathbf{r} - \mathbf{r}_i|^2} d\Gamma_j, \quad G_{ij} = \frac{1}{2\pi} \int_{\Gamma_j} \ln \frac{1}{|\mathbf{r} - \mathbf{r}_i|} d\Gamma_j, \quad (2.21)$$

$i, j = 1, \dots, N$

which are calculated by some numerical integration techniques i.e Gaussian quadrature, when $i \neq j$. When $i = j$, a more accurate integration scheme is required due to the singularity of the fundamental solution. For the constant element case, the coefficients \bar{H}_{ii} are zero since the normal \mathbf{n} and the distance vector $(\mathbf{r} - \mathbf{r}_i)$ from the source point are always perpendicular to each other, and the entries G_{ii} are calculated analytically by

$$G_{ii} = \frac{l}{2\pi} \left\{ \ln\left(\frac{2}{l}\right) + 1 \right\} \quad (2.22)$$

where l is the length of the element, [61].

Finally, to introduce the boundary conditions into the system (2.20), the system is rearranged by moving the columns of \mathbf{H} and \mathbf{G} from one side to other so that all unknowns are passed to the left-hand side. Hence, we have a system of linear equations

$$\mathbf{A}\mathbf{x} = \mathbf{y} \quad (2.23)$$

where \mathbf{A} is invertible matrix, \mathbf{x} is the vector containing the unknown boundary values of u and q , and \mathbf{y} is obtained by multiplying the corresponding columns of \mathbf{H} and \mathbf{G}

by the known values of u or q . Once the system (2.23) is solved, the values of u and q will be obtained on the whole boundary, and the value of u at any internal point i is calculated using Equation (2.17) by taking $c_i = 1$, that is

$$u_i = \sum_{j=1}^N q_j \int_{\Gamma_j} u^* d\Gamma - \sum_{j=1}^N u_j \int_{\Gamma_j} q^* d\Gamma = \sum_{j=1}^N G_{ij} q_j - \sum_{j=1}^N H_{ij} u_j \quad (2.24)$$

where the coefficients G_{ij} and H_{ij} are calculated with formulas given in Equation (2.21) for each internal point i .

2.1.2.2 Discretization with linear elements

In this case, the linear variation of u and q will be considered for which the nodes are taken to be the end points of the elements. When the boundary is discretized into N linear elements, Equation (2.16) can be written as in the case of constant elements:

$$c_i u_i + \sum_{j=1}^N \int_{\Gamma_j} u q^* d\Gamma = \sum_{j=1}^N \int_{\Gamma_j} q u^* d\Gamma \quad (2.25)$$

where u and q are not constant anymore but vary linearly over each element Γ_j , and hence they can not be taken out the integrals.

The values of u and q at any point on the element can be defined in terms of their nodal values and two linear interpolation functions ϕ_1 and ϕ_2 as follows:

$$\begin{aligned} u(\xi) &= \phi_1 u_1 + \phi_2 u_2 = \begin{bmatrix} \phi_1 & \phi_2 \end{bmatrix} \begin{bmatrix} u_1 \\ u_2 \end{bmatrix} \\ q(\xi) &= \phi_1 q_1 + \phi_2 q_2 = \begin{bmatrix} \phi_1 & \phi_2 \end{bmatrix} \begin{bmatrix} q_1 \\ q_2 \end{bmatrix} \end{aligned} \quad (2.26)$$

where ϕ_1 and ϕ_2 are given in terms of the dimensionless coordinates $\xi \in [-1, 1]$:

$$\phi_1 = \frac{1}{2}(1 - \xi), \quad \phi_2 = \frac{1}{2}(1 + \xi). \quad (2.27)$$

Then the integral on the left and right-hand sides of Equation (2.25) can be written respectively as

$$\int_{\Gamma_j} u q^* d\Gamma = \int_{\Gamma_j} \begin{bmatrix} \phi_1 & \phi_2 \end{bmatrix} q^* d\Gamma \begin{bmatrix} u_1 \\ u_2 \end{bmatrix} = \begin{bmatrix} h_{ij}^1 & h_{ij}^2 \end{bmatrix} \begin{bmatrix} u_1 \\ u_2 \end{bmatrix} \quad (2.28)$$

and

$$\int_{\Gamma_j} q u^* d\Gamma = \int_{\Gamma_j} \begin{bmatrix} \phi_1 & \phi_2 \end{bmatrix} u^* d\Gamma \begin{bmatrix} q_1 \\ q_2 \end{bmatrix} = \begin{bmatrix} g_{ij}^1 & g_{ij}^2 \end{bmatrix} \begin{bmatrix} q_1 \\ q_2 \end{bmatrix} \quad (2.29)$$

where

$$h_{ij}^1 = \int_{\Gamma_j} \phi_1 q^* d\Gamma, \quad h_{ij}^2 = \int_{\Gamma_j} \phi_2 q^* d\Gamma, \quad g_{ij}^1 = \int_{\Gamma_j} \phi_1 u^* d\Gamma, \quad g_{ij}^2 = \int_{\Gamma_j} \phi_2 u^* d\Gamma. \quad (2.30)$$

Substitution of Equations (2.28) and (2.29) into Equation (2.25) for each element j results in

$$c_i u_i + \begin{bmatrix} \bar{H}_{i1} & \bar{H}_{i2} & \dots & \bar{H}_{iN} \end{bmatrix} \begin{bmatrix} u_1 \\ u_2 \\ \vdots \\ u_N \end{bmatrix} = \begin{bmatrix} G_{i1} & G_{i2} & \dots & G_{iN} \end{bmatrix} \begin{bmatrix} q_1 \\ q_2 \\ \vdots \\ q_N \end{bmatrix} \quad (2.31)$$

for node i , where \bar{H}_{ij} is the summation of the h_{ij}^1 term of element j and $h_{i,j-1}^2$ term of element $j - 1$. The entries of G_{ij} are similarly obtained by adding the g_{ij}^1 term of the element j and $g_{i,j-1}^2$ term of element $j - 1$. Then, Equation (2.31) which is the assembled equation for node i can be written as

$$c_i u_i + \sum_{j=1}^N \bar{H}_{ij} u_j = \sum_{j=1}^N G_{ij} q_j, \quad (2.32)$$

where j is the node in between two elements. Then, the matrix form becomes

$$\mathbf{H}\mathbf{u} = \mathbf{G}\mathbf{q} \quad (2.33)$$

as in the case of constant elements. Once the system is solved after the insertion of the boundary conditions, the unknown values of u and q are obtained on the boundary. Then, the value of u at any internal point i can be calculated by taking $c_i = 1$ in Equation (2.32) with a new calculated entires of \bar{H}_{ij} and G_{ij} for each internal point i similar to the case of constant elements.

2.2 Integral Formulation of The Poisson's Equation

In this section, the integral formulation will be derived for the Poisson's equation

$$\nabla^2 u = b \quad \text{in } \Omega \quad (2.34)$$

where b is a known function. The basic integral equation can be derived by weighting Equation (2.34) by an appropriate weight function and integrating over the domain Ω , similar to the case of Laplace Equation given in Section 2.1.1. That is,

$$\int_{\Omega} (\nabla^2 u - b) u^* d\Omega = \int_{\Gamma_2} (q - \bar{q}) u^* d\Gamma - \int_{\Gamma_1} (u - \bar{u}) q^* d\Gamma. \quad (2.35)$$

The application of integration by parts twice results in

$$\int_{\Omega} (\nabla^2 u^*) u d\Omega - \int_{\Omega} b u^* d\Omega = - \int_{\Gamma_2} \bar{q} u^* d\Gamma - \int_{\Gamma_1} q u^* d\Gamma + \int_{\Gamma_2} u q^* d\Gamma + \int_{\Gamma_1} \bar{u} q^* d\Gamma. \quad (2.36)$$

When the weight function u^* is taken as the fundamental solution of Laplace equation and grouping all boundary terms as in Equation (2.15), one can obtain

$$c_i u_i + \int_{\Gamma} u q^* d\Gamma - \int_{\Gamma} q u^* d\Gamma = - \int_{\Omega} b u^* d\Omega \quad (2.37)$$

which contains not only boundary but also a domain integral. The domain integral can be calculated by subdividing the region into a series of internal cells on each of which a numerical integration scheme is applied. However, this causes the BEM lose its most important property of boundary-only nature. That is, it requires integration over the domain rather than only on the boundary. Therefore, some other approaches have been introduced to simplify the evaluation of these integrals. One of the most efficient technique, which is subject to this thesis, is the DRBEM that transforms the domain integrals to the boundary integrals by using particular solutions through radial basis function approximation.

2.3 Dual Reciprocity Boundary Element Method

The boundary element method always requires a fundamental solution to the original partial differential equations to avoid domain integrals in the resulting integral equation, which is one of the drawbacks of the method. Another is that the non-homogeneous and non-linear terms are inserted in the formulation by means of domain integrals. These domain integrals can be evaluated using internal discretization, which increases the cost of the solution in terms of time and allocated memory. Therefore, the boundary element method loses the attraction of its boundary-only character compared to other numerical techniques which require domain discretization.

In order to deal with this problem, as previously mentioned many different methodologies have been developed. One of the well-developed techniques is the dual reciprocity boundary element method. The main idea of DRBEM is to employ a fundamental solution corresponding to a simpler equation involving some of the dominant terms in the governing equation, and to treat the remaining terms involving the non-homogeneous and non-linear terms in the original equation via a procedure in which some special approximation functions are used through the application of reciprocity principles.

This section provides a detailed explanation of the DRBEM application for Poisson equation which contains the non-homogeneous terms as a known function of space, i.e. $b = b(x, y)$ (see Section 2.3.1). Moreover, this technique is extended to the time-dependent problems in which the right hand side function b is an unknown function which is a linear combination of the problem variable u and its derivatives with respect to space and time, i.e. $b = b(x, y, u, u_x, u_y, u_t)$ (see Section 2.3.3).

2.3.1 DRBEM for Poisson's equation

In this section, the dual reciprocity boundary element method is given for the Poisson equation

$$\nabla^2 u = b \quad (2.38)$$

where b is considered to be a known function of position, i.e. $b = b(x, y)$. The solution to Equation (2.38) can be expressed as

$$u = u_h + \hat{u} \quad (2.39)$$

where u_h is the solution of a homogeneous Laplace equation and \hat{u} is a particular solution of the Poisson's equation such that

$$\nabla^2 \hat{u} = b. \quad (2.40)$$

In general to find a solution \hat{u} which satisfies Equation (2.40) is difficult, mainly in the case of non-linear and time-dependent problems. The DRBEM proposes the use of a series of particular solutions \hat{u}_j instead of a single function \hat{u} . The number of \hat{u}_j is equal to the total number of nodes used in the problem. Then, the function b is

approximated as

$$b \approx \sum_{j=1}^{N+L} \alpha_j f_j \quad (2.41)$$

where N and L represent the boundary and internal nodes, respectively. The constants α_j are a set of unknown coefficients and f_j are approximating functions which are linked to the particular solutions \hat{u}_j through the relation

$$\nabla^2 \hat{u}_j = f_j. \quad (2.42)$$

The functions f_j are only geometry-dependent and there is no restriction on these functions. In fact, many different types of f_j may be used, each of which results in a different function \hat{u}_j as determined from Equation (2.42).

Substituting Equation (2.42) into Equation (2.41) gives

$$b \approx \sum_{j=1}^{N+L} \alpha_j (\nabla^2 \hat{u}_j) \quad (2.43)$$

and substitution of Equation (2.43) into the original Equation (2.38) results in

$$\nabla^2 u = \sum_{j=1}^{N+L} \alpha_j (\nabla^2 \hat{u}_j). \quad (2.44)$$

The process explained in Section 2.1.1 to develop the BEM for the Laplace equation can now be applied, [61]. That is, Equation (2.44) is multiplied with the fundamental solution u^* of the Laplace equation and is integrated over the domain Ω , which results in

$$\int_{\Omega} (\nabla^2 u) u^* d\Omega = \sum_{j=1}^{N+L} \alpha_j \int_{\Omega} (\nabla^2 \hat{u}_j) u^* d\Omega. \quad (2.45)$$

Integrating by parts twice, the Laplacian terms in Equation (2.45) as in Section 2.1.1, produces the following integral equation for each source node i :

$$c_i u_i + \int_{\Gamma} q^* u d\Gamma - \int_{\Gamma} u^* q d\Gamma = \sum_{j=1}^{N+L} \alpha_j \left(c_i \hat{u}_{ij} + \int_{\Gamma} q^* \hat{u}_j d\Gamma - \int_{\Gamma} u^* \hat{q}_j d\Gamma \right) \quad (2.46)$$

where

$$\hat{q}_j = \frac{\partial \hat{u}_j}{\partial n} = \frac{\partial \hat{u}_j}{\partial x} \frac{\partial x}{\partial n} + \frac{\partial \hat{u}_j}{\partial y} \frac{\partial y}{\partial n}. \quad (2.47)$$

Equation (2.46) involves no domain integrals, that is, the domain integral of the source term b in Equation (2.37) has now been substituted with the boundary integrals by

means of approximating functions. The discretized form of Equation (2.46) for a source node i becomes

$$c_i u_i + \sum_{k=1}^N \int_{\Gamma_k} q^* u d\Gamma - \sum_{k=1}^N \int_{\Gamma_k} u^* q d\Gamma = \sum_{j=1}^{N+L} \alpha_j (c_i \hat{u}_{ij} + \sum_{k=1}^N \int_{\Gamma_k} q^* \hat{u}_j d\Gamma - \sum_{k=1}^N \int_{\Gamma_k} u^* \hat{q}_j d\Gamma) \quad (2.48)$$

when the boundary Γ is discretized by using N boundary elements. The functions \hat{u}_j and \hat{q}_j are known once f_j are defined. After introducing the interpolation functions and integrating over each element, we have

$$c_i u_i + \sum_{k=1}^N H_{ik} u_k - \sum_{k=1}^N G_{ik} q_k = \sum_{j=1}^{N+L} \alpha_j (c_i \hat{u}_{ij} + \sum_{k=1}^N H_{ik} \hat{u}_k - \sum_{k=1}^N H G_{ik} \hat{q}_k) \quad (2.49)$$

where index k is used for the boundary nodes. After the application to all boundary nodes using a collocation technique, Equation (2.49) can be expressed in matrix form as

$$\mathbf{H}\mathbf{u} - \mathbf{G}\mathbf{q} = \sum_{j=1}^{N+L} \alpha_j (\mathbf{H}\hat{\mathbf{u}}_j - \mathbf{G}\hat{\mathbf{q}}_j) \quad (2.50)$$

in which the matrices \mathbf{H} and \mathbf{G} are the same with the ones given in Section 2.1.2.1 when constant elements are used or in Section 2.1.2.2 when linear elements are used. If each of the vectors $\hat{\mathbf{u}}_j$ and $\hat{\mathbf{q}}_j$ are considered to be one column of the matrices $\hat{\mathbf{U}}$ and $\hat{\mathbf{Q}}$ of size $N \times (N + L)$, respectively, then Equation (2.50) can be written as

$$\mathbf{H}\mathbf{u} - \mathbf{G}\mathbf{q} = (\mathbf{H}\hat{\mathbf{U}} - \mathbf{G}\hat{\mathbf{Q}})\boldsymbol{\alpha} \quad (2.51)$$

where $\boldsymbol{\alpha}$ is the vector of size $(N + L)$ containing the unknown coefficients α_j . Equation (2.51) is the basis of the application of DRBEM which requires discretization of the boundary only. The definition of interior nodes is not necessary to obtain a boundary solution, however, the solution will be more accurate if a number of such nodes is used. One can calculate the values of u at the internal nodes by redefining the entries H_{ik} and G_{ik} in Equation (2.49) in such a way given in Section 2.1.2 that they contain the point i as an interior node. That is, Equation (2.51) can be written for the solution of the boundary nodes as

$$\mathbf{H}^{\text{bs}}\mathbf{u}^{\text{bs}} - \mathbf{G}^{\text{bs}}\mathbf{q}^{\text{bs}} = (\mathbf{H}^{\text{bs}}\hat{\mathbf{U}}^{\text{bs}} - \mathbf{G}^{\text{bs}}\hat{\mathbf{Q}}^{\text{bs}})\boldsymbol{\alpha} \quad (2.52)$$

and for the solution of the internal nodes as

$$\mathbf{H}^{is}\mathbf{u}^{is} - \mathbf{G}^{is}\mathbf{q}^{is} = (\mathbf{I}\hat{\mathbf{U}}^{is} + \mathbf{H}^{is}\hat{\mathbf{U}}^{is} - \mathbf{G}^{is}\hat{\mathbf{Q}}^{is})\boldsymbol{\alpha} \quad (2.53)$$

where bs and is refer to boundary and internal solutions, respectively, and \mathbf{I} is the identity matrix of size $L \times L$. When Equations (2.51) and (2.53) are combined, one can write them in an enlarged matrix form:

$$\begin{bmatrix} \mathbf{H}_{bs} & \mathbf{0} \\ \mathbf{H}_{is} & \mathbf{0} \end{bmatrix} \begin{bmatrix} \mathbf{u}_{bs} \\ \mathbf{u}_{is} \end{bmatrix} - \begin{bmatrix} \mathbf{G}_{bs} & \mathbf{0} \\ \mathbf{G}_{is} & \mathbf{0} \end{bmatrix} \begin{bmatrix} \mathbf{q}_{bs} \\ \mathbf{0} \end{bmatrix} = \left(\begin{bmatrix} \mathbf{H}_{bs} & \mathbf{0} \\ \mathbf{H}_{is} & \mathbf{I} \end{bmatrix} \begin{bmatrix} \hat{\mathbf{U}}_{bs} \\ \hat{\mathbf{U}}_{is} \end{bmatrix} - \begin{bmatrix} \mathbf{G}_{bs} & \mathbf{0} \\ \mathbf{G}_{is} & \mathbf{0} \end{bmatrix} \begin{bmatrix} \hat{\mathbf{Q}}_{bs} \\ \mathbf{0} \end{bmatrix} \right) \boldsymbol{\alpha} \quad (2.54)$$

where $\mathbf{0}$ denotes zero matrix and this system can be represented in a compact form:

$$\mathbf{H}\mathbf{u} - \mathbf{G}\mathbf{q} = (\mathbf{H}\hat{\mathbf{U}} - \mathbf{G}\hat{\mathbf{Q}})\boldsymbol{\alpha}. \quad (2.55)$$

Here, all matrices are of size $(N + L) \times (N + L)$. Thus, one need to use $(N + L)$ nodes in DRBEM in order to obtain the solution at both boundary and interior nodes at one stroke. By taking the value of b at $(N + L)$ points, a set of equations like (2.41) is obtained which can be written in matrix form as

$$\mathbf{b} = \mathbf{F}\boldsymbol{\alpha} \quad (2.56)$$

where \mathbf{F} is called the coordinate matrix and each column of \mathbf{F} consists of a vector \mathbf{f}_j containing values of f_j at $(N + L)$ nodes. Thus, $\boldsymbol{\alpha}$ is obtained as

$$\boldsymbol{\alpha} = \mathbf{F}^{-1}\mathbf{b} \quad (2.57)$$

and when it is substituted in Equation (2.55), one get the system

$$\mathbf{H}\mathbf{u} - \mathbf{G}\mathbf{q} = (\mathbf{H}\hat{\mathbf{U}} - \mathbf{G}\hat{\mathbf{Q}})\mathbf{F}^{-1}\mathbf{b}. \quad (2.58)$$

Applying boundary conditions to Equation (2.58) as given in Section 2.1.2.1, we get

$$\mathbf{A}\mathbf{x} = \mathbf{y} \quad (2.59)$$

where \mathbf{x} contains the N unknown boundary values of u or q and L unknown interior values of u .

2.3.2 Approximating functions f_j

The particular solution \hat{u} , its normal derivative \hat{q} and the corresponding approximating function f used in DRBEM application are not limited except that the resulting coordinate matrix \mathbf{F} should be non-singular. These functions are commonly defined by proposing an expansion for f , and then computing \hat{u} and \hat{q} using Equations (2.42) and (2.47). Thus, one can use different types of approximating functions, namely polynomials ($f = 1 + r + r^2 + \dots + r^m$), thin-plate splines ($f = r^2 \ln r$), multi-quadratics ($f = \sqrt{r^2 + c^2}$ with shape parameter c), inverse multi-quadratics ($f = 1/\sqrt{r^2 + c^2}$). In this thesis, basically polynomial type radial basis functions are employed in the application of DRBEM. Thus, if the approximating functions f_j are distance or radial basis functions of the form

$$f = 1 + r + r^2 + \dots + r^m \quad (2.60)$$

where $r^2 = r_x^2 + r_y^2$ in the two-dimensional case. Writing Equation (2.42) in polar coordinates we have

$$\nabla^2 \hat{u} = \frac{1}{r} \frac{\partial}{\partial r} \left(r \frac{\partial \hat{u}}{\partial r} \right) = 1 + r + r^2 + \dots + r^m = f \quad (2.61)$$

and the corresponding particular solution \hat{u} is obtained as

$$\hat{u} = \frac{r^2}{4} + \frac{r^3}{9} + \dots + \frac{r^{m+2}}{(m+2)^2}. \quad (2.62)$$

Further, the substitution of \hat{u} in Equation (2.47), gives the normal derivative \hat{q} as

$$\hat{q} = \left(r_x \frac{\partial x}{\partial n} + r_y \frac{\partial y}{\partial n} \right) \left(\frac{1}{2} + \frac{r}{3} + \dots + \frac{r^m}{m+2} \right). \quad (2.63)$$

2.3.3 DRBEM for the time-dependent Poisson's type equations

In this section, the application of the DRBEM explained in previous section is extended to the problems governed by the equation

$$\nabla^2 u = b(x, y, t, u, u_x, u_y, u_t) \quad (2.64)$$

where the non-homogeneous term b consists of a linear combination of the unknown u itself, the convection terms u_x and u_y , and the time derivative term u_t . Then, the function b can be written as

$$b = u_t + b_1(x, y) + b_2(x, y)u + b_3(x, y)u_x + b_4(x, y)u_y \quad (2.65)$$

which can be approximated by radial basis functions f_j as

$$b = u_t + b_1 + b_2 u + b_3 u_x + b_4 u_y \approx \sum_{j=1}^{N+L} \alpha_j(t) f_j(x, y) \quad (2.66)$$

where α_j are unknown functions of time. The approximating functions f_j are linked with the particular solutions \hat{u}_j through Equation (2.42). Similar to Section 2.3.1, the DRBEM application results in the same enlarged matrix form given in Equation (2.55)

$$\mathbf{H}\mathbf{u} - \mathbf{G}\mathbf{q} = (\mathbf{H}\hat{\mathbf{U}} - \mathbf{G}\hat{\mathbf{Q}})\boldsymbol{\alpha}. \quad (2.67)$$

The vector $\boldsymbol{\alpha}$ is obtained from Equations (2.57) and (2.66) as

$$\boldsymbol{\alpha} = \mathbf{F}^{-1}(\mathbf{u}_t + \mathbf{b}_1 + \mathbf{B}_2\mathbf{u} + \mathbf{B}_3\mathbf{u}_x + \mathbf{B}_4\mathbf{u}_y) \quad (2.68)$$

where \mathbf{F} is the coordinate matrix given in Equation (2.56), \mathbf{b}_1 is the vector with components $b_1(x_i, y_i)$ at nodes $i = 1, \dots, (N+L)$. The $(N+L) \times (N+L)$ matrices \mathbf{B}_2 , \mathbf{B}_3 and \mathbf{B}_4 represent the diagonal matrices with $b_2(x_i, y_i)$, $b_3(x_i, y_i)$, $b_4(x_i, y_i)$ ($i = 1, \dots, N+L$) on the diagonal entries, respectively. Moreover, the matrices \mathbf{H} , \mathbf{G} , $\hat{\mathbf{U}}$ and $\hat{\mathbf{Q}}$ are of size $(N+L) \times (N+L)$. When the solution u is also approximated by using the same coordinate functions f_j

$$u \approx \sum_{j=1}^{N+L} \beta_j(t) f_j(x, y) \quad (2.69)$$

where $\beta_j \neq \alpha_j$ are the unknown coefficients of time. Equation (2.69) can also be written in matrix form as

$$\mathbf{u} = \mathbf{F}\boldsymbol{\beta}. \quad (2.70)$$

The space derivatives of \mathbf{u} with respect to x and y are

$$\frac{\partial \mathbf{u}}{\partial x} = \frac{\partial \mathbf{F}}{\partial x} \boldsymbol{\beta} \quad \text{and} \quad \frac{\partial \mathbf{u}}{\partial y} = \frac{\partial \mathbf{F}}{\partial y} \boldsymbol{\beta} \quad (2.71)$$

and by rewriting Equation (2.70) as $\boldsymbol{\beta} = \mathbf{F}^{-1}\mathbf{u}$, then Equation (2.71) becomes

$$\mathbf{u}_x = \frac{\partial \mathbf{u}}{\partial x} = \frac{\partial \mathbf{F}}{\partial x} \mathbf{F}^{-1} \mathbf{u} \quad \text{and} \quad \mathbf{u}_y = \frac{\partial \mathbf{u}}{\partial y} = \frac{\partial \mathbf{F}}{\partial y} \mathbf{F}^{-1} \mathbf{u}. \quad (2.72)$$

Thus, by substituting the approximations for the convective terms in Equation (2.68) and inserting the resulting vector $\boldsymbol{\alpha}$ in Equation (2.67), we have

$$\mathbf{H}\mathbf{u} - \mathbf{G}\mathbf{q} = (\mathbf{H}\hat{\mathbf{U}} - \mathbf{G}\hat{\mathbf{Q}})\mathbf{F}^{-1}(\mathbf{u}_t + \mathbf{b}_1 + \mathbf{B}_2\mathbf{u} + \mathbf{B}_3 \frac{\partial \mathbf{F}}{\partial \mathbf{x}} \mathbf{F}^{-1} \mathbf{u} + \mathbf{B}_4 \frac{\partial \mathbf{F}}{\partial \mathbf{y}} \mathbf{F}^{-1} \mathbf{u}). \quad (2.73)$$

Finally, rearranging Equation (2.73), the following first order system of ordinary differential equations in time is obtained as

$$\mathbf{C}\dot{\mathbf{u}} + (\mathbf{H} + \mathbf{R})\mathbf{u} = \mathbf{G}\mathbf{q} - \mathbf{C}\mathbf{b}_1 \quad (2.74)$$

where superscript dot denotes the time derivative. The matrices \mathbf{C} and \mathbf{R} of size $(N + L) \times (N + L)$ are

$$\mathbf{C} = -(\mathbf{H}\hat{\mathbf{U}} - \mathbf{G}\hat{\mathbf{Q}})\mathbf{F}^{-1}, \quad \mathbf{R} = \mathbf{C}(\mathbf{B}_2 + \mathbf{B}_3 \frac{\partial \mathbf{F}}{\partial \mathbf{x}} \mathbf{F}^{-1} + \mathbf{B}_4 \frac{\partial \mathbf{F}}{\partial \mathbf{y}} \mathbf{F}^{-1}). \quad (2.75)$$

The system (2.74) can be solved by using any time integration scheme. However, in this thesis, a two-level time integration scheme combined with a forward difference formula for the time derivative is employed for discretizing Equation (2.74) with respect to time.

2.3.3.1 Time integration scheme

In this section, a two-level time integration scheme [61] is applied to the resulting DRBEM system (2.74). The first order time derivative in Equation (2.74) is approximated by

$$\dot{\mathbf{u}} = \frac{1}{\Delta t}(\mathbf{u}^{m+1} - \mathbf{u}^m) \quad (2.76)$$

where m denotes the time level and Δt is the time step size. Further, a linear approximation for the variation of \mathbf{u} and \mathbf{q} within each time level can be suggested in the following form

$$\mathbf{u} = (1 - \beta_u)\mathbf{u}^m + \beta_u\mathbf{u}^{m+1} \quad (2.77)$$

$$\mathbf{q} = (1 - \beta_q)\mathbf{q}^m + \beta_q\mathbf{q}^{m+1} \quad (2.78)$$

where β_u and β_q are parameters which position the values of \mathbf{u} and \mathbf{q} , respectively, between the time levels m and $m+1$. Substituting these approximations and Equation (2.76) into Equation (2.74) yields:

$$\begin{aligned} \left[\frac{1}{\Delta t} \mathbf{C} + \beta_u (\mathbf{H} + \mathbf{R}) \right] \mathbf{u}^{m+1} - \beta_q \mathbf{G} \mathbf{q}^{m+1} &= \left[\frac{1}{\Delta t} \mathbf{C} - (1 - \beta_u) (\mathbf{H} + \mathbf{R}) \right] \mathbf{u}^m \\ &\quad + (1 - \beta_q) \mathbf{G} \mathbf{q}^m - \mathbf{C} \mathbf{b}_1 \end{aligned} \quad (2.79)$$

in which the right hand side is known since it consists of the values specified as initial conditions or calculated previously. After employing the boundary conditions at the $(m + 1)$ -st time level, the left hand side of Equation (2.79) can be rearranged and the solution can be obtained for each time level. It is also noted that the matrices \mathbf{H} , \mathbf{G} , \mathbf{C} and \mathbf{R} can be computed once and stored because their components depend only on the geometrical data, which will reduce the computational effort.

2.4 Numerical Stability Analysis

The numerical stability analysis of the present combined technique of dual reciprocity BEM with a two-level time integration scheme is explained in the present section. First, we are going to consider the stability analysis of a single step method for the numerical solution of an initial value problem. Later, we will extend this analysis to the DRBEM solution of Poisson's type equations where the non-homogeneous term b consists of a linear combination of the unknown u itself, the convection terms u_x and u_y , and the time derivative u_t (see Section 2.3.3).

2.4.1 Stability Analysis of single step method

In this section, the stability of a single step method for the system of first order differential equations will be discussed. The system of m equations in the vector form may be written as

$$\begin{aligned} \mathbf{y}' &= \frac{d\mathbf{y}}{dt} = \mathbf{f}(t, \mathbf{y}), \quad t_0 \leq t \leq b \\ \mathbf{y}(t_0) &= \mathbf{y}_0, \end{aligned} \tag{2.80}$$

where

$$\mathbf{y} = \begin{bmatrix} y_1 \\ y_2 \\ \vdots \\ y_m \end{bmatrix}, \quad \mathbf{f}(t, \mathbf{y}) = \begin{bmatrix} f_1(t, y_1, y_2, \dots, y_m) \\ f_2(t, y_1, y_2, \dots, y_m) \\ \vdots \\ f_m(t, y_1, y_2, \dots, y_m) \end{bmatrix} \quad \text{and} \quad \mathbf{y}_0 = \begin{bmatrix} y_{1,0} \\ y_{2,0} \\ \vdots \\ y_{m,0} \end{bmatrix}.$$

Further, the single step method developed for the system of first order equations can be written as

$$\mathbf{y}_{i+1} = \mathbf{y}_i + h\Phi(t_i, \mathbf{y}_i, h) \tag{2.81}$$

where

$$\Phi(t_i, \mathbf{y}_i, h) = \begin{bmatrix} \phi_1(t_i, y_{1,i}, y_{2,i}, \dots, y_{m,i}, h) \\ \phi_2(t_i, y_{1,i}, y_{2,i}, \dots, y_{m,i}, h) \\ \vdots \\ \phi_m(t_i, y_{1,i}, y_{2,i}, \dots, y_{m,i}, h) \end{bmatrix}. \quad (2.82)$$

Φ is the increment function for the single step method. When the functions f_i have continuous partial derivatives $\partial f_i / \partial y_j = a_{ij}$, $1 \leq i, j \leq m$, the first order system of equations (2.80) can be written as

$$\frac{d\mathbf{y}}{dt} = \mathbf{A}\mathbf{y} \quad (2.83)$$

where \mathbf{A} denotes the $m \times m$ Jacobian matrix $[a_{ij}]$. Equation (2.83) is the homogeneous locally linearized form of Equation (2.80) and the stability characteristics of Equations (2.80) and (2.81) are similar.

Here, we observe that the matrix \mathbf{A} depends on the variables \mathbf{y} and t , but considering a simple case of \mathbf{A} the general behavior of the solution of Equation (2.83) can be estimated. Let \mathbf{A} is a constant matrix with distinct eigenvalues, then the analytic solution $\mathbf{y}(t)$ to Equation (2.83) is given by [36]

$$\mathbf{y}(t) = e^{\mathbf{A}t} \mathbf{y}_0 \quad (2.84)$$

where \mathbf{y}_0 is the initial condition and the exponential matrix $e^{\mathbf{A}t}$ is defined as a matrix function

$$e^{\mathbf{A}t} = \mathbf{I} + \mathbf{A}t + \frac{(\mathbf{A}t)^2}{2!} + \frac{(\mathbf{A}t)^3}{3!} \dots \quad (2.85)$$

with the identity matrix \mathbf{I} .

Moreover, for a diagonalizable matrix \mathbf{A} , there exists an invertible matrix \mathbf{P} satisfying $\mathbf{P}^{-1}\mathbf{A}\mathbf{P} = \mathbf{D}$ where \mathbf{D} is a diagonal matrix with the eigenvalues of \mathbf{A} , λ_i , $i = 1, \dots, m$ on the diagonals, i.e. $\mathbf{D} = \text{diag}(\lambda_1, \dots, \lambda_m)$. Further, \mathbf{P} also diagonalizes $e^{\mathbf{A}t}$ with the following relation [36]

$$\mathbf{P}^{-1}e^{\mathbf{A}t}\mathbf{P} = e^{\mathbf{D}t} \quad (2.86)$$

in which $e^{\mathbf{D}t}$ represents the diagonal matrix with $e^{\lambda_1 t}, e^{\lambda_2 t}, \dots, e^{\lambda_m t}$ on the diagonals.

If λ_j are distinct or possibly complex eigenvalues of \mathbf{A} with negative real parts then Equation (2.83) can be written as

$$\frac{d\mathbf{v}}{dt} = \mathbf{D}\mathbf{v}, \quad \mathbf{v}_0 = \mathbf{P}^{-1}\mathbf{y}_0 \quad (2.87)$$

by defining $\mathbf{v} = \mathbf{P}^{-1}\mathbf{y}$. Hence, the analytic solution to Equation (2.84), obtained by using Equation (2.86), can be written as

$$\mathbf{v}(t) = e^{\mathbf{D}t}\mathbf{v}_0. \quad (2.88)$$

The numerical values of the vector function $\mathbf{v}(t)$ can be obtained for each t_i by using the recurrence relation

$$\mathbf{y}(t_{i+1}) = e^{\mathbf{A}h}\mathbf{y}(t_i) \quad (2.89)$$

in the system (2.84), but its applicability depends on the computation of $e^{\mathbf{A}h}$ or $\mathbf{P}e^{\mathbf{D}h}\mathbf{P}^{-1}$.

The application of the single step method (2.81) to the system (2.87) gives the relation

$$\mathbf{v}_{i+1} = \mathbf{E}(\mathbf{D}h)\mathbf{v}_i, \quad (2.90)$$

where $\mathbf{E}(\mathbf{D}h)$ is an approximation to $e^{\mathbf{D}h}$. The matrix $\mathbf{E}(\mathbf{D}h)$ is diagonal and each of its diagonal entries ($E_j(\lambda_j h)$, $j = 1, 2, \dots, m$) is an approximation to the diagonal entries ($e^{\lambda_j h}$, $j = 1, 2, \dots, m$) of the matrix $e^{\mathbf{D}h}$. This means that the stability analysis of the single step method applied to the system (2.83) is equivalent to the application of single step method to the scalar equation

$$y' = \lambda_j y \quad (2.91)$$

where λ_j 's are the eigenvalues of the matrix \mathbf{A} . Hence, the single step method is absolutely stable if

$$|E_j(\lambda_j h) - 1| < 1, \quad j = 1, 2, \dots, m, \quad (2.92)$$

where the real parts of eigenvalues λ_j are negative.

In the next section, we are going to consider the stability analysis of the dual reciprocity BEM applied to non-linear systems. We must solve the non-linear system at each step by using the iterative process, this means that the stability requirement depends on not only the choice of step size but also the relaxation parameters and the other problem parameters.

2.4.2 Stability analysis of DRBEM

In this section, the stability analysis will be performed for the resulting time-dependent DRBEM system (2.79)

$$\left[\frac{1}{\Delta t} \mathbf{C} + \beta_u (\mathbf{H} + \mathbf{R}) \right] \mathbf{u}^{m+1} - \beta_q \mathbf{G} \mathbf{q}^{m+1} = \left[\frac{1}{\Delta t} \mathbf{C} - (1 - \beta_u) (\mathbf{H} + \mathbf{R}) \right] \mathbf{u}^m + (1 - \beta_q) \mathbf{G} \mathbf{q}^m - \mathbf{C} b_1$$

which is obtained in Section 2.3.3 for the time-dependent Poisson's type equation. The stability of dual reciprocity BEM will be discussed through the eigenvalue analysis similar to the one explained Section 2.4.1. The corresponding boundary conditions are inserted into Equation (2.79) at both time levels, and then the known and unknown values are shuffled according to the given boundary conditions in order to obtain the following equation [64, 70]

$$\mathbf{K} \mathbf{u}^{m+1} + \mathbf{L} \mathbf{u}^m = \mathbf{b}. \quad (2.93)$$

Here \mathbf{K} and \mathbf{L} are the matrices for which the components are constructed by shuffling the columns of the coefficient matrices in Equation (2.79), corresponding to the unknown values and its normal derivatives at the $(m+1)$ th time level and the known values and its normal derivatives at the m th time level, respectively. In addition, \mathbf{u}^{m+1} includes the unknown values of \mathbf{u} and \mathbf{u}_q at the time level $m+1$, while \mathbf{u}^m contains the known values of \mathbf{u} and \mathbf{u}_q at the time level m . Similarly, the right hand side vector \mathbf{b} includes the known values of \mathbf{u} and \mathbf{u}_q at both time levels. The equation given in (2.93) is rearranged as

$$\mathbf{K} \mathbf{u}^{m+1} = \mathbf{b} - \mathbf{L} \mathbf{u}^m, \quad (2.94)$$

and finally we get

$$\mathbf{u}^{m+1} = \mathbf{K}^{-1} \mathbf{b} - \mathbf{K}^{-1} \mathbf{L} \mathbf{u}^m. \quad (2.95)$$

Therefore, this iterative technique will be stable when the spectral radius of the matrix $\mathbf{K}^{-1} \mathbf{L}$ is smaller than unity, [36], that is $\rho(\mathbf{K}^{-1} \mathbf{L}) < 1$.

CHAPTER 3

MIXED CONVECTION FLOW IN LID-DRIVEN CAVITIES IN THE PRESENCE OF UNIFORM MAGNETIC FIELD

In this chapter, the DRBEM solution to the steady/unsteady two-dimensional, laminar flow of an incompressible, viscous and electrically conducting fluid subject to an externally applied uniform magnetic field in channels with irregular cross-sectional enclosures is presented. The equations governing the mixed convection MHD flow and the application of the numerical method are given briefly in Section 3.1 and Section 3.2, respectively. First, the steady, mixed convection flow in a channel of square cross-section with a moving left wall and a right wall involving heaters of different shapes subject to an externally applied uniform magnetic field is considered in Section 3.3. In this sense, the flow characteristics and the temperature distribution for a wide range of physical problem parameters are investigated in irregular cavities with one and two semi-circular or semi-rectangular heaters along the right wall in Section 3.3.1 and Section 3.3.2, respectively, and finally when the right wall has a heater of sinusoidal wavy shape in Section 3.3.3. Later, the problem in a lid-driven cavity with sinusoidal wavy hot right wall is solved for the unsteady case to analyze the numerical stability of dual reciprocity BEM with a two-level time integration scheme in Section 3.4.

3.1 Governing Equations for the Unsteady MHD Mixed Convection Flow

In this section, we are going to present the governing equations and the corresponding boundary conditions of the unsteady hydromagnetic mixed convection flow and the heat transfer under the effect of a uniform oblique magnetic field. The problem

is defined in a two-dimensional square cavity with side length ℓ , which is filled with a viscous and electrically conducting fluid. The left wall of the cavity is kept at a constant cold temperature T_c and moves upwards at a constant velocity U_0 (which is considered to be the characteristic velocity in non-dimensionalization of the equations), while the other walls remains stationary (i.e. no-slip walls). The right wall involves a heat source of different types (i.e. semi-circular, semi-rectangular and sinusoidal heaters) which is kept at constant hot temperature $T_h > T_c$ for all problems considered in this chapter. The type of the heater determines the shape of the irregular cavity. The flat parts of the right wall not containing the heater and also the horizontal walls of the cavity are considered to be thermally insulated, i.e. adiabatic. An oblique magnetic field of strength B_0 forming an angle λ with the x -axis is applied and the gravity acts in the negative y -direction. The induced magnetic field is neglected by the assumption that the magnetic Reynolds number is so small. Moreover, the flow generated inside the cavity is assumed to be unsteady and laminar for which the Joule heating effect is taken into account. The flow obeys the Boussinesq approximation while the effects of the radiation and viscous dissipation are neglected. Air is selected as the working fluid which yields Prandtl number of 0.71. Thus, following the aforementioned assumptions, the non-dimensional governing equations given in stream function ψ , vorticity ω and temperature θ form can be written as

$$\nabla^2 \psi = -\omega \quad (3.1)$$

$$\begin{aligned} \frac{1}{Re} \nabla^2 \omega = & \frac{\partial \omega}{\partial t} + u \frac{\partial \omega}{\partial x} + v \frac{\partial \omega}{\partial y} - \frac{Ha^2}{Re} \left(\frac{\partial u}{\partial x} \sin \lambda \cos \lambda - \frac{\partial v}{\partial y} \sin \lambda \cos \lambda \right. \\ & \left. - \frac{\partial v}{\partial x} \cos^2 \lambda + \frac{\partial u}{\partial y} \sin^2 \lambda \right) - \frac{Ra}{Re^2 Pr} \frac{\partial \theta}{\partial x} \end{aligned} \quad (3.2)$$

$$\frac{1}{Re Pr} \nabla^2 \theta = \frac{\partial \theta}{\partial t} + u \frac{\partial \theta}{\partial x} + v \frac{\partial \theta}{\partial y} - J (u \sin \lambda - v \cos \lambda)^2 \quad (3.3)$$

which is derived in Chapter 1 (see Equations (1.48)-(1.50)).

Equations (3.2)-(3.3) are subject to initial conditions

$$\omega(x, y, 0) = \omega_0(x, y) \quad \text{and} \quad \theta(x, y, 0) = \theta_0(x, y) \quad (3.4)$$

where ω_0, θ_0 are known functions of space at time $t = 0$. In the present numerical calculations, the initial conditions for the vorticity and temperature are taken as $\omega_0 = \theta_0 = 0$. The corresponding non-dimensional boundary conditions for stream function and temperature are

$$\begin{aligned}
\text{At the horizontal walls} & : \psi = \partial\psi/\partial x = \partial\psi/\partial y = 0, \quad \partial\theta/\partial n = 0 \\
\text{At sliding left wall} & : \psi = \partial\psi/\partial y = 0, \quad \partial\psi/\partial x = -1, \quad \theta = 0 \\
\text{At flat parts of right wall} & : \psi = \partial\psi/\partial x = \partial\psi/\partial y = 0, \quad \partial\theta/\partial n = 0 \\
\text{At heat source} & : \psi = \partial\psi/\partial x = \partial\psi/\partial y = 0, \quad \theta = 1.
\end{aligned} \tag{3.5}$$

On the other hand, the unknown boundary conditions of the vorticity is derived from the stream function equation (3.1) by using a radial basis function approximation through the application of dual reciprocity BEM, which is one of the basic advantage of DRBEM.

In each problem considered in the chapter, we focus on investigating the combined effect of the shape of the heater and the physical controlling parameters, namely, Joule heating parameter, Hartmann and Rayleigh numbers, not only on the flow and temperature in terms of streamlines and isotherms but also on the heat transfer rate analyzed through the average Nusselt number \overline{Nu} on the hot wall of the cavity. The average Nusselt number \overline{Nu} is evaluated by the formula (given in Chapter 1, Equation (1.84))

$$\overline{Nu} = \frac{1}{S} \int_0^s Nu \, ds \tag{3.6}$$

where $Nu = \partial\theta/\partial n$ is the local Nusselt number, s is the coordinate along the hot surface and S is the arc length of the hot surface.

3.2 Numerical Method and Stability Analysis

This section is devoted for the numerical method and its stability analysis. Thus, in Section 3.2.1 the application of the dual reciprocity BEM to Equations (3.1)-(3.3) in space with a two level integration scheme in time is going to be explained in a similar way given in Chapter 2, Section 2.3.3 for the time-dependent Poisson's type equations. Then, the numerical stability analysis explained in Chapter 2, Section 2.4

will be modified for the DRBEM solutions of the MHD mixed convection flow in Section 3.2.2.

3.2.1 Application of dual reciprocity boundary element method

The DRBEM is employed to transform the governing Equations (3.1)-(3.3) into the equivalent boundary integrals by using the fundamental solution of Laplace equation $u^* = 1/2\pi \ln(1/r)$. Hence, Equations (3.1)-(3.3) are weighted with u^* over the computational domain Ω , and the application of the Divergence theorem successively two times, results in the following integral equations:

$$c_i \psi_i + \int_{\Gamma} (q^* \psi - u^* \frac{\partial \psi}{\partial n}) d\Gamma = - \int_{\Omega} (-\omega) u^* d\Omega \quad (3.7)$$

$$\begin{aligned} \frac{1}{Re} (c_i \omega_i + \int_{\Gamma} (q^* \omega - u^* \frac{\partial \omega}{\partial n}) d\Gamma) = & - \int_{\Omega} \left[\frac{\partial \omega}{\partial t} + u \frac{\partial \omega}{\partial x} + v \frac{\partial \omega}{\partial y} - \frac{Ra}{Re^2 Pr} \frac{\partial \theta}{\partial x} \right. \\ & - \frac{Ha^2}{Re} \left(\frac{\partial u}{\partial x} \sin \lambda \cos \lambda - \frac{\partial v}{\partial y} \sin \lambda \cos \lambda \right. \\ & \left. \left. - \frac{\partial v}{\partial x} \cos^2 \lambda + \frac{\partial u}{\partial y} \sin^2 \lambda \right) \right] u^* d\Omega \end{aligned} \quad (3.8)$$

$$\begin{aligned} \frac{1}{Re Pr} (c_i \theta_i + \int_{\Gamma} (q^* \theta - u^* \frac{\partial \theta}{\partial n}) d\Gamma) = & - \int_{\Omega} \left[\frac{\partial \theta}{\partial t} + u \frac{\partial \theta}{\partial x} + v \frac{\partial \theta}{\partial y} \right. \\ & \left. - J(u \sin \lambda - v \cos \lambda)^2 \right] u^* d\Omega \end{aligned} \quad (3.9)$$

where $q^* = \partial u^* / \partial n$, Γ is the boundary of the domain Ω and the subscript i denotes the source point. The constant c_i is given by $c_i = \theta_i / 2\pi$ with the internal angle θ_i at the source point.

The integrands of the domain integrals on the right hand side of equations (3.7)-(3.9) are treated as non-homogeneity. Thus, they are approximated by a set of radial basis functions $f_j(x, y)$ linked with the particular solutions \hat{u}_j to the equation $\nabla^2 \hat{u}_j = f_j$, [13]. That is, these approximations are given by

$$\sum_{j=1}^{N+L} \alpha_j f_j(x, y) = \sum_{j=1}^{N+L} \alpha_j \nabla^2 \hat{u}_j \quad (3.10)$$

$$\sum_{j=1}^{N+L} \beta_j(t) f_j(x, y) = \sum_{j=1}^{N+L} \beta_j(t) \nabla^2 \hat{u}_j \quad (3.11)$$

$$\sum_{j=1}^{N+L} \gamma_j(t) f_j(x, y) = \sum_{j=1}^{N+L} \gamma_j(t) \nabla^2 \hat{u}_j \quad (3.12)$$

respectively for Equations (3.7), (3.8) and (3.9) where α_j are undetermined constants for the stream function and β_j and γ_j are the undetermined time-dependent coefficients for the vorticity and temperature, respectively. The numbers of the boundary and the internal nodes are denoted by N and L , respectively. After the insertion of approximations (3.10)-(3.12) in Equations (3.7)-(3.9), their right hand sides will also involve the multiplication of the Laplace operator with the fundamental solution u^* , which can be treated in a similar manner by the use of DRBEM to obtain the following boundary only integrals:

$$c_i \psi_i + \int_{\Gamma} (q^* \psi - u^* \frac{\partial \psi}{\partial n}) d\Gamma = \sum_{j=1}^{N+L} \alpha_j \left[c_i \hat{u}_{ji} + \int_{\Gamma} (q^* \hat{u}_j - u^* \hat{q}_j) d\Gamma \right] \quad (3.13)$$

$$c_i \omega_i + \int_{\Gamma} (q^* \omega - u^* \frac{\partial \omega}{\partial n}) d\Gamma = \sum_{j=1}^{N+L} \beta_j(t) \left[c_i \hat{u}_{ji} + \int_{\Gamma} (q^* \hat{u}_j - u^* \hat{q}_j) d\Gamma \right] \quad (3.14)$$

$$c_i \theta_i + \int_{\Gamma} (q^* \theta - u^* \frac{\partial \theta}{\partial n}) d\Gamma = \sum_{j=1}^{N+L} \gamma_j(t) \left[c_i \hat{u}_{ji} + \int_{\Gamma} (q^* \hat{u}_j - u^* \hat{q}_j) d\Gamma \right] \quad (3.15)$$

where $\hat{q} = \partial \hat{u}_j / \partial n$. After the discretization of boundary with constant elements the following time-dependent DRBEM matrix-vector form of Equations (3.13)-(3.15) are obtained as:

$$\mathbf{H}\psi - \mathbf{G}\psi_q = (\mathbf{H}\hat{\mathbf{U}} - \mathbf{G}\hat{\mathbf{Q}})\mathbf{F}^{-1}(-\boldsymbol{\omega}), \quad (3.16)$$

$$\begin{aligned} \frac{1}{Re}(\mathbf{H}\boldsymbol{\omega} - \mathbf{G}\boldsymbol{\omega}_q) = & (\mathbf{H}\hat{\mathbf{U}} - \mathbf{G}\hat{\mathbf{Q}})\mathbf{F}^{-1} \left[\frac{\partial \boldsymbol{\omega}}{\partial t} + \mathbf{u} \frac{\partial \boldsymbol{\omega}}{\partial x} + \mathbf{v} \frac{\partial \boldsymbol{\omega}}{\partial y} \right. \\ & - \frac{Ha^2}{Re} \left(\frac{\partial \mathbf{u}}{\partial x} \sin \lambda \cos \lambda - \frac{\partial \mathbf{v}}{\partial y} \sin \lambda \cos \lambda \right. \\ & \left. \left. - \frac{\partial \mathbf{v}}{\partial x} \cos^2 \lambda + \frac{\partial \mathbf{u}}{\partial y} \sin^2 \lambda \right) - \frac{Ra}{Re^2 Pr} \frac{\partial \boldsymbol{\theta}}{\partial x} \right], \end{aligned} \quad (3.17)$$

$$\begin{aligned} \frac{1}{Re Pr}(\mathbf{H}\boldsymbol{\theta} - \mathbf{G}\boldsymbol{\theta}_q) = & (\mathbf{H}\hat{\mathbf{U}} - \mathbf{G}\hat{\mathbf{Q}})\mathbf{F}^{-1} \left(\frac{\partial \boldsymbol{\theta}}{\partial t} + \mathbf{u} \frac{\partial \boldsymbol{\theta}}{\partial x} + \mathbf{v} \frac{\partial \boldsymbol{\theta}}{\partial y} \right. \\ & \left. - J(\mathbf{u} \sin \lambda - \mathbf{v} \cos \lambda)^2 \right) \end{aligned} \quad (3.18)$$

where $\psi, \psi_q = \partial \psi / \partial n, \boldsymbol{\omega}, \boldsymbol{\omega}_q = \partial \boldsymbol{\omega} / \partial n, \mathbf{u}$ and \mathbf{v} are the vectors containing the values at $N + L$ points. The matrices \mathbf{G} and \mathbf{H} are the usual DRBEM matrices (obtained

in Chapter 2, Section 2.3.3) with the components involving the integrals of fundamental solution and its normal derivative, respectively, at each boundary elements:

$$\begin{aligned} H_{ij} &= c_i \delta_{ij} + \frac{1}{2\pi} \int_{\Gamma_j} \frac{\partial}{\partial n} \ln\left(\frac{1}{r}\right) d\Gamma_j, \quad G_{ij} = \frac{1}{2\pi} \int_{\Gamma_j} \ln\left(\frac{1}{r}\right) d\Gamma_j, \\ G_{ii} &= \frac{l}{2\pi} (\ln(2/l) + 1). \end{aligned} \quad (3.19)$$

The $(N+L) \times (N+L)$ matrices \hat{U} and \hat{Q} are constructed by taking each of the vectors \hat{u}_j and \hat{q}_j as columns, respectively, and F is the coordinate matrix of size $(N+L)$ as given in Equation (2.56). The stream function, vorticity and energy equations can be written as

$$H\psi - G\psi_q = \tilde{b} \quad (3.20)$$

$$-C\dot{\omega} + H_\omega \omega - G_\omega \omega_q = \tilde{c} \quad (3.21)$$

$$-C\dot{\theta} + H_\theta \theta - G_\theta \theta_q = \tilde{d} \quad (3.22)$$

where the superscript dot denotes the time derivative, $C = (H\hat{U} - G\hat{Q})F^{-1}$, $H_\omega = (1/Re)H - D$, $G_\omega = (1/Re)G$, $H_\theta = (1/RePr)H - D$, $G_\theta = (1/RePr)G$ and $D = C(u \frac{\partial F}{\partial x} F^{-1} + v \frac{\partial F}{\partial y} F^{-1})$. The right hand side vectors are as follows

$$\begin{aligned} \tilde{b} &= C(-\omega) \\ \tilde{c} &= -C \frac{Ha^2}{Re} \left(\left(\frac{\partial u}{\partial x} - \frac{\partial v}{\partial y} \right) \sin \lambda \cos \lambda - \frac{\partial v}{\partial x} \cos^2 \lambda + \frac{\partial u}{\partial y} \sin^2 \lambda \right) \\ &\quad - C \frac{Ra}{Re^2 Pr} \frac{\partial \theta}{\partial x} \\ \tilde{d} &= -C J (u \sin \lambda - v \cos \lambda)^2. \end{aligned} \quad (3.23)$$

Equation (3.21) and Equation (3.22) involve the time derivative for which a two-level time integration scheme will be employed as given in Chapter 2, Section 2.3.3.1. That is, linear approximations for the variation of ω and ω_q within each time step

$$\omega = (1 - \beta_\omega) \omega^m + \beta_\omega \omega^{m+1}, \quad \omega_q = (1 - \beta_{\omega_q}) \omega_q^m + \beta_{\omega_q} \omega_q^{m+1} \quad (3.24)$$

are used where β_ω and β_{ω_q} are the parameters which position the values of ω and ω_q , respectively, between the time levels m and $m+1$. Then, the first order time derivative is approximated by

$$\frac{\partial \omega}{\partial t} = \frac{1}{\Delta t} (\omega^{m+1} - \omega^m). \quad (3.25)$$

The substitution of the approximations (3.24)-(3.25) into Equation (3.21) yields:

$$\begin{aligned} \left(\frac{-C}{\Delta t} + \beta_\omega \mathbf{H}_\omega\right) \omega^{m+1} - \beta_{\omega_q} \mathbf{G}_\omega \omega_q^{m+1} = \tilde{c}^m - \left(\frac{C}{\Delta t} + (1 - \beta_\omega) \mathbf{H}_\omega\right) \omega^m \\ + (1 - \beta_{\omega_q}) \mathbf{G}_\omega \omega_q^m. \end{aligned} \quad (3.26)$$

Similarly, the final form of the temperature equation is obtained as

$$\begin{aligned} \left(\frac{-C}{\Delta t} + \beta_\theta \mathbf{H}_\theta\right) \theta^{m+1} - \beta_{\theta_q} \mathbf{G}_\theta \theta_q^{m+1} = \tilde{d}^m - \left(\frac{C}{\Delta t} + (1 - \beta_\theta) \mathbf{H}_\theta\right) \theta^m \\ + (1 - \beta_{\theta_q}) \mathbf{G}_\theta \theta_q^m, \end{aligned} \quad (3.27)$$

where

$$\theta = (1 - \beta_\theta) \theta^m + \beta_\theta \theta^{m+1}, \quad \theta_q = (1 - \beta_{\theta_q}) \theta_q^m + \beta_{\theta_q} \theta_q^{m+1} \quad (3.28)$$

and

$$\frac{\partial \theta}{\partial t} = \frac{1}{\Delta t} (\theta^{m+1} - \theta^m). \quad (3.29)$$

The right hand sides of Equations (3.26) and (3.27) are known since it involves values which have been specified as initial conditions or calculated previously. By introducing the boundary conditions at time $(m + 1)\Delta t$, one can rearrange the left sides of Equations (3.26) and (3.27) and solve the resulting system of equations for each time level iteratively, [13]. First, the stream function equation (3.20) is solved by using the initial condition for the vorticity. Thus, we obtain both the interior and boundary values of stream function, which will be used to calculate the spatial derivatives of itself by means of radial basis functions in each time level. The insertion of these derivative values in the vorticity equation (3.26) and the use of the initial value for the temperature lead to the linearization of the vorticity equation. Once the vorticity values are obtained at all points in the domain, a similar procedure is employed for the solution of the energy equation (3.27). In each time level the required space derivatives of the unknowns ψ , ω and θ and also the unknown vorticity boundary conditions are obtained by using the coordinate matrix \mathbf{F} as

$$\frac{\partial \mathbf{R}}{\partial x} = \frac{\partial \mathbf{F}}{\partial x} \mathbf{F}^{-1} \mathbf{R}, \quad \frac{\partial \mathbf{R}}{\partial y} = \frac{\partial \mathbf{F}}{\partial y} \mathbf{F}^{-1} \mathbf{R}, \quad \omega = -\left(\frac{\partial \mathbf{F}}{\partial x} \mathbf{F}^{-1} \frac{\partial \psi}{\partial x} + \frac{\partial \mathbf{F}}{\partial y} \mathbf{F}^{-1} \frac{\partial \psi}{\partial y}\right) \quad (3.30)$$

where \mathbf{R} is used to represent the each unknown ψ , ω and θ . The iterative process is terminated when a preassigned tolerance ($\epsilon = 10^{-4}$) is reached between two successive iterations.

3.2.2 Stability analysis of the numerical method

In this section, the stability analysis of the numerical method which combines the DRBEM in space with a two-level integration scheme in time is performed through the eigenvalue analysis as given in Chapter 2, Section 2.4. That is, the boundary conditions for the vorticity and the temperature at both time levels are inserted to Equations (3.26)-(3.27), and the known and unknown values are shuffled accordingly in order to obtain the following equations [64, 70]:

$$\mathbf{K}_\omega \mathbf{x}_\omega^{m+1} + \mathbf{L}_\omega \mathbf{x}_\omega^m = \mathbf{b}_\omega, \quad \mathbf{K}_\theta \mathbf{x}_\theta^{m+1} + \mathbf{L}_\theta \mathbf{x}_\theta^m = \mathbf{b}_\theta. \quad (3.31)$$

Here \mathbf{K}_ω , \mathbf{K}_θ , \mathbf{L}_ω and \mathbf{L}_θ are the matrices for which the components are constructed by shuffling the columns of the coefficient matrices in Equation (3.26) and Equation (3.27), corresponding to the unknown values and its normal derivatives at the $(m + 1)$ th time level and the known values and its normal derivatives at the m th time level, respectively. In addition, \mathbf{x}_ω^{m+1} and \mathbf{x}_θ^{m+1} include the unknown values of ω , ω_q and θ , θ_q at the time level $m + 1$, while \mathbf{x}_ω^m , \mathbf{x}_θ^m contain the known values of ω , ω_q and θ , θ_q at the time level m . Likewise, the right hand side vectors \mathbf{b}_ω and \mathbf{b}_θ include the known values of ω , ω_q and θ , θ_q at both levels.

The equations given in (3.31) are rearranged as

$$\mathbf{K}_\omega \mathbf{x}_\omega^{m+1} = \mathbf{b}_\omega - \mathbf{L}_\omega \mathbf{x}_\omega^m, \quad \mathbf{K}_\theta \mathbf{x}_\theta^{m+1} = \mathbf{b}_\theta - \mathbf{L}_\theta \mathbf{x}_\theta^m \quad (3.32)$$

and finally, we get

$$\mathbf{x}_\omega^{m+1} = \mathbf{K}_\omega^{-1} \mathbf{b}_\omega - \mathbf{K}_\omega^{-1} \mathbf{L}_\omega \mathbf{x}_\omega^m, \quad \mathbf{x}_\theta^{m+1} = \mathbf{K}_\theta^{-1} \mathbf{b}_\theta - \mathbf{K}_\theta^{-1} \mathbf{L}_\theta \mathbf{x}_\theta^m. \quad (3.33)$$

Thus, these iterative techniques will be stable when the spectral radius of the matrices $\mathbf{K}_\omega^{-1} \mathbf{L}_\omega$ and $\mathbf{K}_\theta^{-1} \mathbf{L}_\theta$ are smaller than unity, that is $\rho(\mathbf{K}_\omega^{-1} \mathbf{L}_\omega) < 1$ and $\rho(\mathbf{K}_\theta^{-1} \mathbf{L}_\theta) < 1$.

3.3 Steady MHD Mixed Convection Flow in Lid-Driven Cavities with Different Types of Heaters

As the first application of the DRBEM for the MHD mixed convection flow problems, we consider a simpler form of the governing Equations (3.1)-(3.3) by considering

the steady flow in a lid-driven cavity subject to a uniform magnetic field applied in horizontal direction normal to the moving left wall (i.e. the inclination angle $\lambda = 0$). Thus, the equation governing the steady flow can be written as

$$\nabla^2 \psi = -\omega \quad (3.34)$$

$$\frac{1}{Re} \nabla^2 \omega = u \frac{\partial \omega}{\partial x} + v \frac{\partial \omega}{\partial y} + \frac{Ha^2}{Re} \frac{\partial v}{\partial x} - \frac{Ra}{Re^2 Pr} \frac{\partial \theta}{\partial x} \quad (3.35)$$

$$\frac{1}{Re Pr} \nabla^2 \theta = u \frac{\partial \theta}{\partial x} + v \frac{\partial \theta}{\partial y} - Jv^2 \quad (3.36)$$

by taking $\lambda = 0$ in the corresponding unsteady form of Equations (3.1)-(3.3), and the same type of boundary conditions given in Equation (3.5) are taken. That is, the boundary conditions are

$$\begin{aligned} \text{At the horizontal walls} & : \quad \psi = \partial\psi/\partial x = \partial\psi/\partial y = 0, \quad \partial\theta/\partial n = 0 \\ \text{At sliding left wall} & : \quad \psi = \partial\psi/\partial y = 0, \quad \partial\psi/\partial x = -1, \quad \theta = 0 \\ \text{At flat parts of right wall} & : \quad \psi = \partial\psi/\partial x = \partial\psi/\partial y = 0, \quad \partial\theta/\partial n = 0 \\ \text{At heat source} & : \quad \psi = \partial\psi/\partial x = \partial\psi/\partial y = 0, \quad \theta = 1. \end{aligned} \quad (3.37)$$

When the DRBEM with the fundamental solution of Laplace equation is applied to Equations (3.34)-(3.36), one can obtain the following system of equations for stream function, vorticity and temperature, respectively as:

$$\mathbf{H}\psi - \mathbf{G} \frac{\partial \psi}{\partial n} = (\mathbf{H}\hat{\mathbf{U}} - \mathbf{G}\hat{\mathbf{Q}}) \mathbf{F}^{-1} \{-\omega\} \quad (3.38)$$

$$\begin{aligned} \frac{1}{Re} (\mathbf{H}\omega - \mathbf{G} \frac{\partial \omega}{\partial n}) = & (\mathbf{H}\hat{\mathbf{U}} - \mathbf{G}\hat{\mathbf{Q}}) \mathbf{F}^{-1} \left\{ \mathbf{u} \frac{\partial \omega}{\partial x} + \mathbf{v} \frac{\partial \omega}{\partial y} \right. \\ & \left. - \frac{Ra}{Re^2 Pr} \frac{\partial \theta}{\partial x} + \frac{Ha^2}{Re} \frac{\partial v}{\partial x} \right\} \end{aligned} \quad (3.39)$$

$$\frac{1}{Re Pr} (\mathbf{H}\theta - \mathbf{G} \frac{\partial \theta}{\partial n}) = (\mathbf{H}\hat{\mathbf{U}} - \mathbf{G}\hat{\mathbf{Q}}) \mathbf{F}^{-1} \left\{ \mathbf{u} \frac{\partial \theta}{\partial x} + \mathbf{v} \frac{\partial \theta}{\partial y} - Jv^2 \right\}. \quad (3.40)$$

The DRBEM Equations (3.38)-(3.40) are coupled so that they are solved iteratively with initial estimates for vorticity and temperature. In each iteration, the required space derivatives of the unknown ψ , ω and θ , and also the unknown vorticity boundary conditions are obtained by using the coordinate matrix \mathbf{F} as in Equation (3.30).

In this section, three steady MHD mixed convection flow problems are considered in an irregular lid-driven cavity of which the shape is determined by using different types of heaters along the right vertical wall, i.e. semi-circular, semi-rectangular

and sinusoidal wavy heaters. Thus, the effect of the shape of the heater under various combinations of physical parameters on the flow and temperature distribution is investigated and the results are visualized in terms of streamlines, isotherms and average Nusselt numbers along the hot wall.

3.3.1 Semi-rectangular and semi-circular heaters

The hydromagnetic mixed convection flow in a lid-driven square cavity involving either a semi-rectangular or semi-circular heater, the schematic presentation of which is given in Figure 3.1, is considered. The length of the vertical side of the rectangular heater and the diameter of the semicircle is taken as 0.2ℓ .

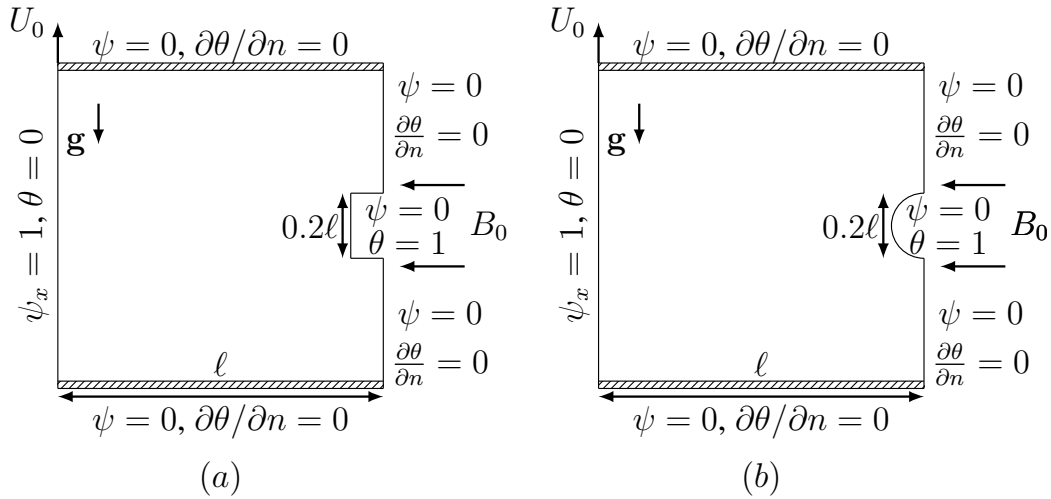


Figure 3.1: Geometry of the problem: (a) semi-rectangular, (b) semi-circular heaters

The DRBEM analysis for the two-dimensional steady MHD mixed convection flow under consideration is performed at fixed Reynolds number of $Re = 100$ and Prandtl number of $Pr = 0.71$ to investigate the effects of the Hartmann number ($0 \leq Ha \leq 100$), Rayleigh number ($Ra = 10^3, 10^4, 10^5$) and the Joule heating parameter ($J = 0, 1, 3, 5$) on the flow and temperature fields. The boundary of the cavity is discretized by using $N = 300$ constant boundary elements. The choice of this grid based on the grid refinement study conducted by using both constant and linear elements for the case when $Ha = 10$, $Ra = 10^5$ and $J = 1$ in order to determine the appropriate grid size required for the optimal relationship between the computational cost and numerical accuracy. The results are visualized in terms of $|\psi|_{max}$, $|\theta|_{max}$ and the average Nusselt number \overline{Nu} along the hot wall. Figure 3.2 displays that the grid of

$N = 300$ constant or linear boundary elements ensures the grid independence. Thus, due to the easiness of the constant boundary elements in the application of DRBEM when compared to the use of linear element, we prefer to use the constant elements in the subsequent computations.

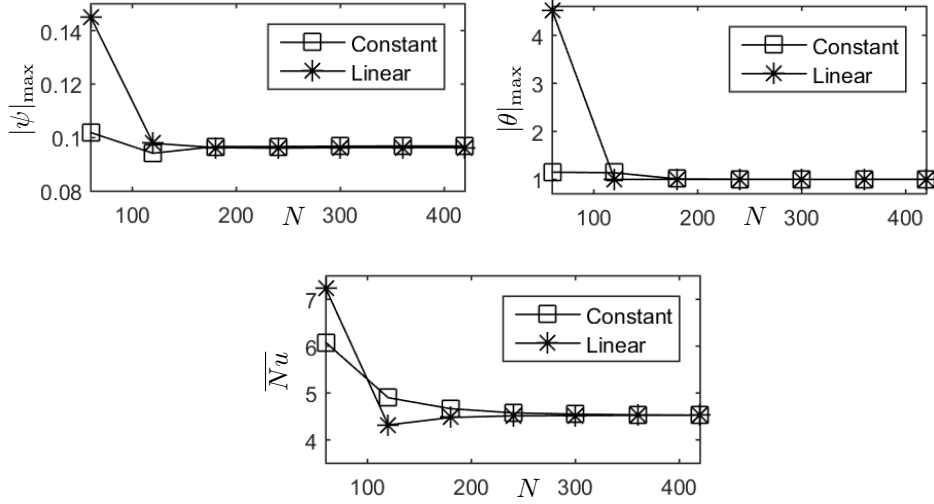


Figure 3.2: Grid dependency: $Ha = 10$, $Ra = 10^5$, $J = 1$.

For the visualization of the obtained results, two types of grid distribution, namely equally-spaced and Gauss-Chebyshev-Lobatto (GCL) points, are performed for the choice of interior points. The equally-spaced points in x and y -directions are given by

$$x_i = \frac{i-1}{m-1}(b-a), \quad y_i = \frac{j-1}{n-1}(d-c), \quad i = 1, 2, \dots, m, \quad j = 1, 2, \dots, n \quad (3.41)$$

in which m and n are the number of points taken in x and y -direction, respectively, for a region $\Omega = \{(x, y) | a \leq x \leq b, c \leq y \leq d\}$. On the other hand, GCL points are the Chebyshev collocation points x_i which satisfy $|T_m(x_i)| = 1$ where $T_m(x)$ is the Chebyshev polynomial. Thus, x_i are given by [43]

$$x_i = \cos\left(\frac{i-1}{m-1}\pi\right), \quad i = 1, 2, \dots, m \quad (3.42)$$

for the interval $[-1, 1]$. However, for an arbitrary interval $[a, b]$ the GCL points are given by [43]

$$x_i = \frac{b+a}{2} - \frac{b-a}{2} \cos\left(\frac{i-1}{m-1}\pi\right), \quad i = 1, 2, \dots, m. \quad (3.43)$$

Figure 3.3 shows the comparison of the results obtained by using either equally-spaced or GCL points taken as the interior points for the visualization of the obtained results for streamlines and isotherms inside the cavity when $Ha = 50$, $Ra = 10^5$, $J = 1$. It is well observed that to capture the behavior of the flow along the moving left vertical wall and around the heated surface on the right wall accurately, the GCL points should be employed for the interior discretization. When the equally-spaced points are used some disruptions in the region around the heater occur and the vortex which is formed near the left wall due to its motion can not be well-captured. Therefore, in all computations done in the present chapter the interior grids are taken as the GCL points.

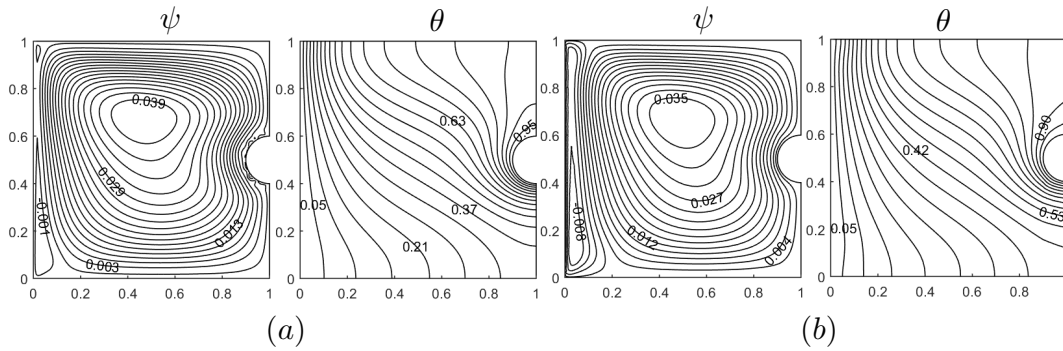


Figure 3.3: The streamlines and isotherms drawn by using (a) equally-spaced, (b) GCL grids: $Ha = 50$, $Ra = 10^5$, $J = 1$.

In the application of DRBEM for the approximation of the non-homogeneity, several types of radial basis functions are used for the solution of MHD mixed convection with a semi-circular heater. The corresponding iteration number ($iter$) and the allocated CPU times (T) to reach the required preassigned tolerance are $iter = 103$ and $T = 90.766\text{sec}$ for the linear polynomials ($f = 1 + r$), $iter = 103$ and $T = 110.782\text{sec}$ for the quadratic polynomials ($f = 1 + r + r^2$), $iter = 106$ and $T = 97.910\text{sec}$ for thin-plate splines ($r^2 \ln r$) and $iter = 280$ and $T = 224.972\text{sec}$ for multi-quadratic ($\sqrt{r^2 + c^2}$ with $c = 0.007$), respectively. It is observed that using the linear polynomial RBFs requires less number of iteration and computational time. Thus, in all computations done in the thesis, the linear polynomial type RBFs will be employed.

In order to assess the validity of our numerical scheme, we solve the problem in a lid-driven cavity with a semi-circular heater for the cases when $Ha = 10$ and $Ha = 50$

at $Ra = 10^5$, $J = 1$ to compare the present results with result of Rahman [67]. The streamlines and isotherms are displayed in Figure 3.4 and the obtained results are in very well-agreement with the ones given in the work of Rahman (see Figure 3 in [67]). Moreover, the average Nusselt number along the circular heater calculated

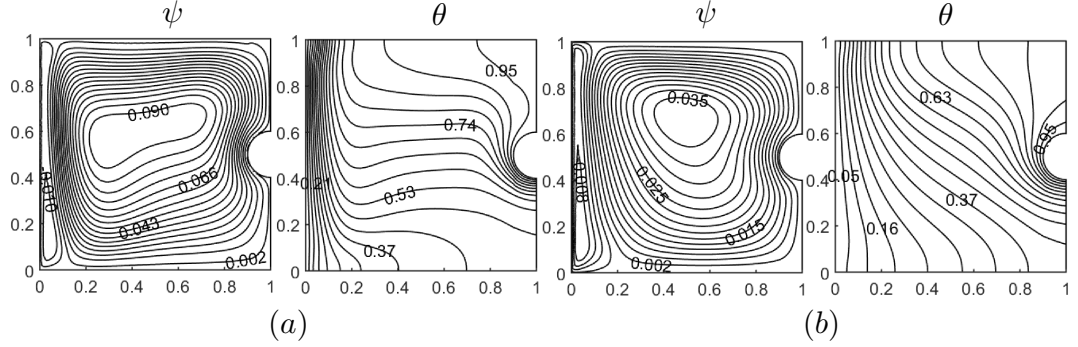


Figure 3.4: Streamlines and isotherms for (a) $Ha = 10$, (b) $Ha = 50$: $Ra = 10^5$, $J = 1$.

with the present numerical method are displayed and compared with the ones obtained in the work of Rahman [67] in Table 3.1 for several values of Hartmann number. It is observed that the present results agree well with those of [67].

Table 3.1: Average Nusselt number along the semi-circular heater: $Ra = 10^5$, $J = 1$

Ha	\overline{Nu} (Present study)	\overline{Nu} (Rahman [67])
10	4.540	4.52
20	4.960	4.89
50	4.072	4.10
100	2.947	2.99

First, the numerical simulations are conducted for the values of Hartmann number $Ha = 0, 25, 50$ at fixed values of $Ra = 10^5$ and $J = 1$ to see the effect of Ha on the flow field and temperature distribution. Figure 3.5 displays the streamlines and isotherms when the right wall is heated with (a) semi-rectangular and (b) semi-circular heaters. It is observed that two counter rotating vortices are formed inside the cavity for streamlines in all cases. These two vortices are basically an outcome of the forced flow as a result of the combination of lid-movement and the buoyancy-driven flow due to the differential heating. The vortex adjacent to the left moving wall has

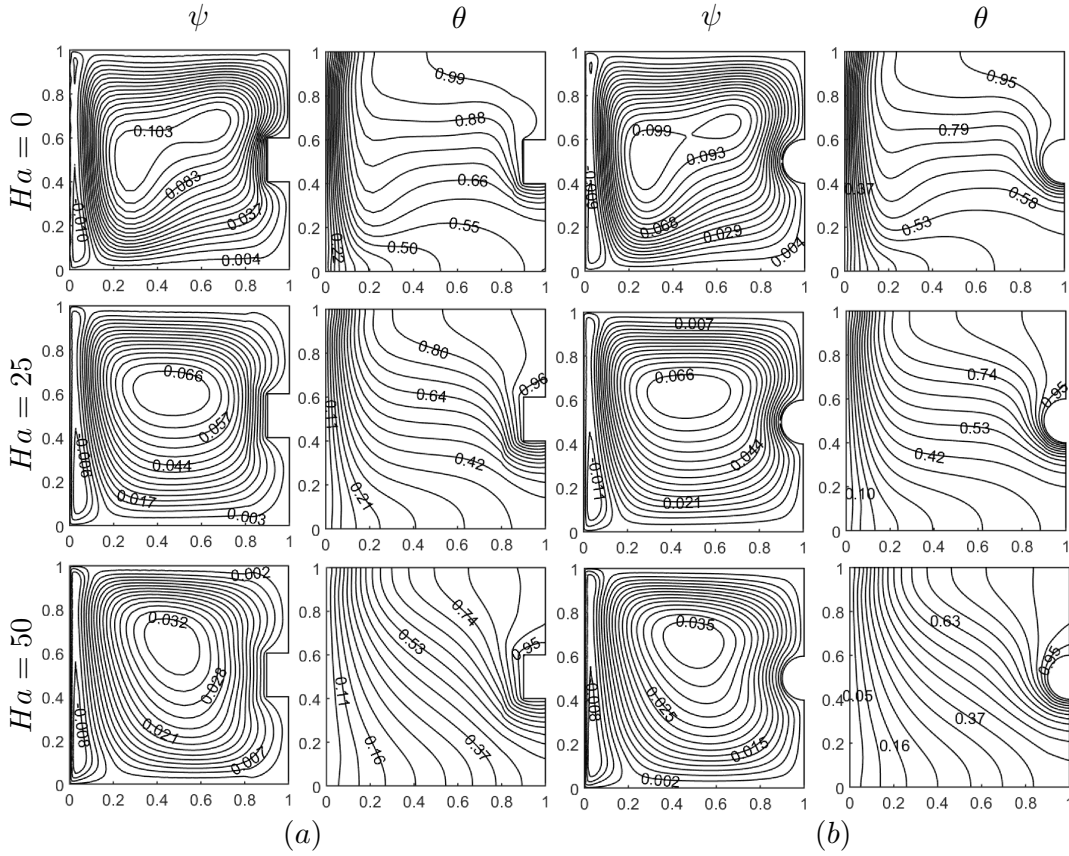


Figure 3.5: Effect of Ha on streamlines and isotherms at $Ra = 10^5$, $J = 1$: (a) semi-rectangular heater, (b) semi-circular heater.

a clockwise (negative) rotation, since the lid moves from bottom to top. The main vortex close to the right hot wall has a counterclockwise (positive) rotation due to the thermal buoyancy effect. An increase in Ha enhances the strength of the magnetic force, and hence the effect of thermal buoyancy on the flow and temperature fields reduces. The positive vortex of an almost elliptical shape formed at the center of the cavity moves slightly upward and becomes circular as Ha increases and the strength of the main flow decreases. In addition, the secondary negative vortex expands horizontally with increasing Ha . On the other hand, a thin thermal boundary layer in isotherms is observed along the vertical left wall and around the heater for low values of Ha , and the isotherms become more parallel to the vertical walls for higher Ha indicating the dominance of conduction on heat transfer.

Secondly, Figure 3.6 displays the streamlines and isotherms for different values of Rayleigh number at $J = 1$ and $Ha = 10$. At $Ra = 10^3$, a negative main eddy with an almost circular core is formed in streamlines. When Ra increases, the main

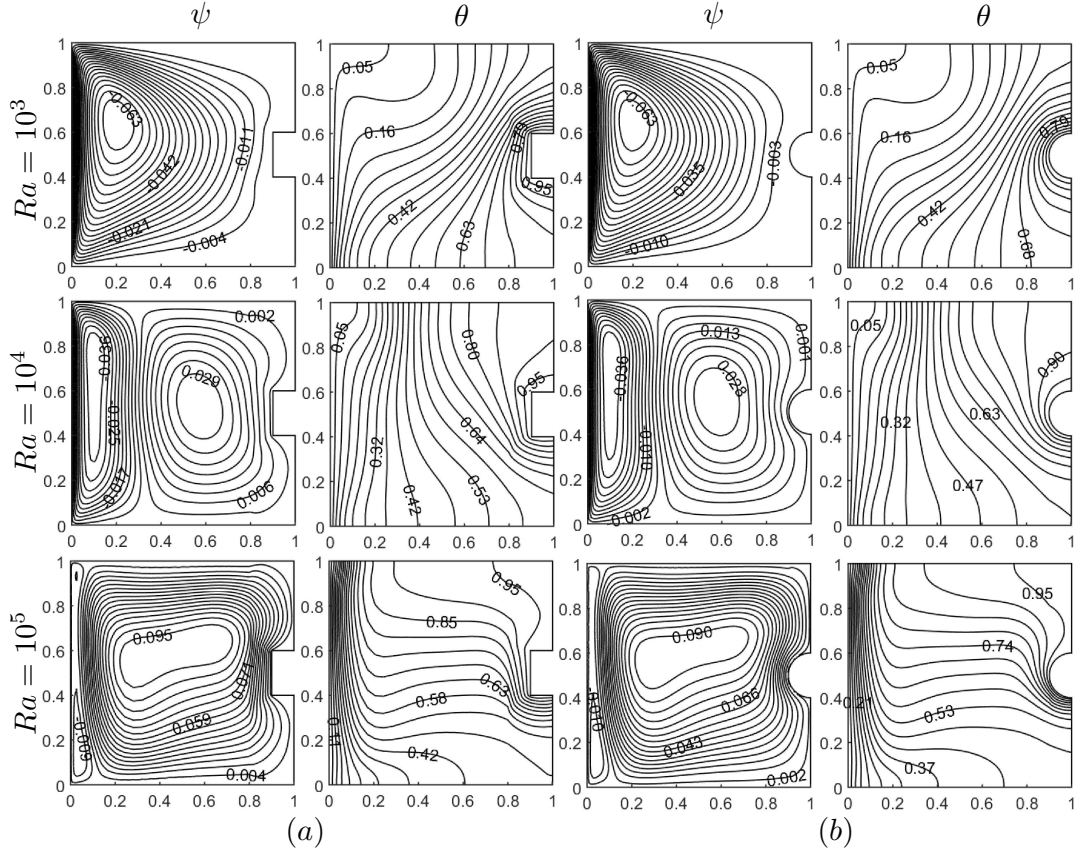


Figure 3.6: Effect of Ra on streamlines and isotherms at $Ha = 10$, $J = 1$: (a) semi-rectangular heater, (b) semi-circular heater.

eddy extends vertically taking a more elliptical shape and it shrinks towards the left wall following the formation of a positive secondary vortex in front of the heater. The secondary vortex expands towards the left wall and the flow is dominated by this circulation as Ra increases. On the other hand, the isotherms accumulated above the heater at $Ra = 10^3$ disperse horizontally along the top wall with an increase in Rayleigh number to $Ra = 10^4$. Further, the isotherms become horizontal at the center of the cavity and form a boundary layer along the left wall and below the heater for the highest value of $Ra = 10^5$ following the convection mode on the heat transfer.

Finally, the effect of Joule heating parameter on the fluid flow and temperature distribution is investigated by taking $J = 0, 1, 3, 5$ when $Ra = 10^5$ and $Ha = 10$ for semi-rectangular and semi-circular heaters (see Figure 3.7). It is observed that as the Joule heating parameter increases, the strength of the main vortex in streamlines decreases following the formation of a third vortex in the opposite direction with the main vortex near the right top corner. On the other hand, the temperature of the fluid

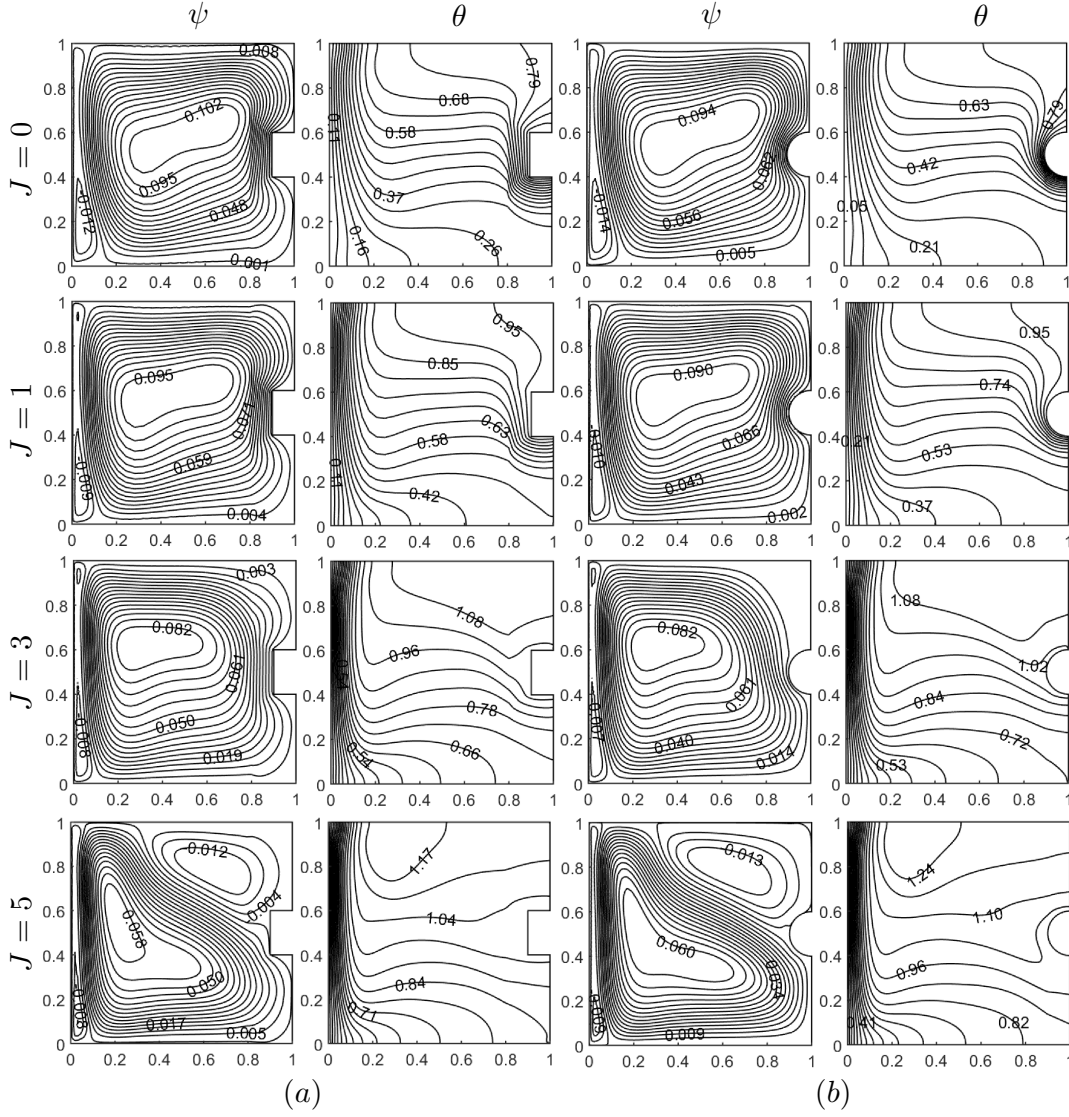


Figure 3.7: Effect of J on streamlines and isotherms at $Ra = 10^5$, $Ha = 10$: (a) semi-rectangular heater, (b) semi-circular heater.

inside the cavity increases by the additional heat due to the increase in J .

As it can be seen from Figures 3.5, 3.6 and 3.7, generally, no significant alterations are observed in the profiles of streamlines and isotherms due to the shape of the heat source and hence in the shape of the computational domain. However, the heat transfer rate from the heater is more in the semi-rectangular heater compared to its semi-circular counterpart, since the length of the heated portion is larger when the source is semi-rectangular. This situation will be shown through the following analysis in terms of average Nusselt number along the hot portion of the right vertical wall.

The influence of Hartmann and Rayleigh numbers with semi-rectangular and semi-

circular heater on the average Nusselt number are graphically established in Figure 3.8 for $J = 0$ and in Figure 3.9 for $J = 1$. The results exhibit that, when $J = 0$, \overline{Nu} decreases as Ha increases (see Figure 3.8 (a)) which is an expected outcome since the magnetic field intensity reduces the fluid velocity, and accordingly the rate of convection heat transfer decreases at each Ra . On the other hand, \overline{Nu} on the heat

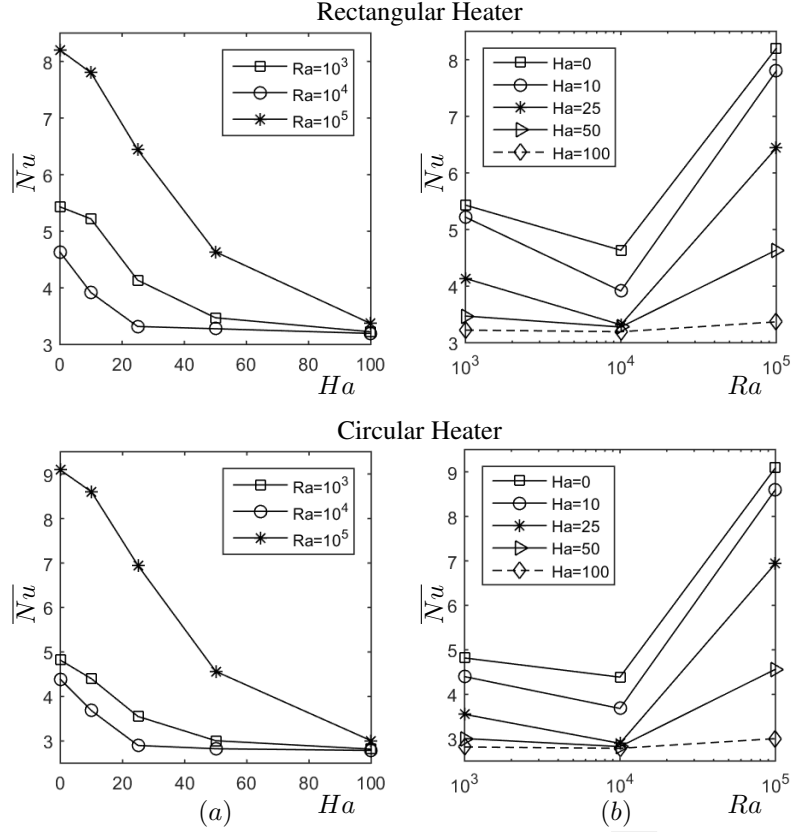


Figure 3.8: Effects of (a) Ra and (b) Ha on \overline{Nu} at $J = 0$.

transfer shows increasing tendency with values $Ra \geq 10^4$ at each Ha (see Figure 3.8 (b)). However, the heat transfer rate decreases when Ra increases from 10^3 to 10^4 since the heat transfer changes from conduction to convection and the buoyancy force is not strong enough to resist the magnetic field effect. Furthermore, when $J = 1$, it is interesting to note that the heat transfer rate increases with an increase in Ha for $Ha \leq 25$ at each Ra while \overline{Nu} decreases at $J = 0$. At higher $Ha \geq 25$, the conduction contribution on heat transfer is more in comparison to the convection, consequently \overline{Nu} decreases at $Ra = 10^3$ and $Ra = 10^5$, while increasing Ha have no significant effect on \overline{Nu} at $Ra = 10^4$. On the other hand, Ra has similar effect on \overline{Nu} as in the case when $J = 0$. That is, \overline{Nu} decreases as Ra enhances from 10^3 to 10^4 and \overline{Nu} increases with a further increase in Ra to 10^5 at each Ha . Moreover,

the average Nusselt number decreases with an increase in J from $J = 0$ to $J = 1$ for each combination of Ra and Ha . On the other hand, the variation of \overline{Nu} with respect to Ra and Ha is similar for both types of the heater. However, it is well-observed that \overline{Nu} is higher when the heater is rectangular irrespective of the values of Ha , Ra and J (except the case when $Ra = 10^5$, $J = 0$), since the length of the heated portion on the right wall is longer when the source is rectangular as mentioned before. Thus, the heat transfer rate can be enhanced with the type of heat source.

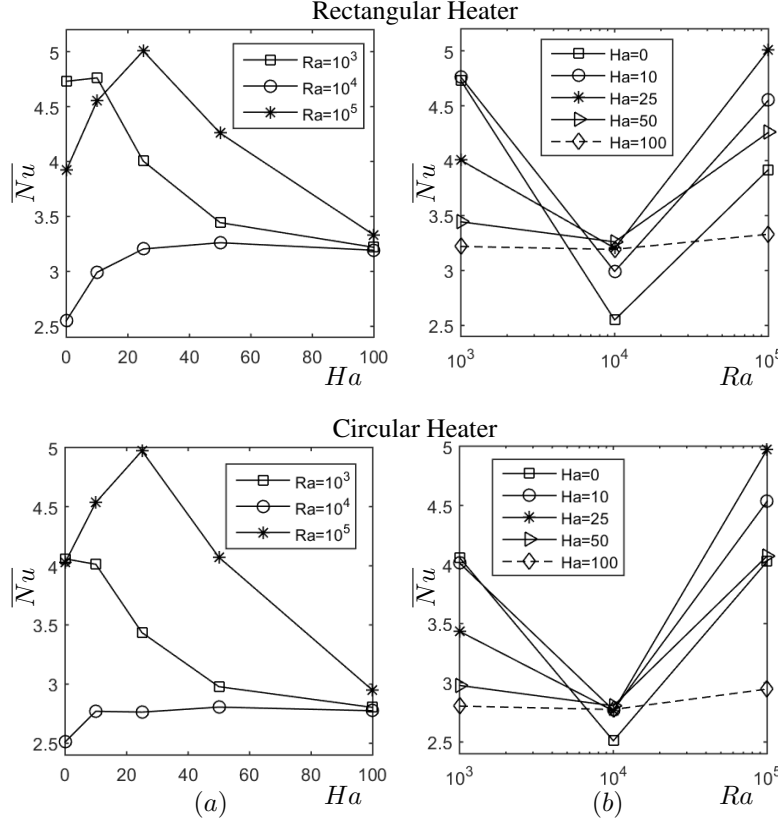


Figure 3.9: Effects of (a) Ra and (b) Ha on \overline{Nu} at $J = 1$.

Further, the effects of the shape of the heater with respect to Ha at $Ra = 10^4$ (see Figure 3.10(a)) and $Ra = 10^5$ (see Figure 3.10(c)) at $J = 0$ and with respect to Ra at $Ha = 10$ (see Figure 3.10(b)) and $Ha = 50$ (Figure 3.10(d)) at $J = 0$ are investigated. It is observed that \overline{Nu} and hence the heat transfer rate increases when the length of the heated portion on right wall increases (i.e. by inserting to the system a circular and finally rectangular heaters instead of a flat heater) irrespective of Ha and Ra numbers. However, at $Ra = 10^5$, the average Nusselt number of semi-circular heater is greater than semi-rectangular counter part for the values for $Ha < 50$. This means that the convective flow at $Ra = 10^5$ has more influence on the heat transfer

rate when the heater has a curvy shape (i.e. circular) than the heater of flat shape for $Ha < 50$. However, for higher $Ha \geq 50$, the average Nusselt number in the case of rectangular heater becomes higher than the one obtained for circular heater following the suppression of the Ha on the convective mode on heat transfer.

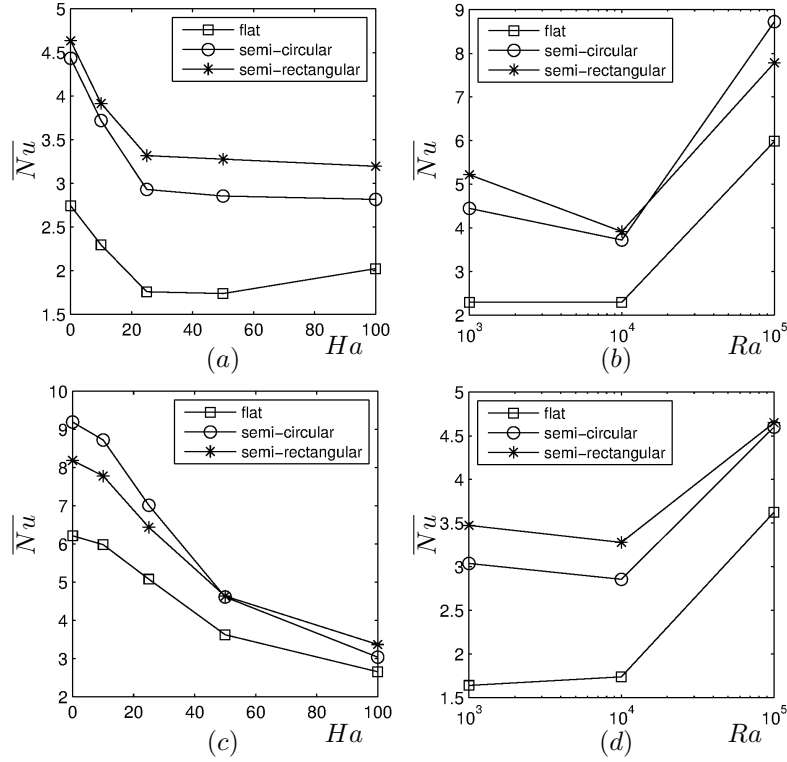


Figure 3.10: Effect of the shape of the heater on \overline{Nu} at (a) $Ra = 10^4$, (b) $Ha = 10$, (c) $Ra = 10^5$, (d) $Ha = 50$.

3.3.2 Two semi-rectangular and two semi-circular heaters

In this section, we extend the problem given in Section 3.3.1 by inserting two heaters either rectangular or circular along the right vertical wall (see Figure 3.11) in order to understand the effect of additional heaters on the flow field and temperature distribution. The boundary of the cavity is discretized by using $N = 300$ constant boundary elements where the end points of each element are distributed using GCL points as in the Section 3.3.1.

The effects of Hartmann and Rayleigh numbers on the flow field and temperature distribution are displayed, respectively, in Figure 3.12 when $Ra = 10^5$, $J = 1$ and in

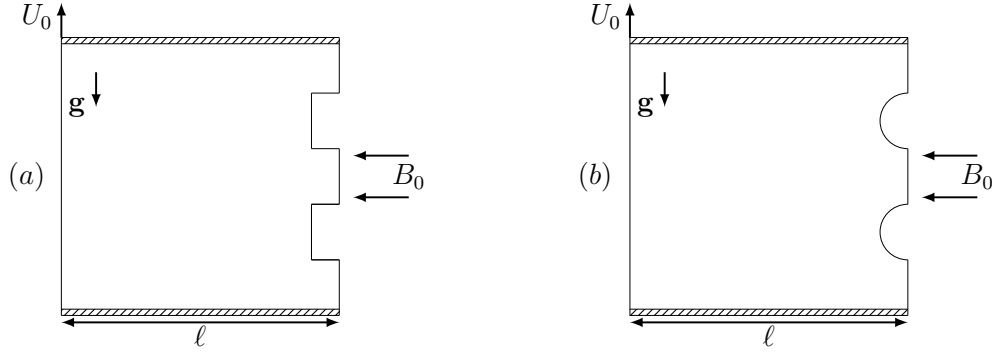


Figure 3.11: Geometry of the problem: (a) semi-rectangular, (b) semi-circular heaters

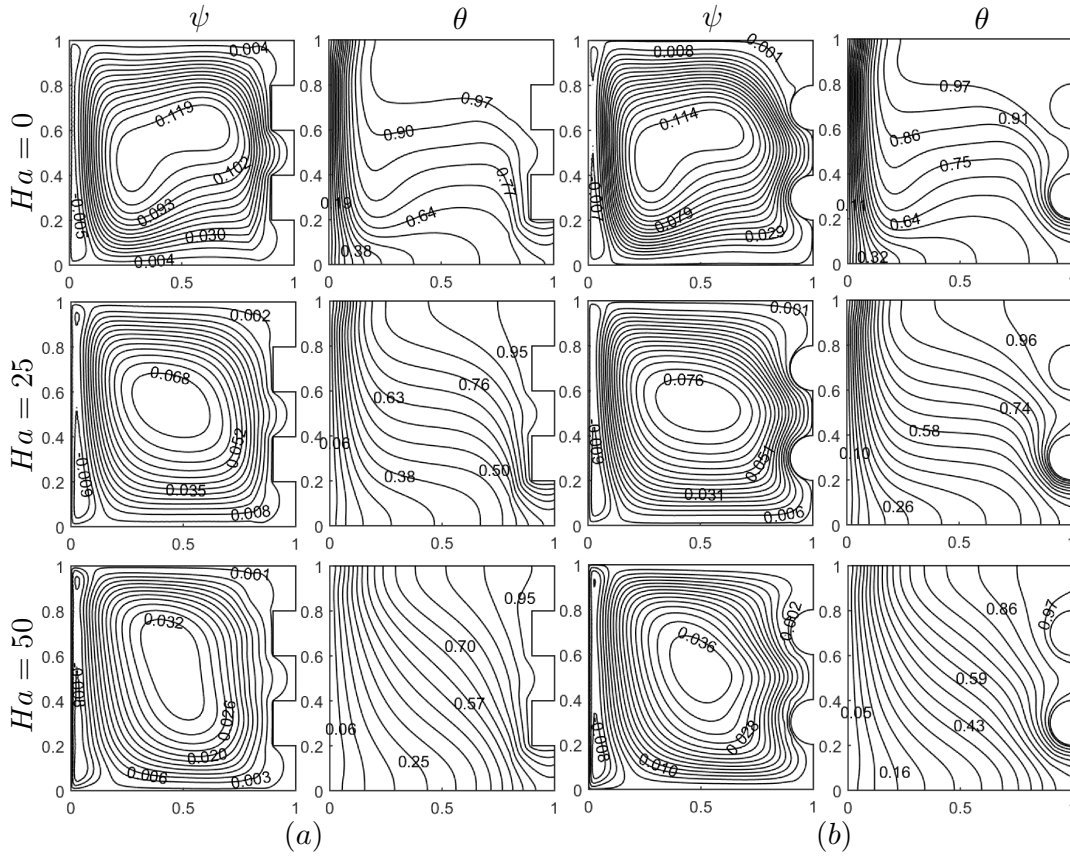


Figure 3.12: Effect of Ha on streamlines and isotherms at $Ra = 10^5$, $J = 1$: (a) semi-rectangular heaters, (b) semi-circular heaters.

Figure 3.13 when $Ha = 10$, $J = 1$. It is observed that there is no significant change in the profiles of streamlines and isotherms when compared the case with only one heater given in Section 3.3.1 (see Figures 3.5 and 3.6). That is, the flow field and temperature distribution have the same behavior in terms of the formation of vortices and the thermal boundary layers. However, one can notice from Figure 3.13 that there is an increase in the magnitude of ψ especially for $Ha = 0, 25$ and the core of

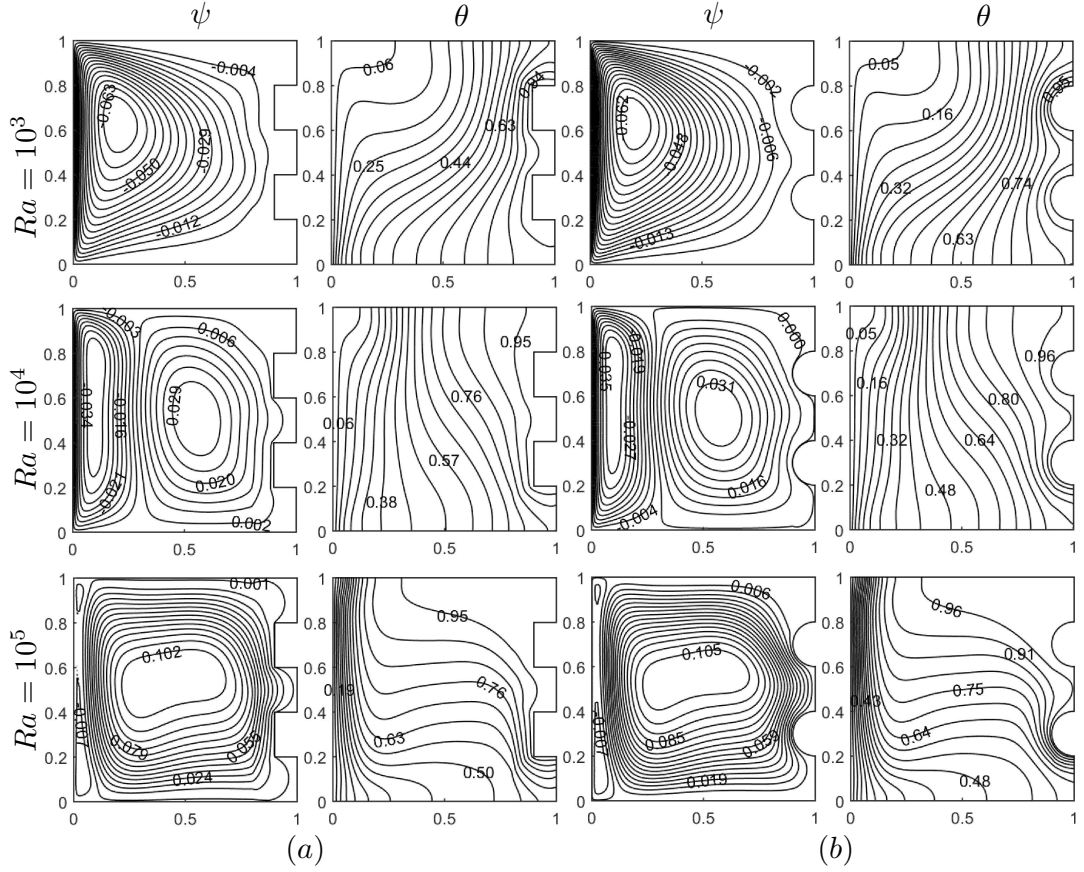


Figure 3.13: Effect of Ra on streamlines and isotherms at $Ha = 10$, $J = 1$: (a) semi-rectangular heaters, (b) semi-circular heaters.

the main vortex which is circular in the case of one heater (see Figure 3.5) extends vertically towards the bottom wall at $Ha = 50$ by the inclusion of the second heater to the right wall. On the other hand, as it is expected the temperature of the fluid all over the cavity increases with the additional heat source when compared to the case of one heater (see Figure 3.5 and 3.6).

The effect of the Joule heating parameter on the flow and temperature is further depicted in Figure 3.14. The flow and temperature show similar behavior as in the case of one heater (see Figure 3.7). However, the third vortex formed on the right top corner of the cavity at $J = 5$ in the one heater case now occurs for a smaller Joule heating parameter $J = 3$ with the insertion of an additional second heater to the system. That is, the increase in the number of heaters magnifies the effect of the Joule heating, and as a result the third vortex becomes more strong and bigger in size for a higher value of $J = 5$. Moreover, the increase in the temperature of the fluid in the enclosure due to the Joule heating increases more with an additional heater; and

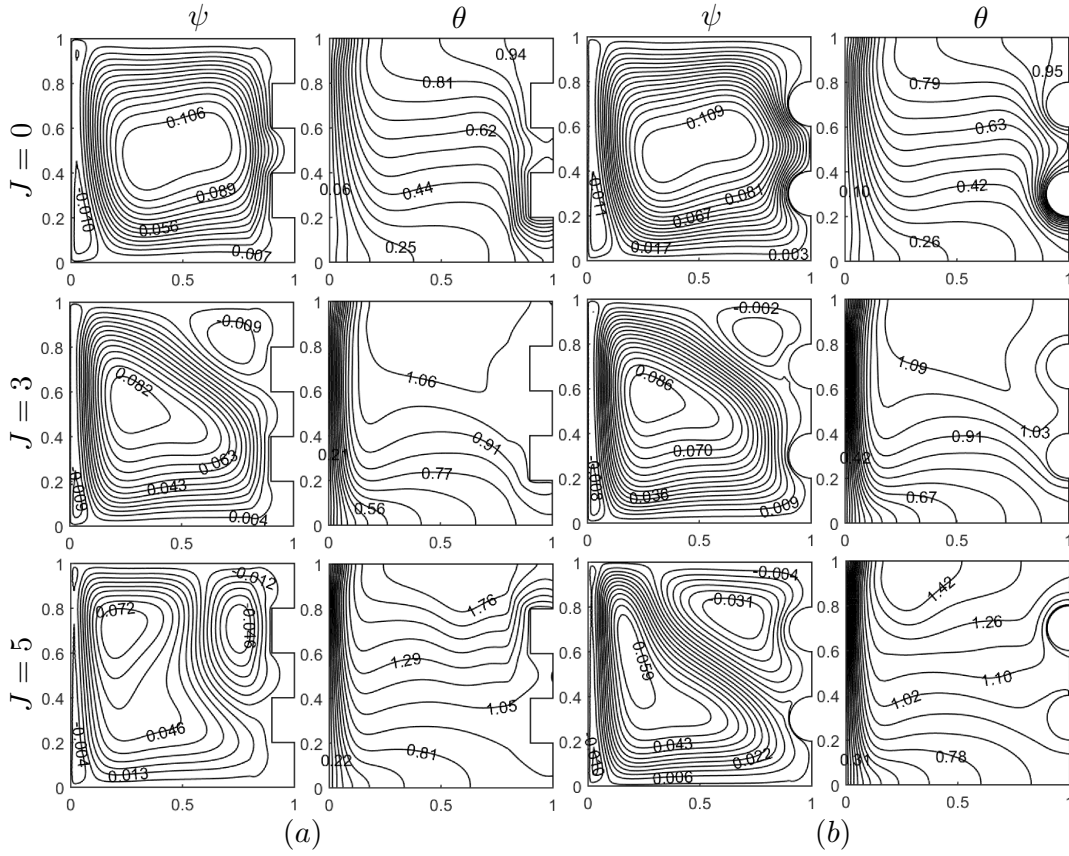


Figure 3.14: Effect of J on streamlines and isotherms at $Ra = 10^5$, $Ha = 10$: (a) semi-rectangular heaters, (b) semi-circular heaters.

the isotherms moves upwards and are concentrated around the upper heater with an increase in J .

Figure 3.15 shows the effect of Hartmann and Rayleigh numbers on the average Nusselt number along the hot portions of right wall when $J = 1$. The increase in the temperature of the fluid inside the enclosure, and as a result in the heat transfer rate by an additional heat source can be well-observed by the increase in \overline{Nu} irrespective of the values of Ha and Ra when compared to the case of one heater (see Figure 3.9). Moreover, the additional heater magnifies the effect of Rayleigh number on \overline{Nu} especially at $Ra = 10^4$, 10^5 . That is, the decrease observed in \overline{Nu} at $Ra = 10^4$ at each Ha in the case of one heater vanishes with the additional heater, and actually the \overline{Nu} increases continuously with an increase in Ra at each Ha in the case of two heaters (see Figures 3.9 (b) and 3.15 (b)). On the other hand, in the case of two heaters an increase in Ha at $Ra = 10^4$ results in a decrease in \overline{Nu} while \overline{Nu} increases slightly for $Ha \leq 10$ and becomes constant for $Ha > 10$ in the case of one heater. Moreover,

a similar behavior is observed in \overline{Nu} for values of $Ra = 10^3, 10^5$ as Ha increases in both cases of one or two heaters (see Figures 3.9 (a) and 3.15 (a)).

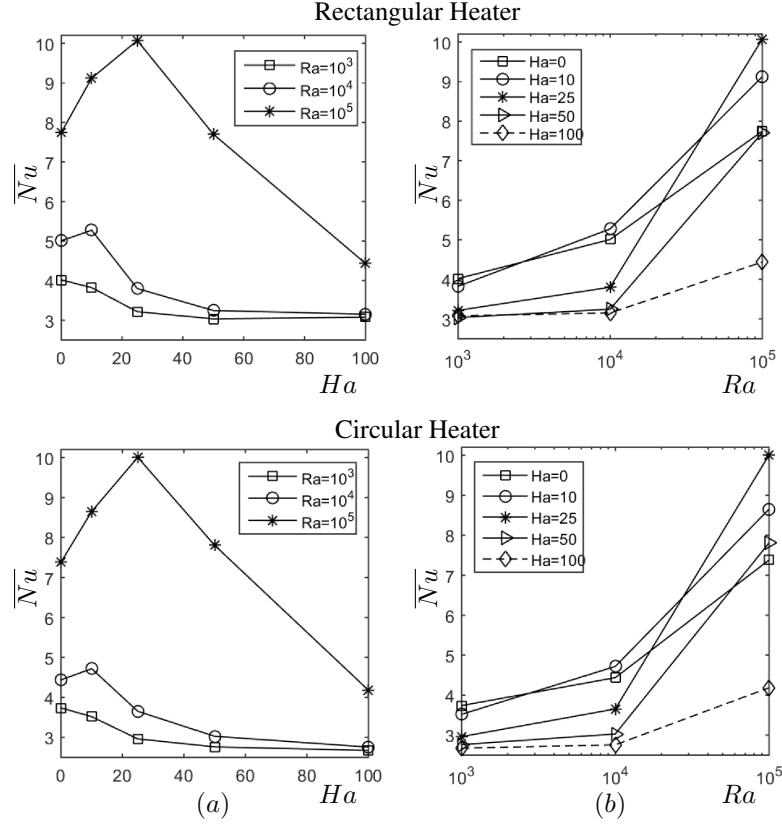


Figure 3.15: Effects of (a) Ra and (b) Ha on \overline{Nu} at $J = 1$.

3.3.3 Sinusoidal heater

In this section, the steady MHD flow in a lid-driven cavity with a hot right wall of sinusoidal shape is considered (see Figure 3.16) in which the effect of Joule heating is neglected (i.e. $J = 0$ is taken in Equation (3.36)). The shape of the right wall is defined by $x = 1 - A[1 - \cos(2n\pi y)]$ where A is the dimensionless amplitude of the wavy surface and n is the number of undulations.

The numerical simulations are carried out for a wide range of physical parameters, such as Hartmann number $Ha = 0, 10, 25, 50, 100$, Rayleigh number $Ra = 10^3, 10^4, 10^5, 10^6$ and the number of undulations ($n = 0, 1, 2, 3$) by keeping the amplitude of wavy wall, Reynolds and Prandtl numbers fixed as $A = 0.05$, $Re = 100$ and $Pr = 0.71$, respectively. The boundary of the cavity is discretized by using

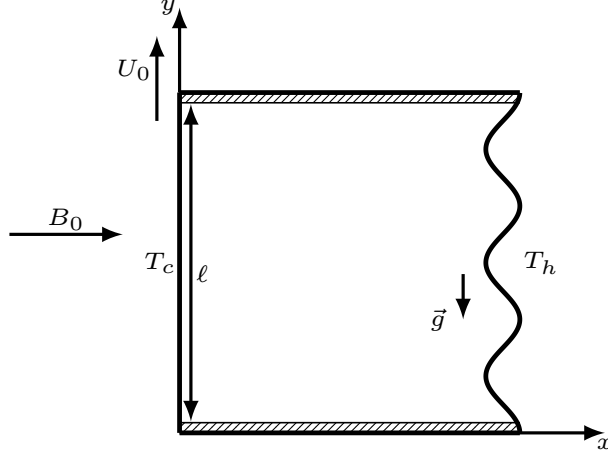


Figure 3.16: Geometry of the problem for sinusoidal heater

$N = 350$ constant boundary elements. The choice of this grid is based on the grid resolution test performed for the case when $Ha = 50$, $Ra = 10^5$ and $n = 3$ in terms of $|\Psi|_{max}$, $|\theta|_{max}$ and \overline{Nu} along the hot wall. Figure 3.17 displays that the grid of $N \approx 350$ boundary elements ensures the grid independence, and hence is used in the computations of the present section. Furthermore, in order to assess the validity of our numerical procedure, a test problem of the mixed convection flow in a lid-driven cavity with a heated wavy bottom wall of three undulations given in the work of Al-Amiri et al. [1] is solved. It is observed that the present results $\Psi_{min} = -0.0928, -0.1351, -0.2997$ and $\overline{Nu} = 7.4325, 3.1515, 2.6646$, respectively at $Ri = 0.01, 1, 10$, are in good agreement with the numerical results of Al-Amiri et al. [1] $\Psi_{min} = -0.0919, -0.1278, -0.2564$ and $\overline{Nu} = 7.9331, 3.2711, 2.7192$ (calculated from the formula

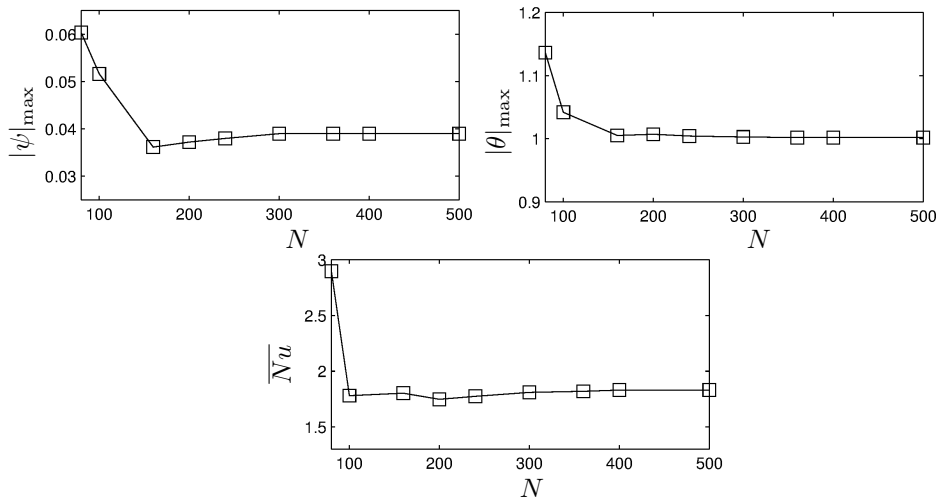


Figure 3.17: Grid dependency: $Ra = 10^5$, $Ha = 50$, $n = 3$.

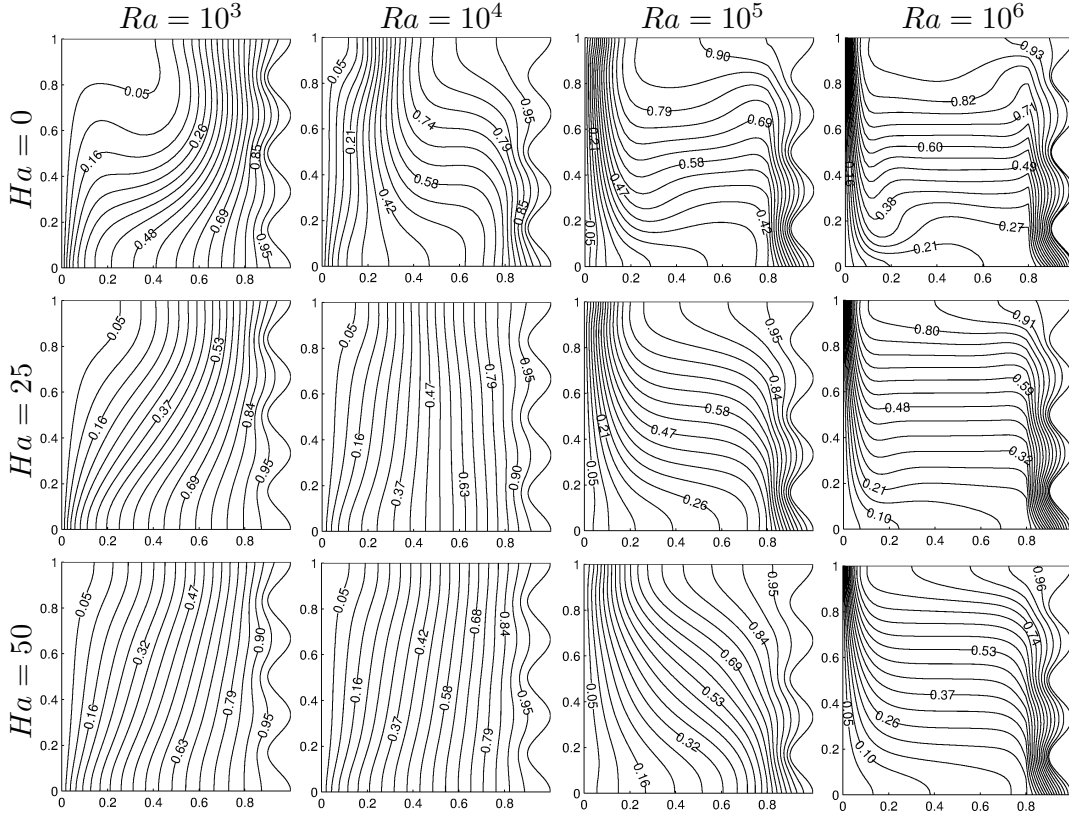


Figure 3.19: Effects of Ha and Ra on isotherms at $n = 3$.

effect of the magnetic field on the fluid flow, while it increases at higher values of Ra . On the other hand, the isotherms distribute uniformly in the cavity displaying almost similar behavior for each Ha at low values of Ra ($= 10^3$ and 10^4) when the heat transfer is due to the conduction. By an increase in Ra , the flow becomes convection dominated. As a result, isotherms change their profiles from being vertical to almost horizontal at the centre of the cavity forming a thermal boundary layer along the vertical walls as Ra increases. However, Ha has a reverse effect on isotherms, that is, the isotherms tend to go from horizontal to vertical (especially at $Ra = 10^5$) indicating the suppression of convective flow for higher Ha .

The effect of the number of undulation n on the average Nusselt number at different values of Ra is shown in Figure 3.20 (a) $Ha = 0$, (b) $Ha = 10$, (c) $Ha = 25$, (d) $Ha = 50$. At each Ha , the \overline{Nu} is increasing as Ra increases from $Ra = 10^4$ to 10^6 for all n since the heat transfer becomes dominated by convection for higher values of Ra as in the case of rectangular/circular heater. However, \overline{Nu} decreases slightly when the flow is transferred from the conducting regime (i.e. $Ra = 10^3$) to the transition regime (from conduction to convective) at $Ra = 10^4$ regardless of the

values of Ha and n similar to the case of rectangular/circular heater. Moreover, the number of undulation has no significant effect on \overline{Nu} at $Ra = 10^4$. It is well observed that, an increase in the number of undulation results in a slight increase in \overline{Nu} at each Ha and Ra numbers.

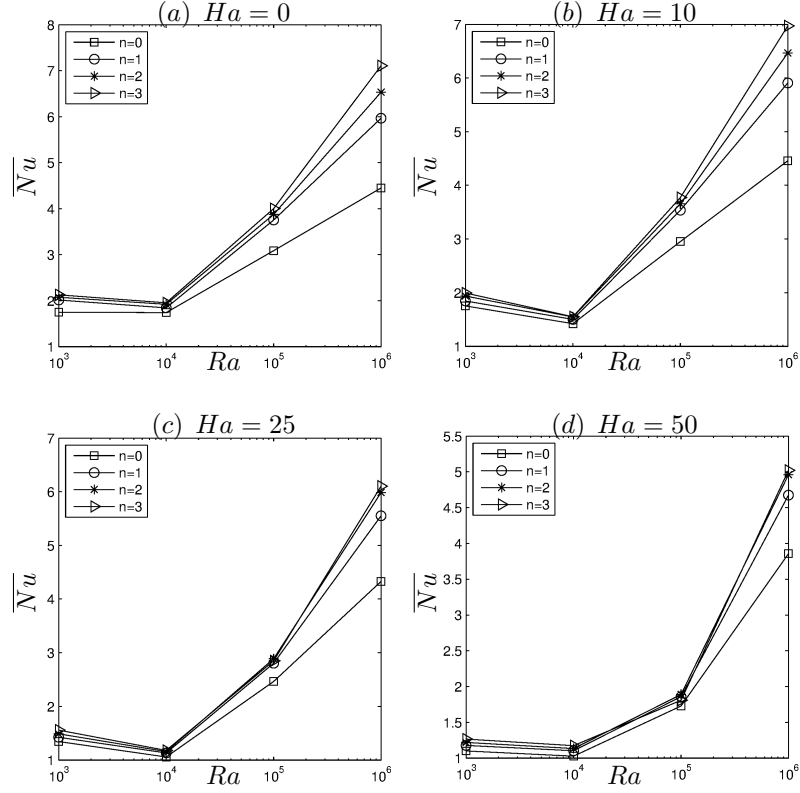


Figure 3.20: Variation of \overline{Nu} with Ra at different numbers of undulation n when $J = 0$: (a) $Ha = 0$, (b) $Ha = 10$, (c) $Ha = 25$, (d) $Ha = 50$.

In Figure 3.21 the variation of \overline{Nu} along the hot wall of $n = 3$ undulations with Hartmann and Rayleigh numbers are shown. The average Nusselt number varies similar to the cases of rectangular and circular heaters (see Figure 3.8). That is, \overline{Nu} decreases as Ha increases at each Ra and \overline{Nu} increases as Ra increases from 10^4 to 10^6 at each Ha . However, as mentioned before as Ra increases from $Ra = 10^3$ to $Ra = 10^4$, the \overline{Nu} decreases especially for $Ha \geq 10$ since at the transition regime from conduction to convection (i.e. $Ra = 10^4$), the buoyancy force is not strong enough to resist the magnetic field. Thus, the heat transfer rate reduces. Moreover, the rate of decrease in \overline{Nu} increases as Ra increases.

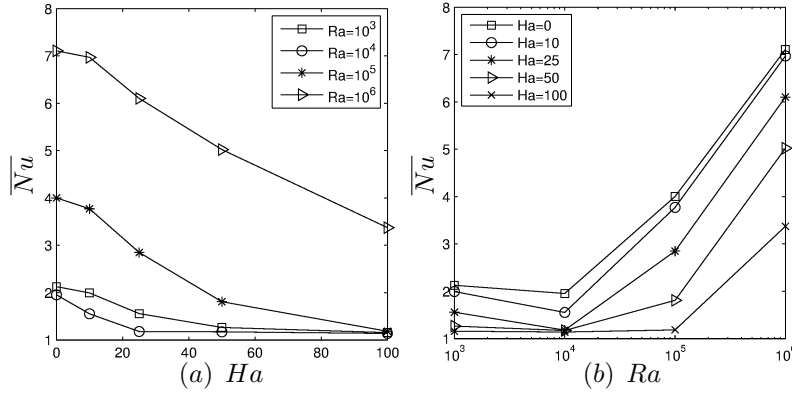


Figure 3.21: Effects of (a) Ha and (b) Ra on \overline{Nu} at $n = 3$.

3.4 Unsteady MHD Mixed Convection Flow in a Lid-Driven Cavity with Sinusoidal Heater

This section provides a detailed investigation of the numerical solution to the unsteady MHD mixed convection flow in a lid-driven cavity with a sinusoidal hot right wall subjected to a uniform inclined magnetic field. The equations governing this problem and the application of combined numerical technique of DRBEM in space with a two-level integration in time are given respectively in Section 3.1 and Section 3.2 in details. The shape of the sinusoidal wall is defined by $x = 1 - A[1 - \cos(2n\pi y)]$ as given in Section 3.3.3. The physical configuration of the problem is displayed in Figure 3.22.

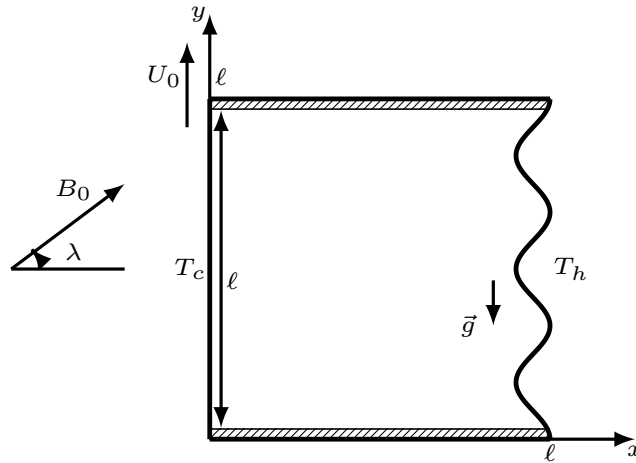


Figure 3.22: Geometry of the unsteady problem for sinusoidal hot wall

The characteristics of the flow field and temperature distribution are investigated in

order to understand the impact of Hartmann number ($Ha = 0, 25, 50$), Rayleigh number ($Ra = 10^3, 10^4, 10^5$), Joule heating parameter ($J = 0, 1, 3, 5$), inclination angle ($\lambda = 0, \frac{\pi}{6}, \frac{\pi}{4}, \frac{\pi}{2}$) and number of undulation ($n = 0, 1, 2, 3$) by keeping the amplitude of sinusoidal wall, Reynolds and Prandtl numbers fixed as $A = 0.05$, $Re = 100$ and $Pr = 0.71$, respectively. It is observed from Figure 3.23 for the case when $Ha = 50$, $Ra = 10^5$, $J = 1$, $n = 3$ and $\lambda = 0$ the grid of $N \approx 400$ constant boundary elements ensures the grid independence, and hence it is used in the subsequent computations. As in the previous sections, in all computations the GCL points are taken as interior points and the linear polynomial type radial basis functions are used through the DRBEM application. Moreover, the validity of the code has already been ascertained in Section 3.3.3 for the test problem given in the work of Al-Amiri [1].

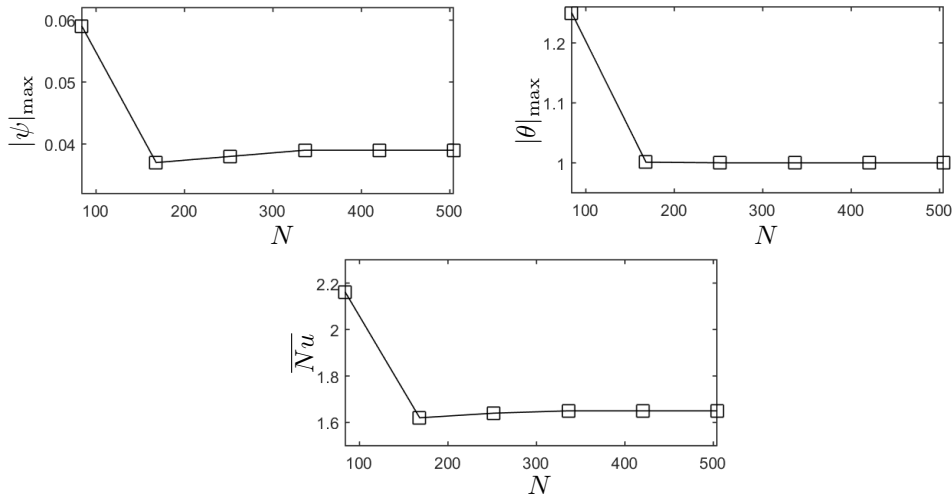


Figure 3.23: Grid dependency: $Ra = 10^5$, $Ha = 50$, $J = 1$, $n = 3$ and $\lambda = 0$.

First, the stability of the numerical method is investigated in details for different time increments and relaxation parameters by considering $\beta_{\omega} = \beta_{\theta} = \beta$ and $\beta_{\omega_q} = \beta_{\theta_q} = \beta_q$. Table 3.2 displays the relation between the maximum eigenvalues of the coefficient matrices and the relaxation parameters when $Ra = 10^4$, $Ha = 25$, $J = 1$, $\lambda = 0$ and the time step size $\Delta t = 0.8$. One can observe that as the relaxation parameters β and β_q decrease, the spectral radius of vorticity and temperature decrease. But, when $\beta = \beta_q = 0.6$ only 1 of the 6 requested eigenvalues converges, and the method becomes unstable with a further decrease to $\beta = \beta_q = 0.5$. Depending on the results of the Table 3.2, the optimum relaxation parameter is $\beta = \beta_q = 0.7$ when $Ra = 10^4$, $Ha = 25$, $J = 1$ and $\lambda = 0$.

Table 3.2: Spectral radius of vorticity and temperature equations: $Ra = 10^4$, $Ha = 25$, $\Delta t = 0.8$, $J = 1$, $\lambda = 0$, $\epsilon = 10^{-4}$.

β, β_q	spectral radius for vorticity	spectral radius for temperature
0.9	0.83139	0.87018
0.8	0.82744	0.86767
0.7	0.82441	0.86407
0.6	0.82127 (only 1 of the 6 req. eig. con.)	0.86492
0.5	-	-

Table 3.3 indicates the spectral radius of coefficient matrices for several time increments when $Ra = 10^4$ and $Ha = 25$, $J = 1$, $\lambda = 0$ by fixing $\beta = \beta_q = 0.7$. It can be seen that, increasing time increment leads to a decrease on maximum eigenvalues of vorticity and temperature, and reduces the number of iterations required to reach the steady-state. However, when $\Delta t = 0.9$ and $\Delta t = 1$ only 5 and 3 of the 6 requested eigenvalues converge, respectively. Hence, the optimum time increment for $Ra = 10^4$, $Ha = 25$, $J = 1$, $\lambda = 0$ with $\beta = \beta_q = 0.7$ is $\Delta t = 0.8$.

Table 3.3: Spectral radius of vorticity and temperature equations: $Ra = 10^4$, $Ha = 25$, $J = 1$, $\lambda = 0$, $\beta = \beta_q = 0.7$, $\epsilon = 10^{-4}$.

Δt	spectral radius for vorticity	spectral radius for temperature
0.5	0.88495	0.91312
0.6	0.86413	0.897
0.7	0.84396	0.88126
0.8	0.82441	0.86589
0.9	0.80545 (only 5 of the 6 req. eig. con.)	0.85088
1	0.78706 (only 3 of the 6 req. eig. con.)	0.83621

On the other hand, Table 3.4 shows the relation between spectral radius of coefficient matrices according to the different values of relaxation parameters for vorticity ($\beta_\omega = \beta_{\omega_q}$) and temperature ($\beta_\theta = \beta_{\theta_q}$) at $Ra = 10^4$, $Ha = 25$, $J = 1$, $\lambda = 0$, $\Delta t = 0.8$. It is well observed that, when the relaxation parameter for vorticity $\beta_\omega, \beta_{\omega_q}$ decreases and

the relaxation parameter for temperature $\beta_\theta, \beta_{\theta_q}$ increases, the maximum eigenvalue of coefficient matrices decrease and they reach the minimum (i.e. optimal) value when $\beta_\omega = \beta_{\omega_q} = \beta_\theta = \beta_{\theta_q} = 0.7$, as shown in Table 3.2. However, when $\beta_\omega = \beta_{\omega_q} = 0.6$ and $\beta_\theta = \beta_{\theta_q} = 0.9$ only 1 of the 6 requested eigenvalues of vorticity, and only 3 of 6 requested eigenvalues of temperature converge. Further, when $\beta_\omega = \beta_{\omega_q} = 0.5$ and $\beta_\theta = \beta_{\theta_q} = 0.9$, the method becomes unstable.

Table 3.4: Spectral radius of vorticity and temperature equations: $Ra = 10^4$, $Ha = 25$, $\Delta t = 0.8$, $J = 1$, $\lambda = 0$, $\epsilon = 10^{-4}$.

$\beta_\omega, \beta_{\omega_q}$	$\beta_\theta, \beta_{\theta_q}$	spectral radius for vorticity	spectral radius for temperature
0.9	0.5	-	1
0.9	0.6	0.83037	0.8694
0.8	0.7	0.82744	0.86767
0.7	0.8	0.82441	0.86589
0.7	0.7	0.82441	0.86407
0.6	0.9	0.82127 (only 1 of the 6 req. eig.)	0.86407 (only 3 of the 6 req. eig.)
0.5	0.9	-	1

The stability of the DRBEM discretization with a two-level time integration is further checked for various values of Ra and Ha numbers by the choice of optimal values obtained for $\Delta t = 0.8$ and relaxation parameters $\beta = \beta_q = 0.7$. It is well observed from Tables 3.5 and Table 3.6 that these choices are also valid for various values of $Ra(= 10^3, 10^4, 10^5)$ and $Ha(= 10, 25, 50)$, that is they satisfy the stability conditions. Thus, in the following computations, the optimal values ($\beta = \beta_q = 0.7$ and $\Delta t = 0.8$) are used to guarantee the stability of the numerical method.

Table 3.5: Spectral radius of vorticity and temperature equations for several Ra : $Ha = 25$, $J = 1$, $\lambda = 0$, $\beta = \beta_q = 0.7$, $\Delta t = 0.8$, $\epsilon = 10^{-4}$.

Ra	spectral radius for vorticity	spectral radius for temperature
10^3	0.82203	0.85205
10^4	0.82441	0.86589
10^5	0.84268	0.83932

Table 3.6: Spectral radius of vorticity and temperature equations for several Ha :
 $Ra = 10^4$, $J = 1$, $\lambda = 0$, $\beta = \beta_q = 0.7$, $\Delta t = 0.8$, $\epsilon = 10^{-4}$.

Ha	spectral radius for vorticity	spectral radius for temperature
10	0.81927	0.85176
25	0.82441	0.86589
50	0.84356	0.87734

Figure 3.24 displays the variation of the stream function, vorticity and temperature along (a) the vertical centerline ($x = 0.5$, $0 \leq y \leq 1$) and (b) the horizontal centerline ($y = 0.5$, $0 \leq x \leq 1$), respectively, at different time levels $t = 1, 3, 5, 10, 20, 50$ when $Ha = 25$, $Ra = 10^4$ and $\Delta t = 0.8$. In general, as time advances, the values of ψ , ω and θ increase and converge to the steady-state both along the vertical and horizontal centerlines. The temperature increases along the horizontal centerline as expected since the left wall is cold while the right wall is heated. Thus, in the subsequent figures, the streamlines and isotherms are drawn at steady-state and the average Nusselt number is calculated when the temperature reaches its steady-state.

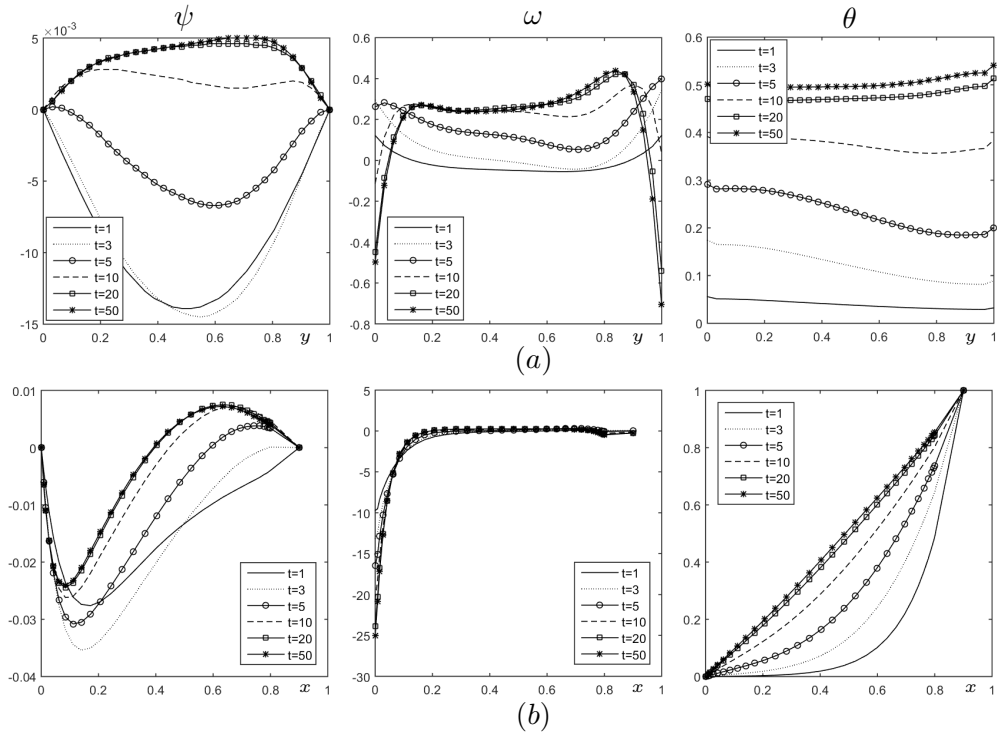


Figure 3.24: Time evolution of ψ , ω , θ along (a) vertical centerline $x = 0.5$, and (b) horizontal centerline $y = 0.5$: $Ra = 10^4$, $Ha = 25$, $\Delta t = 0.8$, $J = 1$ and $\lambda = 0$.

The steady-state streamlines and isotherms are drawn in Figure 3.25 and Figure 3.26, respectively, at $Ha(= 0, 25, 50)$ and $Ra = (10^3, 10^4, 10^5)$ when the number of undulation $n = 3$ under the horizontal magnetic field ($\lambda = 0$) and $J = 1$. As expected, the obtained results are similar with the steady case given in Section 3.3.3 in Figures 3.18 and 3.19 when $J = 0$. Consideration of the effect of Joule heating results in a slight decrease in the magnitude of ψ at each combination of Ra and Ha numbers while the temperature of the fluid inside the cavity increases with the additional heating due to Joule heating at $J = 1$. In addition, the formation of thermal boundary layer along the left vertical wall, which indicates that the temperature gradients are strong in this region, becomes more observable at $Ra = 10^5$ when $J = 1$ compared to the case when $J = 0$. However, Ha has an opposite effect on isotherms, that is, as Ha increases the conduction contribution to the overall heat transfer enlarges and the thermal boundary layer becomes weaker while the isotherms become vertical.

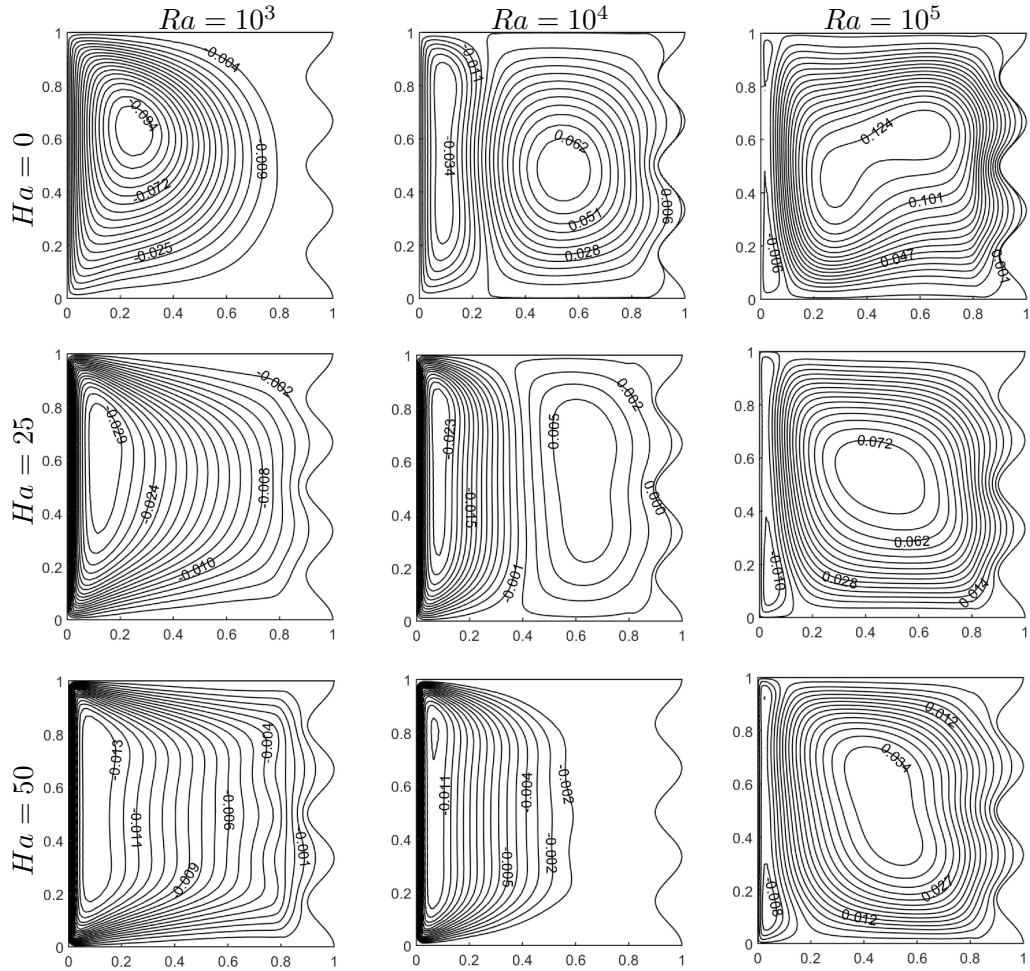


Figure 3.25: Effects of Ha and Ra on streamlines: $n = 3$, $\lambda = 0$, $J = 1$.

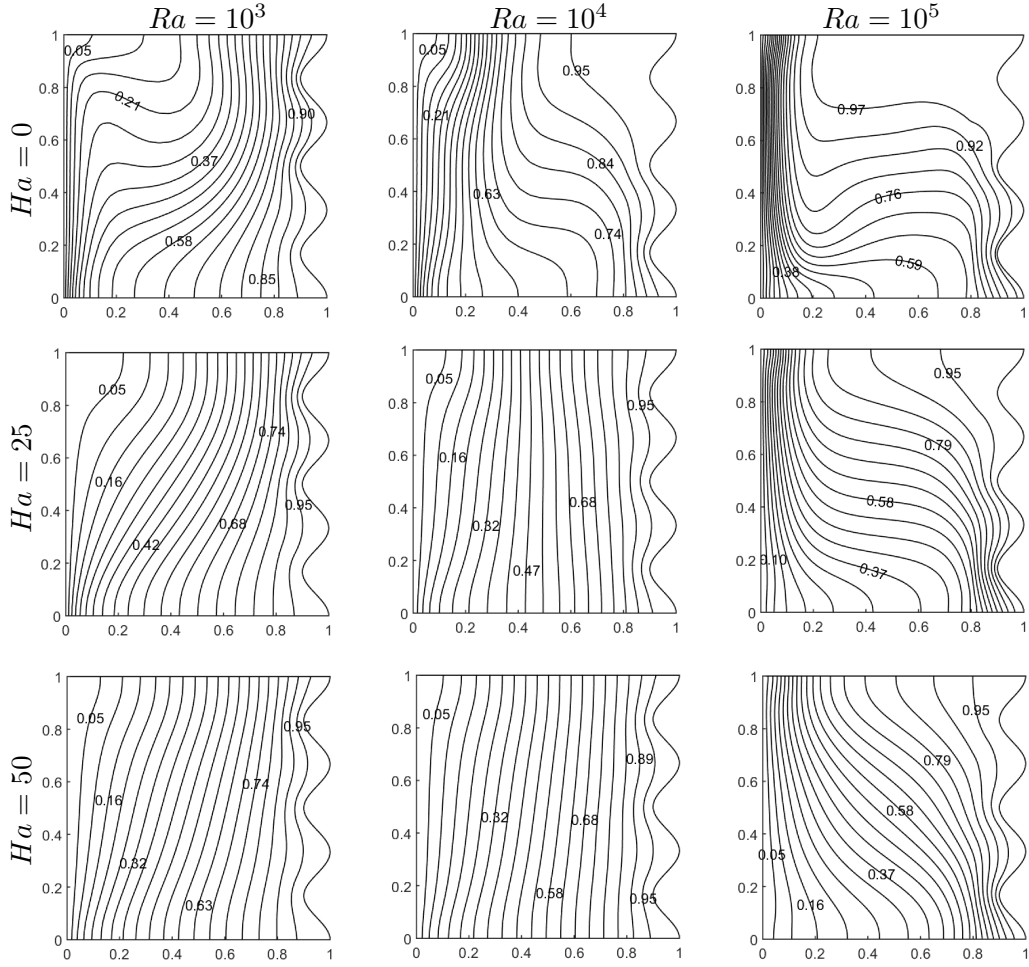


Figure 3.26: Effects of Ha and Ra on isotherms: $n = 3$, $\lambda = 0$, $J = 1$.

The impact of varying Joule heating parameter on hydrodynamic and the thermal fields is further displayed in Figure 3.27 and Figure 3.28, respectively, for $Ra = 10^3$, 10^4 , 10^5 at a fixed $Ha (= 10)$, when $n = 3$ and $\lambda = 0$. At the conduction regime when $Ra = 10^3$, there is no significant change on streamlines for each J , however, a small decrease in the strength of positive vortex is observed with an increase in J at $Ra = 10^4$. On the other hand, at the highest $Ra = 10^5$, when $J = 0$ two counter rotating vortices are observed inside the streamline profile as in the case when $J = 1$ (see Figure 3.25). However, with a further increase to $J = 3$, a third negative eddy is formed at the upper right corner of the cavity close to wavy wall and this eddy becomes bigger and stronger as J increases to $J = 5$. Further, the positive vortex becomes weaker and shrinks diagonally as a result of the formation and development of the third vortex towards the left wall. Similar to streamlines, there is no significant effect of J on isotherms for low values of Ra ($= 10^3$ and 10^4). However, the

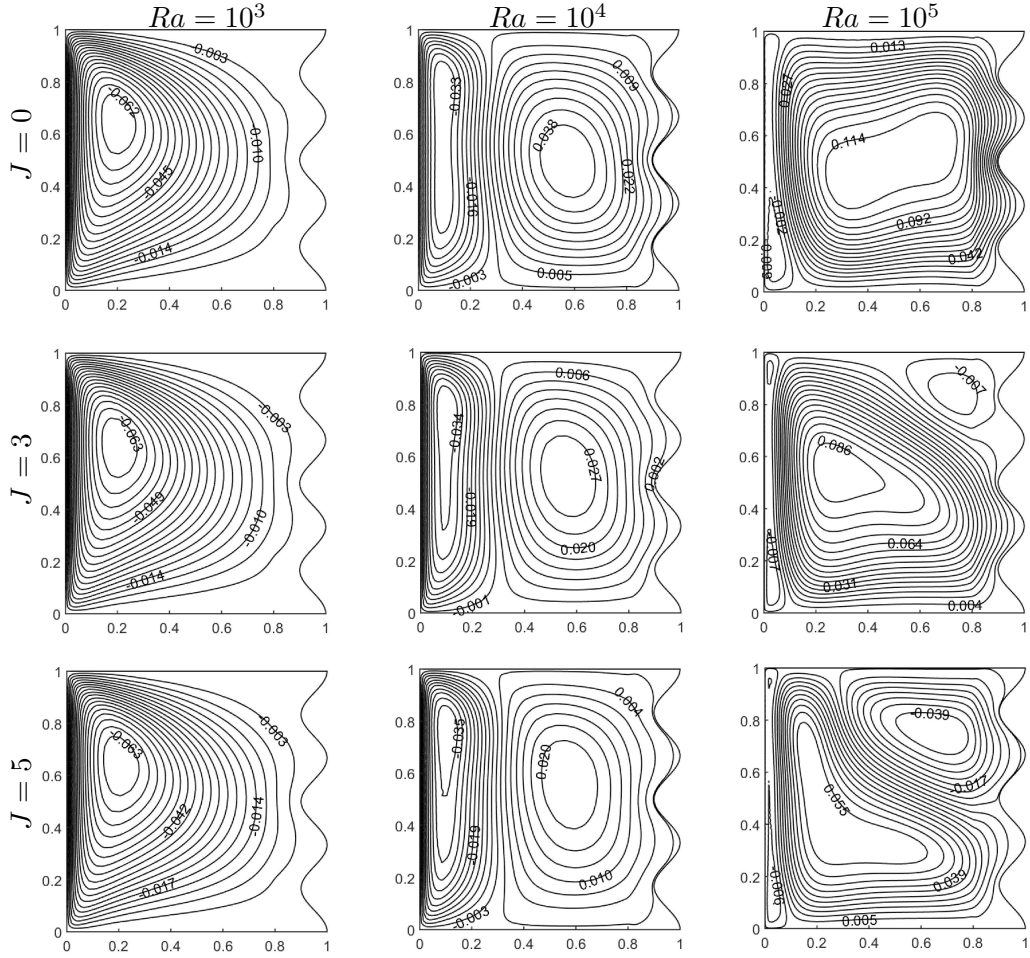


Figure 3.27: Effects of J and Ra on streamlines: $n = 3$, $\lambda = 0$, $Ha = 10$.

isotherms tend to move towards the left moving wall and start to form a boundary layer as J increases at $Ra = 10^3$, 10^4 . Finally, at the highest $Ra = 10^5$, the formation of thermal boundary layer along the left vertical wall becomes more observable and the temperature of the fluid increases following an increase in J at the convection dominant mode. Moreover, when we compare the results at $Ra = 10^5$ with the rectangular/circular heaters (see Figures 3.7 and 3.14) it is observed that both the strength of ψ and the temperature of the fluid increase when the right wall is sinusoidal at each J .

The influence of the inclination angle of magnetic field λ on the velocity and the temperature fields is shown in Figure 3.29 and Figure 3.30, respectively, when $n = 3$, $Ha = 10$ and $J = 1$. At $Ra = 10^3$ and $Ra = 10^4$, there is no significant change in the profiles of streamlines and isotherms as λ increases from $\pi/6$ to $\pi/2$. However, at $Ra = 10^5$, the main positive vortex moves towards the left bottom corner of the

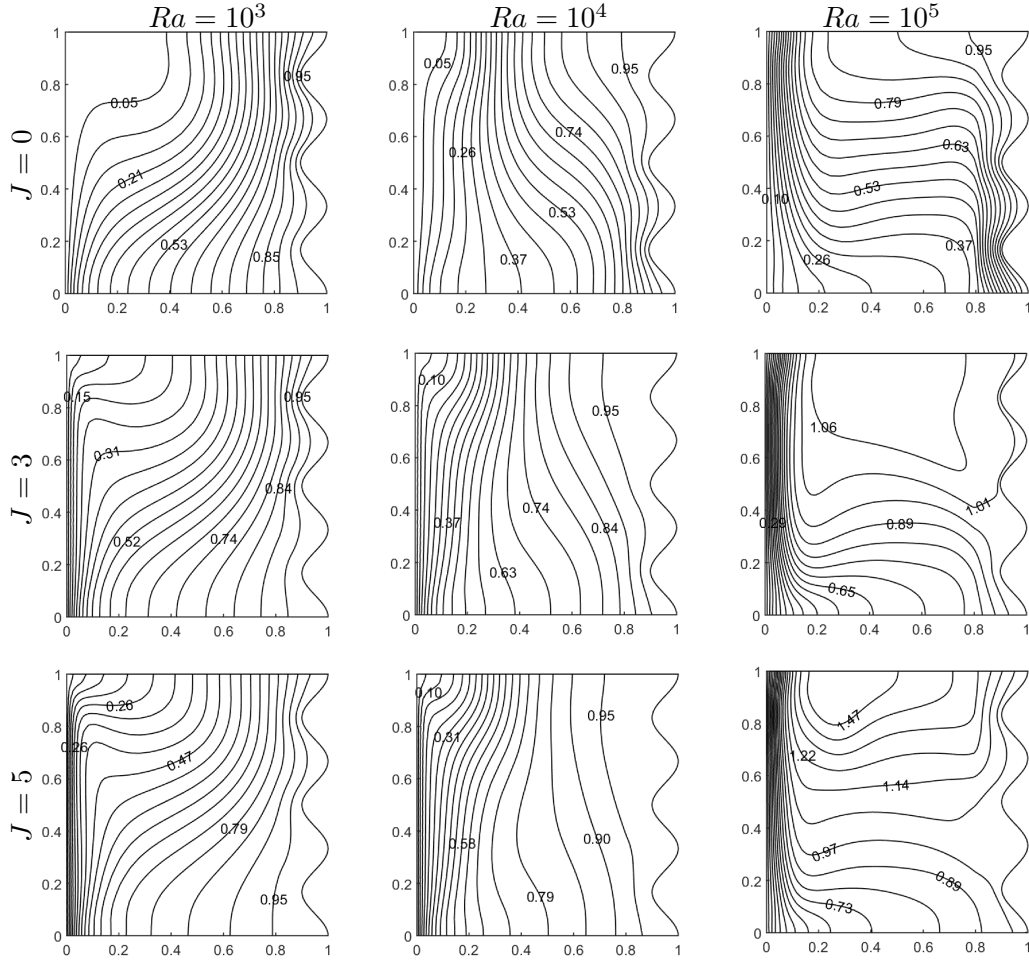


Figure 3.28: Effects of J and Ra on isotherms: $n = 3$, $\lambda = 0$, $Ha = 10$.

cavity and becomes circular with an increase in λ . Moreover, the strength of the positive vortex increases at $Ra = 10^4$, 10^5 as λ increases. On the other hand, at $Ra = 10^5$, the isotherms move upwards following an increase in the temperature inside the cavity as λ increases to $\pi/2$.

Further, the effect of the number of undulation on the flow structure and heat transfer characteristics is demonstrated in Figure 3.31 and Figure 3.32, respectively when $Ha = 10$, $J = 1$ and $\lambda = 0$. It is observed that at a fixed Ra both the velocity and thermal fields remain almost similar throughout the cavity except the region close to the right vertical wall where both streamlines and isotherms comply with the profile of the wavy wall.

In the rest of this section, the heat transfer rate is investigated in terms of the average Nusselt number along the hot wavy wall at various combinations of problem param-

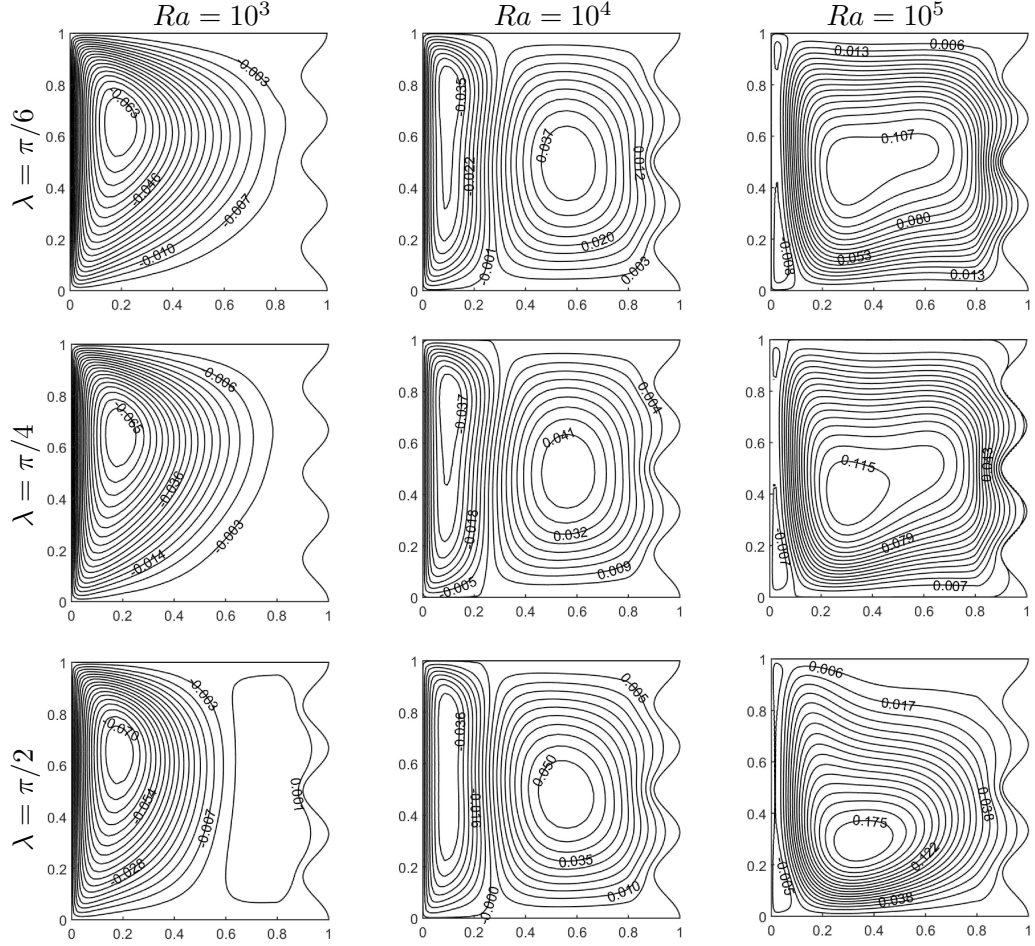


Figure 3.29: Effects of λ and Ra on streamlines: $n = 3$, $Ha = 10$, $J = 1$.

eters. In Figure 3.33, the variation of average Nusselt number on the heated wall with Hartmann and Rayleigh numbers are displayed for the cavity with a right wavy wall of $n = 3$ undulations at $J = 0$. The average Nusselt number increases as Ra increases from $Ra = 10^4$ to $Ra = 10^5$ at each Ha since the heat transfer is due to the convection. However, \overline{Nu} decreases as Ra increases from $Ra = 10^3$ to $Ra = 10^4$ especially for $Ha \geq 10$. The reason for this phenomena is that at $Ra = 10^4$, namely at the transition regime from conduction to convection, the buoyancy force is not strong enough to resist the magnetic field, and hence the heat transfer rate reduces. On the other hand, the average Nusselt number decreases as Ha increases at each Ra . Moreover, the rate of decrease in \overline{Nu} increases with an increase in Ra . Further, we investigate the effect of Ra and Ha numbers on \overline{Nu} along the hot wavy wall taking into account the Joule heating parameter, i.e. $J = 1$ when $n = 3$ (see Figure 3.34). Similar to the case when $J = 0$, \overline{Nu} decreases as Ra increases from 10^3 to 10^4 , while \overline{Nu} increases as Ra increases from 10^4 to 10^5 for each Ha . However, by the Joule

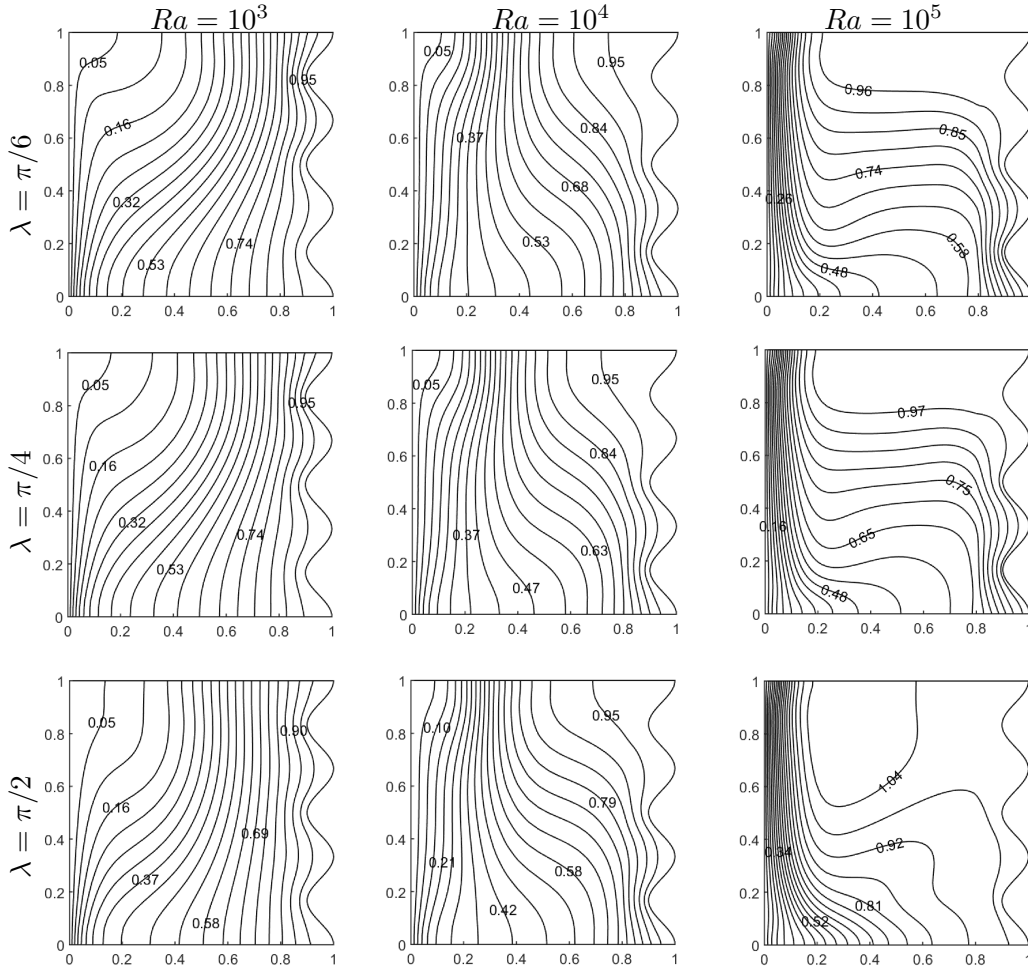


Figure 3.30: Effects of λ and Ra on isotherms: $n = 3$, $Ha = 10$, $J = 1$.

effect, \overline{Nu} increases with an increase in Ha for $Ha < 25$ when $Ra = 10^4$, $Ra = 10^5$ while \overline{Nu} decreases when $J = 0$. Moreover, for $Ha \geq 25$, \overline{Nu} starts to decrease in the conduction ($Ra = 10^3$) and convection ($Ra = 10^5$) modes, while increasing Ha have no significant effect on \overline{Nu} at the transition regime when $Ra = 10^4$.

In order to see the further effect of Joule heating parameter on the average Nusselt number along the hot wavy wall, Figure 3.35 is drawn by fixing (a) $Ra = 10^5$ and (b) $Ha = 10$. An increase in J results in a decrease in \overline{Nu} since the temperature inside the cavity becomes higher than the temperature of the wall. In the conduction mode between $Ra = 10^3$ and $Ra = 10^4$, \overline{Nu} decreases irrespective of values of J . However, when the convection becomes dominant with a further increase in Ra to 10^5 for low $J(= 0, 1)$ \overline{Nu} increases whereas for higher $J(= 3, 5)$ the average Nusselt number along the hot wall continues to decrease indicating the suppressive effect of J on the heat transfer rate at the convection mode. On the other hand, as Ha increases to

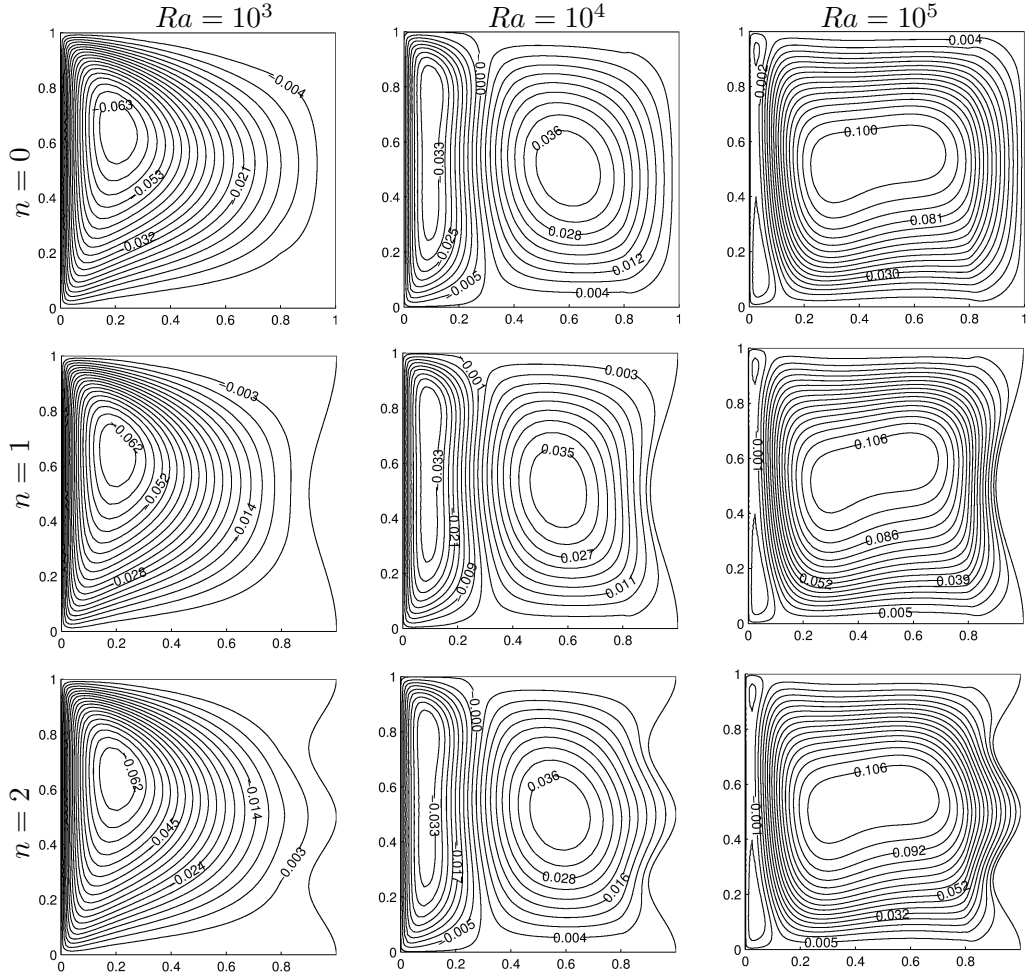


Figure 3.31: Effects of n and Ra on streamlines: $Ha = 10$, $\lambda = 0$, $J = 1$.

25 the average Nusselt number increases by the Joule effect. However, after $Ha = 25$ for $J = 0, 1$ average Nusselt number starts to decrease with an increase in Ha while it continues to increase for higher values of $J(= 3, 5)$. Thus, a strong Joule heating parameter has a reverse effect on the variation of \overline{Nu} with increasing Ha and Ra .

The effect of the shape of the wavy wall determined by different numbers of undulation ($n = 0, 1, 2, 3$) is analyzed in terms of the average Nusselt number along the hot wall. The variation of \overline{Nu} with n at (a) $Ha = 0$, (b) $Ha = 10$, (c) $Ha = 25$, (d) $Ha = 50$ is displayed for different values of $Ra(= 10^3, 10^4, 10^5)$ at a fixed $J = 0$ in Figure 3.36 and for different values of $J(= 0, 1, 3)$ at a fixed $Ra = 10^3$ in Figure 3.37, respectively. It is well observed from figures that an increase in n results in an increase in \overline{Nu} at each combination of the values of Ha , Ra and J , which indicates the enhancement of the heat transfer rate following an increase in the length of the heated surface. The increase rate in \overline{Nu} with n is higher in the convection regime at

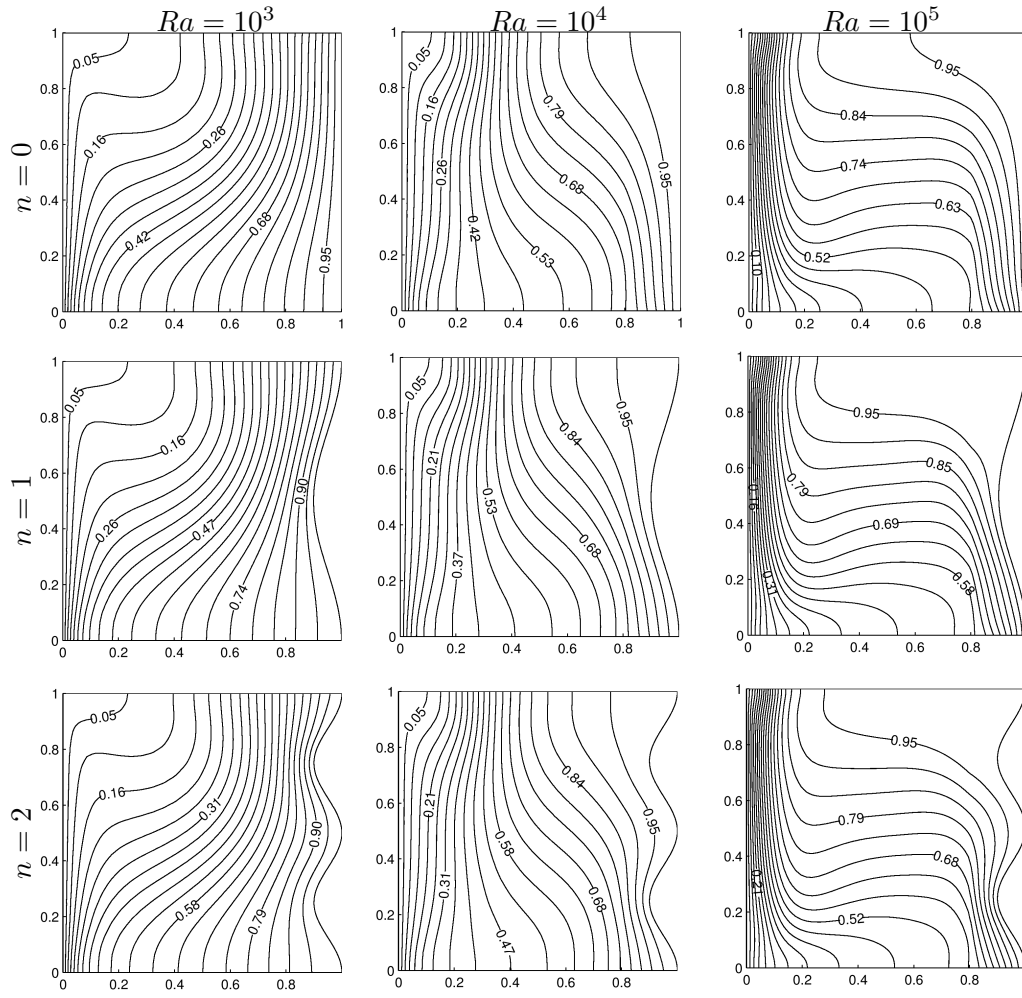


Figure 3.32: Effects of n and Ra on isotherms: $Ha = 10$, $\lambda = 0$, $J = 1$.

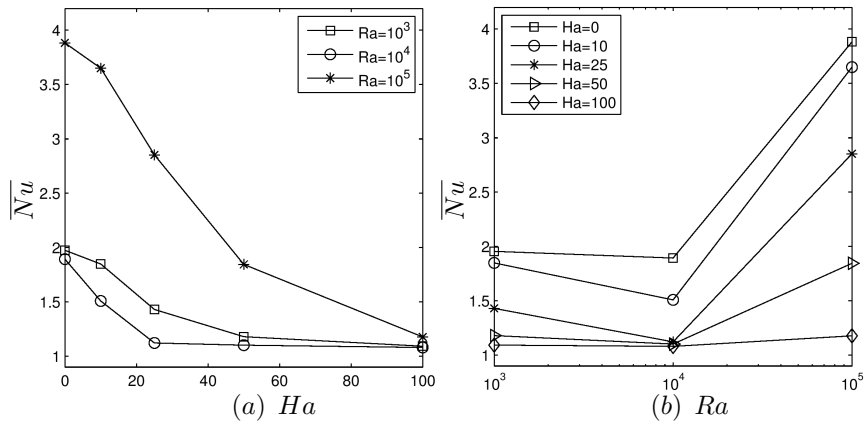


Figure 3.33: Effects of (a) Ha and (b) Ra on \overline{Nu} : $n = 3$, $J = 0$, $\lambda = 0$.

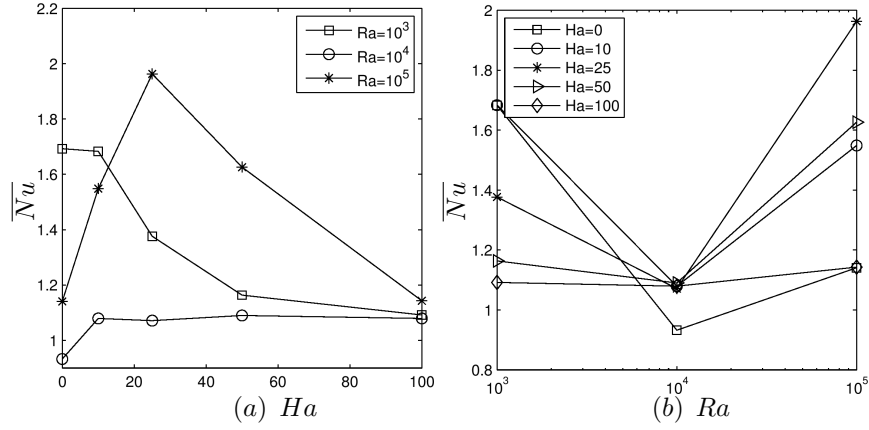


Figure 3.34: Effects of (a) Ha and (b) Ra on \overline{Nu} : $n = 3$, $J = 1$, $\lambda = 0$.

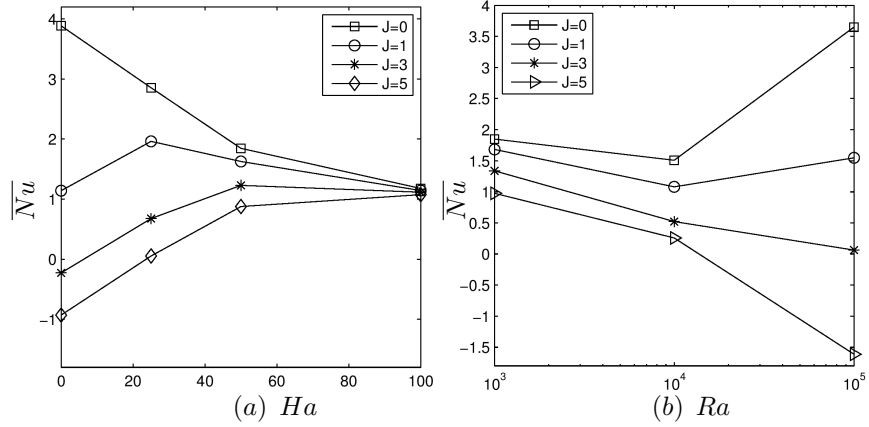


Figure 3.35: Effect of J on \overline{Nu} at $n = 3$, $\lambda = 0$ by fixing (a) $Ra = 10^5$, (b) $Ha = 10$.

$Ra = 10^5$ when compared with the ones in the conduction and transition regimes at $Ra = 10^3, 10^4$. Moreover, \overline{Nu} decreases when the flow is transferred from conducting regime ($Ra = 10^3$) to the transition regime ($Ra = 10^4$) while it increases with a further increase in Ra to 10^5 regardless of the values of n and Ha (see Figure 3.36). On the other hand, Figure 3.37 displays that Joule effect results in a decrease in \overline{Nu} at each Ha in the conduction regime irrespective of the geometry of the problem domain. As mentioned previously, this occurs since the temperature inside the cavity becomes higher than the temperature of the wavy wall. It is also observed from both of the figures that an increase in the strength of the magnetic field leads to a general decrease in \overline{Nu} according to the given values of Ra , J and n .

Finally, variation of \overline{Nu} for various inclination angles λ with Ra at (a) $Ha = 10$ and (b) $Ha = 100$ is shown in Figure 3.38. When the conduction mode of heat transfer is

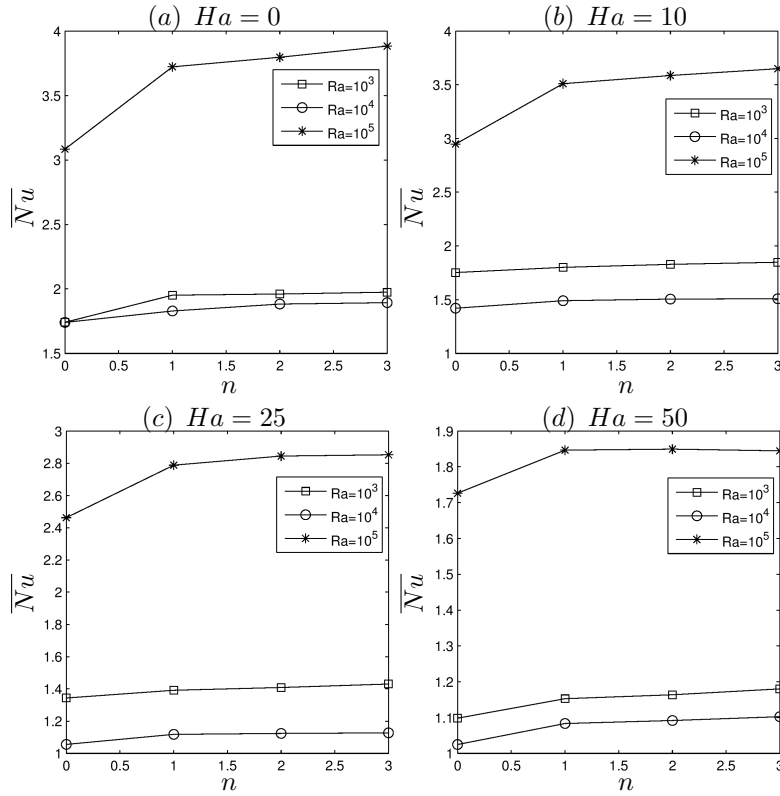


Figure 3.36: Variation of \overline{Nu} with n at $Ra = 10^3, 10^4, 10^5$ when $J = 0$, $\lambda = 0$: (a) $Ha = 0$, (b) $Ha = 10$, (c) $Ha = 25$, (d) $Ha = 50$.

dominant (i.e. $Ra = 10^3$), it is clearly seen that the average Nusselt number decreases by increasing inclination angle of magnetic field for both $Ha = 10$ and $Ha = 100$. On the other hand, in the convection mode (i.e. $Ra = 10^5$), \overline{Nu} slightly increases as λ increases from 0 to $\frac{\pi}{2}$ when $Ha = 10$ while a significant increase in \overline{Nu} is observed when $Ha = 100$. In the transition regime ($Ra = 10^4$), at $Ha = 10$ the average Nusselt number increases by increasing values of angle of inclination λ , however, at $Ha = 100$ no change is observed in \overline{Nu} with a variation in λ . To conclude for small $Ha = 10$, the effect of inclination angle on the \overline{Nu} is more pronounced in conduction and transition regimes (i.e. $Ra = 10^3, 10^4$), whereas at $Ha = 100$ its effect is well observed at the convection regime when $Ra = 10^5$. Thus, for high values of Ha which causes a reduction in \overline{Nu} to increase the heat transfer rate the magnetic field can be applied horizontally to the hot wall i.e. $\lambda = \pi/2$.

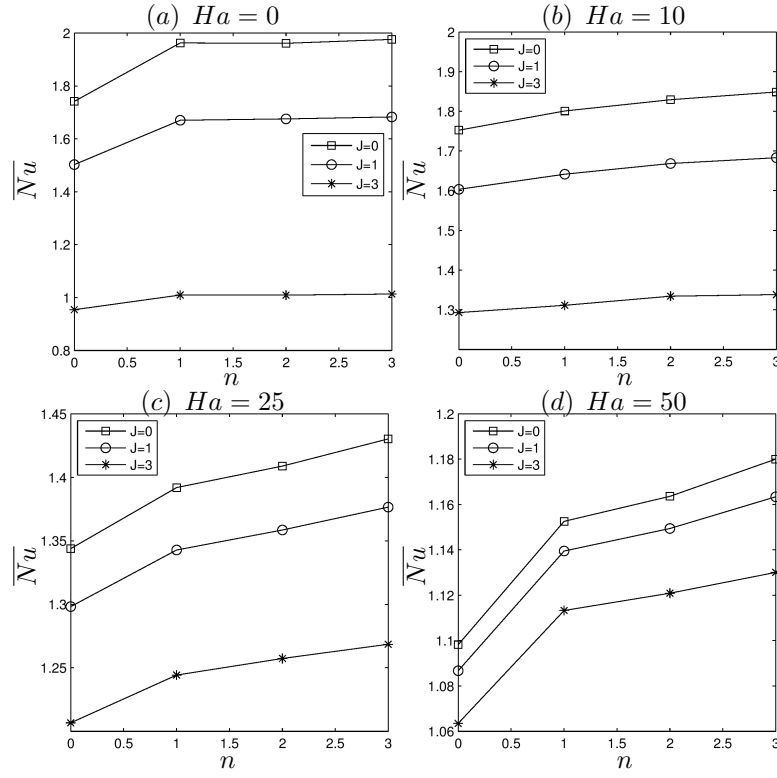


Figure 3.37: Variation of \overline{Nu} with n at $J = 0, 1, 3$ when $Ra = 10^3$, $\lambda = 0$: (a) $Ha = 0$, (b) $Ha = 10$, (c) $Ha = 25$, (d) $Ha = 50$.

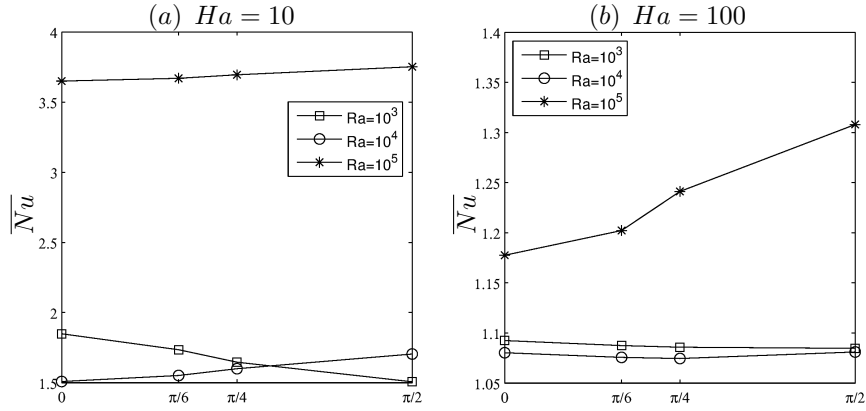


Figure 3.38: Variation of \overline{Nu} with Ra at different inclination angles of magnetic field λ when $J = 0$, $n = 3$: (a) $Ha = 10$, (b) $Ha = 100$.

3.5 Summary of the Results Obtained in Chapter 3

To conclude, in the present chapter the effects of both number and shape of the heat sources on the flow and temperature fields are investigated for several values of physical parameters and are displayed in terms of streamlines, isotherms and average Nus-

selt number. It is observed that:

- As Hartmann number increases, the strength of stream function decreases in magnitude due to the retarding effect of the magnetic field on the fluid flow, further, the isotherms become more parallel to vertical walls because of the dominance of conduction on heat transfer.
- When the Rayleigh number increases, the flow becomes convection dominated which leads the isotherms change their profiles from being vertical to almost horizontal at the center of the cavity forming a thermal boundary layer along the vertical walls.
- An increase in Joule heating parameter reduces the magnitude of stream function whereas temperature of the fluid inside the cavity increases.
- The inclination angle of magnetic field λ has no significant effect on the streamline and isotherm profiles, however, at $Ra = 10^5$, as λ increases, the main vortex moves towards the left bottom corner of the cavity, becomes circular, and also its strength increases. On the other hand, the isotherms move upwards following an increase in the temperature inside the cavity.
- Hartmann number has a negative effect on \overline{Nu} , that is, \overline{Nu} decreases with an increase in Ha irrespective of values of Ra at $J = 0$. However, when $J = 1$, the heat transfer rate increases with an increases in Ha for $Ha \leq 25$ at each Ra , which is observed for all heater types.
- The \overline{Nu} increases, when $Ra \geq 10^4$ since the heat transfer becomes dominated by convection for higher values of Ra . However, \overline{Nu} decreases as Ra increases from $Ra = 10^3$ to 10^4 at each Ha , since the flow is transferred from conduction regime to transition regime, which occurs irrespective of the types of heater.
- For all types of heater, as J increases, the temperature inside the cavity becomes higher than the wall temperature, thus \overline{Nu} along the hot wall decreases.
- Insertion of a circular and rectangular heater instead of a flat heater to the system makes no significant difference on streamline and isotherm profiles, but it is observed that the average Nusselt number increases when the length of the heated portion on the right wall increases in the case of rectangular heater.

- It is observed that, the effect of the number of undulation has no significant change on the profiles of streamlines and isotherms except the right wall where both streamlines and isotherms comply with the profile of the wall.
- However, an increase in the number of undulation results in increase in \overline{Nu} at each Ha and Ra and J as a result of an enhancement of the heat transfer rate following an increase in the length of the heated surface.
- All these results indicate that the strength of the magnetic field and the shape of the computational domain play an important role on the flow and heat transfer, thus these can be used to control the fluid flow and temperature distribution in an enclosure.

CHAPTER 4

NATURAL CONVECTION FLOW IN SEMI-ANNULUS ENCLOSURES FILLED WITH WATER-BASED NANOFLUIDS UNDER THE EFFECT OF UNIFORM MAGNETIC FIELD

The natural convection and heat transfer in enclosures under the influence of a magnetic field have a wide range of application areas in engineering and industry as mentioned in Introduction. On the other hand, there has been a considerable amount of interest on the engineering applications related to the nanotechnology due to the suitability of the nanofluids in the convective heat transfer phenomena. The nanofluids are the fluids obtained by incorporating small-sized particles called nanoparticles (e.g. metals, carbides or oxides) into base fluids (e.g. water, oil or ethylene glycol). Thus, the resulting nanofluid has a higher thermal conductivity compared to conventional fluids, which plays an important role on the enhancement of the heat transfer rate inside the enclosure. Thus, it is not only interesting but also significant to investigate the convective heated flows in enclosures filled with nanofluids in the presence of uniform magnetic field to control the flow behavior and to improve the heat transfer capacitance inside the enclosures of especially irregular shapes with various thermal boundary conditions. Thus, the present chapter is devoted to consider the dual reciprocity BEM solution of steady/unsteady two-dimensional laminar flow of an incompressible, viscous and electrically conducting nanofluid in semi-annulus with either circular or sinusoidal wavy inner walls subject to an externally applied uniform magnetic field. The physical problem and its mathematical model are introduced in Section 4.1, and then the application of the numerical method which is the combination of DRBEM in space and the two-level scheme in time to the problem under consideration is explained briefly in Section 4.2. The numerical simulations are carried out in a semi-annulus with a circular or sinusoidal inner wall in the presence

of a uniform inclined magnetic field in order to analyze the effects of these on the natural convective heat transfer. First, the steady MHD natural convection flow in an inclined channel of semi-circular cross-section with an inner wall involving constant heat flux is solved in Section 4.3. Later, the unsteady case is considered in a more complex problem domain enclosed by a semi-annulus with a sinusoidal inner wavy wall and the stability analysis of the numerical method is performed in Section 4.4.

4.1 Governing Equations for the Unsteady MHD Natural Convection Nanofluid Flow

In this section, the governing equations for the unsteady magnetohydrodynamic natural convection nanofluid flow and the heat transfer in two-dimensional geometries filled with water-based nanofluid under the effect of a uniform inclined magnetic field are presented. The applied magnetic field makes an angle λ with the x -axis and the gravity acts in the negative y -direction. The radiation, viscous dissipation and Joule heating are neglected. The induced magnetic field can also be neglected in comparison to the applied magnetic field since the magnetic Reynolds number is assumed to be too small. The nanofluid is supposed to be Newtonian and incompressible; the flow is unsteady, laminar and two-dimensional. The nanofluid has constant thermophysical properties and obeys the Boussinesq approximation. The thermal equilibrium is assumed between the nanoparticles (Cu) and the base fluid (water). Under the light of these assumptions the governing equations of unsteady, laminar, incompressible flow of a viscous and electrically conducting nanofluid subjected to a uniform oblique magnetic field can be written in the non-dimensional stream function ψ , vorticity ω and temperature θ form as given in Chapter 1, Equations (1.51)-(1.54):

$$\nabla^2 \psi = -\omega \quad (4.1)$$

$$\begin{aligned} \nabla^2 \omega = & \frac{\mu_f \rho_{nf}}{\mu_{nf} \rho_f Pr_f} \left[\frac{\partial \omega}{\partial t} + u \frac{\partial \omega}{\partial x} + v \frac{\partial \omega}{\partial y} - Ra_f Pr_f \frac{\beta_{nf}}{\beta_f} \frac{\partial \theta}{\partial x} - Ha^2 Pr_f \frac{\sigma_{nf} \rho_f}{\sigma_f \rho_{nf}} \right. \\ & \left. \times \left(\left(\frac{\partial u}{\partial x} - \frac{\partial v}{\partial y} \right) \sin \lambda \cos \lambda - \frac{\partial v}{\partial x} \cos^2 \lambda + \frac{\partial u}{\partial y} \sin^2 \lambda \right) \right] \end{aligned} \quad (4.2)$$

$$\nabla^2 \theta = \frac{(\rho C_p)_{nf} k_f}{(\rho C_p)_f k_{nf}} \left(\frac{\partial \theta}{\partial t} + u \frac{\partial \theta}{\partial x} + v \frac{\partial \theta}{\partial y} \right) \quad (4.3)$$

where

$$\begin{aligned}
\frac{\mu_f \rho_{nf}}{\mu_{nf} \rho_f} &= (1 - \phi)^{2.5} \left[(1 - \phi) + \frac{\rho_s}{\rho_f} \phi \right], \quad \frac{\beta_{nf}}{\beta_f} = (1 - \phi) + \frac{\beta_s}{\beta_f} \phi, \\
\frac{\sigma_{nf} \rho_f}{\sigma_f \rho_{nf}} &= \left[1 + \frac{3(\frac{\sigma_s}{\sigma_f} - 1)\phi}{(\frac{\sigma_s}{\sigma_f} + 2)} - (\frac{\sigma_s}{\sigma_f} - 1)\phi \right] \frac{1}{(1 - \phi) + \frac{\rho_s}{\rho_f} \phi}, \\
\frac{(\rho C_p)_{nf} k_f}{(\rho C_p)_f k_{nf}} &= \left[(1 - \phi) + \frac{(\rho C_p)_s}{(\rho C_p)_f} \phi \right] \frac{k_s + 2k_f - 2\phi(k_f - k_s)}{k_s + 2k_f + \phi(k_f - k_s)}.
\end{aligned} \tag{4.4}$$

in which $\rho_f, \beta_f, \sigma_f, \rho(C_p)_f, k_f$ and $\rho_s, \beta_s, \sigma_s, \rho(C_p)_s, k_s$ represent the effective density, the thermal expansion coefficient, electrical conductivity, the heat capacitance, thermal conductivity of the fluid and solid particles, respectively. The solid volume fraction of nanoparticles is denoted by ϕ .

Equations (4.2)-(4.3) are subjected to initial conditions

$$\omega(x, y, 0) = \omega_0(x, y), \quad \theta(x, y, 0) = \theta_0(x, y),$$

where ω_0, θ_0 are known functions of space at $t = 0$. In the present numerical computations, the initial conditions for vorticity and temperature are taken as $\omega_0 = \theta_0 = 0$. The corresponding non-dimensional boundary conditions for stream function and temperature is going to be given for each problems in the related sections, and the unknown boundary conditions for the vorticity are derived from the stream function equation (4.1) by using radial basis function approximation through the application of dual reciprocity BEM as in Chapter 3, Section 3.1. Similarly, the average Nusselt number \overline{Nu} is evaluated by the formula given in Chapter 1, Equation (1.84) in which $Nu = \frac{k_{nf}}{k_f} \frac{1}{\theta}$.

Further, the nanoparticles (Cu) and the base fluid (water) are supposed to be in thermal equilibrium and their thermo-physical properties are given in Table 4.1 [86].

Table 4.1: Thermo-physical properties of water and nanoparticle [86]

	$\rho(kg/m^3)$	$C_p(j/kgK)$	$k(W/mk)$	$\beta(K^{-1})$	$\sigma(\Omega m)^{-1}$
Pure water	997.1	4179	0.613	21×10^{-5}	0.05
Copper(Cu)	8933	385	401	1.67×10^{-5}	5.96×10^7

4.2 Numerical Method and Stability Analysis

In this section, the application of the numerical method to the unsteady MHD natural convection nanofluid flow and its stability analysis is explained as in Section 3.2.1. Hence, in Section 4.2.1 the discretization of the Equations (4.1)-(4.3) by the combined technique of DRBEM and two-level time integration scheme is going to be explained. Then, the stability of the numerical method will be given in Section 4.2.2.

4.2.1 Application of DRBEM

When Equations (4.1)-(4.3) are weighted with the fundamental solution of Laplace equation $u^* = 1/2\pi \ln(\frac{1}{r})$ and the Divergence theorem is successively applied at two times, the following integral equations

$$c_i R_i + \int_{\Gamma} (q^* R - u^* \frac{\partial R}{\partial n}) d\Gamma = - \int_{\Omega} b_R u^* d\Omega \quad (4.5)$$

are obtained through the process of DRBEM as in the same way given in Section 3.2. Here, R is used to represent each unknown ψ , ω and θ and b_R denotes the right hand sides of the stream function, vorticity and temperature equations (4.1), (4.2) and (4.3), respectively, as

$$b_{\psi} = -\omega \quad (4.6)$$

$$b_{\omega} = \frac{\mu_f \rho_{nf}}{\mu_{nf} \rho_f Pr_f} \left[\frac{\partial \omega}{\partial t} + u \frac{\partial \omega}{\partial x} + v \frac{\partial \omega}{\partial y} - \frac{\beta_{nf}}{\beta_f} Ra_f Pr_f \frac{\partial \theta}{\partial x} - \frac{\sigma_{nf} \rho_f}{\sigma_f \rho_{nf}} Ha^2 Pr_f \left(\left(\frac{\partial u}{\partial x} - \frac{\partial v}{\partial y} \right) \sin \lambda \cos \lambda - \frac{\partial v}{\partial x} \cos^2 \lambda + \frac{\partial u}{\partial y} \sin^2 \lambda \right) \right] \quad (4.7)$$

$$b_{\theta} = \frac{(\rho C p)_{nf} k_f}{(\rho C p)_f k_{nf}} \left(\frac{\partial \theta}{\partial t} + u \frac{\partial \theta}{\partial x} + v \frac{\partial \theta}{\partial y} \right). \quad (4.8)$$

The non-homogeneous term b_R is approximated by polynomial type radial basis functions f_j as

$$b_R \approx \sum_{j=1}^{N+L} \alpha_{R_j} f_j = \sum_{j=1}^{N+L} \alpha_{R_j} \nabla^2 \hat{u}_j \quad (4.9)$$

where α_{R_j} are the undetermined constants for the stream function while they are time-dependent for ω and θ , and f_j satisfy the Poisson equation $\nabla^2 \hat{u}_j = f_j$. Then, Equation (4.5) becomes

$$c_i R_i + \int_{\Gamma} (q^* R - u^* \frac{\partial R}{\partial n}) d\Gamma = \sum_{j=1}^{N+L} \alpha_{R_j} \left[c_i \hat{u}_{ji} + \int_{\Gamma} (q^* \hat{u}_j - u^* \hat{q}_j) d\Gamma \right] \quad (4.10)$$

which is a boundary-only integral equation where $\hat{q} = \partial \hat{u} / \partial n$. When the boundary is discretized with constant boundary elements, Equation (4.1)-(4.3) can be written as

$$\mathbf{H}\psi - \mathbf{G}\psi_q = (\mathbf{H}\hat{\mathbf{U}} - \mathbf{G}\hat{\mathbf{Q}})\mathbf{F}^{-1}(-\omega), \quad (4.11)$$

$$\begin{aligned} \frac{\mu_{nf}\rho_f}{\mu_f\rho_{nf}} Pr_f (\mathbf{H}\omega - \mathbf{G}\omega_q) = & (\mathbf{H}\hat{\mathbf{U}} - \mathbf{G}\hat{\mathbf{Q}})\mathbf{F}^{-1} \left[\frac{\partial \omega}{\partial t} + \mathbf{u} \frac{\partial \omega}{\partial x} + \mathbf{v} \frac{\partial \omega}{\partial y} \right. \\ & - \frac{\sigma_{nf}\rho_f}{\sigma_f\rho_{nf}} Ha^2 Pr_f \left(\left(\frac{\partial \mathbf{u}}{\partial x} - \frac{\partial \mathbf{v}}{\partial y} \right) \sin \lambda \cos \lambda \right. \\ & \left. \left. - \frac{\partial \mathbf{v}}{\partial x} \cos^2 \lambda + \frac{\partial \mathbf{u}}{\partial y} \sin^2 \lambda \right) - \frac{\beta_{nf}}{\beta_f} Ra_f Pr_f \frac{\partial \theta}{\partial x} \right], \end{aligned} \quad (4.12)$$

$$\frac{(\rho Cp)_f k_{nf}}{(\rho Cp)_{nf} k_f} (\mathbf{H}\theta - \mathbf{G}\theta_q) = (\mathbf{H}\hat{\mathbf{U}} - \mathbf{G}\hat{\mathbf{Q}})\mathbf{F}^{-1} \left(\frac{\partial \theta}{\partial t} + \mathbf{u} \frac{\partial \theta}{\partial x} + \mathbf{v} \frac{\partial \theta}{\partial y} \right) \quad (4.13)$$

where H , G , \hat{U} , \hat{Q} and F are the usual DRBEM matrices obtained by the use of fundamental solution of Laplace equation as given in Section 3.2.1. The compact form of stream function, vorticity and energy equations is

$$\mathbf{H}\psi - \mathbf{G}\psi_q = \tilde{\mathbf{b}} \quad (4.14)$$

$$- \mathbf{C}\dot{\omega} + \mathbf{H}_\omega \omega - \mathbf{G}_\omega \omega_q = \tilde{\mathbf{c}} \quad (4.15)$$

$$- \mathbf{C}\dot{\theta} + \mathbf{H}_\theta \theta - \mathbf{G}_\theta \theta_q = \tilde{\mathbf{d}}. \quad (4.16)$$

similar to Equations (3.20-3.22). However, here

$$\begin{aligned} \mathbf{C} &= (\mathbf{H}\hat{\mathbf{U}} - \mathbf{G}\hat{\mathbf{Q}})\mathbf{F}^{-1}, \quad \mathbf{H}_\omega = \frac{\mu_{nf}\rho_f}{\mu_f\rho_{nf}} Pr_f \mathbf{H} - \mathbf{D}, \\ \mathbf{G}_\omega &= \frac{\mu_{nf}\rho_f}{\mu_f\rho_{nf}} Pr_f \mathbf{G}, \quad \mathbf{H}_\theta = \frac{k_{nf}(\rho Cp)_f}{k_f(\rho Cp)_{nf}} \mathbf{H} - \mathbf{D}, \\ \mathbf{G}_\theta &= \frac{k_{nf}(\rho Cp)_f}{k_f(\rho Cp)_{nf}} \mathbf{G} \quad \text{and} \quad \mathbf{D} = \mathbf{C} \left(\mathbf{u} \frac{\partial \mathbf{F}}{\partial v} \mathbf{F}^{-1} + \mathbf{v} \frac{\partial \mathbf{F}}{\partial y} \mathbf{F}^{-1} \right) \end{aligned}$$

and the right hand side vectors are

$$\begin{aligned}
\tilde{\mathbf{b}} &= \mathbf{C}(-\boldsymbol{\omega}) \\
\tilde{\mathbf{c}} &= -\mathbf{C} \frac{\sigma_{nf}\rho_f}{\sigma_f\rho_{nf}} Ha^2 Pr_f \left(\left(\frac{\partial \mathbf{u}}{\partial x} - \frac{\partial \mathbf{v}}{\partial y} \right) \sin \lambda \cos \lambda - \frac{\partial \mathbf{v}}{\partial x} \cos^2 \lambda + \frac{\partial \mathbf{u}}{\partial y} \sin^2 \lambda \right) \\
&\quad - \mathbf{C} \frac{\beta_{nf}}{\beta_f} Ra_f Pr_f \frac{\partial \boldsymbol{\theta}}{\partial x} \\
\tilde{\mathbf{d}} &= 0.
\end{aligned} \tag{4.17}$$

Equation (4.15) and Equation (4.16) involve the time derivatives and a two-level time integration scheme will be employed in similar way given in Chapter 3, Section 3.2.1. Thus, a linear approximation is proposed for the variation of $\boldsymbol{\omega}$ and $\boldsymbol{\omega}_q$ and $\boldsymbol{\theta}$ and $\boldsymbol{\theta}_q$ within each time step as given in Equations (3.24) and (3.28). The first order time derivative is also approximated as in Chapter 3, Equation (3.25). Substitution of these approximations into Equations (4.15) and (4.16), results in:

$$\begin{aligned}
\left(\frac{-\mathbf{C}}{\Delta t} + \beta_\omega \mathbf{H}_\omega \right) \boldsymbol{\omega}^{m+1} - \beta_{\omega_q} \mathbf{G}_\omega \boldsymbol{\omega}_q^{m+1} &= \tilde{\mathbf{c}}^m - \left(\frac{\mathbf{C}}{\Delta t} + (1 - \beta_\omega) \mathbf{H}_\omega \right) \boldsymbol{\omega}^m \\
&\quad + (1 - \beta_{\omega_q}) \mathbf{G}_\omega \boldsymbol{\omega}_q^m,
\end{aligned} \tag{4.18}$$

$$\begin{aligned}
\left(\frac{-\mathbf{C}}{\Delta t} + \beta_\theta \mathbf{H}_\theta \right) \boldsymbol{\theta}^{m+1} - \beta_{\theta_q} \mathbf{G}_\theta \boldsymbol{\theta}_q^{m+1} &= \tilde{\mathbf{d}}^m - \left(\frac{\mathbf{C}}{\Delta t} + (1 - \beta_\theta) \mathbf{H}_\theta \right) \boldsymbol{\theta}^m \\
&\quad + (1 - \beta_{\theta_q}) \mathbf{G}_\theta \boldsymbol{\theta}_q^m,
\end{aligned} \tag{4.19}$$

respectively for the vorticity and the temperature. The coupled equations in ψ , ω and θ will be solved iteratively for each time level m as explained in Chapter 3, Section 3.2.1.

4.2.2 Stability analysis of the numerical method

Stability analysis for the present numerical method will be carried out through Equations (4.18) and (4.19) as explained in Chapter 3, Section 3.2.2. Thus, Equations (4.18) and (4.19) can be written as

$$\mathbf{x}_\omega^{m+1} = \mathbf{K}_\omega^{-1} \mathbf{b}_\omega - \mathbf{K}_\omega^{-1} \mathbf{L}_\omega \mathbf{x}_\omega^m, \quad \mathbf{x}_\theta^{m+1} = \mathbf{K}_\theta^{-1} \mathbf{b}_\theta - \mathbf{K}_\theta^{-1} \mathbf{L}_\theta \mathbf{x}_\theta^m \tag{4.20}$$

where K_ω , L_ω , K_θ and L_θ are the matrices obtained by shuffling of the coefficient matrices in Equation (4.18) and Equation (4.19), corresponding to the unknown values

and its normal derivatives at the $(m + 1)$ -th time level and the known values and its normal derivatives at the m -th time level, respectively. The stability of the numerical method is checked through the spectral radius of matrices $\mathbf{K}_\omega^{-1}\mathbf{L}_\omega$ and $\mathbf{K}_\theta^{-1}\mathbf{L}_\theta$. That is, if $\rho(\mathbf{K}_\omega^{-1}\mathbf{L}_\omega) < 1$ and $\rho(\mathbf{K}_\theta^{-1}\mathbf{L}_\theta) < 1$, then the iterative scheme is stable.

4.3 Steady MHD Convective Nanofluid Flow in an Inclined Semi-Annulus with Circular Inner Wall

As a first application, the steady natural convection nanofluid flow in an inclined semi-circular annulus filled with a water-based nanofluid involving Cu-nanoparticles is solved by using DRBEM in the presence of a uniform inclined magnetic field.

The equations governing the steady counterpart of the unsteady Equations (4.1)-(4.3) for the flow and heat transfer can be written as

$$\nabla^2 \psi = -\omega \quad (4.21)$$

$$\begin{aligned} \nabla^2 \omega = & (1 - \phi)^{2.5} [(1 - \phi) + \frac{\rho_s}{\rho_f} \phi] \frac{1}{Pr_f} [(u \frac{\partial \omega}{\partial x} + v \frac{\partial \omega}{\partial y}) \\ & - Ra_f [(1 - \phi) + \phi \frac{\beta_s}{\beta_f}] \frac{\partial \theta}{\partial x} \\ & - \frac{Ha^2}{(1 - \phi) + \phi \frac{\rho_s}{\rho_f}} (1 + \frac{3(\frac{\sigma_s}{\sigma_f} - 1)\phi}{(\frac{\sigma_s}{\sigma_f} + 2) - (\frac{\sigma_s}{\sigma_f} - 1)\phi}) \\ & \times ((\frac{\partial u}{\partial x} - \frac{\partial v}{\partial y}) \sin \lambda \cos \lambda - \frac{\partial v}{\partial x} \cos^2 \lambda + \frac{\partial u}{\partial y} \sin^2 \lambda)] \end{aligned} \quad (4.22)$$

$$\nabla^2 \theta = [(1 - \phi) + \frac{(\rho C_p)_s}{(\rho C_p)_f} \phi] \frac{k_s + 2k_f - 2\phi(k_f - k_s)}{k_s + 2k_f + \phi(k_f - k_s)} (u \frac{\partial \theta}{\partial x} + v \frac{\partial \theta}{\partial y}). \quad (4.23)$$

The flow configuration of the problem is displayed in Figure 4.1. The enclosure forms an angle β with the x -axis and it is subject to an inclined uniform magnetic field making an angle λ with the x -axis. The enclosure with stationary walls (i.e. no-slip boundary conditions are considered) is filled with Cu-water nanofluid. The outer wall is kept at cold temperature (T_c) while the inner wall is under a constant heat flux (q''). The straight boundaries are thermally insulated, i.e. adiabatic. Thus,

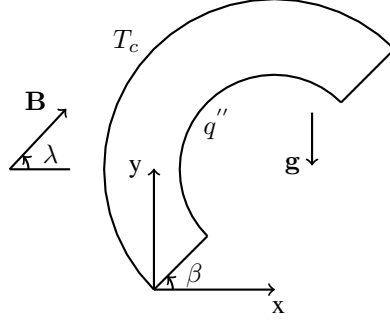


Figure 4.1: Geometry of the problem.

the non-dimensional boundary conditions for the ψ and θ become

$$\begin{aligned}
 \text{At the stationary walls : } & \psi = \partial\psi/\partial x = \partial\psi/\partial y = 0, \quad \partial\theta/\partial n = 0 \\
 \text{At inner circular wall : } & \psi = \partial\psi/\partial x = \partial\psi/\partial y = 0, \quad \partial\theta/\partial n = -1 \\
 \text{At outer circular wall : } & \psi = \partial\psi/\partial x = \partial\psi/\partial y = 0, \quad \theta = 0.
 \end{aligned} \tag{4.24}$$

Finally, the corresponding DRBEM equations for Equations (4.21)-(4.23) can be obtained as explained in Section 4.2.1 for the stream function, vorticity and temperature as:

$$\mathbf{H}\psi - \mathbf{G}\frac{\partial\psi}{\partial n} = (\mathbf{H}\hat{\mathbf{U}} - \mathbf{G}\hat{\mathbf{Q}})\mathbf{F}^{-1}\{-\omega\} \tag{4.25}$$

$$\begin{aligned}
 (\mathbf{H}\omega - \mathbf{G}\frac{\partial\omega}{\partial n}) &= (1-\phi)^{2.5}[(1-\phi) + \frac{\rho_s}{\rho_f}\phi]\frac{1}{Pr_f}(\mathbf{H}\hat{\mathbf{U}} - \mathbf{G}\hat{\mathbf{Q}})\mathbf{F}^{-1} \\
 &\quad \{(\mathbf{u}\frac{\partial\omega}{\partial x} + \mathbf{v}\frac{\partial\omega}{\partial y}) - Ra_f[(1-\phi) + \phi\frac{\beta_s}{\beta_f}]\frac{\partial\theta}{\partial x} \\
 &\quad - (1 + \frac{3(\frac{\sigma_s}{\sigma_f} - 1)\phi}{(\frac{\sigma_s}{\sigma_f} + 2) - (\frac{\sigma_s}{\sigma_f} - 1)\phi})(\frac{Ha^2}{(1-\phi) + \phi\frac{\rho_s}{\rho_f}}) \\
 &\quad \times ((\frac{\partial\mathbf{u}}{\partial x} - \frac{\partial\mathbf{v}}{\partial y})\sin\lambda\cos\lambda - \frac{\partial\mathbf{v}}{\partial x}\cos^2\lambda + \frac{\partial\mathbf{u}}{\partial y}\sin^2\lambda)\}
 \end{aligned} \tag{4.26}$$

$$\begin{aligned}
 (\mathbf{H}\theta - \mathbf{G}\frac{\partial\theta}{\partial n}) &= [(1-\phi) + \frac{(\rho C_p)_s}{(\rho C_p)_f}\phi]\frac{k_s + 2k_f - 2\phi(k_f - k_s)}{k_s + 2k_f + \phi(k_f - k_s)}(\mathbf{H}\hat{\mathbf{U}} - \mathbf{G}\hat{\mathbf{Q}})\mathbf{F}^{-1} \\
 &\quad \times (\mathbf{u}\frac{\partial\theta}{\partial x} + \mathbf{v}\frac{\partial\theta}{\partial y}).
 \end{aligned} \tag{4.27}$$

The numerical simulations are carried out to investigate the effect of various controlling parameters, such as Hartmann number ($Ha = 0, 20, 50, 100, 300, 500$), Rayleigh

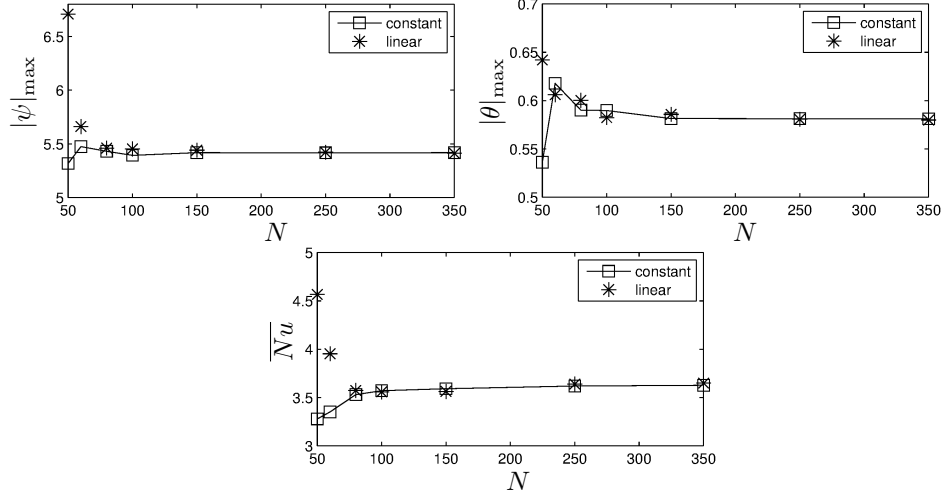


Figure 4.2: Grid dependency: $Ra = 10^5$, $Ha = 50$, $\phi = 0.06$, $\lambda = \beta = 0$.

number ($Ra = 10^3, 10^4, 10^5$), the inclination angles of the magnetic field (λ) and the enclosure (β) ($\lambda, \beta = 0, \frac{\pi}{6}, \frac{\pi}{4}, \frac{\pi}{3}, \frac{\pi}{2}$) and the solid volume fraction of nanoparticles ($\phi = 0, 0.02, 0.06, 0.1, 0.2$) at a fixed Prandtl number of $Pr_f = 6.2$. The radius of inner and outer circles are taken as $r_{in} = 1$ and $r_{out} = 2$, respectively, to construct the computational domain. The grid independency test is performed in terms of the variations of $|\psi|_{\max}$, $|\theta|_{\max}$ and \overline{Nu} along the inner wall with respect to the number of boundary elements N when $Ha = 50, 10^5$, $\phi = 0.06$. Figure 4.2 displays that $N \approx 130$ boundary elements are enough for the grid independence for a moderate value of $Ha = 50$. However, for higher values of Ha and Ra , it is well-known that a finer mesh is required, for example $N \approx 350$ elements are used when $Ha = 500$, $Ra = 10^4$. In addition, the CPU time is ranging from 88 (in seconds, for the smallest values of $Ha = 0$ and $Ra = 10^3$) to 133 (in seconds, for the highest values of $Ha = 50$, $Ra = 10^5$) at fixed $\lambda = \beta = 0$ and $\phi = 0.06$ when the runs are performed in a computer of Intel(R) Core(TM) i7-4700HQ CPU @ 2.40GHz 16,00 GB, 64bit. It is also well-observed that using linear elements makes no difference compared to constant elements, thus the subsequent computations are done by using constant elements since it is computationally easier than linear elements. The code validation is performed by evaluating the average Nusselt number at various combination of controlling parameters, namely Ha , Ra and inclination angles λ and β , and the obtained results are compared with the ones given in the work of Sheikholeslami [86]. The present results $\overline{Nu} = 3.685, 3.558, 3.12$ ($Ha = 0, Ra = 10^4$) and $\overline{Nu} = 2.385, 2.495, 2.471$ ($Ha = 20, Ra = 10^4$) respectively at $\lambda = \beta = 0$,

$\pi/4$, $\pi/2$ are in good agreement with the numerical results of Sheikholeslami [86] $\overline{Nu} \approx 3.69, 3.55, 3.1$ ($Ha = 0$, $Ra = 10^4$) and $\overline{Nu} \approx 2.39, 2.49, 2.47$ ($Ha = 20$, $Ra = 10^4$) measured from Figure 7 given in [86], respectively at $\lambda = \beta = 0, \pi/4, \pi/2$.

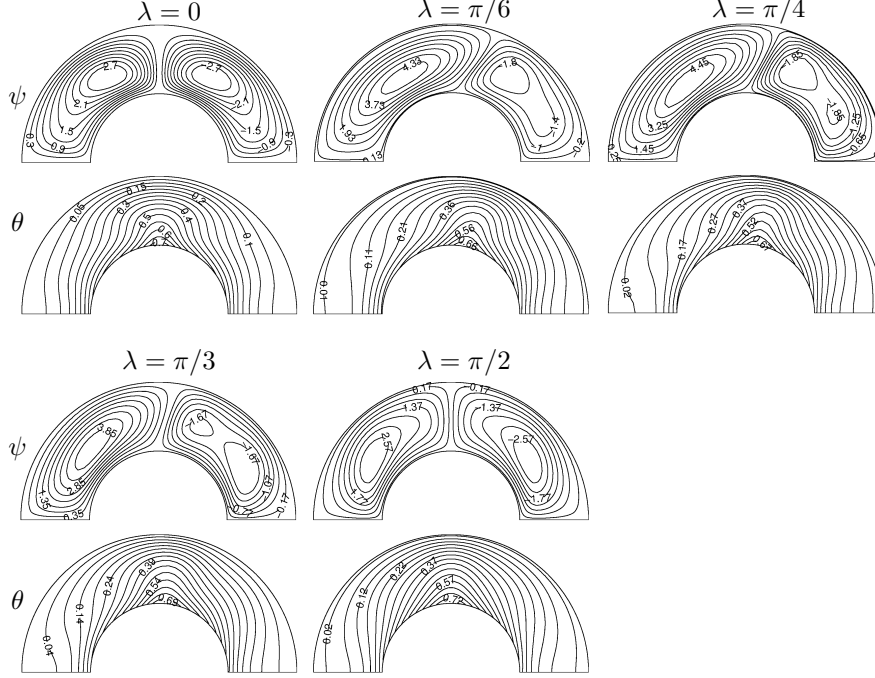


Figure 4.3: Effect of λ on streamlines and isotherms: $\beta = 0$, $\phi = 0.06$, $Ra = 10^4$, $Ha = 20$.

The effect of the inclination angle λ of the magnetic field on the streamlines and isotherms are displayed in Figure 4.3 at $Ha = 20$, $Ra = 10^4$, $\phi = 0.06$ and $\beta = 0$. At $\lambda = 0$, two symmetric counter-rotating eddies are formed in streamlines. The cores of eddies are located symmetrically along the vertical centerline of the cavity. However, the positive vortex gets stronger and expands in the direction of magnetic field which forces the negative vortex to shrink, thus the symmetry is destroyed with an increase in λ to $\pi/6$. The core of the negative vortex is separated, and two small negative eddies are formed around $\lambda = \pi/4$. As λ increases to $\pi/3$, one of these negative eddies close to the bottom horizontal wall of the cavity gets larger, while the other becomes smaller and finally it vanishes with a further increase in λ to $\pi/2$. As a result, when $\lambda = \pi/2$ the counter-rotating vortices become again symmetric, but now their cores are located above the thermally insulated walls instead of the center of the cavity as in the case of $\lambda = 0$. On the other hand, the thermal plume formed at the middle of the cavity just above the inner wall when $\lambda = 0$ moves along the inner wall

in the direction of the magnetic field as expected.

Figures 4.4-4.6 show the effects of the Rayleigh and Hartmann numbers on the streamlines and isotherms when λ and β are taken as equal to each other (i.e. $\lambda = \beta = 0, \pi/4, \pi/2$). The cores of the two equal counter-rotating vortices formed inside the enclosure at $\lambda = \beta = 0$ (see Figure 4.4) move upward following the increase in velocity of the fluid at high Ra for each Ha . The effect of convection on heat transfer dominated by conduction at $Ra = 10^3$ becomes more significant as Ra increases, and thus a thermal plume is formed above the inner wall. The plume gets bigger leading the formation of a thermal boundary layer close to the outer wall at the highest $Ra (= 10^5)$. However, the thermal plume over the inner wall vanishes with an increase in Ha , which forces the isotherms to become more parallel to each other, the symmetry of the eddies observed at $\lambda = \beta = 0$ is destroyed following the formation

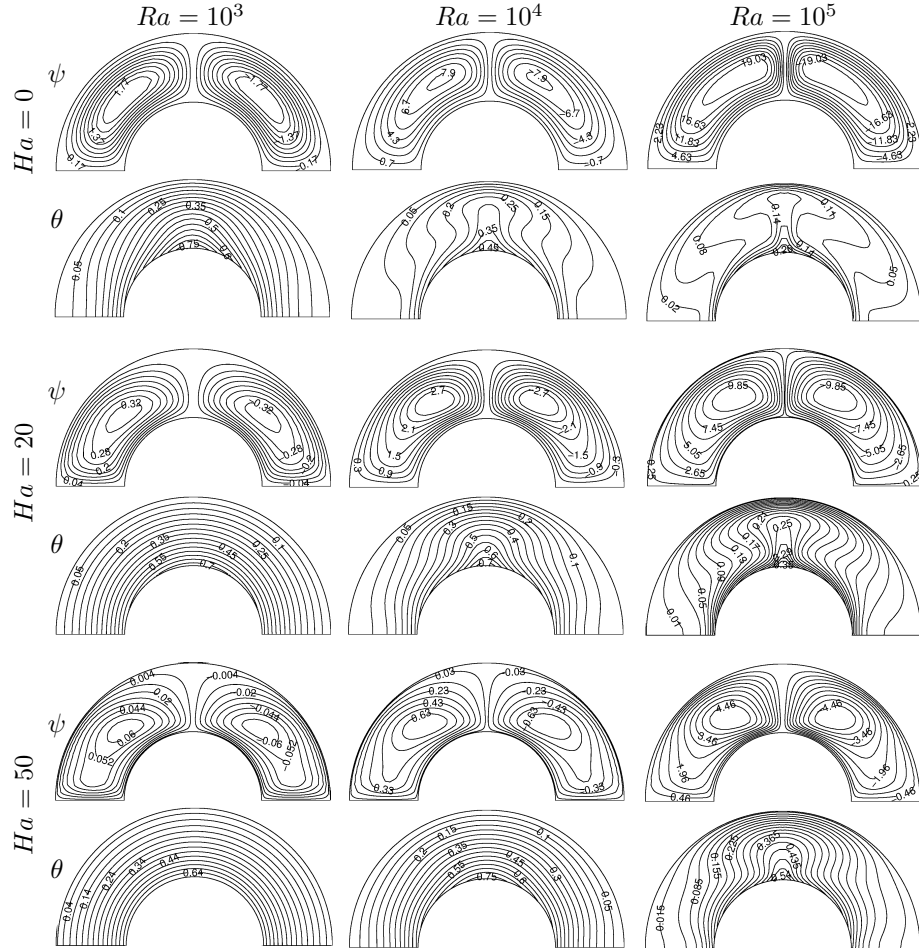


Figure 4.4: Effects of Ha and Ra on streamlines and isotherms: $\lambda = \beta = 0, \phi = 0.06$.

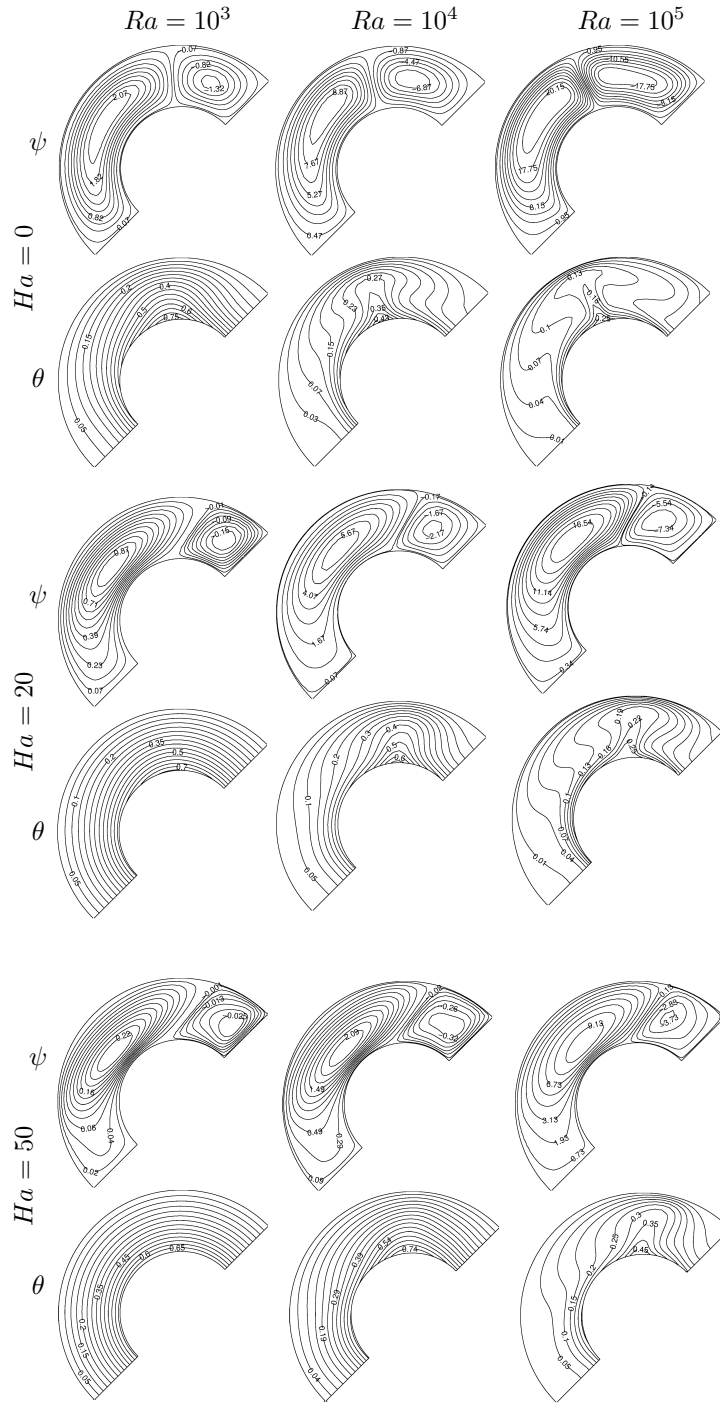


Figure 4.5: Effects of Ha and Ra on streamlines and isotherms: $\lambda = \beta = \pi/4$, $\phi = 0.06$.

of a bigger and stronger positive vortex in streamlines as in the case when $\beta = 0$ displayed in Figure 4.3. Moreover, positive vortex elongates with the inclination of the enclosure and becomes dominant to the secondary negative vortex. Since the enclosure is also inclined (i.e. $\beta = \pi/4$), the secondary vortex at $\lambda = \pi/4$ has only one core while it has two cores in the case $\lambda = \pi/4, \beta = 0$ (see Figure 4.3). The core of the main vortex moves upward closer to the negative vortex due to the convection dominance for higher Ra at each Ha . However, velocity is reduced due to the retarding effect of Lorentz force as Ha increases, which limits the motion of the core in the upward direction. It is observed from Figure 4.6 that when the inclination angles are $\lambda = \beta (= \pi/2)$ only one positive eddy occurs in streamlines and its

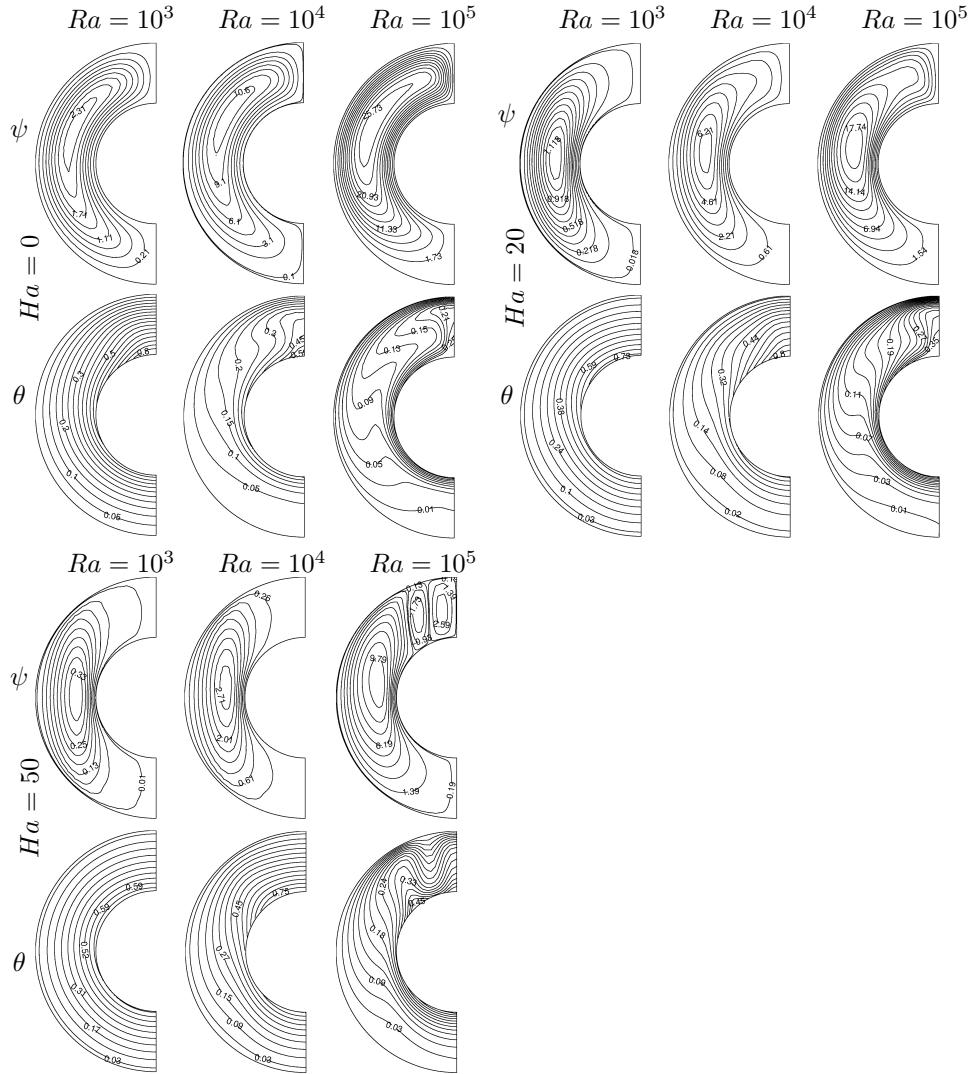


Figure 4.6: Effects of Ha and Ra on streamlines and isotherms: $\lambda = \beta = \pi/2$, $\phi = 0.06$.

core moves upwards as Ra increases similar to the other cases. On the other hand, at $\lambda = \beta = \pi/4, \pi/2$, a formation of a plume in isotherms occurs on the surface of inner wall in the direction of the magnetic field as Ra increases following the convection mode of the flow. However, the intensity of convection and the plume become weaker and isotherms becomes more parallel to each other as Ha increases. Moreover, irrespective of λ and β , the values of ψ decreases in magnitude as Ha increases, but it increases with Ra .

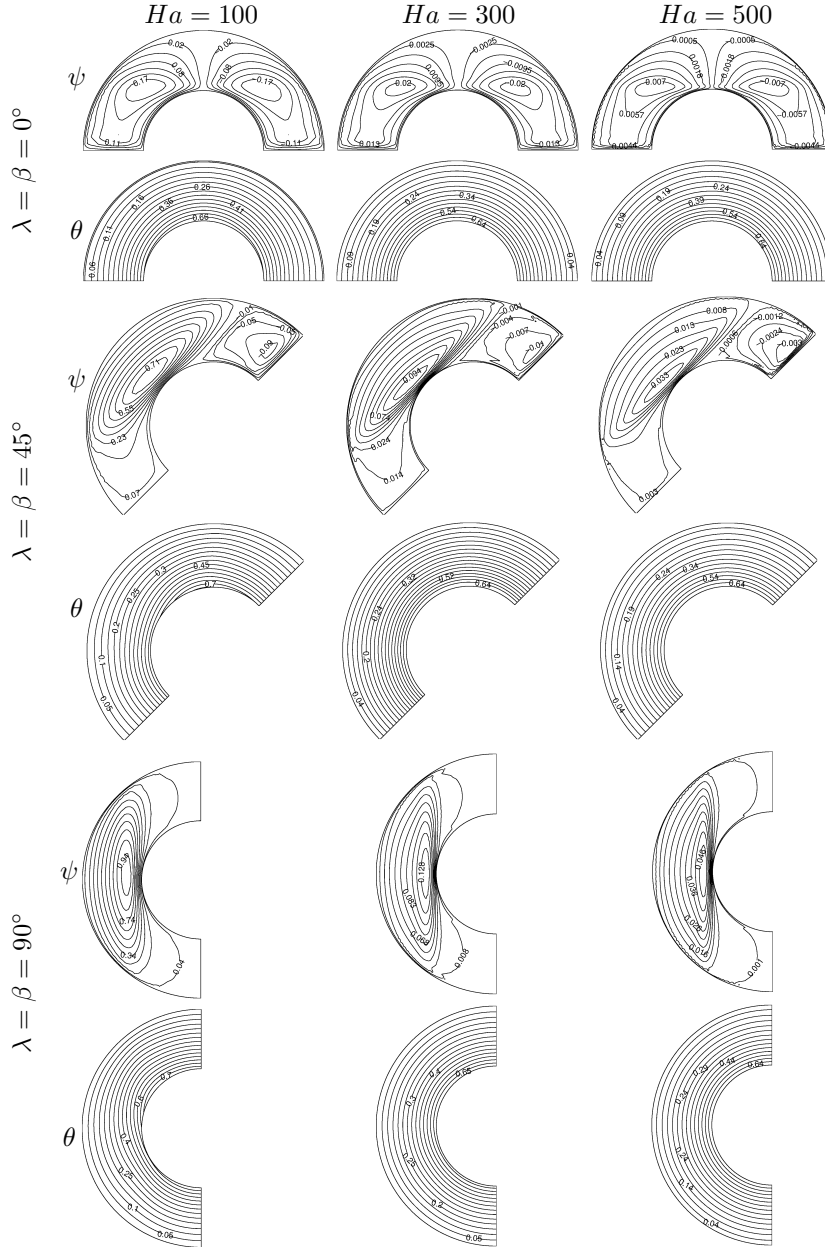


Figure 4.7: Streamlines and isotherms: $Ra = 10^4$, $\phi = 0.06$, $Ha = 100, 300, 500$
 $\lambda = \beta = 0, \pi/4, \pi/2$.

The effect of high $Ha (= 100, 300, 500)$ on the streamlines and temperature profiles is drawn in Figure 4.7 at the inclination angles ($\lambda = \beta = 0, \pi/4, \pi/2$) when $Ra = 10^4$, $\phi = 0.06$. As it is expected, an increase in Ha results in a decrease on the values of the stream function while the isotherms display the similar behavior at each inclination angles since the high Ha reduces the effect of Ra on heat transfer. On the other hand, some distortions are observed on the streamlines close to the outer circular boundary at high Ha , especially when $Ha = 500$. It is well-known that a finer mesh should be used when Ha increases. DRBEM matrices are full matrices and do not show a special form although their sizes are small due to the boundary only discretization. However, for large Ha , the number of boundary elements has to be increased which results in larger DRBEM matrices that are full. Thus, they represent computational difficulties for large values of Ha due to the resulting rather large-sized systems.

The pure effect of the inclination angle β of the enclosure on the flow field and temperature distribution is visualized in terms of streamlines and isotherms in Figure 4.8 at fixed $\lambda = \pi/4$ when $\phi = 0.06$, $Ra = 10^4$ and $Ha = 20$. When the enclosure is horizontal (i.e. $\beta = 0$), the positive vortex expands upward in the direction of the applied magnetic field ($\lambda = \pi/4$), and thus the negative vortex with two cores shrinks in the right part of the annulus. As β increases, the negative vortex shrinks further and its cores merge forming one vortex close to the straight wall of the annulus, and finally it vanishes when $\beta = \pi/2$ due to the slip of the core of the positive vortex in the direction of the enclosure. The thermal plume formed on the right part of the inner circular wall in the direction of the magnetic field ($\lambda = \pi/4$) when $\beta = 0$, is relocated by moving right on the surface of the inner wall as β increases. Finally, when $\beta = \pi/2$ the plume is formed on the top of the enclosure.

Figure 4.9 displays the variation in the stream function, vorticity and temperature along (a) the vertical centerline ($x = 0, 1 \leq y \leq 2$) and (b) the horizontal line ($y = 1.25, -2 \leq x \leq 2$), respectively, at different solid volume fractions $\phi = 0, 0.02, 0.06, 0.1, 0.2$ when $Ha = 20$ and $Ra = 10^3$. As ϕ increases, the values of stream function increase in magnitude both along the vertical centerline $x = 0$ and horizontal line $y = 1.25$, while no significant effect of ϕ is observed on the vorticity and temperature variations. However, the temperature drops from inner to outer wall along the vertical centerline as expected since the outer wall is cold. On the other

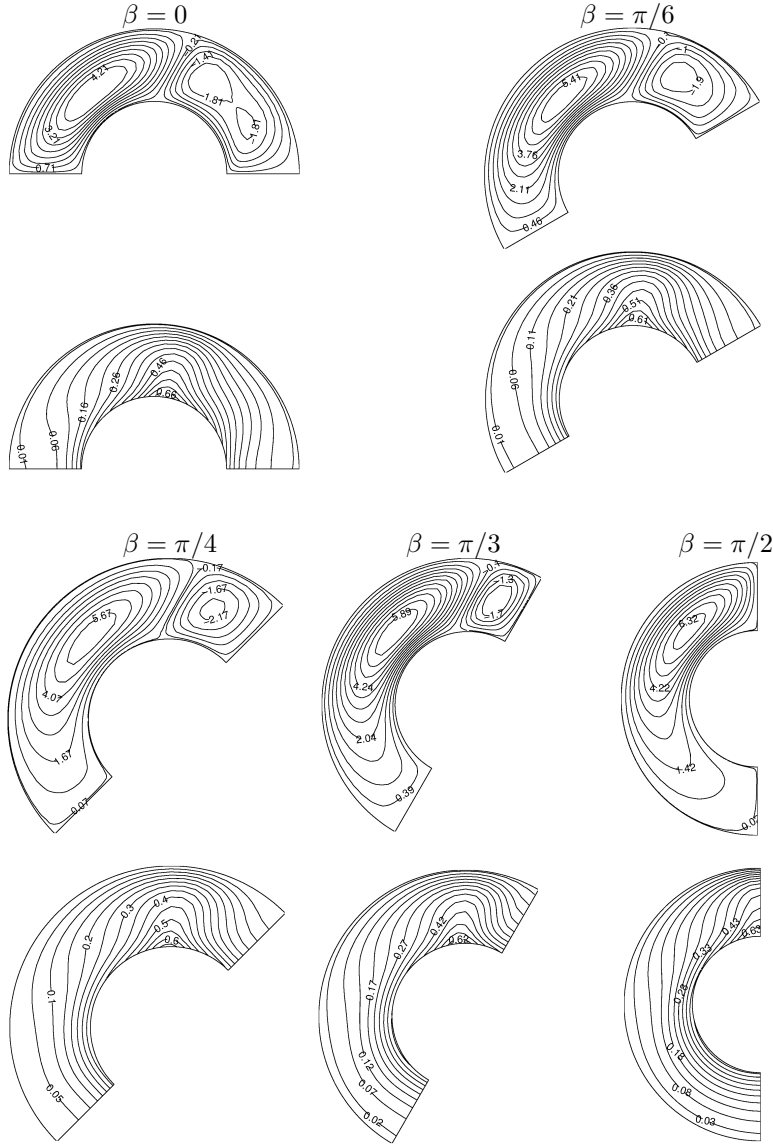


Figure 4.8: Effect of β on streamlines and isotherms: $\lambda = \pi/4$, $\phi = 0.06$, $Ra = 10^4$, $Ha = 20$.

hand, temperature rises in the left half of the annulus while it drops in the right half of the enclosure along the line $y = 1.25$ irrespective of the values of ϕ .

The heat transfer rate inside the annulus is further investigated in terms of average Nusselt number along the inner wall at various combination of Ra , Ha and inclination angles of the magnetic field and enclosure at $\phi = 0.06$. Figure 4.10(a) displays the variation of \overline{Nu} along the inner wall with respect to Ra at $\lambda = \beta = 0, \pi/4, \pi/2$ by fixing $Ha = 20$. \overline{Nu} increases as Ra increases indicating enhancement of heat transfer inside the enclosure. Although there is no obvious difference in \overline{Nu} at

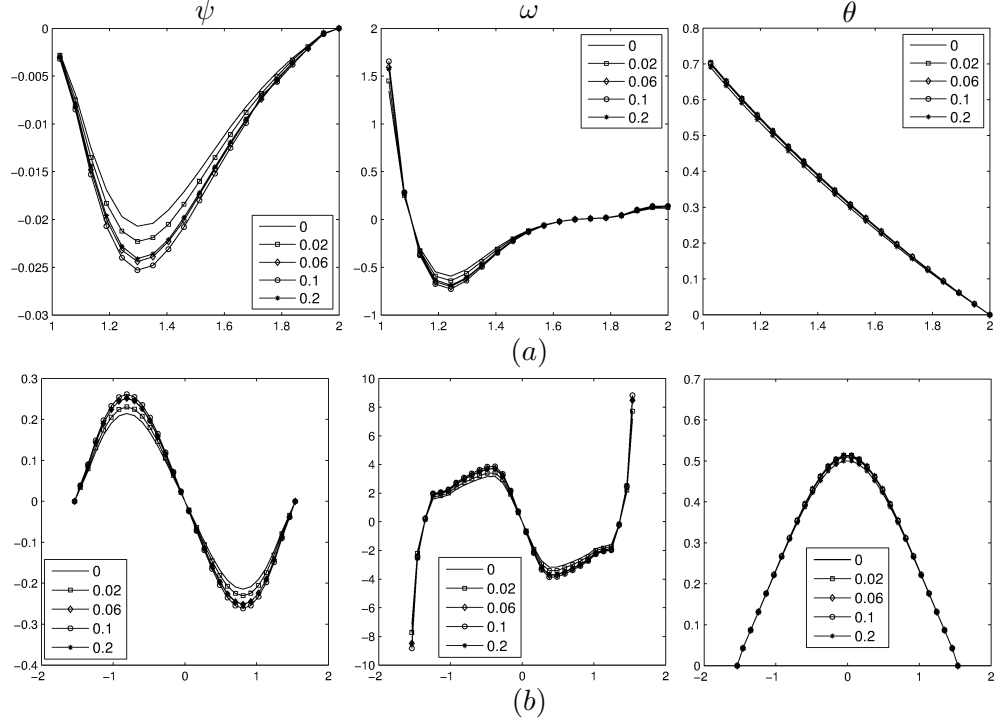


Figure 4.9: Variation of ψ , ω and θ along (a) vertical centerline $x = 0$, $1 \leq y \leq 2$, (b) horizontal line $y = 1.25$, $-2 \leq x \leq 2$ at different ϕ : $Ra = 10^3$, $Ha = 20$, $\lambda = \beta = 0$.

different λ , β for $Ra \leq 10^4$, \overline{Nu} reaches its maximum at $\lambda = \beta = \pi/4$ for $Ra > 10^4$. In addition, the variation of \overline{Nu} versus Ha is shown in Figure 4.10(b) at $\lambda = \beta = 0$, $\pi/4$, $\pi/2$ when $Ra = 10^4$. It is observed that Ha has an opposite effect on \overline{Nu} compared to Ra , that is, the average Nusselt number reduces for higher values of Ha for each $\lambda = \beta$. The rate of decrease is slower at $\lambda = \beta = \pi/2$ than at $\lambda = \beta = 0$. The maximum of \overline{Nu} is observed at $\lambda = \beta = 0$ in the absence of magnetic field (i.e.

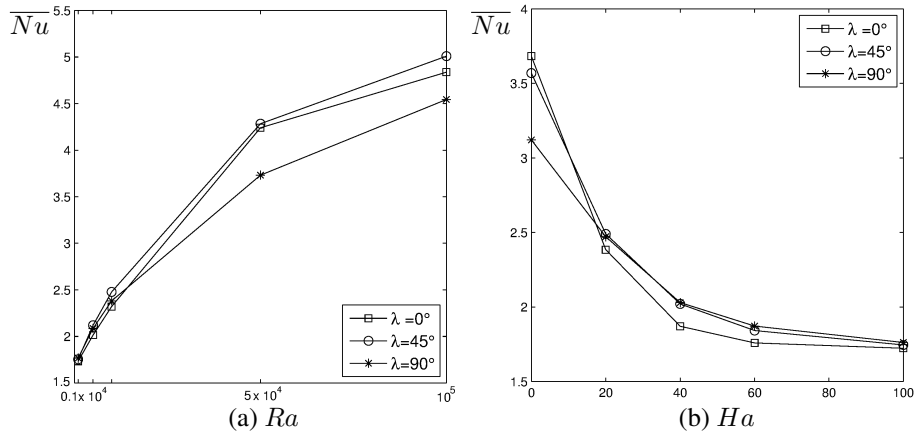


Figure 4.10: Effects of (a) Ra and (b) Ha on \overline{Nu} : $\lambda = \beta = 0, \pi/4, \pi/2$.

$Ha = 0$) while it occurs at $\lambda = \beta = \pi/2$ for higher values of Ha .

Finally, the effect of Hartmann number on (a) the horizontal velocity u and (b) vertical velocity v along the vertical centerline of the enclosure are shown in Figure 4.11 at $Ra = 10^3, 10^4$ when $\lambda = \beta = 0, \phi = 0.06$. Due to the retarding effect of magnetic force on the flow, both the horizontal and vertical velocities decrease in magnitude as Ha increases. This phenomena is more significant at $Ra = 10^3$ in the conduction mode which can be affected by the magnetic field. On the other hand, the horizontal and vertical velocities increase with an increase in Ra due to the strong buoyancy force.

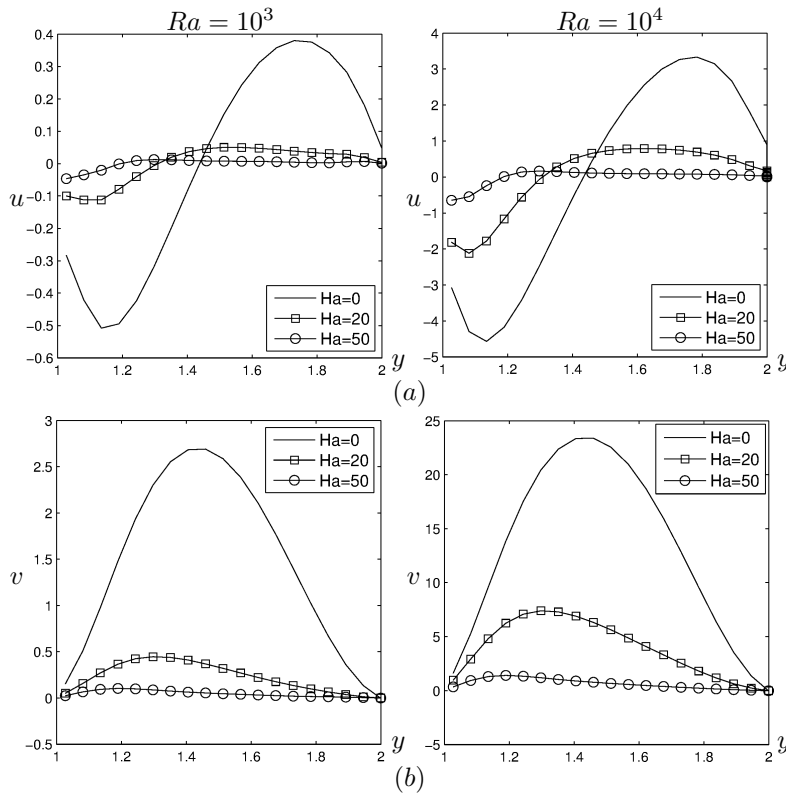


Figure 4.11: Horizontal velocity u and vertical velocity v along the vertical centerline $x = 0, 1 \leq y \leq 2$: $Ra = 10^3, 10^4$ for $Ha = 0, 20, 50$.

4.4 Unsteady MHD Natural Convection Nanofluid Flow in a Semi-Annulus with a Sinusoidal Inner Wall

The unsteady case of the problem considered in Section 4.3 is solved in a semi-annulus with an irregular wavy wall in order to see the effect of the irregular inner

wall on the flow and temperature distributions at several combinations of problem physical parameters. The equations governing the problem and the application of numerical technique are given respectively in Section 4.1 and Section 4.2 in details. The computational domain and boundary conditions are shown in Figure 4.12.

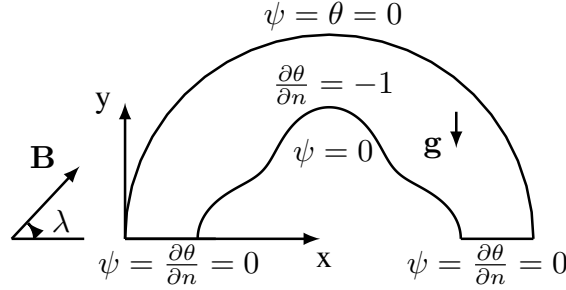


Figure 4.12: Geometry of the problem with boundary conditions.

The results are presented over a wide range of problem parameters: $10^3 \leq Ra \leq 10^5$, $0 \leq Ha \leq 100$, $0 \leq \phi \leq 0.1$, $0 \leq \lambda \leq \frac{\pi}{2}$ by keeping Prandtl number fixed as $Pr_f = 6.2$. The problem domain is determined by taking several number of undulation ($0 \leq n \leq 6$) of the inner wavy wall defined by $r = r_{in} + A \cos(n\zeta)$ in which $A = 0.2$, $r_{in} = 1$ are the amplitude and radius of the sinusoidal wall, respectively, and $0 \leq \zeta \leq \pi$. Figure 4.13 reveals that it is enough to use $N \approx 350$ constant boundary elements to ensure the grid independence, for the highest values of $Ha = 50$ and $Ra = 10^5$, and hence it is used in the following computations.

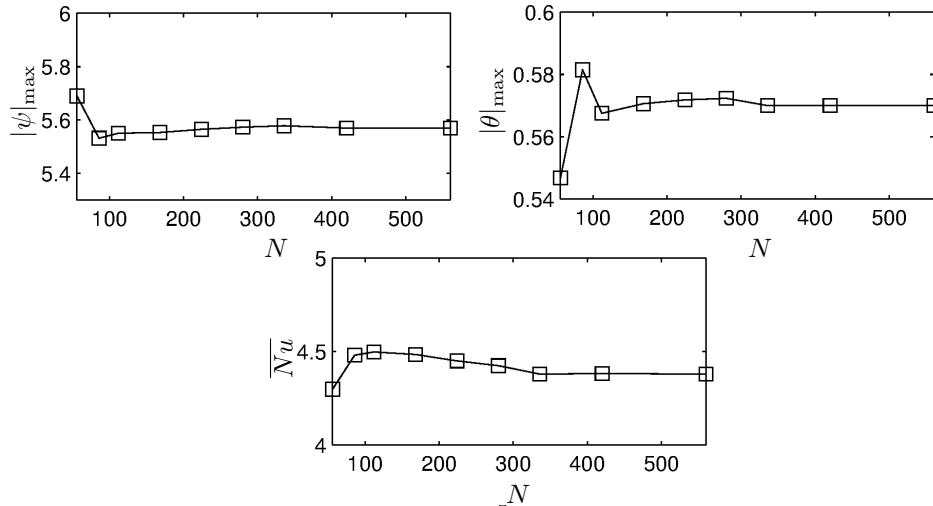


Figure 4.13: Grid dependency: $Ra = 10^5$, $Ha = 50$, $\phi = 0.06$, $A = 0.2$, $n = 4$, $\lambda = 0$.

The stability analysis of the numerical method is performed for different time increments and relaxation parameters by taking $\beta_\omega = \beta_\theta = \beta$ and $\beta_{\omega_q} = \beta_{\theta_q} = \beta_q$. Table

4.2 shows the variation of the spectral radius for the coefficient matrices of the vorticity and temperature with respect to relaxation parameters and the time step size when $Ra = 10^4$, $Ha = 20$, $\phi = 0.06$, $\lambda = 0$, $n = 4$. One can observe that the optimum relaxation parameter and time increment are $\beta = \beta_q = 0.9$ and $\Delta t = 0.9$, respectively, since a decrease in both relaxation parameters and time step size results in an increase in the spectral radius of coefficient matrices and moreover some of the eigenvalues become to diverge. The symbol *star* given in the table indicates that some of the eigenvalues diverges.

Table 4.2: Spectral radius of vorticity and temperature equations when $Ra = 10^4$, $Ha = 20$, $\lambda = 0$, $\phi = 0.06$, $n = 4$, $\epsilon = 10^{-4}$.

$\beta = \beta_q$	$\Delta t = 0.9$		$\Delta t = 0.6$		$\Delta t = 0.3$	
	$\rho(\mathbf{K}_\omega^{-1}\mathbf{L}_\omega)$	$\rho(\mathbf{K}_\theta^{-1}\mathbf{L}_\theta)$	$\rho(\mathbf{K}_\omega^{-1}\mathbf{L}_\omega)$	$\rho(\mathbf{K}_\theta^{-1}\mathbf{L}_\theta)$	$\rho(\mathbf{K}_\omega^{-1}\mathbf{L}_\omega)$	$\rho(\mathbf{K}_\theta^{-1}\mathbf{L}_\theta)$
0.9	0.1111	0.11413	*	0.15342	*	0.31621
0.8	*	0.253820	0.25	0.25574	*	*
0.7	0.42857	0.43419	0.42857	0.43607	*	0.44366
0.6	0.66667	0.67432	0.66657	*	*	0.68724
0.5	1	1	1	1	1	1

On the other hand, Table 4.3 indicates the relation between spectral radius of coefficient matrices considering different values of relaxation parameters for vorticity ($\beta_\omega = \beta_{\omega_q}$) and temperature ($\beta_\theta = \beta_{\theta_q}$) when $Ra = 10^4$, $Ha = 20$, $\lambda = 0$, $\phi = 0.06$, $n = 4$ and the time step size $\Delta t = 0.9$. It can be seen that, as $\beta_\omega = \beta_{\omega_q}$ decreases

Table 4.3: Spectral radius of vorticity and temperature equations when $Ra = 10^4$, $Ha = 20$, $\lambda = 0$, $\phi = 0.06$, $\Delta t = 0.9$, $n = 4$, $\epsilon = 10^{-4}$.

$\beta_\omega, \beta_{\omega_q}$	$\beta_\theta, \beta_{\theta_q}$	$\rho(\mathbf{K}_\omega^{-1}\mathbf{L}_\omega)$	$\rho(\mathbf{K}_\theta^{-1}\mathbf{L}_\theta)$
0.9	0.5	*	*
0.9	0.6	0.66667	0.66667
0.9	0.9	0.1111	0.11413
0.8	0.7	*	*
0.7	0.8	0.42851	*
0.6	0.9	0.66658	*
0.5	0.9	1	1

and $\beta_\theta = \beta_{\theta_q}$ increases, the spectral radius of vorticity and temperature decrease up to the case when $\beta_\omega = \beta_{\omega_q} = 0.7$ and $\beta_\theta = \beta_{\theta_q} = 0.9$, however, some eigenvalues diverge. Hence, it can be said that the optimal values for the spectral radius of vorticity and temperature are obtained when $\beta_\omega = \beta_{\omega_q} = \beta_\theta = \beta_{\theta_q} = 0.9$ as observed in Table 4.2. When $\beta_\omega = \beta_{\omega_q} = 0.6$ and $\beta_\theta = \beta_{\theta_q} = 0.9$ maximum eigenvalues of coefficient matrices start to increase and the method becomes unstable with a further decrease in $\beta_\omega = \beta_{\omega_q} = 0.5$.

In order to verify that the choice of $\beta = \beta_q = 0.9$ and $\Delta t = 0.9$ are the optimal values and satisfy the stability conditions for several combinations of Hartmann and Rayleigh numbers, the spectral radius of the coefficient matrices for the vorticity and temperature equations are calculated and presented in Table 4.4. The simulations are done for $Ra (= 10^3, 10^4, 10^5)$ at a fixed $Ha = 20$ and for $Ha (= 10, 20, 50)$ at a fixed $Ra = 10^4$. It is well observed that the choice of $\beta = \beta_q = \Delta t = 0.9$ is valid for each Ra and Ha , and hence in the subsequent computations these values are employed and the results obtained at steady-state are drawn in terms of streamlines and isotherms.

Table 4.4: Spectral radius of vorticity and temperature equations: $\phi = 0.06$, $\lambda = 0$, $\beta = \beta_q = 0.9$, $\Delta t = 0.9$, $\epsilon = 10^{-4}$.

$Ha = 20$			$Ra = 10^4$		
Ra	$\rho(\mathbf{K}_\omega^{-1}\mathbf{L}_\omega)$	$\rho(\mathbf{K}_\theta^{-1}\mathbf{L}_\theta)$	Ha	$\rho(\mathbf{K}_\omega^{-1}\mathbf{L}_\omega)$	$\rho(\mathbf{K}_\theta^{-1}\mathbf{L}_\theta)$
10^3	0.1111	0.11179	10	0.1111	0.11178
10^4	0.1111	0.11413	20	0.1111	0.11413
10^5	0.1111	0.15827	50	0.1111	0.14916

In Figure 4.14, the effect of the inclination angle of magnetic field λ on the flow and temperature fields are displayed at $Ra = 10^4$, $Ha = 20$, $n = 4$ and $\phi = 0.06$. The profiles of both the stream function and temperature fields in each λ are similar to the case in a semi-annulus with circular inner wall shown in Section 4.3, Figure 4.3. However, the sinusoidal inner wall causes an increase in the magnitude of the stream function at each λ ; and the two-cores for the negative vortex observed in the circular inner wall when $\lambda = \pi/4, \pi/3$ merge forming a stronger vortex in the case of sinusoidal inner wall. On the other hand, the thermal plume formed just above the inner wall in the direction of applied magnetic field weakens when compared to the case of annulus with circular wall at each λ .

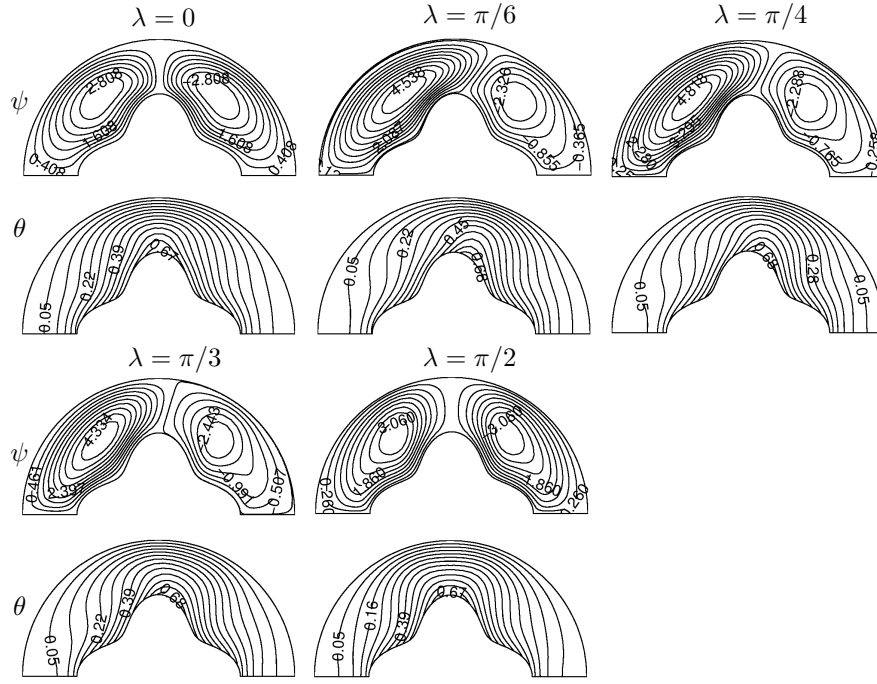


Figure 4.14: Effect of λ on the steady-state streamlines and isotherms: $n = 4$, $\phi = 0.06$, $Ra = 10^4$, $Ha = 20$.

Figure 4.15 illustrates the variation of stream function, vorticity and temperature along the (a) vertical centerline $x = 0$ and (b) horizontal line $y = 1.6$ at various time levels $t = 1, 3, 5, 10, 50, 155$, when $Ra = 10^4$, $Ha = 20$, $\phi = 0.06$, $n = 4$ and

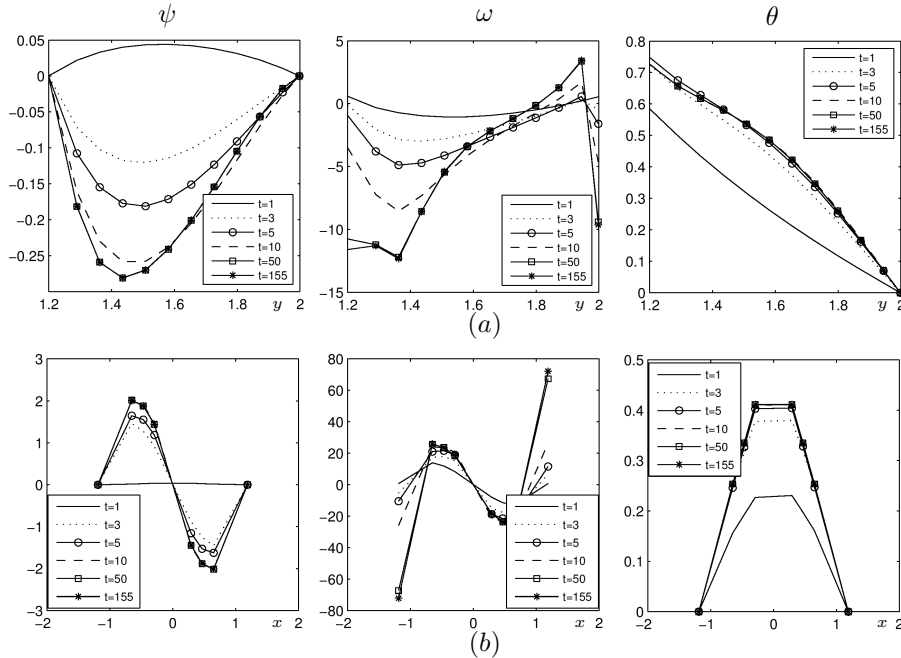


Figure 4.15: Time evolution of ψ , ω , θ along (a) vertical centerline $x = 0$, $1.2 \leq y \leq 2$, (b) horizontal line $y = 1.6$, $-2 \leq x \leq 2$: $Ra = 10^4$, $Ha = 20$, $\Delta t = 0.9$, $\phi = 0.06$, $n = 4$, $\lambda = 0$.

$\Delta t = 0.9$. It can be seen that as time advances the values of all unknowns ψ , ω and θ increase in magnitude and reach to the steady-state. Thus, in the rest of the section all figures drawn for stream function and temperature are obtained at steady-state.

The steady-state streamlines and isotherms are displayed in Figure 4.16 for $0 \leq Ha \leq 50$ and $10^3 \leq Ra \leq 10^5$ when the number of undulation $n = 4$ and the magnetic field is applied horizontally $\lambda = 0$. The obtained results for both flow field and temperature distribution show a similar behavior with the case of inner circular wall (see Figure 4.4) at each Ha and Ra . However, with the fluctuation in the inner wall, the strength of stream function increases for each combination of Ha and Ra . On the

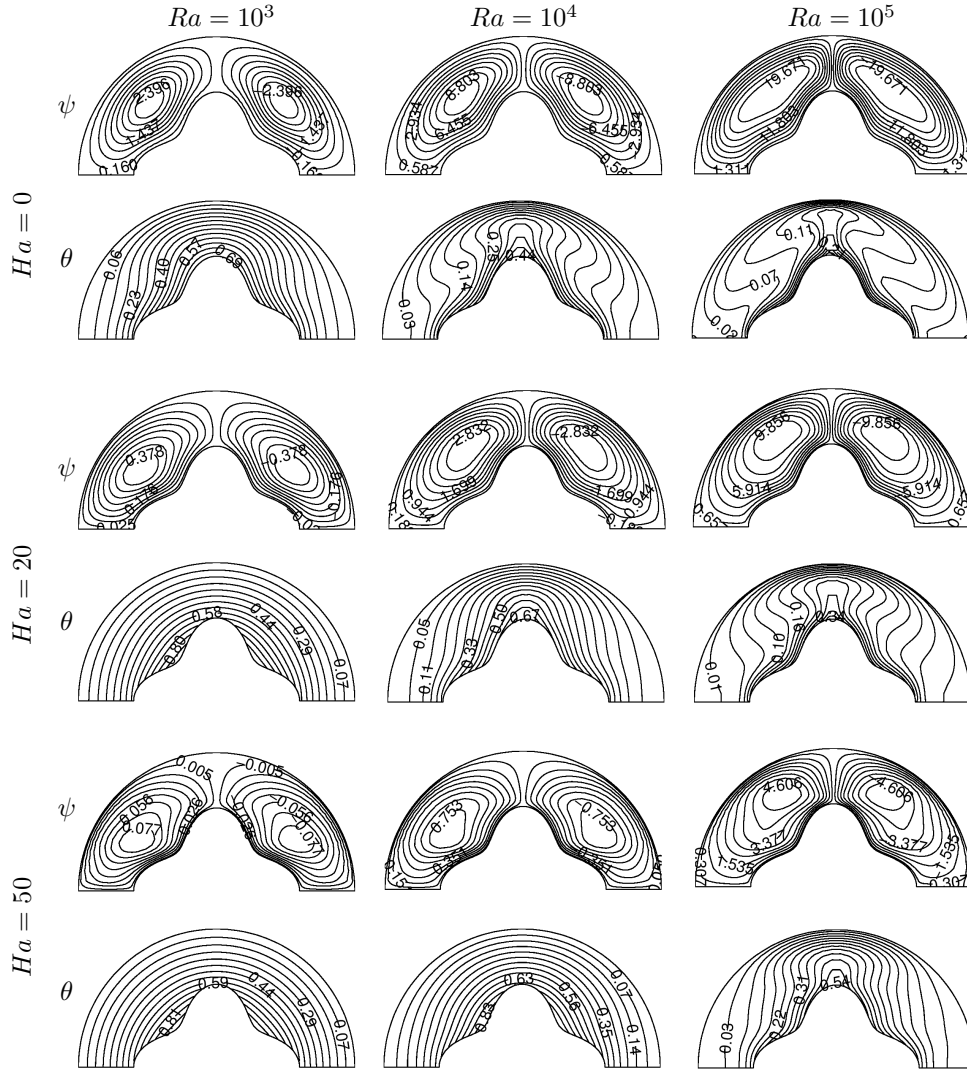


Figure 4.16: Effects of Ha and Ra on streamlines and isotherms: $\lambda = 0$, $\phi = 0.06$, $n = 4$.

other hand, the isotherms are distributed smoothly taking the shape of the inner wavy wall irrespective of the values of Ha and Ra , while there is no change in the values of temperature when compared to the case with circular inner wall.

The effect of (a) Hartmann and (b) Rayleigh numbers on \overline{Nu} is shown in Figure 4.17. It is observed that the average Nusselt number decreases with increasing Hartmann number while it increase for high values of Ra .

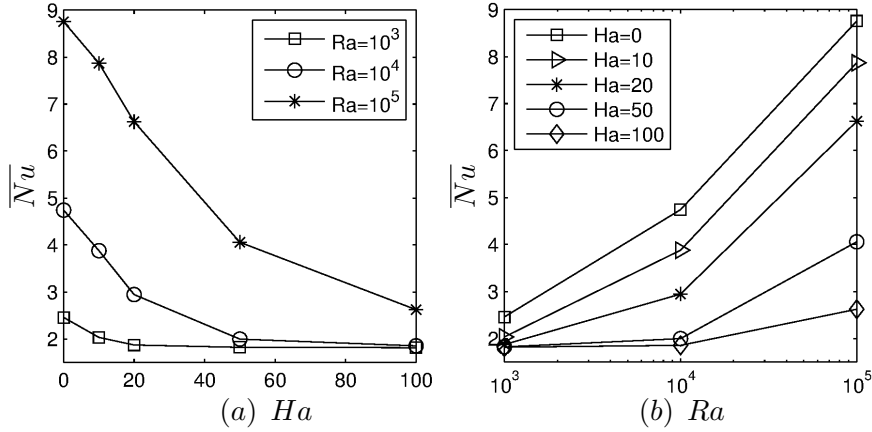


Figure 4.17: Effects of (a) Ha and (b) Ra on \overline{Nu} : $n = 4$, $\phi = 0.06$, $\lambda = 0$.

Further, the effect of solid volume fraction ϕ on \overline{Nu} is displayed in Figure 4.18. The variation of \overline{Nu} with Ha is drawn in Figure 4.18 (a) by fixing $Ra = 10^4$, and its variation with respect to Ra is shown in Figure 4.18 (b) with fixed $Ha = 10$. The average Nusselt number increases as ϕ increases at each Ha and Ra due to the addition of nanoparticles with high thermal conductivity into the base fluid.

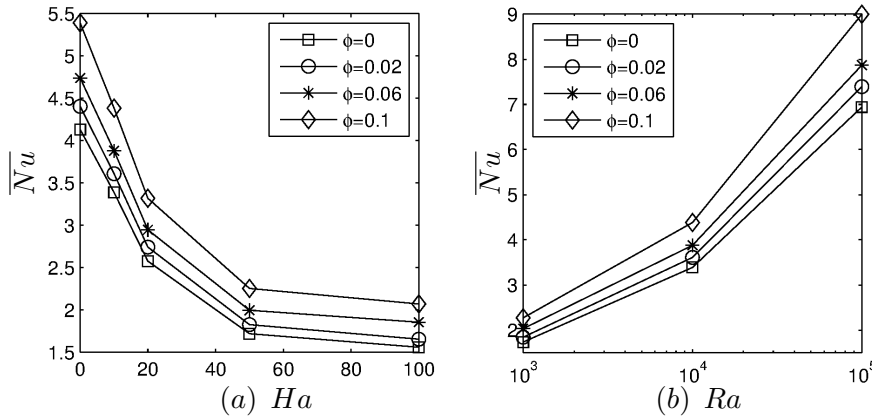


Figure 4.18: Variation of \overline{Nu} with (a) Ha and (b) Ra at different ϕ : $n = 4$, $\lambda = 0$.

The variation of \overline{Nu} with Rayleigh number at different n are displayed in Figure 4.19

(a) $Ha = 0$, (b) $Ha = 10$, (c) $Ha = 50$, (d) $Ha = 100$. At small $Ha = 0, 10$, an increase in n results in an increase in \overline{Nu} at each Ra . In addition, the increase rate in \overline{Nu} gets more as Ra increases. On the other hand, when $Ha \geq 50$ and $Ra = 10^3, 10^4$ the increasing effect of n on \overline{Nu} is deteriorated, while \overline{Nu} reincreases with n in the case of convective heat transfer at $Ra = 10^5$. This indicates that the heat transfer is enhanced when the length of the hot surface gets longer by taking more number of undulations at specific combinations of Ha and Ra .

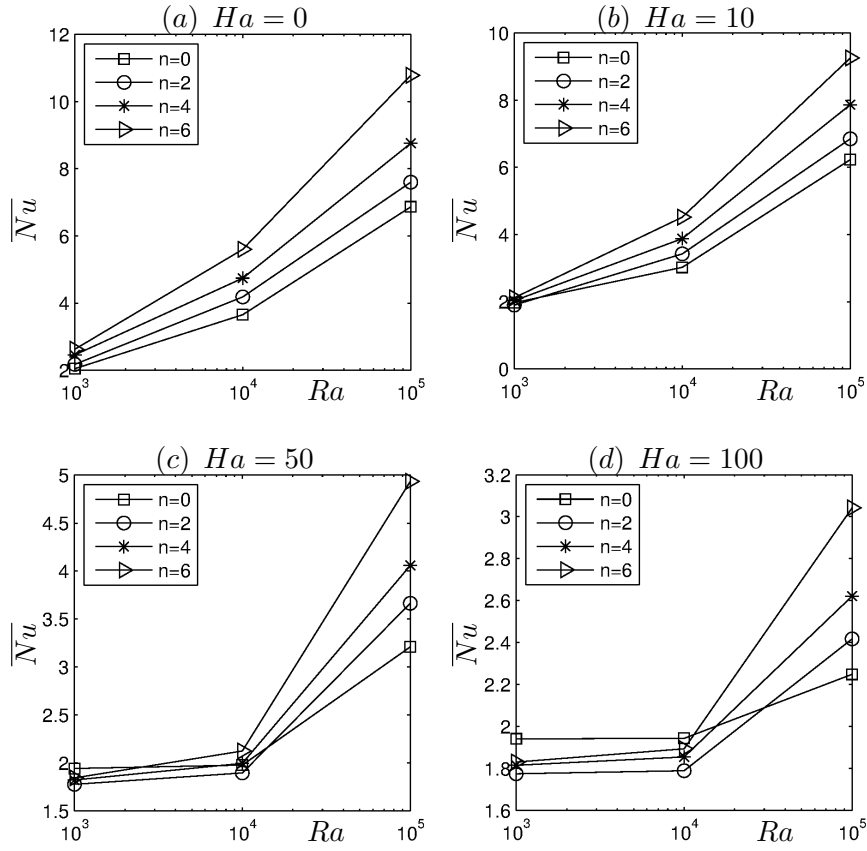


Figure 4.19: Variation of \overline{Nu} with Ra at different numbers of undulation n when $\phi = 0.06$, $\lambda = 0$: (a) $Ha = 0$, (b) $Ha = 10$, (c) $Ha = 50$, (d) $Ha = 100$.

Finally, the influence of the amplitude A of the inner wavy wall on \overline{Nu} is investigated at $Ha = 0, 10, 50, 100$, $n = 4$, $\phi = 0.06$, $\lambda = 0$ (see Figure 4.20). It is well-observed that an increase in the amplitude leads to an increase in the length of the heated portion of the inner wall, which subsequently enhances the heat transfer with increasing \overline{Nu} irrespective of the values of Ha and Ra .

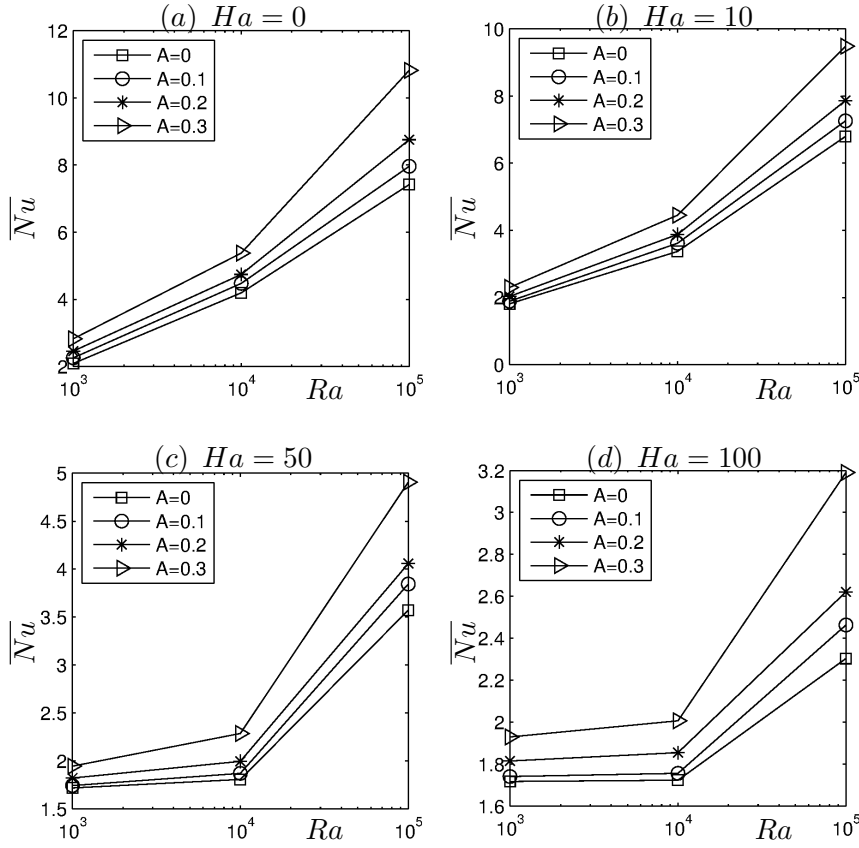


Figure 4.20: Variation of \overline{Nu} with Ra at different amplitudes A when $n = 4$, $\phi = 0.06$, $\lambda = 0$: (a) $Ha = 0$, (b) $Ha = 10$, (c) $Ha = 50$, (d) $Ha = 100$.

4.5 Summary of the Results Obtained in Chapter 4

In this chapter, we investigated a steady/unsteady MHD natural convection flow of a nanofluid in a semi-annulus enclosure with either circular or sinusoidal wavy inner walls under the effect of uniform magnetic field. The numerical results for the streamlines and isotherms, as well as the Nusselt number, are studied and depicted graphically for the effect of pertinent physical parameters. Generally, our results revealed that:

- When the inclination angle of magnetic field (λ) and the enclosure (β) are taken as zero ($\lambda = \beta = 0$), at $Ra = 10^3$ and $Ha = 0$, the cores of two equal counter-rotating vortices formed inside the enclosure. The strength of stream function decreases in magnitude as the Ha increases whereas it increases with an increase in Ra irrespective of the types of inner wall.

- On the other hand, a thermal plume is observed just above the inner circular/sinusoidal wall, when the convection regime starts to dominate the convection heat transfer. At $Ra = 10^5$, the plume gets bigger and the thermal boundary layer is formed close to the outer wall.
- As the inclination angle of enclosure increases, the symmetry of the eddies observed at $\lambda = \beta = 0$ is destroyed, positive vortex elongates with the inclination of the enclosure and becomes dominant to the secondary vortex. On the other hand, a formation of a plume in isotherms occurs on the surface of inner wall in the direction of magnetic field.
- The inclination angle of magnetic field affects the streamline and isotherm profile inside the enclosure for both circular and sinusoidal inner walls. When the magnetic field applied in horizontal direction two symmetric counter-rotating eddies are formed in streamlines, but, this symmetry is destroyed with an increase in λ . As λ reaches $\pi/2$ the counter-rotating vortices become again symmetric. On the other hand, at $\lambda = 0$, the thermal plume formed at the middle of the cavity just above the inner wall moves along the inner wall in the direction of the magnetic field.
- As expected, average Nusselt number increases with an increase in Ra whereas it decreases as Ha increases. In addition, the maximum \overline{Nu} is observed at $\lambda = \beta = 0$ in the absence of magnetic field ($Ha = 0$) and $\lambda = \beta = \pi/2$ for higher values of Ha .
- Average Nusselt number increases with increase of solid volume fraction, since the addition of high thermal conductivity nanoparticles will increase the heat transfer enhancement.
- Furthermore, at $Ha = 0, 10$, an increase in the number of undulation n of wavy wall results in an increase in \overline{Nu} at each Ra . On the other hand, when $Ha \geq 50$ and $Ra = 10^3, 10^4$, the increasing effect of n on \overline{Nu} is degenerated, while \overline{Nu} again increases in the case of convective heat transfer at $Ra = 10^5$.
- Finally, an increase in the amplitude of the inner wall leads to an enhancement in the heat transfer with increasing \overline{Nu} .

CHAPTER 5

NATURAL CONVECTION FLOW IN SEMI-ANNULUS ENCLOSURES FILLED WITH WATER-BASED FERROFLUID IN THE PRESENCE OF SPATIALLY VARIABLE MAGNETIC SOURCES

Thermal conductivity of fluid with metals, non-metals and their oxides are found more effective than the commonly used fluids such as; water, ethyle glycol, mineral oils; since using small-sized solid particles inside fluids increases their thermal conductivity as mentioned in Chapter 4. On the other hand, the dynamics of ferrofluid in the presence of magnetic field plays a significant role for an external thermal control in industry, medical technology and bio-engineering. Ferrofluids, which have the ability to reduce friction, are industrially prepared by magnetic fluids which consist of ferromagnetic particles such as; magnetite (Fe_3O_4) and hematite (Fe_2O_3), as given in details in Introduction. Briefly, ferrohydrodynamics is concerned with the mechanics of fluid motion which is influenced by strong force of magnetic polarization. This chapter deals with the dual reciprocity BEM solution of the viscous, steady, two dimensional, incompressible, laminar, ferrofluid flow in a complex geometry with sinusoidal inner wall under the effect of nodal magnetic sources. For the mathematical formulation of the problem both magnetization and electrical conductivity effects on ferrofluid are taken into account and thence the combined principles of MHD and FHD are considered. The major difference between the studies in this chapter and those in the previous chapters is to consider the effect of the magnetic field obtained from a nodal source or multiple nodal sources. To achieve the above objective, this chapter is organized as follows. The governing equations of the ferrofluid flow under the action of the applied magnetic field due to nodal magnetic source(s) and corresponding boundary conditions are introduced in Section 5.1. Section 5.2 is devoted to the application of dual reciprocity BEM to the governing equations of the problem

which is under consideration. The effect of externally applied magnetic field produced by one nodal magnet is examined in Section 5.3. In Section 5.4, the study is extended to the discussion of the influence of multiple nodal magnetic sources.

5.1 Governing Equations for the Steady MHD Convection Ferrofluid Flow

In this section, we are going to consider the governing equations of steady convection fluid flow and heat transfer in the presence of spatially variable magnetic sources (i.e. one nodal or multiple nodal magnetic sources). The problem is defined in two-dimensional semi-annulus cavity which has a sinusoidal inner wall. The shape of inner sinusoidal profile is determined by $r = r_{in} + A \cos(n\xi)$ in which r_{in} is the radius of base circle, A , n and ξ are the amplitude, number of undulations and rotation angle, respectively. The difference between radius of outer circle r_{out} and the radius of inner circle r_{in} gives the characteristic length ℓ as defined in Chapter 4. The enclosure with sinusoidal inner wall is filled with a water-based ferrofluid. The working fluid is assumed to be Newtonian and incompressible with the flow set to operate in the laminar convection regime. The magnetic Reynolds number is assumed to be so small that the induced magnetic field is neglected in comparison to the externally applied magnetic field. The governing equations are consistent with the principles of FHD and MHD. The ferrofluid has constant thermophysical properties and obeys the Boussinesq approximation. Under the above assumptions the equations governing the flow under consideration, the stream function ψ , vorticity ω and temperature θ formulation is adopted as given in Chapter 1, Equations (1.76)-(1.78):

$$\nabla^2 \psi = -\omega \quad (5.1)$$

$$\begin{aligned}
\nabla^2 \omega = & \frac{\rho_{nf}/\rho_f}{Pr_f (\mu_{nf}/\mu_f)} \left(\frac{\partial \psi}{\partial y} \frac{\partial \omega}{\partial x} - \frac{\partial \psi}{\partial x} \frac{\partial \omega}{\partial y} \right) \\
& - Mn_f \frac{\rho_{nf}/\rho_f}{\mu_{nf}/\mu_f} \left(\frac{\rho_f}{\rho_{nf}} \right) \left[-\frac{\partial \theta}{\partial x} H \frac{\partial H}{\partial y} + \frac{\partial \theta}{\partial y} H \frac{\partial H}{\partial x} \right] \\
& + Ha^2 \frac{\rho_{nf}/\rho_f}{\mu_{nf}/\mu_f} \frac{\sigma_{nf}/\sigma_f}{\rho_{nf}/\rho_f} \left[2H_x \frac{\partial H_x}{\partial x} v + H_x^2 \left(\frac{\partial v}{\partial x} \right) \right. \\
& - \frac{\partial H_x}{\partial x} H_y u - H_x \frac{\partial H_y}{\partial x} u - H_x H_y \left(\frac{\partial u}{\partial x} \right) - 2H_y \frac{\partial H_y}{\partial y} u \\
& \left. - H_y^2 \left(\frac{\partial u}{\partial y} \right) + \frac{\partial H_x}{\partial y} H_y v + H_x \frac{\partial H_y}{\partial y} v + H_x H_y \left(\frac{\partial v}{\partial y} \right) \right] \\
& - Ra \frac{\rho_{nf}/\rho_f}{\mu_{nf}/\mu_f} \frac{\beta_{nf}}{\beta_f} \frac{\partial \theta}{\partial x}
\end{aligned} \tag{5.2}$$

$$\begin{aligned}
\nabla^2 \theta = & \frac{(\rho Cp)_{nf}}{(\rho Cp)_f} \frac{k_{nf}}{k_f} \left(\frac{\partial \psi}{\partial y} \frac{\partial \theta}{\partial x} - \frac{\partial \psi}{\partial x} \frac{\partial \theta}{\partial y} \right) \\
& - Ha^2 Ec \frac{(\rho Cp)_{nf}}{k_{nf}} \frac{\sigma_{nf}}{(\rho Cp)_f} \frac{\sigma_f}{(\rho Cp)_{nf}} (u H_y - v H_x)^2 \\
& - Mn_f Ec \frac{(\rho Cp)_{nf}}{k_{nf}} \frac{(\rho Cp)_f}{(\rho Cp)_{nf}} \left[u \frac{\partial H}{\partial x} + v \frac{\partial H}{\partial y} \right] H (\epsilon_1 + \theta) \\
& - Ec \frac{(\rho Cp)_{nf}}{k_{nf}} \frac{\mu_{nf}}{(\rho Cp)_f} \left[2 \left(\frac{\partial u}{\partial x} \right)^2 + 2 \left(\frac{\partial v}{\partial y} \right)^2 + \left(\frac{\partial u}{\partial y} + \frac{\partial v}{\partial x} \right)^2 \right].
\end{aligned} \tag{5.3}$$

where $Ra_f = g\beta_f \ell^3 (T - T_c) / (\alpha_f \nu_f)$, $Pr_f = \nu_f / \alpha_f$, $Ha = \ell \mu_0 H_0 \sqrt{\sigma_f / \mu_f}$, $\epsilon_1 = T_1 / \Delta T$, $\epsilon_2 = T'_c / \Delta T$, $Ec = (\mu_f \nu_f) / [(\rho Cp)_f \Delta T \ell^2]$ and $Mn_f = \mu_0 H_0^2 K'(T_h - T_c) \ell^2 / (\mu_f \alpha_f)$ are the Rayleigh number, Prandtl number, Hartmann number arising

from MHD, temperature number, Curie temperature number, Eckert number and magnetic number arising from FHD for the base fluid, respectively.

The corresponding boundary conditions for stream function and temperature will be given in related sections and the unknown boundary conditions for the vorticity will be obtained from the stream function equation (5.1) by using radial basis functions through the application of the dual reciprocity BEM as in the previous chapters.

In addition, the thermo-physical properties of the nanoparticles (Fe_3O_4) and base fluid (water) are taken as in the work of Sheikholeslami [81] (see Table 5.1).

Table 5.1: Thermo-physical properties of water and nanoparticle [81]

	$\rho(kg/m^3)$	$C_p(j/kgK)$	$k(W/mk)$	$\beta \times 10^5(K^{-1})$	$\sigma(\Omega m)^{-1}$
Pure water	997.1	4179	0.613	21	0.05
Fe_3O_4	5200	670	6	1.3	25.000

5.2 Application of Dual Reciprocity Boundary Element Method

The governing equations of the heat transfer and the ferrofluid flow problem are discretized by using the dual reciprocity boundary element method. When we weight Equations (5.1)-(5.3) with the fundamental solution of Laplace equation $u^* = \frac{1}{2\pi} \ln(\frac{1}{r})$ and apply the Divergence theorem, we get the following integral equations

$$c_i R_i + \int_{\Gamma} (q^* R - u^* \frac{\partial R}{\partial n}) = - \int_{\Omega} b_R u^* d\Omega \quad (5.4)$$

where R is used for each unknown ψ , ω and θ and the right hand side of equations (5.1), (5.2), (5.3) are given respectively as

$$b_{\psi} = -\omega \quad (5.5)$$

$$\begin{aligned}
b_\omega = & \frac{(1-\phi)^{2.5}((1-\phi) + \phi \frac{\rho_s}{\rho_f})}{Pr_f} \int_{\Omega} [(\frac{\partial \omega}{\partial x} \frac{\partial \psi}{\partial y} - \frac{\partial \omega}{\partial y} \frac{\partial \psi}{\partial x}) \\
& - \frac{Mn_f Pr_f}{(1-\phi) + \phi \frac{\rho_s}{\rho_f}} (\frac{\partial \theta}{\partial x} H \frac{\partial H}{\partial y} + \frac{\partial \theta}{\partial y} H \frac{\partial H}{\partial x}) \\
& - \frac{Ha^2 Pr_f}{(1-\phi) + \phi \frac{\rho_s}{\rho_f}} (1 + \frac{3(\frac{\sigma_s}{\sigma_f} - 1)}{(\frac{\sigma_s}{\sigma_f} + 2) - (\frac{\sigma_s}{\sigma_f} - 1)\phi}) [2H_x \frac{\partial H_x}{\partial x} v + H_x^2 \frac{\partial v}{\partial x} \\
& - \frac{\partial H_x}{\partial x} H_y u - H_x \frac{\partial H_y}{\partial x} u - H_x H_y \frac{\partial u}{\partial x} - 2H_y \frac{\partial H_y}{\partial y} u - H_y^2 \frac{\partial u}{\partial y} + \frac{\partial H_x}{\partial y} H_y v \\
& + H_x \frac{\partial H_y}{\partial y} v + H_x H_y \frac{\partial v}{\partial y}] - Ra Pr_f ((1-\phi) + \phi \frac{\beta_s}{\beta_f}) \frac{\partial \theta}{\partial x}] u^* d\Omega
\end{aligned} \tag{5.6}$$

$$\begin{aligned}
b_\theta = & \frac{((1-\phi) + \phi \frac{(\rho C_p)_s}{(\rho C_p)_f})}{\frac{k_{nf}}{k_f}} \int_{\Omega} [(\frac{\partial \theta}{\partial x} \frac{\partial \psi}{\partial y} - \frac{\partial \theta}{\partial y} \frac{\partial \psi}{\partial x}) \\
& - \frac{Ha^2 Ec}{(1-\phi) + \phi \frac{(\rho C_p)_s}{(\rho C_p)_f}} (1 + \frac{3(\frac{\sigma_s}{\sigma_f} - 1)}{(\frac{\sigma_s}{\sigma_f} + 2) - (\frac{\sigma_s}{\sigma_f} - 1)\phi}) (u H_y - v H_x)^2 \\
& - \frac{Mn_f Ec}{(1-\phi) + \phi \frac{(\rho C_p)_s}{(\rho C_p)_f}} (u \frac{\partial H}{\partial x} + v \frac{\partial H}{\partial y}) H (\epsilon_1 + \theta) \\
& - \frac{Ec}{(1-\phi)^{2.5}((1-\phi) + \phi \frac{(\rho C_p)_s}{(\rho C_p)_f})} \{2(\frac{\partial u}{\partial x})^2 + 2(\frac{\partial v}{\partial y})^2 \\
& + (\frac{\partial u}{\partial y} + \frac{\partial v}{\partial x})^2\}] u^* d\Omega
\end{aligned} \tag{5.7}$$

where $q^* = \partial u^* / \partial n$. The right hand side of Equations (5.1)-(5.3) denoted by b_R , are treated as inhomogeneity and they are approximated by using the thin-plate spline

radial basis functions ($f_j = r^{2m} \ln r$) f_j as,

$$b_R \approx \sum_{j=1}^{N+L} \alpha_{R_j} f_j = \sum_{j=1}^{N+L} \alpha_{R_j} \nabla^2 \hat{u}_j \quad (5.8)$$

where the coefficients α_{R_j} are undetermined constants and f_j 's are linked through the particular solutions \hat{u}_j of Poisson equation $\nabla^2 \hat{u}_j = f_j$. Thus, Equation (5.4) takes the form

$$c_i R_i + \int_{\Gamma} (q^* R - u^* \frac{\partial R}{\partial n}) d\Gamma = \sum_{j=1}^{N+L} \alpha_{R_j} \left[c_i \hat{u}_{ji} + \int_{\Gamma} (q^* \hat{u}_j - u^* \hat{q}_j) d\Gamma \right] \quad (5.9)$$

which contains only the boundary integral equation and $\hat{q} = \partial \hat{u}_j / \partial n$. By discretizing the boundary with constant elements, the matrix-vector form of Equation (5.9) can be expressed for each unknowns $R (= \psi, \omega, \theta)$, as

$$\mathbf{H}\psi - \mathbf{G}\psi_q = (\mathbf{H}\hat{\mathbf{U}} - \mathbf{G}\hat{\mathbf{Q}})\mathbf{F}^{-1}(-\omega) \quad (5.10)$$

$$\begin{aligned} \mathbf{H}\omega - \mathbf{G}\omega_q &= (\mathbf{H}\hat{\mathbf{U}} - \mathbf{G}\hat{\mathbf{Q}})\mathbf{F}^{-1} \frac{(1-\phi)^{2.5}((1-\phi) + \phi \frac{\rho_s}{\rho_f})}{Pr_f} \left\{ (\mathbf{u} \frac{\partial \omega}{\partial x} + \mathbf{v} \frac{\partial \omega}{\partial y}) \right. \\ &\quad - \frac{Mn_f Pr_f}{(1-\phi) + \phi \frac{\rho_s}{\rho_f}} \left(-\frac{\partial \theta}{\partial x} H \frac{\partial H}{\partial y} + \frac{\partial \theta}{\partial y} H \frac{\partial H}{\partial x} \right) \\ &\quad - \frac{Ha^2 Pr_f}{(1-\phi) + \phi \frac{\rho_s}{\rho_f}} \left(1 + \frac{3(\frac{\sigma_s}{\sigma_f} - 1)}{(\frac{\sigma_s}{\sigma_f} + 2) - (\frac{\sigma_s}{\sigma_f} - 1)\phi} \right) \\ &\quad \times \left[2H_x \frac{\partial H_x}{\partial x} \mathbf{v} + H_x^2 \frac{\partial \mathbf{v}}{\partial x} - \frac{\partial H_x}{\partial x} H_y \mathbf{u} - H_x \frac{\partial H_y}{\partial x} \mathbf{u} - H_x H_y \frac{\partial \mathbf{u}}{\partial x} \right. \\ &\quad \left. - 2H_y \frac{\partial H_y}{\partial y} \mathbf{u} - H_y^2 \frac{\partial \mathbf{u}}{\partial y} + \frac{\partial H_x}{\partial y} H_y \mathbf{v} + H_x \frac{\partial H_y}{\partial y} \mathbf{v} + H_x H_y \frac{\partial \mathbf{v}}{\partial y} \right] \\ &\quad \left. - Ra Pr_f ((1-\phi) + \phi \frac{\beta_s}{\beta_f}) \frac{\partial \theta}{\partial x} \right\} \end{aligned} \quad (5.11)$$

$$\begin{aligned}
\mathbf{H}\boldsymbol{\theta} - \mathbf{G}\boldsymbol{\theta}_q &= (\mathbf{H}\hat{\mathbf{U}} - \mathbf{G}\hat{\mathbf{Q}})\mathbf{F}^{-1} \frac{(1-\phi) + \phi \frac{(\rho C_p)_s}{(\rho C_p)_f}}{\frac{k_{nf}}{k_f}} \left\{ \mathbf{u} \frac{\partial \boldsymbol{\theta}}{\partial x} + \mathbf{v} \frac{\partial \boldsymbol{\theta}}{\partial y} \right. \\
&\quad - \frac{Ha^2 Ec}{(1-\phi) + \phi \frac{(\rho C_p)_s}{(\rho C_p)_f}} \left(1 + \frac{3\left(\frac{\sigma_s}{\sigma_f} - 1\right)}{\left(\frac{\sigma_s}{\sigma_f} + 2\right) - \left(\frac{\sigma_s}{\sigma_f} - 1\right)\phi} \right) (\mathbf{u}H_y - \mathbf{v}H_x)^2 \\
&\quad - \frac{Mn_f Ec}{(1-\phi) + \phi \frac{(\rho C_p)_s}{(\rho C_p)_f}} \left(\mathbf{u} \frac{\partial H}{\partial x} + \mathbf{v} \frac{\partial H}{\partial y} \right) H(\epsilon_1 + \boldsymbol{\theta}) \\
&\quad - \frac{Ec}{(1-\phi)^{2.5}((1-\phi) + \phi \frac{(\rho C_p)_s}{(\rho C_p)_f})} \left[2\left(\frac{\partial \mathbf{u}}{\partial x}\right)^2 + 2\left(\frac{\partial \mathbf{v}}{\partial y}\right)^2 \right. \\
&\quad \left. \left. + \left(\frac{\partial \mathbf{v}}{\partial x} - \frac{\partial \mathbf{u}}{\partial y}\right)^2 \right] \right\}. \tag{5.12}
\end{aligned}$$

where the matrices $\hat{\mathbf{U}}$ and $\hat{\mathbf{Q}}$ are constructed by taking each of the vectors \hat{u}_j and \hat{q}_j as columns, respectively. The matrix \mathbf{F} consists of vectors f_j of size $(N+L)$ as columns. The components of the matrices \mathbf{G} and \mathbf{H} are obtained by taking the integral of the fundamental solution u^* and its normal derivative along each boundary elements Γ_j , respectively. The DRBEM equations (5.10)-(5.12) are coupled so that they are solved iteratively. In each iteration, the required space derivatives of the unknowns ψ , ω and $\boldsymbol{\theta}$, and also the unknown vorticity boundary conditions are obtained by using the coordinate matrix \mathbf{F} .

5.3 Steady MHD Convection Ferrofluid Flow in a Semi-Annulus with Sinusoidal Inner Wall under the Effect of a Nodal Magnetic Source

As a first application, the steady MHD convective fluid flow in a complex geometry of half-annulus enclosure filled with water-based ferrofluid containing Fe_3O_4 particle is solved by using DRBEM. The flow is subjected to an external magnetic field generated with a nodal magnetic source placed just below the inner wall. Hence, the

intensity of the magnetic field depends on the position of a nodal magnet. The non-dimensional form of ψ , ω and θ equations are given in Section 5.1 with Equations (5.1)-(5.3).

The geometry and the boundary conditions of this problem are shown in Figure 5.1 for (a) circular and (b) sinusoidal inner walls. The inner and outer walls are maintained at constant hot ($\theta = 1$) and cold ($\theta = 0$) temperatures, respectively, while the flat walls at the bottom are kept as adiabatic. No-slip boundary conditions are employed at all walls.

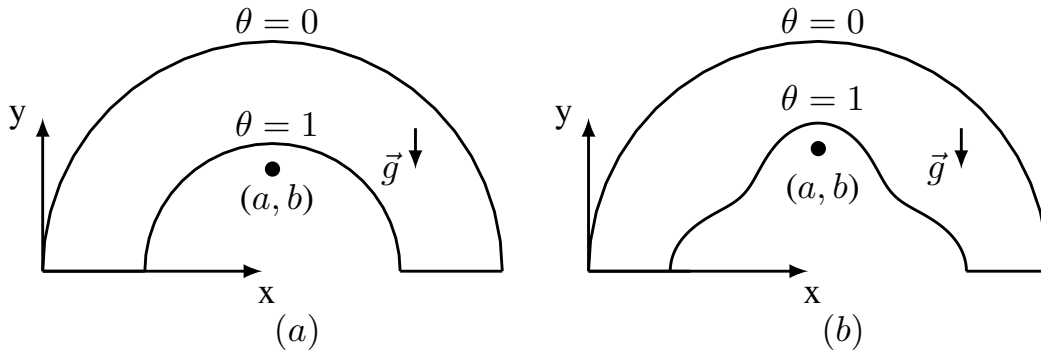


Figure 5.1: Geometry of the problem with boundary conditions

The corresponding boundary conditions for ψ and θ are given as follows:

$$\begin{aligned}
 \text{At the inner circular/sinusoidal wall: } & \psi = 0, \theta = 1 \\
 \text{At the outer circular wall: } & \psi = 0, \theta = 0 \\
 \text{At the flat parts of bottom walls: } & \psi = 0, \frac{\partial \theta}{\partial n} = 0.
 \end{aligned} \tag{5.13}$$

The unknown boundary conditions for the vorticity can be obtained by using the stream function equation (5.1) through the application of DRBEM as in the previous chapters.

A nodal magnetic source is placed below the mid of the inner wall at the position (a, b) . The intensity (H_x, H_y) and the strength of the magnetic field (H) are given in

the following non-dimensional form (as given in Equation (1.79)):

$$H_x = \frac{|b|(y-b)}{(x-a)^2 + (x-b)^2}, \quad H_y = -\frac{|b|(x-a)}{(x-a)^2 + (x-b)^2},$$

$$H = \frac{|b|}{\sqrt{(x-a)^2 + (x-b)^2}}.$$

In the present study, the magnetic source is located at $(a = 0, b = 1.15)$.

The numerical simulations are performed to investigate the influence of the magnetic field produced by a nodal magnet on the flow and heat transfer. The effects of the controlling parameters, namely Rayleigh number ($Ra = 10^3, 10^4, 10^5$), Hartmann number arising from MHD ($Ha = 0, 5, 10$), magnetic number arising from FHD ($Mn_f = 0, 500$), solid volume fraction ($\phi = 0, 0.02, 0.04, 0.1$), number of undulation ($n = 0, 2, 4, 6$) and amplitude ($A = 0, 0.1, 0.2, 0.3$) along the wavy wall are examined for the convective heat transfer enhancement in a semi-annulus enclosure. In all calculations, the Prandtl number ($Pr = 6.8$), temperature number ($\epsilon_1 = 0$) and Eckert number ($Ec = 10^{-5}$) are kept fixed.

Figure 5.2 shows the comparison between pure fluid ($\phi = 0$) and nanofluid ($\phi = 0.04$) via streamlines and isotherm contours. As the solid volume fraction increases, the intensity of streamlines increases, due to an increase in energy transport through the flow because of irregular motion of the ultra fine particles. Hence, the strength of stream function in magnitude ($|\psi|_{\max} = 11.5867$ when $\phi = 0.04$ while $|\psi|_{\max} = 11.0043$ when $\phi = 0$) increases with increasing the volume fraction of nanofluid.

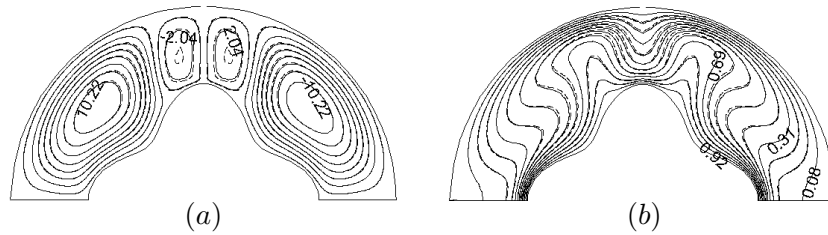


Figure 5.2: Comparison of streamlines and isotherm between nanofluid ($\phi = 0.04$) (---) and pure fluid ($\phi = 0$) (—) when $Ra = 10^4$, $Ha = 5$ and $Mn_f = 500$.

In order to ensure that the computations are accurate and grid independent, the effect of number of boundary elements has been examined in terms of $|\psi|_{\max}$, $|\theta|_{\max}$ and \overline{Nu} using both constant and linear element discretizations. In Figure 5.3, the grid

independence test is displayed for the case when $Ra = 10^4$, $Ha = 5$, $Mn_F = 500$, $\phi = 0.04$. It is evident that \overline{Nu} , $|\psi|_{\max}$ and $|\theta|_{\max}$ show no significant change for $N \geq 450$ in both constant and linear elements. Thus, in the following computations maximum $N = 450$ constant boundary elements have been used.

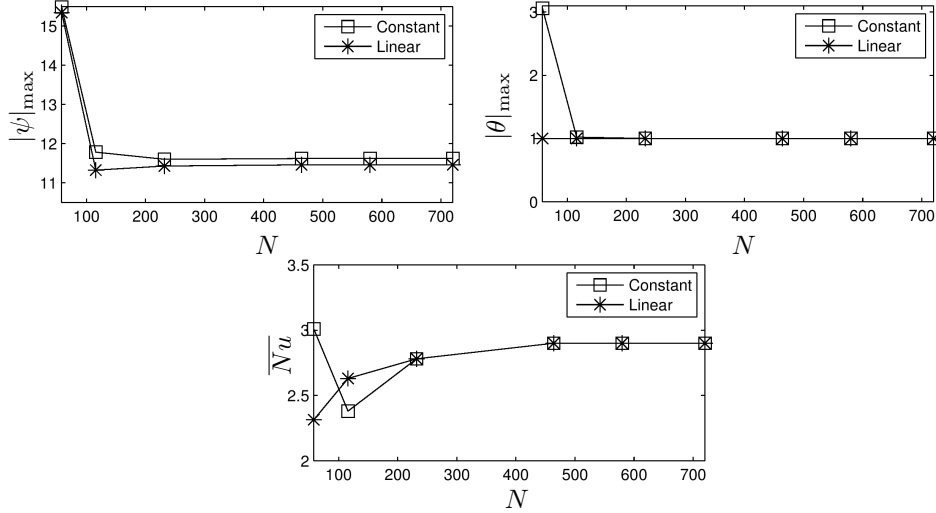


Figure 5.3: Grid dependency: $Ra = 10^4$, $Ha = 5$, $Mn_f = 500$, $\phi = 0.04$, $A = 0.2$, $n = 4$.

In order to demonstrate the validity and accuracy of the numerical scheme, the unsteady natural convection in a nanofluid-filled square enclosure cavity with a heat source at the bottom solved by Nugyen [58] and Aminossadati [5] has been considered as a test problem. The comparison of present results with previously published results is displayed in Table 5.2 in terms of $|\psi|_{\max}$, $|\theta|_{\max}$ and \overline{Nu} at different Ra . It is observed that the present numerical procedure is accurate and there is a quite well agreement between the present calculations and the previous works.

In Figure 5.4, 5.5 and 5.6, the effect of the Hartmann and magnetic numbers on the flow and temperature fields are displayed in an enclosure with (a) circular and (b) sinusoidal inner wall by fixing $Ra = 10^3$, $Ra = 10^4$ and $Ra = 10^5$, respectively. In the absence of magnetic field (i.e. $Mn_f = Ha = 0$) the formation of two symmetrical counter rotating vortices are observed inside the enclosure at each Ra . As the Ha increases, the strength of stream function decreases in magnitude due to the retarding effect of the magnetic field on the velocity. In addition, an increase in Ha from 0 to 5 when $Mn_f = 0$ and $Ra = 10^3$, $Ra = 10^5$ makes no significant difference on the profiles of the stream function and temperature, but the flow behavior

Table 5.2: Code validation in terms of $|\psi|_{max}$, $|\theta|_{max}$ and \overline{Nu} .

		Present study	Nugyen [58]	Aminossadati [5]
$Ra = 10^3$	\overline{Nu}	5.454	5.412	5.451
	$ \psi _{max}$	0.020	0.023	0.023
	$ \theta _{max}$	0.205	0.203	0.205
$Ra = 10^4$	\overline{Nu}	5.475	5.432	5.474
	$ \psi _{max}$	0.216	0.204	0.205
	$ \theta _{max}$	0.206	0.204	0.205
$Ra = 10^5$	\overline{Nu}	7.082	7.016	7.121
	$ \psi _{max}$	2.494	2.966	2.988
	$ \theta _{max}$	0.177	0.171	0.172

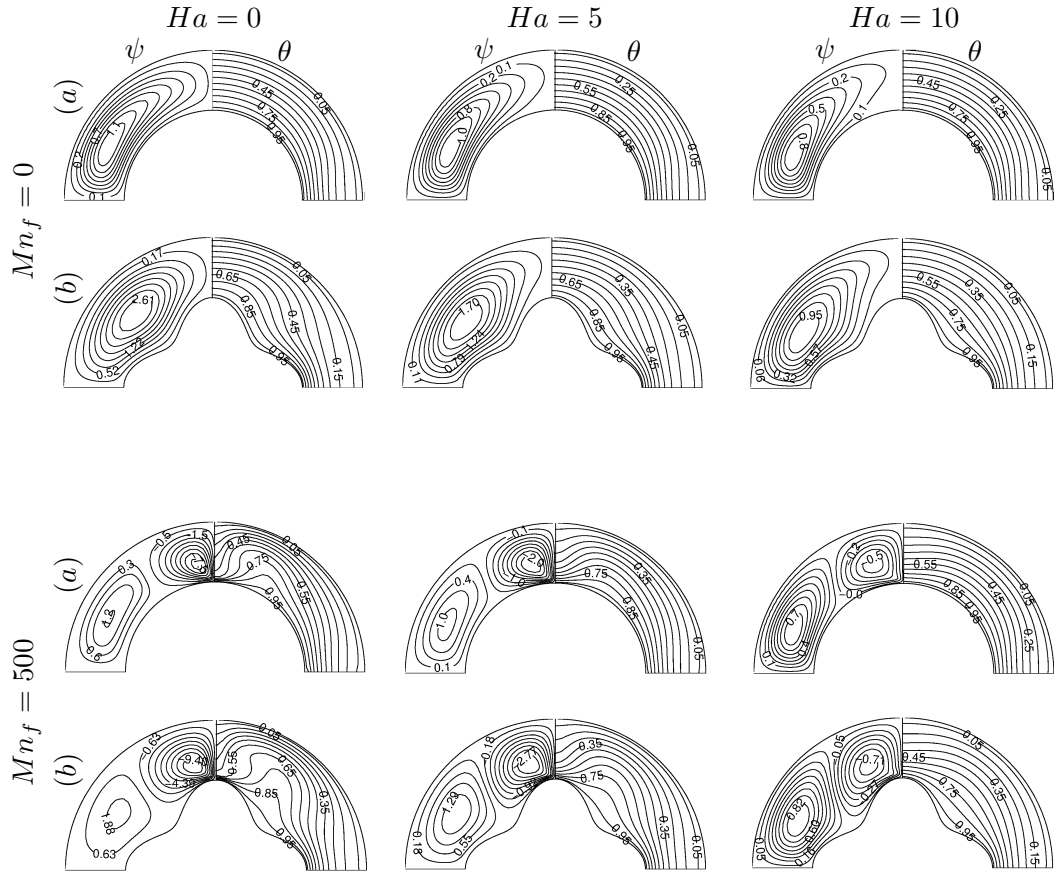


Figure 5.4: Effects of Ha and Mn_f on streamlines and isotherms: $Ra = 10^3$, $\phi = 0.04$, (a) $n = 0$, (b) $n = 4$.

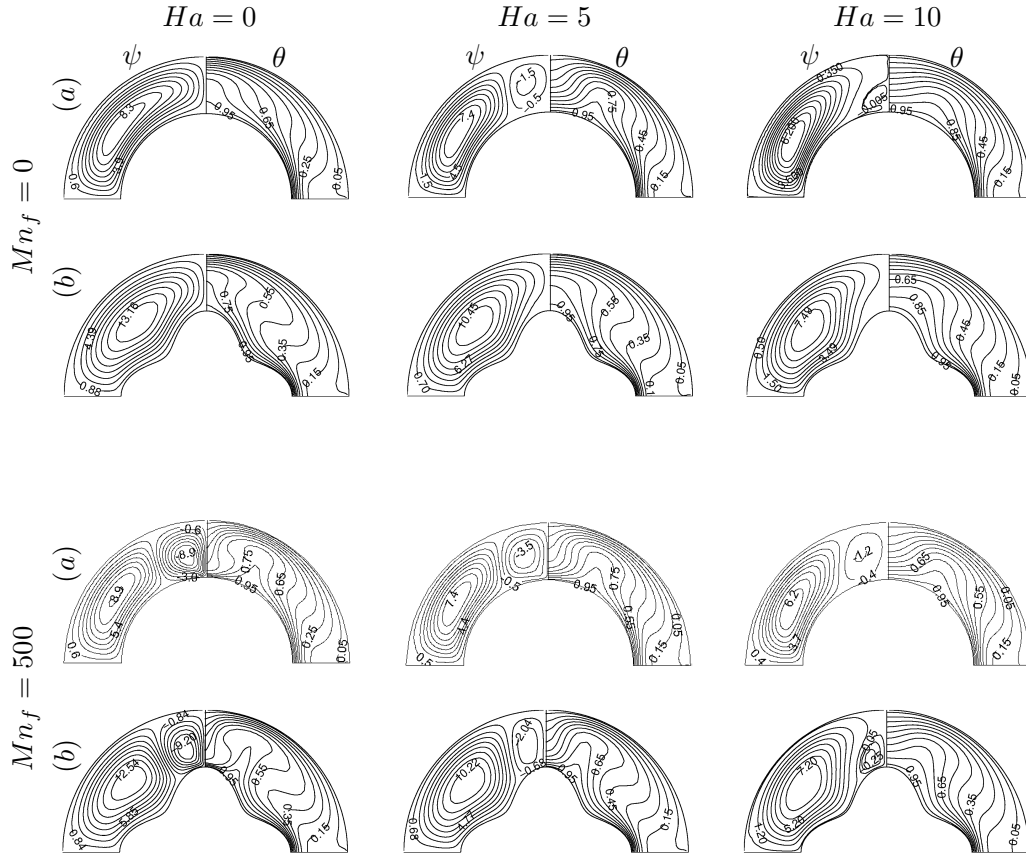


Figure 5.5: Effects of Ha and Mn_f on streamlines and isotherms: $Ra = 10^4$, $\phi = 0.04$, (a) $n = 0$, (b) $n = 4$.

inside the enclosure with circular wall alters dramatically for $Ra = 10^4$. That is, the main vortex moves towards the bottom wall following the formation of small-sized secondary eddy and with a further increase in $Ha = 10$ the secondary eddy gets weaker near the vertical centerline. An increase in Mn_f to 500 at low $Ra = 10^3$, $Ra = 10^4$, results also the formation of a secondary eddy in the region just above the magnetic source. This eddy vanishes at the highest $Ra = 10^5$. This indicates that the convection dominance due to the high Ra , decreases the effect of Mn_f . At $Ra = 10^5$, the symmetric eddies in the streamline profile elongate upward towards the magnetic source and they become stronger when compared to the cases $Ra = 10^3$ and $Ra = 10^4$. On the other hand, at $Ra = 10^3$ and $Mn_f = 0$ the isotherms show similar behavior for $Ha = 0$, $Ha = 5$ and $Ha = 10$ in all cases, which indicates that Ha has no significant role on the temperature distribution. But, as magnetic number increases to $Mn_F = 500$ when $Ra = 10^3$, three thermal plumes occur in the isotherm profiles and the isotherms become dense in the region just above the magnetic source.

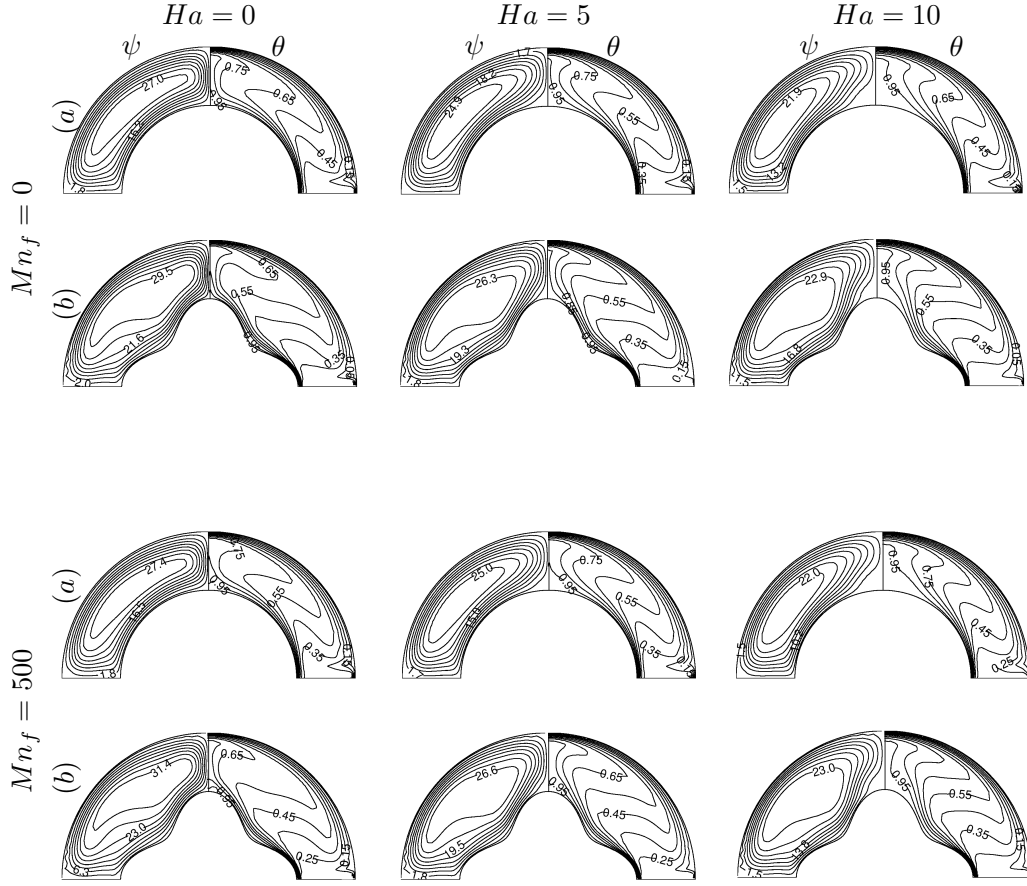


Figure 5.6: Effects of Ha and Mn_f on streamlines and isotherms: $Ra = 10^5$, $\phi = 0.04$, (a) $n = 0$, (b) $n = 4$.

Thermal plumes become weaker and isotherms become more parallel to each other as the Ha increases. Moreover, the thermal plumes formed at only high $Mn_f = 500$ when $Ra = 10^3$, $Ha = 0, 5$ are observed in all cases when $Ra = 10^4$ and $Ra = 10^5$ since the heat transfer becomes dominated by convection. Further, at $Ra = 10^5$, the thermal plumes become stronger and they crush on the outer wall. As a result, the isotherms become dense just under the outer wall. It is also observed that Ha and Mn_f do not have much significant effects on both flow and temperature fields at $Ra = 10^5$.

As it can be seen in Figures 5.4, 5.5 and 5.6, there is no significant changes in the profiles of streamlines and isotherms due to shape of the heat source. However, the strength of stream function in magnitude is bigger in the sinusoidal heater compared to its circular counterpart. Moreover, the basic difference on the streamlines due to the shape of the inner wall occurs when $Ra = 10^4$, $Mn_f = 0$, $Ha = 5$ and $Ha = 10$.

That is, an additional eddy is formed in the streamlines when the inner wall is circular, while in the case of sinusoidal inner wall no secondary eddy is observed.

The effects of Hartmann and Rayleigh numbers on \overline{Nu} are displayed in Figure 5.7 when $n = 4$ and $\phi = 0.04$ at $Mn_f = 0$ and $Mn_f = 500$. It is observed that the \overline{Nu} increases with an increase in Ra whereas it decreases as the Ha increases. On the other hand, magnetic number has different effect on \overline{Nu} according to the corresponding Ra . That is, \overline{Nu} increases with an increase in magnetic number when the conduction and transition regimes are dominant ($Ra = 10^3$ and 10^4). However, at $Ra = 10^5$, \overline{Nu} decreases as the magnetic number increases.

Figure 5.8 shows the variation of \overline{Nu} with Rayleigh number at different (a) number of undulation n and (b) the amplitude A of the inner wall when $Ha = 0$ and $Mn_f = 0$.

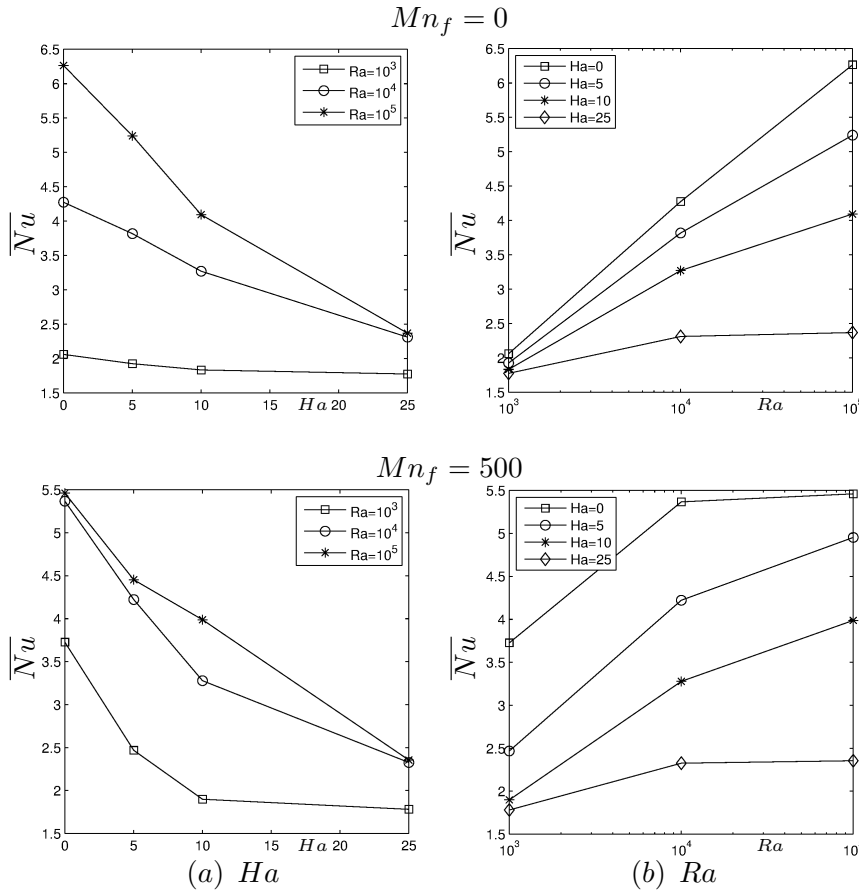


Figure 5.7: Effects of (a) Ha and (b) Ra on \overline{Nu} : $n = 4$, $\phi = 0.04$.

In Figure 5.8(a), generally, an increase in n leads to an increase in \overline{Nu} , but at small $Ra = 10^3$, n increases from 0 to 2, \overline{Nu} decreases. Also it can be seen from the Figure 5.8(a), \overline{Nu} shows almost identical behavior when the transition and convection

regimes are dominant at $n = 0$ and $n = 2$, and at $n = 4$ and $n = 6$, respectively. On the other hand, Figure 5.8(b) displays that an increase in amplitude results in an increase in the length of the hot surface, which leads to an increase in the heat transfer rate with increasing \overline{Nu} at each Ra .

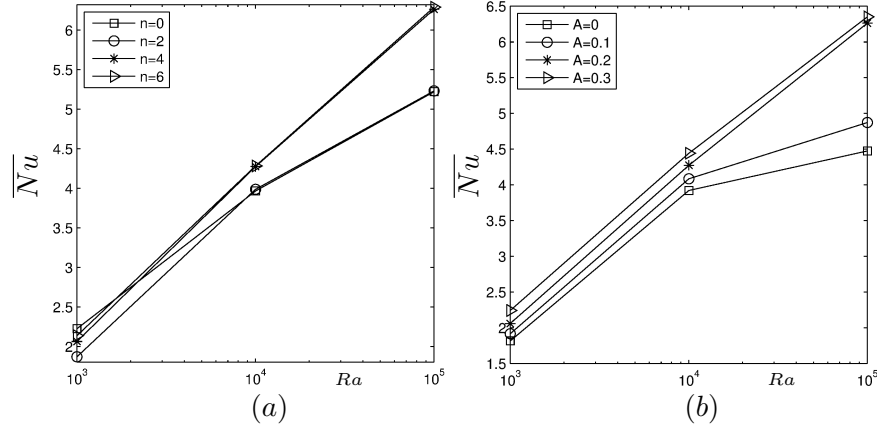


Figure 5.8: Variation of \overline{Nu} with Ra at different numbers of undulation n and amplitude A when $\phi = 0.04$, $Ha = 0$, $Mn_f = 0$.

Moreover, Figure 5.9 shows the influence of solid volume ϕ on \overline{Nu} by fixing $Mn_f = 500$. In Figure 5.9 (a), the variation of \overline{Nu} with Ha is displayed with fixed $Ra = 10^4$, and in Figure 5.9 (b), the variation of \overline{Nu} with respect to Ra is shown by fixing $Ha = 5$. The obtained results revealed that the \overline{Nu} increases with an increase in ϕ at each Ha and Ra since adding nanoparticles to the fluid increases the energy transport through the flow and subsequently enhances the heat transfer rate with increasing \overline{Nu} .

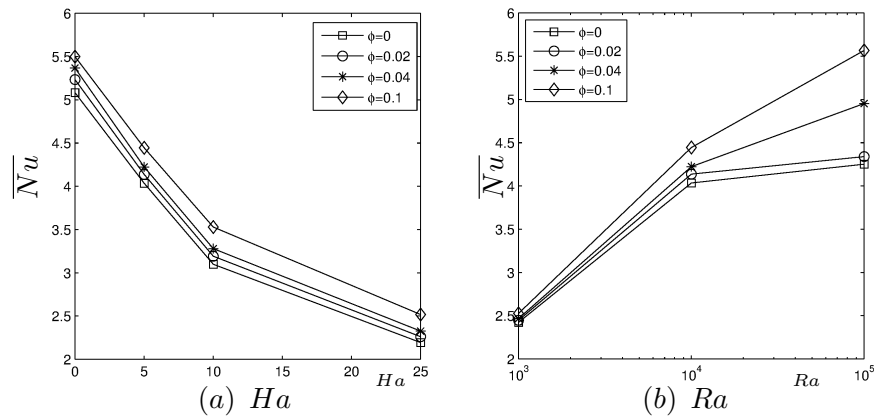


Figure 5.9: Variation of \overline{Nu} with (a) Ha and (b) Ra at different ϕ : $n = 4$.

5.4 Steady MHD Convection Ferrofluid Flow in a Semi-Annulus with Sinusoidal Inner Wall under the Effect of Multiple Nodal Magnetic Sources

A schematic description of the physical domain of the problem is shown in Figure 5.10 (a) where the outer wall is a rectangle and Figure 5.10 (b) where the outer wall is a circle. The enclosure is filled with Fe_3O_4 -water nanofluid. The inner sinusoidal wall is under constant heat flux whereas the outer wall is maintained at constant cold temperature; the bottom horizontal walls are assumed to be adiabatic. The shape of the inner sinusoidal profile is defined by; $r = r_{in} + A \cos(n(\xi))$, where r_{in} is the base circle radius, A and n are amplitude and undulations respectively. ξ is the rotation angle.

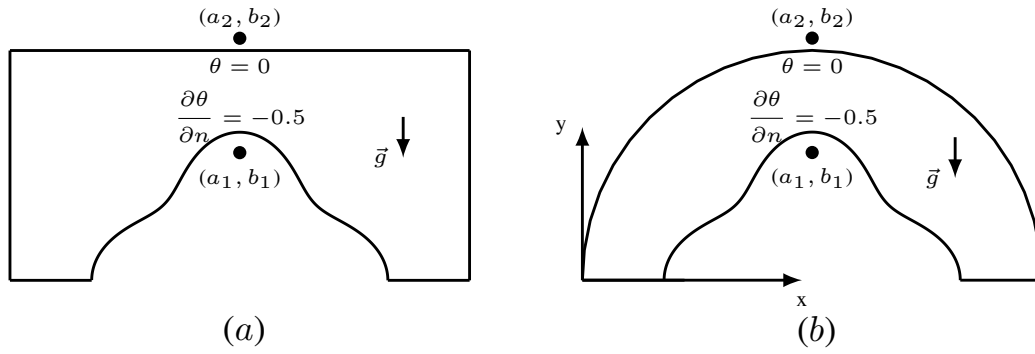


Figure 5.10: Geometry of the problem with boundary conditions

The corresponding boundary conditions are given as follows:

$$\begin{aligned}
 \text{At the inner sinusoidal wall:} \quad & \psi = 0, \quad \frac{\partial \theta}{\partial n} = -0.5 \\
 \text{At the outer rectangular wall:} \quad & \psi = 0, \quad \theta = 0 \\
 \text{At the flat parts of bottom walls:} \quad & \psi = 0, \quad \frac{\partial \theta}{\partial n} = 0.
 \end{aligned} \tag{5.14}$$

The unknown boundary conditions for the vorticity can be obtained by using the stream function equation (5.1) through the application of DRBEM, as in the previous problems.

The non-dimensional form of the components of magnetic field intensity (H_x, H_y) and the strength of magnetic field (H) for two nodal sources are given as in Section

1.4.3, Equation (1.80):

$$H_x = \left| \frac{b_1 b_2}{b_1 + b_2} \right| \left(\frac{y - b_1}{(x - a_1)^2 + (y - b_1)^2} + \frac{y - b_2}{(x - a_2)^2 + (y - b_2)^2} \right),$$

$$H_y = - \left| \frac{b_1 b_2}{b_1 + b_2} \right| \left(\frac{x - a_1}{(x - a_1)^2 + (y - b_1)^2} + \frac{x - a_2}{(x - a_2)^2 + (y - b_2)^2} \right),$$

$$H = \left| \frac{b_1 b_2}{b_1 + b_2} \right| \sqrt{\frac{(2x - a_1 - a_2)^2 + (2y - b_1 - b_2)^2}{[(x - a_1)^2 + (y - b_1)^2][(x - a_2)^2 + (y - b_2)^2]}}.$$

In the present study, the magnetic sources are located below the inner wall at $(a_1 = 0, b_1 = 1.15)$ and above the upper wall at $(a_2 = 0, b_2 = 2.05)$.

A computational analysis has been done to inspect the effect of magnetic field produced by two nodal magnetic sources on the flow and heat transfer. The considered parameters are Rayleigh number ($Ra = 10^3, 10^4, 10^5$), Hartmann number ($Ha = 0, 5, 10$), magnetic number ($Mn_f = 0, 100$), solid volume fraction ($\phi = 0, 0.04, 0.08, 0.1$), number of undulation ($n = 0, 2, 4, 6$) and amplitude ($A = 0, 0.1, 0.2, 0.3$) along the wavy wall. In all calculations, the Prandtl number ($Pr = 6.8$), temperature number ($\epsilon_1 = 0$) and Eckert number ($Ec = 10^{-6}$) are kept fixed. Results are presented by means of streamlines, isotherms and average Nusselt number.

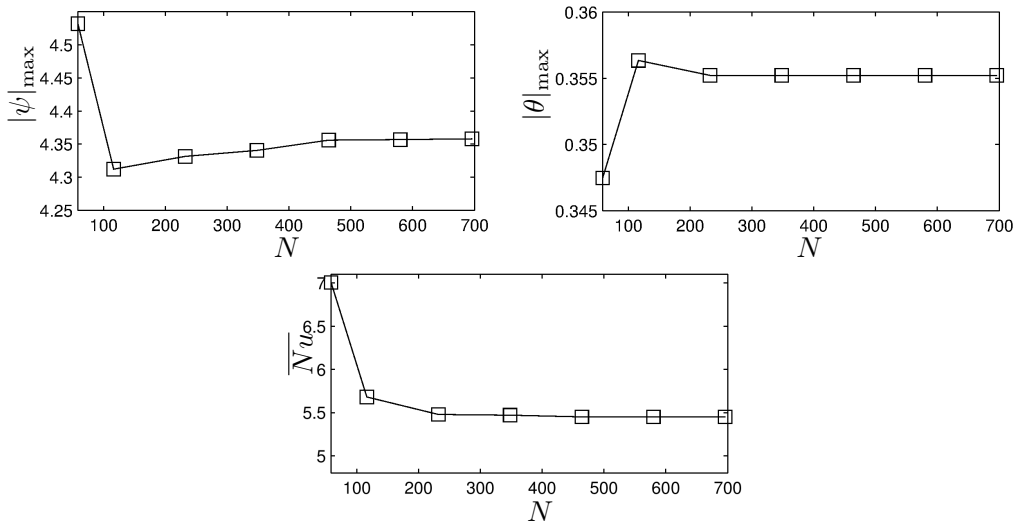


Figure 5.11: Grid dependency: $Ra = 10^4$, $Ha = 10$, $Mn_f = 100$, $\phi = 0.04$, $A = 0.2$, $n = 4$.

In Figure 5.11, a grid independent test is performed to ensure the numerical accuracy of the computation via $|\psi|_{max}$, $|\theta|_{max}$ and \overline{Nu} . It is well-observed that after reaching the grid size having constant element number $N \approx 450$, $|\psi|_{max}$, $|\theta|_{max}$ and \overline{Nu} becomes less sensitive to the number of boundary elements. Thus, for the present problem $N = 450$ is taken as the optimum grid number of boundary elements and all the simulations are carried out at this specified grid size.

Consequences of the magnetic field produced by multiple nodal magnetic sources on streamlines and isotherms are illustrated in Figures 5.12, 5.13 and 5.14 with different Hartmann numbers for $Mn_f = 0$ and $Mn_f = 100$. The effect of pertinent parameters on flow and thermal conductivity are displayed in enclosures with (a) circular, (b) si-

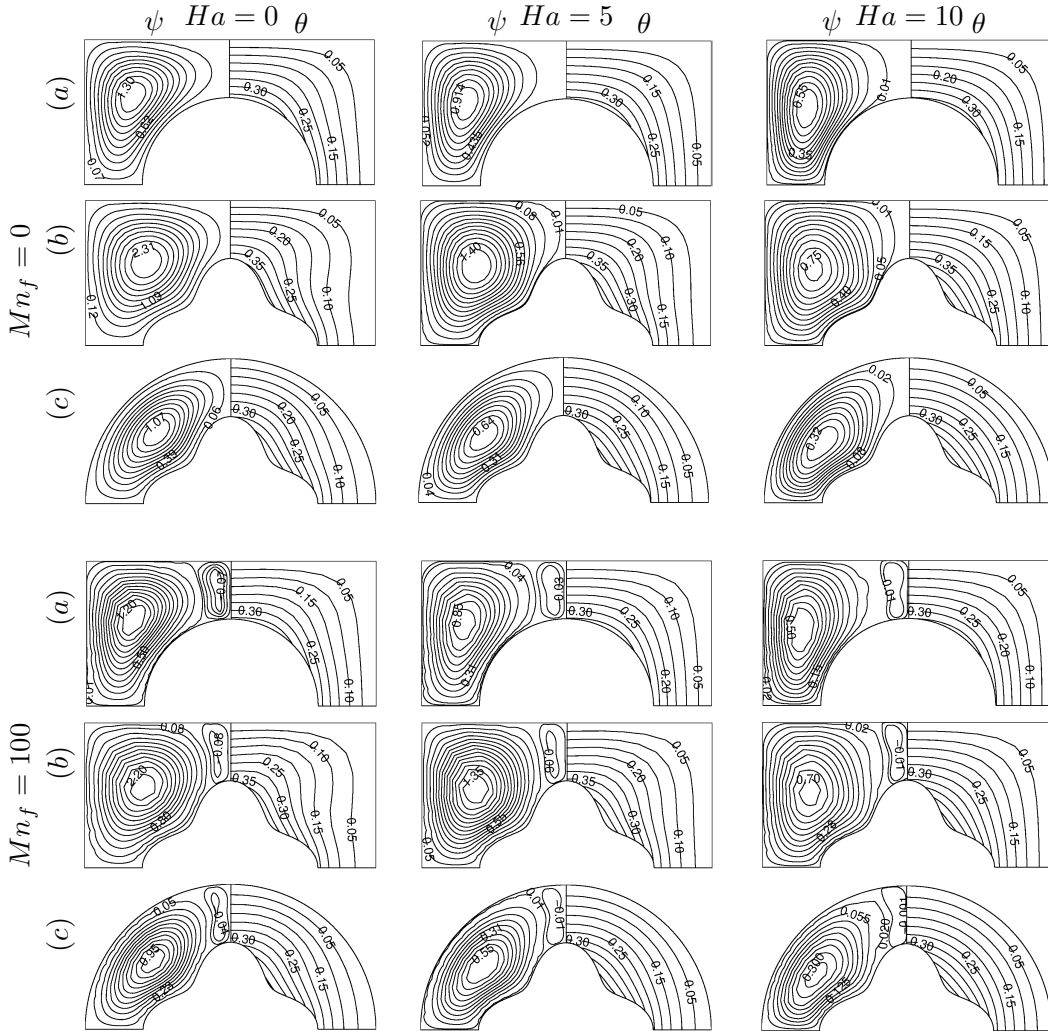


Figure 5.12: Effects of Ha and Mn_f on streamlines and isotherms: $Ra = 10^3$, $\phi = 0.04$.

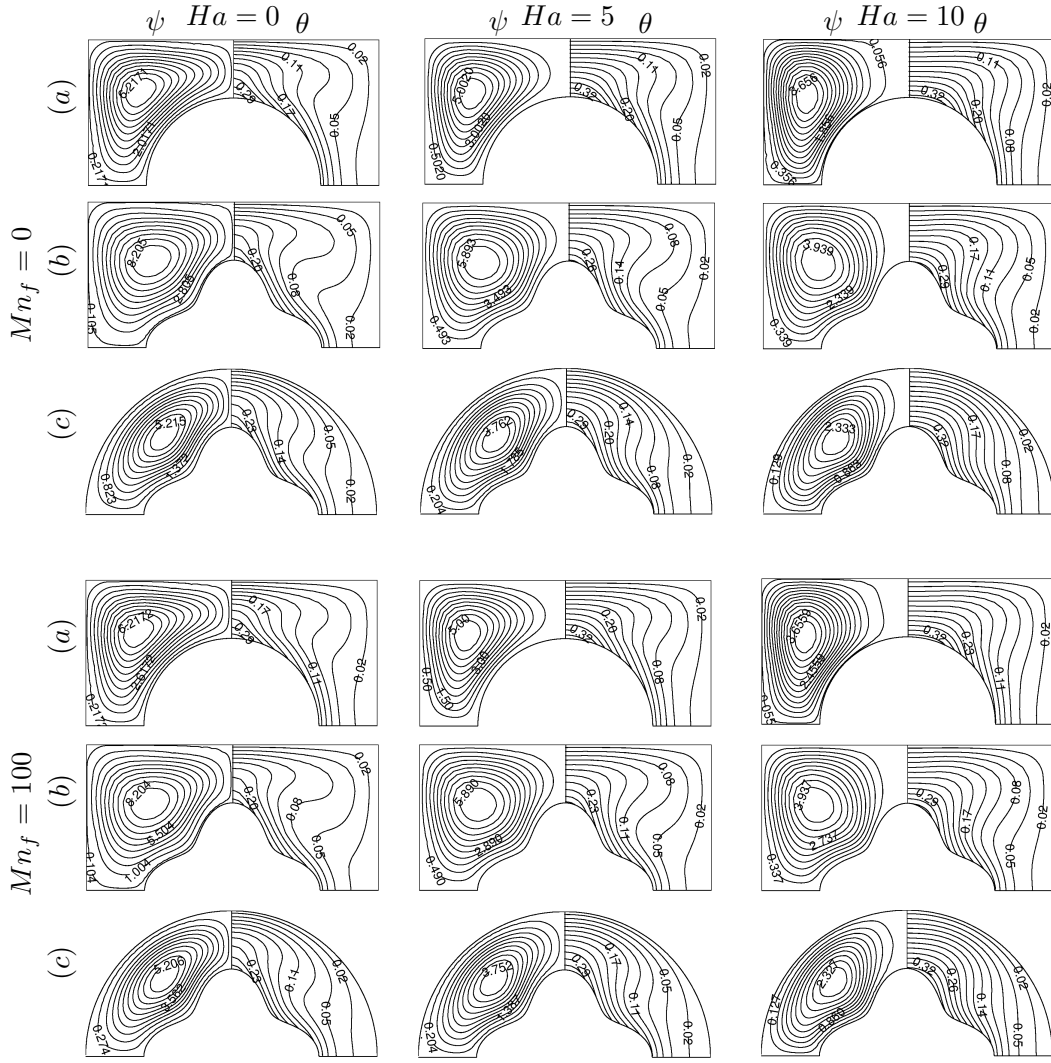


Figure 5.13: Effects of Ha and Mn_f on streamlines and isotherms: $Ra = 10^4$, $\phi = 0.04$.

nusoidal inner walls and rectangular outer wall, and (c) sinusoidal inner and circular outer walls. The Hartmann and magnetic numbers have opposite effects on the flow behavior when compared to Rayleigh number. That is, the strength of streamlines in magnitude decreases with an increase in Hartmann number and magnetic number, whereas it increases with an increase in Rayleigh number. In the absence of magnetic field ($Ha = 0$, $Mn_f = 0$), two counter rotating vortices are formed symmetrically inside the enclosure at each Ra as in the previous problem. When the magnetic number increases, it is observed that a secondary eddy occurs in the region close to the vertical centerline. When Ha increases to 10, the strength of this secondary eddy decreases in magnitude. This secondary eddies vanish with an increase in Ra to $Ra = 10^4$ and 10^5 . This indicates that the convection dominance due to the high Ra , decreases

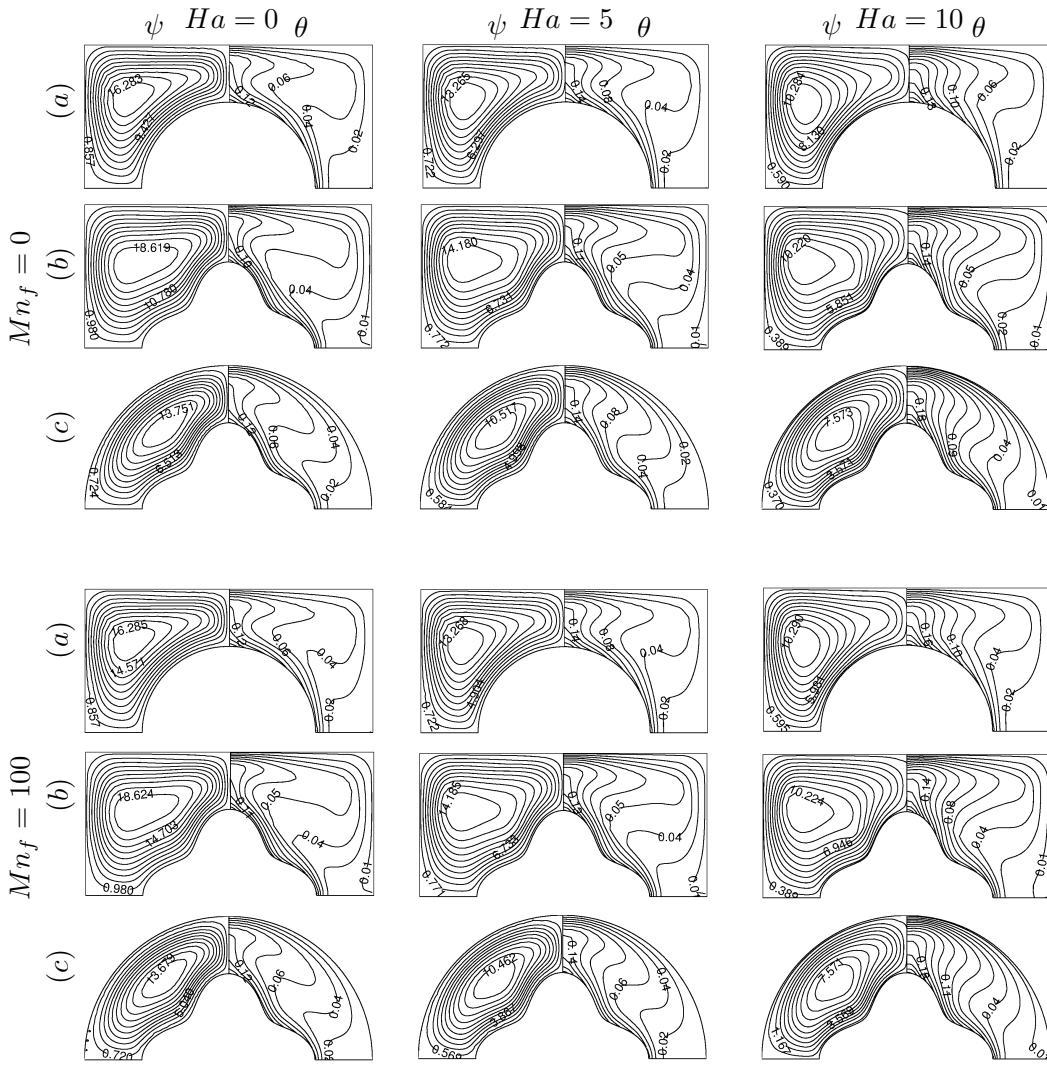


Figure 5.14: Effects of Ha and Mn_f on streamlines and isotherms: $Ra = 10^5$, $\phi = 0.04$.

the effect of Mn_f . On the other hand, the isotherms distribute smoothly inside the annulus region being parallel to each other for small value of $Ra = 10^3$ when the conduction mode is dominant at each Hartmann and magnetic numbers. For higher $Ra (= 10^4, 10^5)$, a thermal plume formed in the middle of the cavity as a result of convection dominance in heat transfer. However, at $Ha = 10$ the strength of the plume decreases when compared to the case of $Ha = 0$. It is also observed that magnetic number has no significant effect on the strength and shape of the plume. It is also seen in Figures 5.12, 5.13 and 5.14 that there is no remarkable variation in the profiles of streamlines and isotherms due to the shape of enclosure and the heat source. But, the strength of stream function in magnitude is bigger in an enclosure with the sinusoidal inner wall compared to its circular counterpart whereas it is smaller in an enclosure

with the circular outer wall compared to its rectangular counterpart.

Figure 5.15 presents the impact of Hartmann and Rayleigh numbers on \overline{Nu} when $n = 4$ and $\phi = 0.04$ for $Mn_f = 0$ and $Mn_f = 100$. It is observed that \overline{Nu} increases with the increment of Ra , whereas it has a small decrease as Ha increases. Further, there is no significant change when the magnetic number increases.

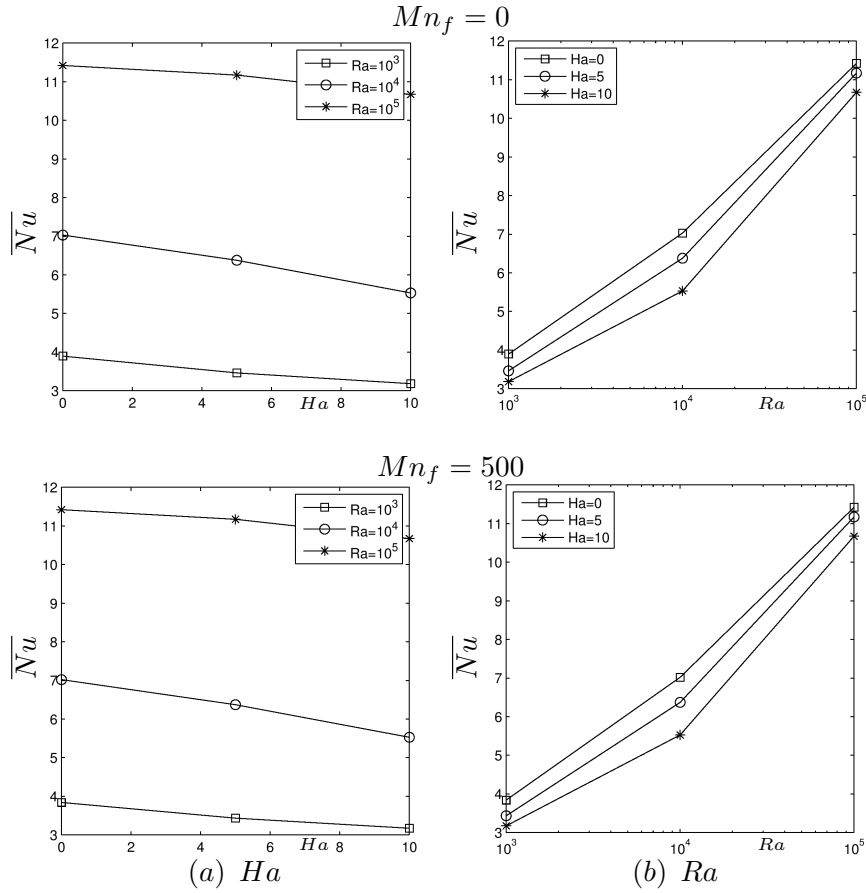


Figure 5.15: Effects of (a) Ha and (b) Ra on \overline{Nu} : $n = 4$, $\phi = 0.04$.

The variation of \overline{Nu} with Rayleigh number at different (a) number of undulation n , fixing $A = 0.2$ and (b) amplitude A of the inner wall fixing $n = 4$ when $Ha = 0$ and $Mn_f = 0$ is illustrated in Figure 5.16. It is well-observed that, in general \overline{Nu} is an increasing function of both number of undulation n and amplitude A of inner sinusoidal wall. However, in all cases as n increases from 0 to 2, \overline{Nu} decreases since the length of the inner wall at $n = 2$ becomes shorter than the one at $n = 0$.

Furthermore, Figure 5.17 displays the effect of solid volume fraction ϕ of ferrofluid on \overline{Nu} at $Mn_f = 100$. In Figure 5.17 (a), the variation of \overline{Nu} with Ha is displayed

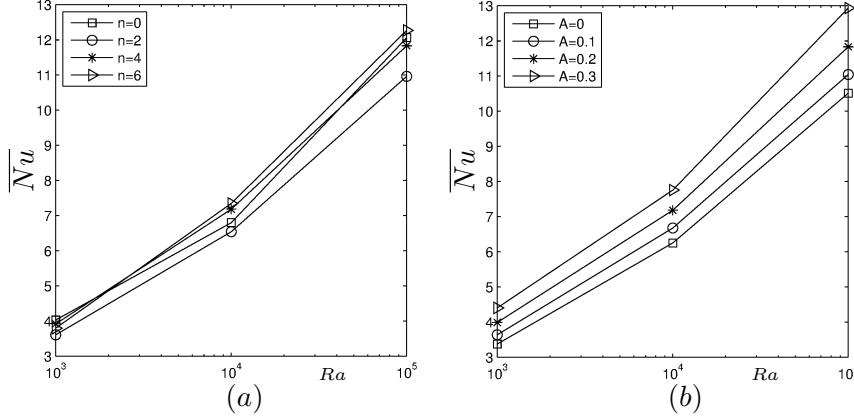


Figure 5.16: Variation of \overline{Nu} with Ra at different numbers of undulation n and amplitude A when $\phi = 0.04$, $Ha = 0$, $Mn_f = 0$.

with a fixed $Ra = 10^4$, and in Figure 5.17 (b), the variation of \overline{Nu} with respect to Ra is shown by fixing $Ha = 5$. As in the previous problem, \overline{Nu} increases with an increase in ϕ due to the high thermal conductivity of nanoparticles irrespective of the values of Ha and Ra .

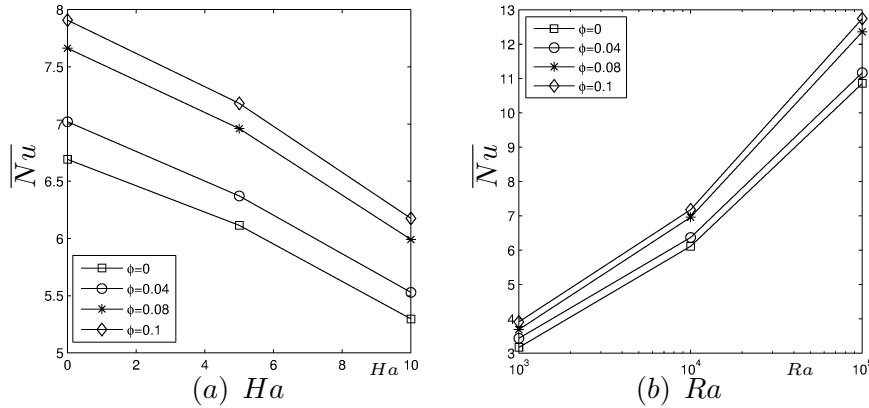


Figure 5.17: Variation of \overline{Nu} with (a) Ha and (b) Ra at different ϕ : $n = 4$.

Figure 5.18 displays the influence of the number of undulation n and amplitude A of sinusoidal wall on the flow and thermal conductivity by means of streamlines and isotherms in the absence of magnetic source for $Ra = 10^4$. When $n = 0$, the strength of stream function decreases while A increases, but, A enhances the magnitude of stream function for $n \geq 2$. Since increasing A leads to a decrease in the gap between the hot and cold walls, the heat transfer enhances. Moreover, the strength of stream function in magnitude increases with an increase in n , except $n = 5$. When $n = 5$, it starts to decrease. When $n = 0$ and $n = 4$, two symmetric eddies rotate in opposite

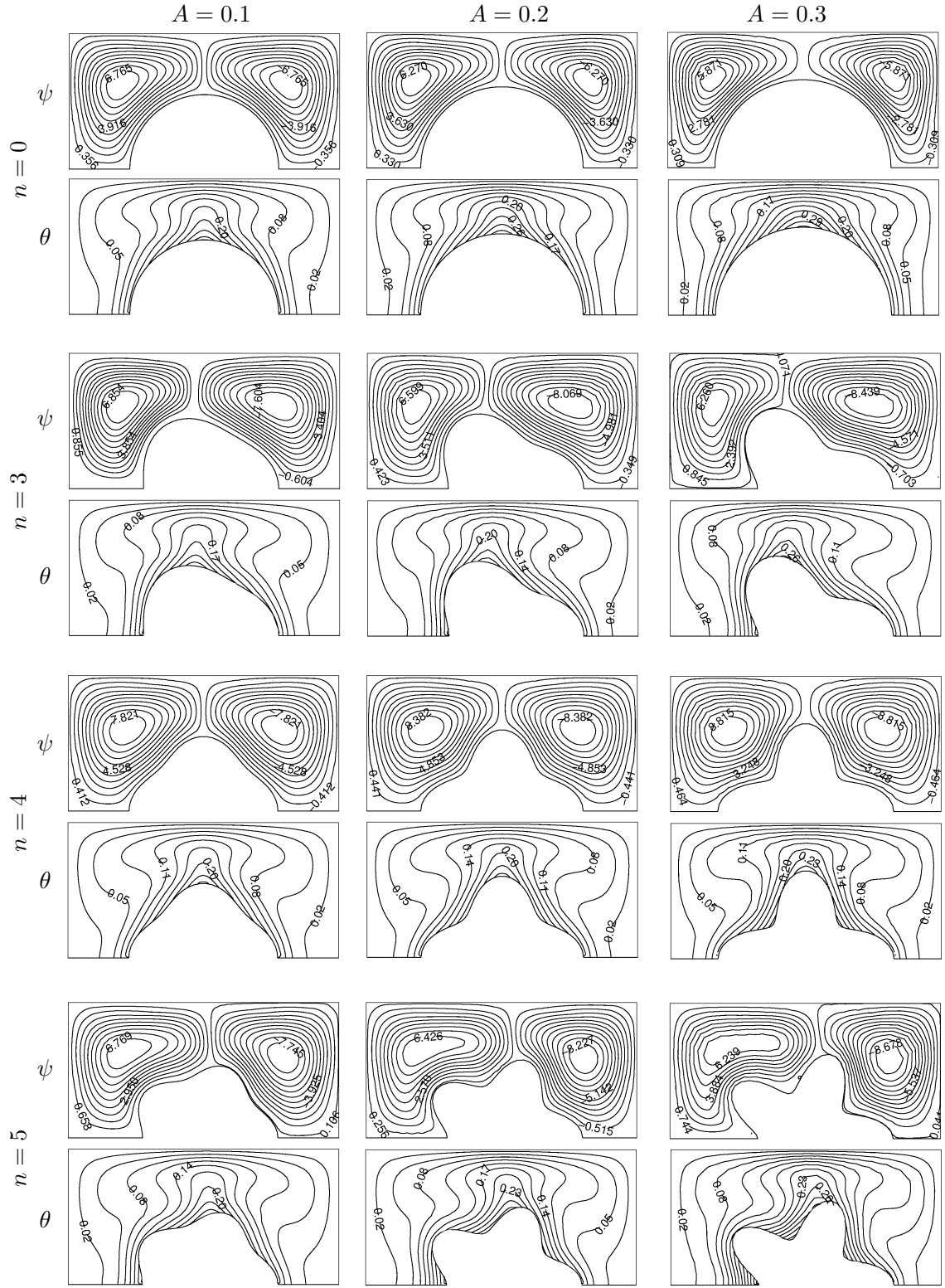


Figure 5.18: The effects of the number of undulation n and the amplitude A of sinusoidal wall on streamlines and isotherms at $Ha = 0$, $Mn_f = 0$, $Ra = 10^4$

direction inside the streamline profiles. On the other hand, when $n = 3$ and $n = 5$, the symmetry vanishes due to the deterioration of the symmetry of the computational domain. In addition, as A increases when $n = 3$, the positive vortices in streamlines, shrink towards the left wall while negative vortices start to spread towards left and fulfill the domain. However, when $n = 5$ an opposite situation is observed. That is, the negative vortices shrink following the extension of the positive vortices to the right as A increases. Moreover, a thermal plume formed just above the inner wall for each values of A and n . This plume becomes more powerful when A increases.

Figure 5.19 depicts the comparison of the effect of magnetic field produced by either one or multiple magnetic sources at $Ra = 10^4$ and $\phi = 0.04$. In the absence of magnetic field (i.e. $Ha = Mn_f = 0$) the behavior of streamlines and isotherms are identical for both one and two magnets. Further, addition of the second magnetic source leads to a decrease in the strength of stream function except the case $Mn_f = 500$ and $Ha = 0$ when an increase in ψ is observed. A secondary eddy is formed in the region close to the vertical centerline in the case of one nodal magnetic source when $Mn_f = 500$, while this secondary eddy does not observed in the presence of

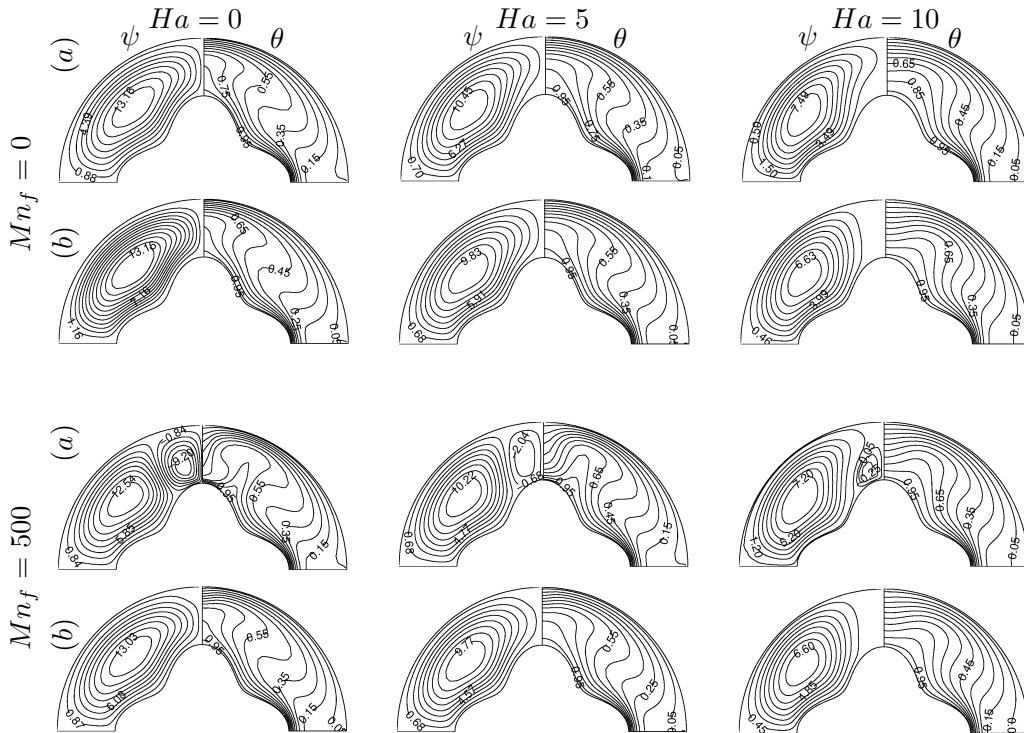


Figure 5.19: Effects of Ha and Mn_f on streamlines and isotherms: $Ra = 10^4$, $\phi = 0.04$, (a) one nodal source, (b) multiple nodal sources.

two nodal sources. Moreover, at $Mn_f = 0$, the isotherm distribution has similar behavior in both cases. However, at $Mn_f = 500$ and $Ha = 0, 5$ only one thermal plume is formed in the case of two sources while three plumes are observed in the presence of one source.

Moreover, Table 5.3 shows the comparison of the influence of magnetic sources produced by either one or two nodal magnetic sources in terms of $|\psi|_{max}$, $|\theta|_{max}$ and \overline{Nu} . As mentioned previously, when two nodal magnetic sources are applied, the strength of stream function decreases in magnitude and no significant change is observed in temperature. However, increasing number of nodal magnetic source leads to a decrease in \overline{Nu} as expected due to the increasing magnetic field intensity.

Table 5.3: Comparison of the effect of magnetic field produced by either one magnet or two magnets in terms of $|\psi|_{max}$, $|\theta|_{max}$ and \overline{Nu} .

		$Mn_f = 0$		$Mn_f = 500$	
		$ \psi _{max}$	\overline{Nu}	$ \psi _{max}$	\overline{Nu}
One magnet	$Ha = 0$	14.917	4.280	14.213	5.367
	$Ha = 5$	11.845	3.818	11.587	4.223
	$Ha = 10$	8.486	3.271	8.464	3.278
Multiple magnets	$Ha = 0$	14.917	4.280	14.767	5.368
	$Ha = 5$	11.134	3.791	11.074	3.724
	$Ha = 10$	7.513	3.143	7.480	3.123

5.5 Summary of the Results Obtained in Chapter 5

This chapter is devoted to the dual reciprocity BEM solutions of the natural convection flow in semi-annulus enclosures with wavy inner walls in the presence of spatially variable magnetic sources and the following results are obtained:

- When the magnetic field is neglected (i.e. $Ha = 0$, $Mn_f = 0$), two symmetrical counter rotating vortices formed inside the enclosure when $Ra = 10^3, 10^4$,

10^5 for both single and multiple magnetic sources.

- The strength of stream function decreases in magnitude with an increase in Ha , but it increases as the Ra increases irrespective of the number and the location of magnetic sources.
- It is observed that \overline{Nu} increases with an increase in Ra whereas it decreases as Ha increases in both cases of one and two nodal magnetic sources.
- Adding nanoparticles leads to an enhancement in the heat transfer rate, and hence it increases \overline{Nu} independent of the spatially varied magnetic sources.
- An increase in amplitude and number of undulation lead to an increase in \overline{Nu} .

In the case of one nodal magnetic source:

- A secondary eddy is formed at $Ra = 10^3, 10^4$ and as magnetic number increases from $Mn_f = 0$ to $Mn_f = 500$ in all cases. This secondary eddy vanishes with an increase in Ra to 10^5 .
- When $Ra = 10^3$ and $Mn_f = 500$, three thermal plumes are formed inside the enclosure. In addition, when Ra increases to $Ra = 10^4$ the thermal plumes are observed in all cases.
- When $Ra = 10^3$ and 10^4 , the \overline{Nu} increases with an increase in Mn_f , but at $Ra = 10^5$, the \overline{Nu} decreases as Mn_f increases.
- The strength of stream function in streamlines profile with sinusoidal heater is bigger than the one in the enclosure with circular heater due to the larger available space for the circulation.
- Moreover, when $Ra = 10^4$, $Mn_f = 0$, $Ha = 5$ and $Ha = 10$, an additional eddy occurs in the streamlines when the inner wall is circular whereas in the case of sinusoidal inner wall no secondary eddy is observed.

In the case of multiple nodal magnetic sources:

- At $Ra = 10^3$ and $Mn_f = 100$, a secondary eddy occurs in the region close to the vertical centerline. When Ha increases to 10, the strength of this secondary eddy decreases in magnitude and it vanishes with a further increase in Ra to 10^4 .
- The isotherms distribute smoothly inside the annulus region when $Ra = 10^3$ at each Hartmann and magnetic numbers. As Ra increases to 10^4 , a thermal plume formed in the middle of the cavity.
- The strength of stream function in magnitude is bigger in the enclosure with the sinusoidal inner wall compared to its circular counterpart whereas it is smaller in the enclosure with the circular outer wall compared to its rectangular counterpart.
- The strength of stream function in magnitude increases with an increase in A except $n = 0$. In addition, generally, the absolute value of stream function increases as n increases.
- Generally, as the number of nodal magnetic source increases from 1 to 2, the strength of stream function in magnitude decreases.
- The formation of secondary eddy, in the case of one nodal source when $Mn_f = 500$ vanishes in the presence of two nodal sources due to the increasing effect of magnetic field intensity.
- Further, increasing number of nodal magnetic sources leads to a decrease in \overline{Nu} since the increasing magnetic effect suppresses the convective heat transfer mechanism.

CHAPTER 6

CONCLUSION

This thesis is devoted to the numerical solutions of steady/unsteady MHD convective flows in enclosures or lid-driven cavities with irregular surfaces by the use of a numerical method which is the coupling of the dual reciprocity BEM with a two level time integration scheme. The boundary of the enclosure is discretized by using both constant and linear elements. Since no significant difference is occurred in the results when the linear elements are employed, in the thesis, we prefer to use the constant elements due to the easiness of the constant elements in the application of DRBEM when compared to the use of linear elements. Moreover, in the application of DRBEM several types of radial basis functions can be used for the approximation of non-homogeneity. However, in the thesis the use of a linear polynomial type of RBFs is preferred since the use of linear polynomial RBFs requires less number of iteration and computational time to reach the preassigned tolerance when compared to other types of RBFs as given in Chapter 3, Section 3.3.1, Page 66, Lines:14-22. Basically, the thesis is divided into two topics according to the MHD flow of either purefluids or nano/ferrofluids in irregular enclosures with wavy walls subject to uniform magnetic field and nodal magnetic sources.

First, we concentrate on the numerical solution of convective purefluid flow under the effect of an inclined uniform magnetic field. The proposed numerical method is employed for the solution of both steady and unsteady mixed convection MHD flow in a lid-driven cavity with circular/rectangular and wavy walls for investigating the effects of irregular surfaces on the flow field and temperature distribution. A stability analysis of numerical method is also performed using physical controlling parameters to be able to find appropriate values for the time increment and the time relaxation

parameters. The results reveal that:

- As the value of the Hartmann number Ha increases, the strength of stream function decreases in magnitude due to the retarding effect of the magnetic field on the fluid flow, in addition, the isotherms become more parallel to vertical walls due to the dominance of conduction on heat transfer (see Figure 3.25).
- With the increase in Rayleigh number the isotherms change their profiles from being vertical to almost horizontal at the center of the cavity forming a thermal boundary layer along the vertical walls because of the convection dominance (see Figure 3.26).
- An increase in Joule heating parameter reduces the strength of stream function in magnitude whereas temperature of the fluid inside the cavity increases (see Figures 3.27,3.28).
- There is no significant effect of inclination angle of magnetic field λ on the streamline and isotherm profiles, but, at $Ra = 10^5$ as λ increases the main vortex moves towards the left bottom corner of the cavity, it becomes circular, and its strength increases. Further, the isotherms move upwards and an increase in the temperature inside the cavity is observed (see Figures 3.29,3.30).
- Alteration on the shape of the heater makes no significant difference on streamline and isotherm profiles, but it is observed that the average Nusselt number increases when the length of the heated portion on the right wall increases (see Figures 3.31,3.32, 3.36).
- When Joule heating effect is neglected, Hartmann number has a negative effect on \overline{Nu} , that is, \overline{Nu} decreases with an increase in Ha irrespective of values of Ra . However, in the presence of Joule heating when J increases the heat transfer rate increases with an increase in Ha for $Ha \leq 25$ at each Ra (see Figures 3.33, 3.34).
- Moreover, the \overline{Nu} increases when $Ra \geq 10^4$. However, \overline{Nu} decreases as Ra increases from $Ra = 10^3$ to 10^4 at each Ha , since the flow is transferred from conduction regime to transition regime, which occurs irrespective of the types of heater.

- In addition, for all types of heater, increasing J leads the temperature inside the cavity to become higher than the wall temperature, thence \overline{Nu} along the hot wall decreases (see Figure 3.35).

In the second part of the thesis, the steady/unsteady differential equations of convective heat transfer and flow of a nanofluid and ferrofluid in enclosures with complex geometries under the effects of either uniform magnetic field or nodal magnetic sources are solved by the proposed numerical method. The effect of the geometry of the computational domain, the inclination angle of the uniform magnetic field, the location and the number of nodal magnetic sources for the magnetic field on the flow behavior and temperature distribution are investigated. The simulations are carried out in terms of streamlines, isotherms and average Nusselt number for various combinations of pertinent physical parameters. The stability analysis of the numerical method for the solution of the unsteady MHD convective flow of nanofluid problem is also performed using the eigenvalue decomposition of the matrix system.

First, we consider the solution of MHD flow in a semi-annulus enclosure filled with a water-based nanofluid subject to a uniform inclined magnetic field. The results indicate that:

- Adding nanoparticles increases the intensity of streamlines and heat transfer rate due to an increase in the energy transport through the flow because of irregular motion of the ultra fine particles (see Figure 4.18).
- The strength of stream function decreases in magnitude as Ha increases whereas it increases with an increase in Ra irrespective of the types of inner wall. A thermal plume is observed just above the inner circular/sinusoidal wall, when the convection regime starts to dominate the heat transfer (see Figure 4.16).
- When the inclination angle of enclosure is taken as zero, two equal counter-rotating vortices formed inside the enclosure. As the inclination angle of enclosure increases, the symmetry of the eddies is destroyed. That is, the positive vortex elongates with the inclination of the enclosure and becomes dominant to the secondary vortex. In addition, it is observed that inside the isotherm profiles a formation of a plume occurs on the surface of inner wall in the direction of

magnetic field (see Figures 4.4,4.5, 4.6,4.8).

- When the magnetic field applied in horizontal direction two symmetric counter-rotating eddies are formed in streamlines, but, this symmetry is destroyed with an increase in λ . As λ reaches to $\pi/2$, the counter-rotating vortices become again symmetric. On the other hand, at $\lambda = 0$, the thermal plume formed at the middle of the cavity just above the inner wall moves along the inner wall in the direction of the magnetic field irrespective of the shape of the inner wall (see Figures 4.3, 4.14).
- As expected, average Nusselt number increases with an increase in Ra and solid volume fraction whereas it decreases as Ha increases. In addition, the maximum \overline{Nu} is observed at $\lambda = \beta = 0$ in the absence of magnetic field ($Ha = 0$) and $\lambda = \beta = \pi/2$ for higher values of Ha (see Figure 4.17).
- When $Ha = 0, 10$ as the number of undulation n of wavy wall increases, the \overline{Nu} increases at each Ra . On the other hand, when $Ha \geq 50$ and $Ra = 10^3, 10^4$, the increasing effect of n on \overline{Nu} is degenerated, while \overline{Nu} again increases in the case of convective heat transfer at $Ra = 10^5$ (see Figure 4.19).
- Increasing the amplitude of the inner wall leads to an enhancement in the heat transfer rate and hence an increase in \overline{Nu} (see Figure 4.20).

Secondly, the natural convection flow in semi-annulus enclosures with wavy inner wall filled with water-based ferrofluids are investigated in the presence of a non-uniform magnetic field, i.e. either single or multiple nodal magnetic sources. Obtained results show that:

- In the absence of magnetic field the formation of two symmetrical counter rotating vortices are observed inside the enclosure when $Ra = 10^3, 10^4, 10^5$ for both single and multiple magnetic sources (see Figures 5.4,5.5,5.6,5.12,5.13,5.14).
- As Ha increases, the strength of stream function decreases in magnitude irrespective of the number and the location of magnetic sources (see Figures 5.4,5.5,5.6,5.12,5.13,5.14).

- \overline{Nu} increases with an increase in Ra whereas it decreases as Ha increases independent of the number of spatially varied magnetic sources (see Figures 5.7,5.15).
- The heat transfer rate enhances with an increase in solid volume fraction of nanoparticles in the presence of both one and multiple nodal sources (see Figures 5.9,5.17).
- Further, an increase in amplitude and number of undulation lead to an increase in \overline{Nu} (see Figure 5.8,5.16).
- The strength of stream function in magnitude decreases, when the number of nodal magnetic source increases (see Figure 5.19).
- When $Mn_f = 500$, in the case of one nodal source the secondary eddy is formed inside the enclosure but it vanishes in the presence of two nodal sources (see Table 5.3).
- \overline{Nu} decreases, as the number of nodal magnetic source increases (see Table 5.3).

In the case of one nodal magnetic source:

- At $Ra = 10^3, 10^4$, and $Mn_f = 500$, a secondary eddy is formed in all cases and this secondary eddy vanishes with an increase in Ra to 10^5 (see Figures 5.4,5.5,5.6).
- Three thermal plumes are observed inside the enclosure when $Ra = 10^3$, and $Mn_f = 500$. Further, at $Ra = 10^4$ the thermal plumes are formed in all cases (see Figures 5.4,5.5).
- \overline{Nu} increases with an increase in Mn_f at $Ra = 10^3$ and 10^4 , but at $Ra = 10^5$ \overline{Nu} decreases as the Mn_f increases (see Figures 5.5,5.6).
- When the inner wall is circular, the strength of stream function in magnitude is smaller than the one when the enclosure is with sinusoidal heater. When $Ra = 10^4$, $Mn_f = 0$, $Ha \geq 5$, an additional eddy occurs in the streamlines which is not observed in the case of sinusoidal inner wall (see Figures 5.4,5.5,5.6).

In the case of multiple nodal magnetic sources:

- At $Ra = 10^3$, increasing Mn_f leads to a formation of secondary eddy. As Ha increases the strength of this eddy decreases in magnitude, and it vanishes when $Ra = 10^4$ (see Figures 5.12,5.13,5.14).
- At $Ra = 10^3$, the isotherms distribute smoothly inside the annulus region while a thermal plume is formed in the middle of the cavity with an increase in Ra to 10^4 (see Figures 5.12,5.13).
- The strength of stream function in magnitude is smaller in the enclosure with a circular inner wall compared to its sinusoidal counterpart whereas it is bigger in the enclosure with the rectangular outer wall compared to its circular counterpart (see Figures 5.12,5.13,5.14).
- The magnitude of stream function increases with an increase in A except $n = 0$. In addition, it is also an increasing function of n (see Figure 5.18).

REFERENCES

- [1] A. Al-Amiri, K. Khanafer, J. Bull, and I. Pop. Effect of sinusoidal wavy bottom surface on mixed convection heat transfer in a lid-driven cavity. *International Journal of Heat and Mass Transfer*, 50(9):1771–1780, 2007.
- [2] A. M. Al-Amiri. Analysis of momentum and energy transfer in a lid-driven cavity filled with a porous medium. *International Journal of Heat and Mass Transfer*, 43(19):3513–3527, 2000.
- [3] K. Al-Salem, H. F. Öztop, I. Pop, and Y. Varol. Effects of moving lid direction on MHD mixed convection in a linearly heated cavity. *International Journal of Heat and Mass Transfer*, 55(4):1103–1112, 2012.
- [4] H. Aminfar, M. Mohammadpourfard, and S. A. Zonouzi. Numerical study of the ferrofluid flow and heat transfer through a rectangular duct in the presence of a non-uniform transverse magnetic field. *Journal of Magnetism and Magnetic materials*, 327:31–42, 2013.
- [5] S. Aminossadati and B. Ghasemi. Natural convection cooling of a localised heat source at the bottom of a nanofluid-filled enclosure. *European Journal of Mechanics-B/Fluids*, 28(5):630–640, 2009.
- [6] S. M. Aminossadati. Hydromagnetic natural cooling of a triangular heat source in a triangular cavity with water CuO nanofluid. *International Communications in Heat and Mass Transfer*, 43:22–29, 2013.
- [7] H. R. Ashorynejad, A. A. Mohamad, and M. Sheikholeslami. Magnetic field effects on natural convection flow of a nanofluid in a horizontal cylindrical annulus using Lattice Boltzmann method. *International Journal of Thermal Sciences*, 64:240–250, 2013.
- [8] M. Bahiraei and M. Hangi. Natural convection of magnetic nanofluid in a

- cavity under non-uniform magnetic field: A novel application. *Journal of Superconductivity and Novel Magnetism*, 27:587–594, 2014.
- [9] T. L. Bergman and F. P. Incropera. *Fundamentals of Heat and Mass Transfer*. John Wiley & Sons, 2011.
- [10] J. Blazek. *Computational Fluid Dynamics: Principles and Applications*. Butterworth-Heinemann, 2015.
- [11] C. Bozkaya. DRBEM simulation on mixed convection with hydromagnetic effect. In *Integral Methods in Science and Engineering*, pages 57–68. Springer, 2015.
- [12] C. A. Brebbia. *The Boundary Element Method for Engineers*. Pentech Press, London, 1980.
- [13] C. A. Brebbia, P. W. Partridge, and L. C. Wrobel. *The Dual Reciprocity Boundary Element Method*. Computational Mechanics Publications, Southampton, Boston, 1992.
- [14] V. Bubnovich, C. Rosas, R. Santander, and G. Caceres. Computation of transient natural convection in a square cavity by an implicit finite-difference scheme in terms of the stream function and temperature. *Numerical Heat Transfer: Part A: Applications*, 42(4):401–425, 2002.
- [15] C. Cha and Y. Jaluria. Recirculating mixed convection flow for energy extraction. *International Journal of Heat and Mass Transfer*, 27(10):1801–1812, 1984.
- [16] A. J. Chamkha. Hydromagnetic combined convection flow in a vertical lid-driven cavity with internal heat generation or absorption. *Numerical Heat Transfer: Part A: Applications*, 41(5):529–546, 2002.
- [17] C. C. Cho, C. L. Chen, and C. K. Chen. Mixed convection heat transfer performance water based nanofluids in lid-driven cavity with wavy surfaces. *International Journal of Thermal Sciences*, 68:181–190, 2013.
- [18] S. U. S. Choi. Enhancing thermal conductivity of fluids with nanoparticles.

in: D. A. Siginer and H. P. Wang, Eds., *Developments and Applications of Non-Newtonian Flows*, ASME, FED 231/MD 66:99–105, 1995.

- [19] P. K. Das and S. Mahmud. Numerical investigation of natural convection inside a wavy enclosure. *International Journal of Thermal Sciences*, 42(4):397–406, 2003.
- [20] S. Das, S. Chakraborty, and P. Dutta. Natural convection in a two-dimensional enclosure heated symmetrically from both sides. *International Communications in Heat and Mass Transfer*, 29(3):345 – 354, 2002.
- [21] I. Di Piazza and M. Ciofalo. MHD free convection in a liquid-metal filled cubic enclosure. i. differential heating. *International Journal of Heat and Mass Transfer*, 45(7):1477–1492, 2002.
- [22] H. M. Elshehabey, F. M. Hady, S. E. Ahmed, and R. A. Mohamed. Numerical investigation for natural convection of a nanofluid in an inclined L -shaped cavity in the presence of an inclined magnetic field. *International Communications in Heat and Mass Transfer*, 57:228–238, 2014.
- [23] J. H. Ferziger and M. Peric. *Computational Methods for Fluid Dynamics*. Springer Science & Business Media, 2012.
- [24] N. L. Gajbhiye and V. Eswaran. Numerical simulation of MHD flow and heat transfer in a rectangular and smoothly constricted enclosure. *International Journal of Heat and Mass Transfer*, 83:441–449, 2015.
- [25] R. Ganguly, S. Sen, and I. K. Puri. Heat transfer augmentation using a magnetic fluid under the influence of a line dipole. *Journal of Magnetism and Magnetic Materials*, 271(1):63–73, 2004.
- [26] B. Ghasemi. Magnetohydrodynamic natural convection of nanofluids in U -shaped enclosures. *Numerical Heat Transfer, Part A*, 63(6):473–487, 2013.
- [27] B. Ghasemi, S. M. Aminossadati, and A. Raisi. Magnetic field effect on natural convection in a nanofluid-filled square enclosure. *International Journal of Thermal Sciences*, 50:1748–1756, 2011.

- [28] M. Goharkhah and M. Ashjaee. Effect of an alternating nonuniform magnetic field on ferrofluid flow and heat transfer in a channel. *Journal of Magnetism and Magnetic Materials*, 362:80–89, 2014.
- [29] S. Gümgüm and M. Tezer-Sezgin. DRBEM solution of natural convection flow of nanofluids with a heat source. *Engineering Analysis with Boundary Elements*, 34:727–737, 2010.
- [30] G. Guo and M. A. Sharif. Mixed convection in rectangular cavities at various aspect ratios with moving isothermal sidewalls and constant flux heat source on the bottom wall. *International Journal of Thermal Sciences*, 43(5):465–475, 2004.
- [31] M. B. B. Hamida and K. Charrada. Natural convection heat transfer in an enclosure filled with an ethylene glycol-copper nanofluid under magnetic fields. *Numerical Heat Transfer, Part A*, 67:902–920, 2015.
- [32] M. Hasanuzzaman, H. F. Öztop, M. Rahman, N. Rahim, R. Saidur, and Y. Varol. Magnetohydrodynamic natural convection in trapezoidal cavities. *International Communications in Heat and Mass Transfer*, 39(9):1384–1394, 2012.
- [33] S. Hussain, K. Mehmood, and M. Sagheer. MHD mixed convection and entropy generation of water–alumina nanofluid flow in a double lid driven cavity with discrete heating. *Journal of Magnetism and Magnetic Materials*, 419:140–155, 2016.
- [34] A. Hussein and S. Hussain. Mixed convection through a lid-driven air-filled square cavity with a hot wavy wall. *International Journal of Mechanical and Materials Engineering*, 5(2):222–235, 2010.
- [35] J. Imberger and P. F. Hamblin. Dynamics of lakes, reservoirs, and cooling ponds. *Annual Review of Fluid Mechanics*, 14(1):153–187, 1982.
- [36] M. K. Jain. *Numerical Solution of Differential Equations*. Wiley, New Delhi, 1979.
- [37] Y. Jaluria. Fluid flow phenomena in materials processing—the 2000 freeman scholar lecture. *Journal of Fluids Engineering*, 123(2):173–210, 2001.

- [38] J. H. Jang and W. M. Yan. Mixed convection heat and mass transfer along a vertical wavy surface. *International Journal of Heat and Mass Transfer*, 47(3):419–428, 2004.
- [39] V. Job and S. Gunakala. Unsteady MHD free convection nanofluid flows within a wavy trapezoidal enclosure with viscous and joule dissipation effects. *Numerical Heat Transfer, Part A: Applications*, 69(4):421–443, 2016.
- [40] V. M. Job, S. R. Gunakala, B. R. Kumar, and R. Sivaraj. Time-dependent hydromagnetic free convection nanofluid flows within a wavy trapezoidal enclosure. *Applied Thermal Engineering*, 115:363–377, 2017.
- [41] T.-C. Jue. Analysis of combined thermal and magnetic convection ferrofluid flow in a cavity. *International Communications in Heat and Mass Transfer*, 33(7):846–852, 2006.
- [42] M. S. Kandelousi. Effect of spatially variable magnetic field on ferrofluid flow and heat transfer considering constant heat flux boundary condition. *The European Physical Journal Plus*, 129(11):1–12, 2014.
- [43] G. Karniadakis and S. Sherwin. *Spectral/hp Element Methods for Computational Fluid Dynamics*. Oxford University Press, 2013.
- [44] K. Khanafer, K. Vafai, and M. Lightstone. Buoyancy-driven heat transfer enhancement in a two dimensional enclosure utilizing nanofluids. *International Journal of Heat and Mass Transfer*, 46:3639–3653, 2003.
- [45] K. M. Khanafer, A. M. Al-Amiri, and I. Pop. Numerical simulation of unsteady mixed convection in a driven cavity using an externally excited sliding lid. *European Journal of Mechanics-B/Fluids*, 26(5):669–687, 2007.
- [46] F. Kobra, N. Quddus, and A. A. Alim. Heat transfer enhancement of Cu-water nanofluid filled in a square cavity with a circular disk under a magnetic field. *Procedia Engineering*, 90:582–587, 2014.
- [47] B. Krishna Satya Sai, K. Seetharamu, and P. Aswatha Narayana. Solution of transient laminar natural convection in a square cavity by an explicit finite element scheme. *Numerical Heat Transfer*, 25(5):593–609, 1994.

- [48] B. R. Kumar. A study of free convection induced by a vertical wavy surface with heat flux in a porous enclosure. *Numerical Heat Transfer: Part A: Applications*, 37(5):493–510, 2000.
- [49] V. Loukopoulos and E. Tzirtzilakis. Biomagnetic channel flow in spatially varying magnetic field. *International Journal of Engineering Science*, 42(5):571 – 590, 2004.
- [50] H. S. Mahdi and R. B. Kinney. Time-dependent natural convection in a square cavity: Application of a new finite volume method. *International Journal for Numerical Methods in Fluids*, 11(1):57–86, 1990.
- [51] A. H. Mahmoudi, I. Pop, and M. Shahi. Effect of magnetic field on natural convection in a triangular enclosure filled with nanofluid. *International Journal of Thermal Sciences*, 59:126–140, 2012.
- [52] J. Maxwell. *A Treatise on Electricity and Magnetism*. Oxford University Press, Second Ed., Cambridge, 1904.
- [53] S. Mekroussi and N. E. S. Chemloul. Numerical investigation of laminar natural convection in an inclined cavity with a wavy wall. *International Journal of Engineering Science and Innovative Technology*, 2(5):446–456, 2013.
- [54] S. Mekroussi, D. Nehari, M. Bouzit, and N. E. S. Chemloul. Analysis of mixed convection in an inclined lid-driven cavity with a wavy wall. *Journal of Mechanical Science and Technology*, 27(7):2181, 2013.
- [55] U. Müller and L. Bühler. *Magnetofluidynamics in Channels and Containers*. Springer Science & Business Media, 2013.
- [56] R. Nasrin and S. Parvin. Hydromagnetic effect on mixed convection in a lid-driven cavity with sinusoidal corrugated bottom surface. *International Communications in Heat and Mass Transfer*, 38(6):781–789, 2011.
- [57] H. Nemati, M. Farhadi, K. Sedighi, H. R. Ashorynejad, and E. Fattahi. Magnetic field effects on natural convection flow of nanofluid in a rectangular cavity using Lattice Boltzmann model. *Scientia Iranica, Transactions B: Mechanical Engineering*, 19(2):303–310, 2012.

- [58] M. T. Nguyen, A. M. Aly, and S. W. Lee. Unsteady natural convection heat transfer in a nanofluid-filled square cavity with various heat source conditions. *Advances in Mechanical Engineering*, 8(5):1687814016646547, 2016.
- [59] P. Nithiarasu, T. Sundararajan, and K. Seetharamu. Finite element analysis of transient natural convection in an odd-shaped enclosure. *International Journal of Numerical Methods for Heat & Fluid Flow*, 8(2):199–216, 1998.
- [60] H. F. Oztop and I. Dagtekin. Mixed convection in two-sided lid-driven differentially heated square cavity. *International Journal of Heat and Mass Transfer*, 47(8):1761 – 1769, 2004.
- [61] P. W. Partridge, C. A. Brebbia, and L. C. Wrobel. *The Dual Reciprocity Boundary Element Method*. Computational Mechanics Publications, Southampton, Boston, 1992.
- [62] N. Parveen and M. Alim. Joule heating effect on magnetohydrodynamic natural convection flow along a vertical wavy surface. *Journal of Naval Architecture and Marine Engineering*, 9(1):11–24, 2012.
- [63] B. Pekmen and M. Tezer-Sezgin. MHD flow and heat transfer in a lid-driven porous enclosure. *Computers & Fluids*, 89:191–199, 2014.
- [64] A. Peratta and V. Popov. Numerical stability of the BEM for advection-diffusion problems. *Numerical Methods for Partial Differential Equations*, 20(5):675–702, 2004.
- [65] L. A. B. Pilkington. Review lecture. the float glass process. *Proceedings of the Royal Society of London. Series A, Mathematical and Physical Sciences*, 314(1516):1–25, 1969.
- [66] M. Rahman and M. Alim. MHD mixed convection flow in a vertical lid-driven square enclosure including a heat conducting horizontal circular cylinder with joule heating. *Nonlinear Analysis: Modelling and Control*, 15(2):199–211, 2010.
- [67] M. Rahman, H. F. Öztop, N. Rahim, R. Saidur, and K. Al-Salem. MHD mixed convection with joule heating effect in a lid-driven cavity with a heated semi-

- circular source using the finite element technique. *Numerical Heat Transfer, Part A: Applications*, 60(6):543–560, 2011.
- [68] M. Rahman, H. F. Öztop, N. Rahim, R. Saidur, K. Al-Salem, N. Amin, M. Mamun, and A. Ahsan. Computational analysis of mixed convection in a channel with a cavity heated from different sides. *International Communications in Heat and Mass Transfer*, 39(1):78–84, 2012.
- [69] M. M. Rahman, M. A. H. Mamun, and R. Saidur. Analysis of magnetohydrodynamic mixed convection and joule heating in lid-driven cavity having a square block. *Journal of the Chinese Institute of Engineers*, 34(5):585–599, 2011.
- [70] P. S. Ramesh and M. H. Lean. Stability of the multiple reciprocity method for transient heat conduction. *International Journal for Numerical Methods in Biomedical Engineering*, 9(7):629–634, 1993.
- [71] J. Ravnik, L. Skerget, and M. Hribersek. Analysis of three dimensional natural convection of nanofluids by BEM. *Engineering Analysis with Boundary Elements*, 34(12):1018–1030, 2010.
- [72] B. N. Roy. *Crystal growth from melts: applications to growth of groups 1 and 2 crystals*. John Wiley & Sons Incorporated, 1992.
- [73] L. K. Saha, M. C. Somadder, and K. S. Uddin. Mixed convection heat transfer in a lid driven cavity with wavy bottom surface. *American Journal of Applied Mathematics*, 1(5):92–101, 2013.
- [74] I. Sarris, S. Kakarantzas, A. Grecos, and N. Vlachos. MHD natural convection in a laterally and volumetrically heated square cavity. *International Journal of Heat and Mass Transfer*, 48(16):3443–3453, 2005.
- [75] F. Selimefendigil and H. Öztop. Natural convection and entropy generation of nanofluid filled cavity having different shaped obstacles under the influence of magnetic field and internal heat generation. *Journal of the Taiwan Institute of Chemical Engineers*, 56:42–56, 2015.

- [76] F. Selimefendigil and H. F. Öztop. Effect of a rotating cylinder in forced convection of ferrofluid over a backward facing step. *International Journal of Heat and Mass Transfer*, 71:142–148, 2014.
- [77] F. Selimefendigil and H. F. Öztop. MHD mixed convection and entropy generation of power law fluids in a cavity with a partial heater under the effect of a rotating cylinder. *International Journal of Heat and Mass Transfer*, 98:40–51, 2016.
- [78] F. Selimefendigil, H. F. Öztop, and K. Al-Salem. Natural convection of ferrofluids in partially heated square enclosures. *Journal of Magnetism and Magnetic Materials*, 372:122–133, 2014.
- [79] F. Selimefendigil, H. F. Öztop, and A. J. Chamkha. MHD mixed convection and entropy generation of nanofluid filled lid driven cavity under the influence of inclined magnetic fields imposed to its upper and lower diagonal triangular domains. *Journal of Magnetism and Magnetic Materials*, 406:266–281, 2016.
- [80] M. Sharif. Laminar mixed convection in shallow inclined driven cavities with hot moving lid on top and cooled from bottom. *Applied Thermal Engineering*, 27(5):1036–1042, 2007.
- [81] M. Sheikholeslami and D. D. Ganji. Ferrohydrodynamic and magnetohydrodynamic effects on ferrofluid flow and convective heat transfer. *Energy*, 75:400–410, 2014.
- [82] M. Sheikholeslami, D. D. Ganji, and M. M. Rashidi. Ferrofluid flow and heat transfer in a semi annulus enclosure in the presence of magnetic source considering thermal radiation. *Journal of the Taiwan Institute of Chemical Engineers*, 47:6–17, 2015.
- [83] M. Sheikholeslami, M. Gorji-Bandpy, R. Ellahi, M. Hasan, and S. Soleimani. Effects of MHD on Cu-water nanofluid flow and heat transfer by means of CVFEM. *Journal of Magnetism and Magnetic Materials*, 349:188–200, 2014.
- [84] M. Sheikholeslami, M. Gorji-Bandpy, D. Ganji, and S. Soleimani. Natural convection heat transfer in a cavity with sinusoidal wall filled with CuO–water

- nanofluid in presence of magnetic field. *Journal of the Taiwan Institute of Chemical Engineers*, 45(1):40 – 49, 2014.
- [85] M. Sheikholeslami, M. Gorji-Bandpy, and D. D. Ganji. Natural convection in a nanofluid filled concentric annulus between an outer square cylinder and an inner elliptic cylinder. *Scientia Iranica*, 20(4):1241–1253, 2013.
- [86] M. Sheikholeslami, M. Gorji-Bandpy, D. D. Ganji, and S. Soleimani. Effect of a magnetic field on natural convection in an inclined half-annulus enclosure filled with Cu-water nanofluid using CVFEM. *Advanced Powder Technology*, 24:980–991, 2013.
- [87] M. Sheikholeslami, M. Gorji-Bandpy, D. D. Ganji, and S. Soleimani. Magneto-hydrodynamic free convection of Al_2O_3 -water nanofluid considering Thermophoresis and Brownian motion effects. *Computers & Fluids*, 94:147–160, 2014.
- [88] M. Sheikholeslami, M. Gorji-Bandpy, D. D. Ganji, S. Soleimani, and S. M. Seyyedi. Natural convection of nanofluids in an enclosure between a circular and a sinusoidal cylinder in the presence of magnetic field. *International Communications in Heat and Mass Transfer*, 39:1435–1443, 2012.
- [89] M. Sheremet, H. Oztop, and I. Pop. MHD natural convection in an inclined wavy cavity with corner heater filled with a nanofluid. *Journal of Magnetism and Magnetic Materials*, 416:37 – 47, 2016.
- [90] M. A. Sheremet, I. Pop, and N. C. Roşca. Magnetic field effect on the unsteady natural convection in a wavy-walled cavity filled with a nanofluid: Buongiorno’s mathematical model. *Journal of the Taiwan Institute of Chemical Engineers*, 61:211 – 222, 2016.
- [91] S. Sivasankaran, A. Malleswaran, J. Lee, and P. Sundar. Hydro-magnetic combined convection in a lid-driven cavity with sinusoidal boundary conditions on both sidewalls. *International Journal of Heat and Mass Transfer*, 54(1):512–525, 2011.
- [92] E. Sourtiji, D. D. Ganji, M. Gorji-Bandpy, and S. M. Seyyedi. Numerical study

of periodic natural convection in a nanofluid filled enclosure due to transitional temperature of heat source. *Powder Technology*, 259:65–73, 2014.

- [93] E. Sourtiji, M. Gorji-Bandpy, D. Ganji, and S. Seyyadi. Magnetohydrodynamic buoyancy-driven heat transfer in a cylindrical-triangular annulus filled by Cu-water nanofluid using CVFEM. *Journal of Molecular Liquids*, 196:370–380, 2014.
- [94] M. Tezer-Sezgin and C. Bozkaya. DRBEM solution of MHD flow and electric potential in a rectangular pipe with a moving lid. In *Numerical Mathematics and Advanced Applications ENUMATH 2015*, pages 3–11. Springer, 2016.
- [95] M. Tezer-Sezgin, C. Bozkaya, and Önder Türk. Natural convection flow of a nanofluid in an enclosure under an inclined uniform magnetic field. *European Journal of Computational Mechanics*, 25(1-2):2–23, 2016.
- [96] M. Tezer-Sezgin, C. Bozkaya, and Ö. Türk. BEM and FEM based numerical simulations for biomagnetic fluid flow. *Engineering Analysis with Boundary Elements*, 37:1127–1135, 2013.
- [97] M. Tezer-Sezgin and B. Pekmen. Unsteady mixed convection in a porous lid-driven enclosure under a magnetic field. In *International Association for Boundary Element Methods*, pages 140–145, Santiago, Chile, 2013.
- [98] E. Tzirtzilakis. Biomagnetic fluid flow in a channel with stenosis. *Physica D: Nonlinear Phenomena*, 237(1):66 – 81, 2008.
- [99] M. Waheed. Mixed convective heat transfer in rectangular enclosures driven by a continuously moving horizontal plate. *International Journal of Heat and Mass Transfer*, 52(21):5055–5063, 2009.
- [100] L. Yao. Natural convection along a vertical wavy surface. *ASME J. Heat Transfer*, 105(3):465–468, 1983.
- [101] X. Zhang and M. Yang. Unsteady numerical computation of combined thermally and electromagnetically driven convection in a rectangular cavity. *International Journal of Heat and Mass Transfer*, 54(1):717–721, 2011.

CURRICULUM VITAE

PERSONAL INFORMATION

Surname, Name: Oğlakkaya, Fatma Sidre
Nationality: Turkish (TC)
Date and Place of Birth: 19 August, Konya
Phone: 090 312 2105382
Fax: 090 312 2101105

EDUCATION

Degree	Institution	Year of Graduation
Ph.D	Department of Mathematics, Middle East Technical University	2012-2018
M.Sc.	Mathematical Education, Selçuk University	2007-2010
B.Sc.	Mathematical Education, Selçuk University	2003-2007
High School	Meram Anatolian High School	1999-2002

PROFESSIONAL EXPERIENCE

Year	Place	Enrollment
2007-2010	Ministry of Education	Teacher
2010-2012	Department of Mathematics, Osmaniye Korkut Ata University	Research Assistant
2012-2018	Department of Mathematics, Middle East Technical University	Teaching Assistant and Researcher

PUBLICATIONS

International Journal Publications

- F.S. Oğlakkaya and C. Bozkaya (2016). MHD natural convection in a semi-annulus enclosure filled with water-based nanofluid using DRBEM. *Engineering Analysis with Boundary Elements*, 71, 151-163.
- F.S. Oğlakkaya and C. Bozkaya (submitted). Unsteady MHD mixed convection flow in a lid-driven cavity with a heated wavy wall. *International Journal of Mechanical Sciences*.

International Conference Proceedings

- F.S. Oğlakkaya and C. Bozkaya (2015). Mixed convection flow in a lid-driven cavity with hydromagnetic effect using DRBEM. Proceedings of Advances in Boundary Element and Meshless Techniques XVI-BETEQ 2015, Valencia, Spain (July 6-8), 44-49.
- F.S. Oğlakkaya and C. Bozkaya (2016). DRBEM solution to ferrofluid flow and heat transfer in semi-annulus enclosure in the presence of magnetic field. Proceedings of Advances in Boundary Element and Meshless Techniques XVII-BETEQ 2016, Ankara, Turkey (July 11-13), 107-112.
- F.S. Oğlakkaya and C. Bozkaya (2017). A numerical simulation of non-uniform magnetic field effect on ferrofluid flow in a half-annulus enclosure with sinu-

soidal hot wall. Proceedings of International Conference of Numerical Analysis and Applied Mathematics XIV-ICNAAM 2016, Rhodes, Greece, (September 19-25), 560067-(1-4).

- F.S. Oğlakkaya and C. Bozkaya (2017). MHD combined convection flow in a lid-driven cavity with sinusoidal wavy wall. Proceedings of The Eleventh UK Conference on Boundary Integral Methods XI-UKBIM-2017, Nottingham, UK (July 10-11), 152-159.
- F.S. Oğlakkaya and C. Bozkaya (2017). Heat transfer in an annulus enclosure under the influence of multiple magnetic sources. Proceedings of Ukrainian Conference on Applied Mathematics UCAM-2017, Lviv, Ukraine (September 28-30), 87-88.

International Conference Abstracts

- F.S. Oğlakkaya, and C. Bozkaya (2015). Natural convection of nanofluid flows in a semicircular annulus using DRBEM. Abstract book of European Conference on Numerical Mathematics and Advanced Applications-ENUMATH-2015, Ankara, Turkey (September 13-18), 200.

Posters Presented in National Workshops

- F.S. Oğlakkaya, and C. Bozkaya, Ferrofluid flow in a sinusoidal enclosure under the effect of nodal magnetic source, 3rd Women Mathematicians Association Workshop, İzmir, 27-29 May 2016.

RESEARCH INTEREST

Numerical Solutions to PDEs, Computational Fluid Dynamics, Magnetohydrodynamics and Ferrohydrodynamics.

NUMERICAL METHODS

Boundary Element Method (BEM), Finite Difference Method (FDM), Finite Element Method (FEM).

TEACHING EXPERIENCE

- Calculus with Analytic Geometry (Math 119), Department of Mathematics, METU.
- Calculus of Functions of Several Variables (Math 120), Department of Mathematics, METU.
- Basic Mathematics I (Math 125), Department of Mathematics, METU.
- Basic Mathematics II (Math 126), Department of Mathematics, METU.

FUNDING AND ACADEMIC PROJECTS

- C. Bozkaya (Coordinator), F.S. Oğlakkaya (Researcher) (January 2015-December 2016). Magnetohydrodynamic nanofluid and convective heat transfer. BAP-1, Department of Mathematics, Middle East Technical University, Project No: BAP-01-01-2015-002, Project Budget: 7000TL.

LANGUAGE SKILLS

English (Advanced), German (Beginner).

COMPUTER SKILLS

Office Programs (Word, Excel, PowerPoint), LaTeX, Matlab, Maplesoft.